

Derivation of sky luminance and spectral sky radiance from images taken with a CCD camera

Von der Fakultät für Mathematik und Physik
der Gottfried Wilhelm Leibniz Universität Hannover
zur Erlangung des Grades
Doktorin der Naturwissenschaften
Dr. rer. nat.
genehmigte Dissertation
von

M.Sc. Korntip Tohsing
geboren am 1. August 1977 in Roi-Et, Thailand

2013

Referent: Prof. Dr. Gunther Seckmeyer, Leibniz Universität Hannover

Korreferenter: 1. Associate Prof. Dr. Serm Janjai, Silpakorn University, Thailand
2. Associate Prof. Dr. Manuel Nunez, University of Tasmania,
Australia

Tag der Promotion: 15. November 2013

Abstract

This thesis demonstrates procedures for measuring sky luminance and spectral sky radiance from different meteorological situations in Hannover, Germany using digital photography. These radiation quantities are important for a better description in solar energy applications.

For a whole sky image acquisition, a new Hemispherical Sky Imager ([HSI](#)) system was designed and developed. The system consists of a commercial digital compact camera equipped with a fish-eye lens, which can provide the hemispherical sky image in three color channels (red, green, blue). A calibration using stars as reference points is performed to check the camera projection of the fish-eye lens. The projection of the camera system has been found to be nearly equidistant. High Dynamic Range ([HDR](#)) image composed from three different exposures of the same scene is proposed in order to overcome the limited dynamic range of the camera's sensor due to the direct sun light or very bright clouds.

Sky luminance is derived by applying the extracted digital counts from images and the careful calibration of the camera sensor in the laboratory. The luminance calibration parameters for determining luminance depend on the exposure times of the camera setting. High spatial and temporal resolutions of the sky luminance from the [HSI](#) images have been calculated and validated with the zenith luminance measured by a [CCD](#) array spectroradiometer during February - May 2012. The deviation between both instruments is less than 10% for cloudless and completely overcast skies and differs by no more than 20% for all sky conditions. The global illuminance is derived from the [HSI](#) and compared with the measured global illuminance by a luxmeter. For a solar zenith angle of less than 80° the comparisons show a deviation of global illuminance less than 5% for cloudless skies and under 20% for cloudy skies.

A non-linear regression technique is applied for reconstructing the spectral sky radiance in the visible wavelength region (380–760 nm) based on [HSI](#) images. The relationship between the measured spectral sky radiance from the [CCD](#) spectroradiometer and digital counts from the three color channels of the [HSI](#) images is found to be a third degree polynomial and the best correlation coefficient of the regression equation has been chosen to reconstruct the spectral sky radiance at each wavelength. The spectral sky radiance derived from the [HSI](#) system is validated with spectral sky radiance measurements from the [CCD](#) spectroradiometer for October 2012. The spectral sky radiance for complete distribution over the hemisphere between both instruments deviates by less than 20% at 400, 500 and 600 nm for all weather conditions and for zenith angles less than 80° . The reconstructed visible spectra at various directions deviate by less than 20% for all sky conditions. Therefore, the [HSI](#) system is capable of measuring sky luminance and spectral sky radiance in the visible with the high spatial and temporal resolutions of more than a million directions (pixels) and every 20 seconds accordingly.

Keywords: Sky luminance, spectral radiance, [CCD](#) camera, hemispherical image

Zusammenfassung

Diese Arbeit beschreibt den Prozess zur Bestimmung der Leuchtdichteverteilung und der spektralen Strahldichteverteilung bei unterschiedlichen Himmelsverhältnissen in Hannover, Deutschland mittels Digitalfotografie. Diese Strahlungsgrößen spielen eine große Rolle im Hinblick auf die effiziente Nutzung der Sonnenenergie.

Ein neues Messgerät zur bildlichen Erfassung des kompletten Himmels (Hemispherical Sky Imager ([HSI](#))) wurde entworfen und entwickelt. Das System besteht aus einer handelsüblichen digitalen Kompaktkamera, welche mit einem Fischaugenobjektiv ausgerüstet ist. Diese Kamera liefert das hemisphärische Himmelbild in drei Farbkanälen (rot, grün, blau). Eine Charakterisierung der Kameraprojektion des Fischaugenobjektivs, bei der Sternenpositionen am Himmel als Bezugspunkte dienten, wurde durchgeführt. Die Charakterisierung ergab, dass das HSI-System nahezu äquidistant abbildet. Um den beschränkten dynamischen Bereich des Kamera-Sensors bei direktem Sonnenlicht oder bei sehr hellen Wolken zu überwinden, wurde die High Dynamic Range ([HDR](#)) Darstellung verwendet, welche aus drei verschiedenen Belichtungen der gleichen Szene ermittelt wird.

Die Leuchtdichte wurde aus Bildern gewonnen, welche vom [HSI](#)-System mit Korrekturparametern aufgenommen wurden. Diese Korrekturparameter, welche durch eine Leuchtdichtekalibrierung im Labor ermittelt wurden, sind von der Belichtungszeit der Kameraeinstellung abhängig. Die hohe räumliche und zeitliche Auflösung der Leuchtdichte wurde aus [HSI](#)-Bildern ermittelt und mit Hilfe von Zenitleuchtdichtemessungen eines [CCD](#)-Array Spektroradiometers im Zeitraum von Februar bis Mai 2012, validiert. Die Abweichung zwischen beiden Geräten ist bei wolkenlosem und bei vollständig bedecktem Himmel kleiner als 10% und unterscheidet sich bei allen Himmelsverhältnissen um nicht mehr als 20%. Außerdem wurde die Beleuchtungsstärke aus [HSI](#)-Messungen ermittelt und mit der gemessenen globalen Beleuchtungsstärke eines Luxmeters verglichen. Dieser Vergleich zeigt bei einem Sonnenzenitwinkel von weniger als 80° eine Abweichung von weniger als 5% bei wolkenlosem Himmel und weniger als 20% bei bewölktem Himmel.

Eine nichtlineare Regressionstechnik wird für die Rekonstruktion der spektralen Strahlungsdichte im sichtbaren Wellenlängenbereich (380-760 nm), basierend auf [HSI](#)-Bildern, angewendet. Das Verhältnis zwischen der gemessenen spektralen Strahldichte vom [CCD](#)-Spektroradiometer und der digitalen Kenngröße von den drei Farbkanälen der [HSI](#)-Bilder liefert eine Regressionsgleichung dritter Ordnung. Diese Gleichung wurde für die Ermittlung der Strahldichteverteilung aus Countwerten der [HSI](#)-Kamera für jede Wellenlänge verwendet. Die spektrale Strahldichteverteilung vom [HSI](#)-System wurde mit der gemessenen spektralen Strahldichte vom [CCD](#) - Spektroradiometer für Oktober 2012 bewertet. Bei allen Wetterbedingungen weicht bei einer vollständigen Verteilung über die Hemisphäre und einem Zenitwinkel von weniger als 80° die spektralen Strahldichtemessungen beider Instrumente bei den Wellenlängen von 400, 500

und 600 nm um weniger als 20% ab. Die rekonstruierten Spektren verschiedener Zenit- und Azimutwinkel weichen bei allen Himmelsverhältnissen um weniger als 20% ab. Aufgrund der Untersuchungsergebnisse ist das HSI-System in der Lage die Himmelsleuchtdichte und die Spektralstrahldichte mit einer hohen räumlichen und zeitlichen Auflösung aus mehr als einer Million Richtungen (Bildpunkten) und alle 20 Sekunden zu bestimmen.

Schlagworte: Leuchtdichte, spektrale Strahldichte, CCD Kamera, hemisphärisches Bild

Contents

Abstract	I
Zusammenfassung	II
Contents	IV
1 Introduction	1
1.1 Motivation	1
1.2 Research Objectives	4
1.3 Synopsis	5
2 State of the Art	7
2.1 Basic Radiometric and Photometric Quantities	7
2.2 Charge Coupled Device (CCD) Camera	10
2.2.1 CCD image sensor basics	10
2.2.2 Encoding of Color	10
2.2.3 JPEG format and RGB Color system	11
2.2.4 Digital photography terminology	13
2.3 Photogrammetry in cloud and radiation measurements	16
3 Instrumentation	20
3.1 The CCD spectroradiometer	20
3.2 Skyscanner	23
3.3 Luxmeter	27
4 Development of Hemispherical Sky Imager (HSI) System	29
4.1 Design, development and features of the HSI system	29
4.1.1 Setup description of HSI	29
4.1.2 Camera housing	30
4.1.3 Camera element and optics	31
4.1.4 Computer and support software	32
4.1.5 Image results of the HSI system	32
4.1.6 Working Scheme for automatic image acquisition of HSI system	34
4.2 Camera sensor characterization	36
4.2.1 Geometric calibration	36
4.2.1.1 Camera projection for fish-eye lens	36
4.2.1.2 Camera distortion determination	38
4.2.1.3 Stars calibration	39
4.2.1.4 Results of the camera projection	40

4.2.2	Radiometric calibration	42
4.2.2.1	Dark current	43
4.2.2.2	Linearity	43
4.2.2.3	Spectral responsivity of CCD camera sensor	46
5	Use of the CCD Camera for Measuring Sky Luminance Distribution	49
5.1	Low and High Dynamic Range image acquisitions from HSI system	49
5.1.1	Low dynamic range (LDR) acquisition	50
5.1.2	High dynamic range (HDR) acquisition	51
5.1.2.1	Image capturing	51
5.1.2.2	HDR processing	52
5.2	Method	55
5.2.1	Conversion of radiance to luminance	55
5.2.2	Sky luminance from HSI images	56
5.2.3	Quality control of luminance data	59
5.3	Results	63
5.3.1	Comparison of sky luminance distribution between the CCD spectroradiometer and HSI system	63
5.3.1.1	Diurnal zenith sky luminance	63
5.3.1.2	Daily averaged zenith sky luminance	69
5.3.1.3	Sky luminance distribution	71
5.3.2	Comparison of global illuminance between the luxmeter and the HSI system	76
5.3.2.1	Diurnal global illuminance	77
5.3.2.2	Daily averaged global illuminance	81
5.4	Remark and discussion	83
6	Reconstruction of Spectral Sky Radiance from the CCD Camera	85
6.1	Data	85
6.2	Regression analysis for spectral sky radiance reconstruction	86
6.3	Spectral Estimated Results and Discussion	88
6.3.1	Regression coefficients and models	89
6.3.2	Spatial comparison of spectral radiance distribution at 400 nm, 500 nm and 600 nm	94
6.3.3	Comparison of spectral radiance distribution	100
6.4	Remark and Discussion	103
7	Conclusions	104
7.1	The HSI System	104
7.2	Sky luminance distribution	105
7.3	Spectral sky radiance distribution	105
7.4	Future work	106
	List of Symbols	108

Contents

List of Acronyms	109
Bibliography	110
A The spherical mirror system	121
B Additional Setup of HSI system at NIWA	123
C Monthly averaged global illuminance	125
D Instruction of image automation	126
List of Figures	VII
List of Tables	X
Acknowledgment	XI
Danksagung	XII

1 Introduction

1.1 Motivation

Solar radiation is the Earth's main source of energy for running the dynamical processes within the atmosphere and for life on the Earth [LIU, 2002]. This incoming energy can be best quantified by spectral sky radiance measurements, which provide both spectral and spatial information of the radiation field. The knowledge of spatial and spectral sky radiance distribution is important for many applications. For example, the sky radiance is used for studying the optical properties of mineral dust [LI et al., 2007] and bidirectional reflectance distributions [DEERING and ECK, 1987]. The optical thickness and the size distribution of aerosols were derived from the measured sky radiance using inversion algorithm [DUBOVIK and KING, 2000]. The aerosol phase function and single scattering albedo can be determined from the sky radiance as well [VERMEULEN et al., 2000]. Furthermore, the spectral sky radiance is also used for the computation of the irradiance on surfaces [LI and LAM, 2004], which is applied on design and performance investigations of spectral selective energy devices, such as photovoltaic (PV) systems [HERNÁNDEZ-ANDRÉS et al., 2001; STEVEN and UNSWORTH, 1977].

Clouds have the strongest impact on solar and terrestrial radiation by decreasing the direct radiation and increasing the diffuse radiation, which leads to a decrease of global radiation [POETZSCH-HEFFTER et al., 1995; QUANTE, 2004]. On the other hand, clouds can also enhance the solar radiation at the surface [PIACENTINI et al., 2011]. The solar radiation affected by clouds at the ground may be higher than the radiation in cloudfree condition [SCHAFER et al., 1996]. Clouds attenuate the solar radiation with a significant spectral dependence, which is weaker at the shorter wavelengths [FOYO-MORENO et al., 2001; DE MIGUEL et al., 2011]. Despite their great importance, investigations on sky radiance with clouds are still necessary for a better understanding of cloud-radiation interaction.

The variation of the sky radiance has been observed and analyzed under different climates and sky conditions by using several types of instruments. One of the first spectral sky radiance measurements was reported by KNESTRICK and CURCIO (1970). The spectral sky radiance data was obtained from the rectangular part of the horizon sky under various weather conditions and at different solar positions. The spectral radiance of the horizon sky was found to be a function of the solar zenith angle (SZA), solar azimuth angle, humidity, cloud cover and visibility. BLUMTHALER et al. (1996) conducted the spectral sky radiance at various locations in Europe for investigating a variety of atmospheric conditions. A variation of the spatial sky radiance distribution in the UV-A was up to a factor of 10 but decreased by a factor of 2 in the UV-B. Furthermore, a distinct minimum of sky radiance depended on the

SZA, but not on the wavelength.

NAGATA (1997) measured the radiance distribution on overcast skies, which were classified into two groups: stable and fluctuating overcast skies. The study showed that the radiance distribution pattern of a stable overcast sky could be characterized by an equation similar to the CIE standard overcast sky for luminance distribution. Moreover, the observed zenith radiance was mostly greater than any other sky elements in a stable overcast sky.

RICCHIAZZI et al. (2000) presented measured sky radiance at a high-latitude and coastal site under clear and cloudy conditions, with an all-sky camera and a narrow field-of-view spectroradiometer. The results from these observations were compared with computational results using a 3D Monte-Carlo radiation model. The sky radiance distribution from the measurement showed good agreement with modelled results and roughly mirrors the spatial distribution of surface albedo.

WEIHS et al. (2000) performed the measurements of sky radiance distribution under different sky conditions by using a spectroradiometer connected to a tube with 1° field of view mounted in a tracker, to cover a full sky radiance distribution. Radiance from cloudy sky locations was either higher by a factor up to of 2.5 or lower with minimum values at only 8% of the cloudless radiances.

HUBER et al. (2004) presented spectral sky radiance measurements over a snow-covered surface at an Alpine site. Due to the mountainous surroundings, the ground was not homogeneously covered with snow. The comparison between the measured spectral sky radiance and the results from a 1D radiative transfer model showed that for the homogeneously snow-covered terrain case, the diffuse sky radiance was reduced up to 40% when the snow melted and was dependent on solar zenith angle. They also indicated that diffuse sky radiance measurements in a low aerosol environment were especially valuable for the assessment and validation of radiative transfer models.

WUTTKE and SECKMEYER (2006) performed the spectral sky radiance measurements of snow-covered surfaces in Antarctic environments in order to investigate the impact of high snow albedo on the sky radiance. The measurements showed that sky radiance distribution over the sky became less homogeneous when the wavelengths increase. These results were confirmed by the results obtained from the LibRadtran radiative transfer model. The sky radiance at the horizon was only about 80% of the zenith sky radiance for a SZA of 86° and 305 nm. At 1000 nm, the sky radiance, which was measured from the opposite the position of the sun exceeded the zenith sky radiance by a factor of 11.

A recent study, PISSULLA et al. (2009), presented an intercomparison of spectral radiance measurements in the UV and visible wavelength with high spectral resolution. These measurements were conducted by using five different instruments from three locations (Izaña, Thessaloniki and Innsbruck). The deviation of the measured spectral sky radiance varied between 3% and 35%, which depends on the wavelength, location and the instruments.

Most of these spectral radiance observations have been compared with the results from a radiative transfer model. These comparisons were mostly under clear sky con-

ditions and under partly cloudy conditions. However, the equipments for measuring spectral radiance distributions are relatively non-mobile and expensive which leads to insufficient spectral radiance data.

Spectral sky radiance is related to other quantities such as the sky luminance, which contains only the information about the spatial distribution of visible solar radiation. The sky luminance provides the daylight or visible light information, which is a natural and renewable energy source. Visible light is defined as the radiation of wavelengths between approximately 380 and 780 nm [CIE, 1970]. Daylight has positive effects on the human psyche [VAN BOMMEL and VAN DEN BELD, 2004; HESCHONG, 2002], which can enhance good vision, safety and productivity. A certain part of visible light such as short wavelength blue radiation regulates the circadian system, positively affecting occupant alertness and mood during the working hours [WEBB, 2006]. In addition, luminance data does not only have a positive effect on humans but also is important for risk assessment of the eye exposure to blue light in outdoor activities [HIETANEN, 1991].

Artificial light is often used to compensate for a lack of proper illumination inside buildings and leads to the increase of the electrical energy consumption. Electricity consumed by lighting accounts for approximately 20% to 30% of the total electricity used in commercial office buildings [ANDER, 2003; KRARTI et al., 2005]. It has been estimated that 20% of the energy consumption could be saved with the improvement of the energy efficiency and development of the renewable and alternative energy sources [EUROPEAN COMMISSION, 2005]. To save the electricity (or energy), most modern buildings are significantly designed by considering the daylight utilization [VARTIAINEN, 2001; YANG and NAM, 2010]. Combination of appropriate energy-efficient lamps and lighting control systems, which is properly linked to daylight, can reduce the electrical demand [KURIAN et al., 2008]. Therefore, the knowledge of sky luminance distribution is an important input quantity to use daylight in desingning energy-efficient buildings.

Therefore, monitoring stations have been established to collect luminance data [FERRARO et al., 2011; KITTLER et al., 1992]. Sky luminance data has been measured in a number of places under the International Daylight Measurement Project (IDMP) [CIE, 1994]. However, due to the cost of daylight instruments and the need of scanning components, the number of stations performing luminance measurements are limited. Thus, many researchers have developed models to determine the sky luminance distribution for different weather conditions.

Commission International de l'Éclairage (CIE) promoted a simplified model as a CIE Standard Overcast Sky in 1955. KITTLER (1967) proposed a model, which was accepted as CIE Standard Clear Sky in 1973 [CIE, 1973]. NAKAMURA et al. (1985) presented an intermediate sky and different sky luminance models, which were also proposed by other authors in the past decades [IGAWA et al., 1999; LITTLEFAIR, 1990]. KROCHMANN and SEIDL (1974), SOLER and GOPINATHAN (2000) presented that the zenith luminance was expressed as a function of the solar elevation for varying turbidity factor.

Advanced sky luminance models proposed by different authors offer more comprehensive description of the real sky conditions. [PEREZ et al. \(1993\)](#) classified a sky into eight categories and proposed the All-sky weather models of the sky luminance distribution as a function of sky clearness and sky brightness. [IGAWA et al. \(1999\)](#) also presented the classification of the all sky condition and All Sky model as a standard sky luminance distribution. [IGAWA et al. \(2004\)](#) proposed the sky luminance distribution and sky radiance distribution models for all-sky weather conditions. Clear sky index was defined based on the global irradiance, whereas cloudless sky index was calculated based on global and diffuse irradiance. [DARULA and KITTLER \(2002\)](#) described the relative sky luminance distribution and sky parameterization of the fifteen standardized patterns (CIE general sky standard). [JANJAI et al. \(2008\)](#) presented the classification of the sky condition using the satellite data for modeling the sky luminance.

According to their great importance and the insufficiency of the sky luminance and sky radiance measurements, some investigations with the photography for measuring luminance and radiance have been performed and presented. Moreover, the popularity of [CCD](#) cameras during the last 10 years, increases the application of digital cameras in scientific investigations. Acquiring high spatial resolution images and analyzing them in near real time become possible.

1.2 Research Objectives

The aim of this thesis is to measure the sky luminance and spectral sky radiance using digital images in order to attain spectral and temporal variations by these solar radiation quantities. The main objectives in this work can be divided into two parts.

Technical objectives:

1. The ground-based Hemispherical Sky Imager ([HSI](#)) system, which is a mobile and low price instrument, is designed and developed in order to observe the sky hemisphere at Institute of Meteorology and Cilmatology ([IMuK](#)), Hannover and National Institute of Water and Atmospheric Research ([NIWA](#)), New Zealand.
2. To setup an automation image acquisition in both stations for further investigations of solar radiation and meteorological quantities.
3. To characterize the geometric and radiometric behaviors of the camera sensor, which was employed in this work.

Scientific objectives:

4. To determine the sky luminance distribution from the [HSI](#) system under different sky conditions ranged from cloudless, broken clouds to complete overcast skies.

5. To derive the spectral sky radiance in the visible wavelength (380 nm - 760 nm) from the [HSI](#) images under all weather conditions.
6. To validate and characterize the camera-based sky luminance and spectral sky radiance distributions with the measurements by the [CCD](#) spectroradiometer.

For the first technical objective, the new [HSI](#) system providing the complete sky hemisphere is designed. This system consists of a digital compact [CCD](#) camera equipped with a fish-eye lens, in which the appropriate camera sensor must be chosen. The weatherproof housing of this system must be built from the suitable materials. Extreme weather conditions through out the year must be stabilized by temperature stabilization, which has been carefully tested to prevent some technical problems, e.g. the condensation inside the housing. This unit needs to collect the images continuously for a whole year, therefore, a huge number of images must be managed and stored. This can be done by an image acquisition routine, which can capture, transfer and store images automatically. This routine must be able to delete nighttime images automatically as well. These two objectives are based on the suggestion of Prof.Dr. Gunther Seckmeyer. The last technical objective refers to determine some general properties of the [CCD](#) camera sensor. A camera projection function, which describes the geometry of the camera sensor, has to be characterized as well as the radiometric calibration including dark current, linearity and spectral response.

The first scientific objective aims at determining the sky luminance distribution from the [HSI](#) system under various sky conditions. Based on the digital counts extracted from images and the calibration, the sky luminance is estimated. Simultaneously, the spectral sky radiance, which will be converted to sky luminance, is measured for the validation. After that the technique for derivation of the spectral sky radiance in the visible wavelength from the discrete bands of the [HSI](#) system is analyzed. Some researches have been successfully estimated the sky luminance and spectral sky radiance from images, but most of them were not compared with the accurate field measurements from various weather conditions. In this thesis these two quantities will be compared with the [CCD](#) spectroradiometer under all weather conditions. This should fulfill the last scientific objectives of this work. These scientific objectives are based on the suggestion of Prof. Dr. Gunther Seckmeyer and were always discussed in the solar radiation and remote sensing working group.

1.3 Synopsis

This thesis starts with the basic radiometric and photometric quantities and gives the background information of solar radiation. The introduction of the [CCD](#) sensor and the terminology in photography are presented briefly. An overview of the sky luminance and spectral sky radiance by using photography is given in Chapter 2.

Chapter 3 aims to describe the existing instruments at IMuK such as the CCD spectroradiometer, Skyscanner and luxmeter gathered the related data for model analysis and validation during this thesis work.

In order to provide a real-time sky hemisphere, the development of the new all-sky camera system owned by IMuK will be introduced. The description of the current HSI system will be given. In last part of the Chapter 4, the geometric and radiometric characterizations of the HSI system are described.

In Chapter 5 an approach for measuring sky luminance distribution from the images acquired by the HSI system is introduced. Starting with the purpose of the High Dynamic Range (HDR) image composition and then the luminance derivation technique is purposed. The resulting comparisons of the predicted sky luminance from the HSI system with the sky luminance measurement conducted by the CCD spectroradiometer are presented and discussed.

Chapter 6 presents a methodology for reconstructing the spectral sky radiance from images of the HSI system in visible spectrum (380 nm - 760 nm). The camera-based and measured spectral sky radiance will be compared and presented to complete this chapter.

Chapter 7 contains the concluding remarks and a brief summary of the HSI itself. Summarized discusses and possible suggestions for the sky luminance and spectral sky radiance measurements with the HSI system are given.

Remark: most results from the determination of the luminance distribution and geometric calibration of the HSI system, which will be presented in the Chapter 4 and Chapter 5, were already published in:

*Tohsing, K., M. Schrempf, S. Riechelmann, H. Schilke and G. Seckmeyer, 2013: Measuring high-resolution sky luminance distributions with a CCD camera. - **Applied Optics**, 52, 8, 1564-1573.*

Most results in Chapter 6 were already submitted for publishing on September 30, 2013 in:

*Tohsing, K., M. Schrempf, S. Riechelmann and G. Seckmeyer,: Spectral and spatial sky radiance distributions in the visible wavelength obtaining from three discrete bands CCD camera. - **Atmospheric Measurement Techniques**.*

2 State of the Art

This chapter consists of three parts. The first part provides background information of the radiometric and photometric quantities to support the comprehension of this study followed by the description of the charge coupled device (CCD) sensor and some necessary terminologies in photography. A brief summary about the previous photogrammetric research works on cloud and radiation measurements, especially on spectral sky radiance and the sky luminance measurements are introduced in the last part of the chapter.

2.1 Basic Radiometric and Photometric Quantities

The optical measurement technique can be roughly divided into two areas: photometry and radiometry. The radiometric and photometric quantities defined in this work are based on the Deutsche Industries Norm [DIN 5031, 1982] and International Commission on Illumination [CIE, 2011].

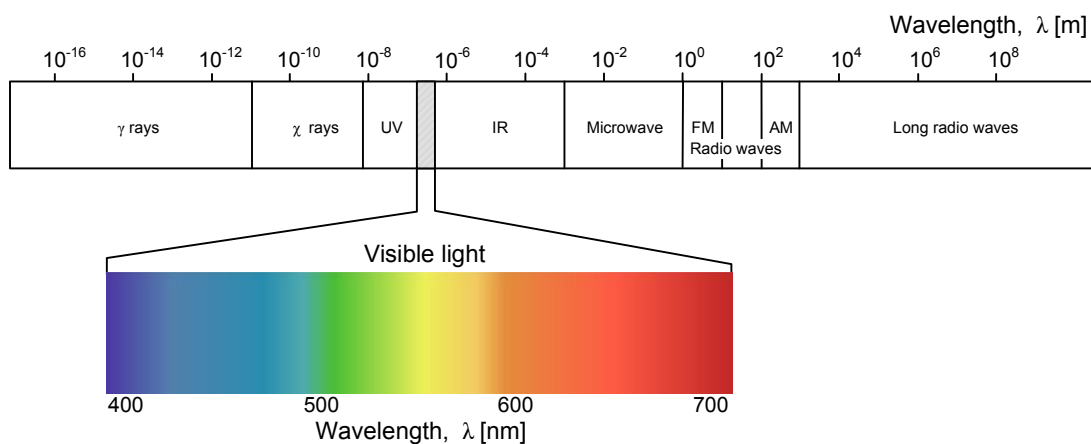


Figure 2.1: Spectrum of the electromagnetic radiation in terms of wavelength (m). The enlarge spectrum represents the visible spectrum (adapted from LIOU (2002)).

Radiometry is the measurement of the energy content of electromagnetic radiation, whose wavelength is ranging from ~ 10 nm to ~ 1 mm. These regions cover the Ultraviolet (UV), Visible (VIS) and Infrared (IR) parts of the electromagnetic spectrum as shown in Figure 2.1 and they are called both light and solar radiation [LIOU, 2002]. The main part of the spectrum investigated in this work is visible spectrum defined from wavelength approximately 380 nm to 780 nm [CIE, 1970].

The basic radiometric quantity is the **radiant energy** Q , which is defined as the energy emitted, transferred or received in the form of electromagnetic radiation. Its common unit is Joule (J). From the radiant energy all following quantities are derived.

1. The **radiant flux** or **radiant power** ϕ is the total power emitted or received (energy per unit time t) at the detector in the form of electromagnetic radiation:

$$\phi = \frac{dQ}{dt}, \quad [\phi = 1W], \quad (2.1)$$

where dQ is the emitted or received energy.

2. The incident of the radiant flux ϕ of electromagnetic radiation on a given element of surface per unit area dA is called **irradiance** E :

$$E = \frac{dQ}{dA}, \quad [E = 1\frac{W}{m^2}]. \quad (2.2)$$

3. The **radiant exitance** M is the radiant flux ϕ of electromagnetic radiation emitted by a source from a given surface per unit area dA :

$$M = \frac{dQ}{dA}, \quad [M] = 1\frac{W}{m^2}. \quad (2.3)$$

4. The definition of the **differential solid angle** $d\Omega$ provided for the following quantities is depicted in Figure 2.2. This illustrates the relationship between the spherical coordinates θ , φ and $d\Omega$:

$$d\Omega = \frac{d\sigma}{r^2} = \sin\theta d\theta d\varphi, \quad [d\Omega] = 1\frac{m^2}{m^2} = 1sr. \quad (2.4)$$

5. The radiance flux ϕ emitted by a source in a differential solid angle $d\Omega$ in a given direction defines the **radiant intensity** I :

$$I = \frac{d\phi}{d\Omega}, \quad [I] = 1\frac{W}{sr}. \quad (2.5)$$

6. The **radiance** R is finally defines as the radiant flux ϕ per surface element dA and per differential solid angle $d\Omega$:

$$R = \frac{d^2\phi}{dAd\Omega\cos(\varepsilon)}, \quad [R] = 1\frac{W}{m^2sr}, \quad (2.6)$$

where ε is the angle between the direction of the beam and the normal of surface element.

7. The **spectral radiance** R_λ describes the spectral distribution of radiation referred to by wavelength:

$$R_\lambda = \frac{dR}{d\lambda}, \quad [R_\lambda] = 1\frac{W}{m^2srnm}. \quad (2.7)$$

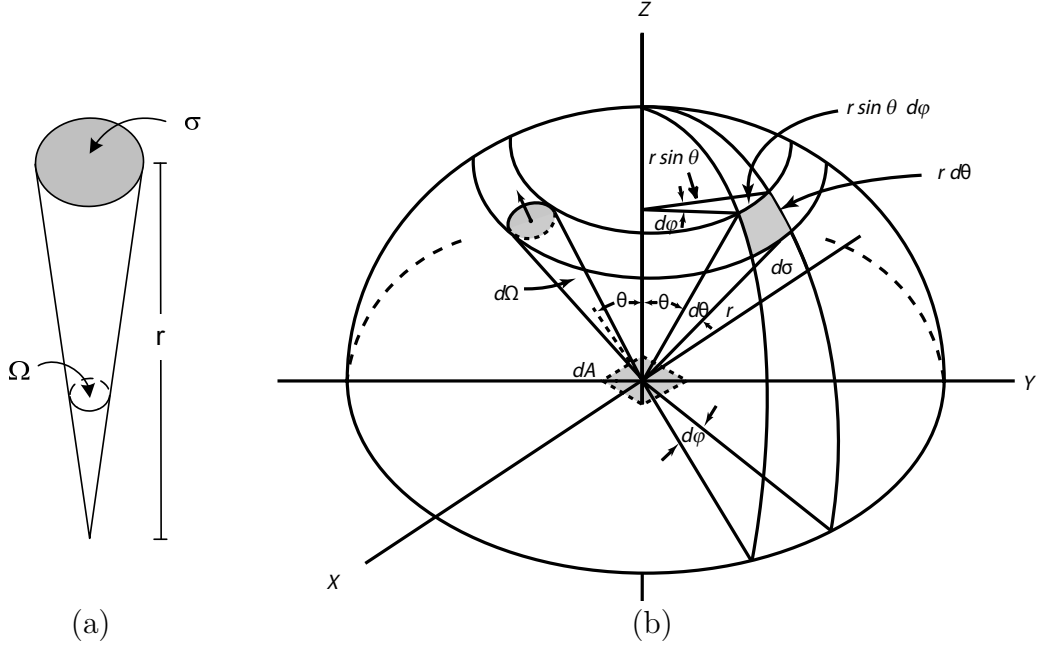


Figure 2.2: (a) Definition of a solid angle Ω , where σ is the area and r is the distance. (b) The illustration of the differential solid angle $d\Omega$ in spherical coordinate θ and ϕ , which denote the zenith and azimuth angle respectively (adapted from [LIU \(2002\)](#)).

Another way to describe a field of radiation is based on the photometric unit **candela** (cd). The candela is the luminous intensity, in a given direction, of a source that emits monochromatic radiation of frequency $540 \cdot 10^{12}$ Hz and that has a radiant intensity in that direction of $\frac{1}{683} \text{ W sr}^{-1}$ [[CIE, 2011](#)]. The following definitions are based on international commission on illumination [[CIE, 2011](#)]:

1. The photometric equivalent of radiant power is luminous flux ϕ_ν derived from the spectral radiance flux by evaluating the radiation according to its action upon the [CIE](#) standard photometric observer:

$$\phi_\nu = K_m \int \phi(\lambda) V(\lambda) d\lambda, \quad [\phi_\nu] = 1 \text{ cdsr} = 1 \text{ lm}, \quad (2.8)$$

where V_λ is the daylight spectral response of the human eye. K_m is the luminous efficacy for photopic vision, which corresponds to the approximately wavelength $\lambda = 555$ nm and is defined as 683 lm/W.

2. **Luminous intensity** I_ν is a photometric equivalent to radiant intensity defining as the luminous flux per differential solid angle $d\Omega$:

$$I_\nu = \frac{d\phi_\nu}{d\Omega}, \quad [I_\nu] = 1 \frac{\text{lm}}{\text{sr}} = 1 \text{ cd}. \quad (2.9)$$

3. **Luminance** L_ν is the photometric equivalent to radiance and is defined as luminous flux ϕ_ν per unit area dA and per differential solid angle $d\Omega$:

$$L_\nu = \frac{d\phi_\nu}{dAd\Omega\cos(\varepsilon)}, \quad [L_\nu] = 1 \frac{lm}{m^2sr} = 1 \frac{cd}{m^2}. \quad (2.10)$$

where ε is the angle between the normal of surface element dA and the direction of luminance.

4. **Illuminance** E_ν is a photometric equivalent to radiant intensity defining as the luminous flux per unit area dA :

$$E_\nu = \frac{d\phi_\nu}{dA}, \quad [E_\nu] = 1 \frac{lm}{m^2} = 1lx. \quad (2.11)$$

2.2 Charge Coupled Device (CCD) Camera

The charge coupled device (CCD) was firstly introduced by Boyle and Smith in 1970 [SHORTIS and BEYER, 1996]. It has been developed primarily as a compact image sensor for costumer and industrial market. Nowadays it is widely developed for the visible and ultraviolet wavelength image sensor in many fields of scientific research. In this subsection, the concept of the CCD sensor and the color system used in the camera sensor will be introduced.

2.2.1 CCD image sensor basics

The CCD works with a photoelectric effect, which converts incoming light into a pattern of electronic charge in a silicon ship. This pattern of charge will be converted into a video waveform, digitized and stored as an image file.

The CCD sensor consists of large arrays of thousands or millions of light-sensing elements commonly called pixels. In the photo-sensitive area of each pixel, light directed from the camera lens is converted into electrons that is collected in a semiconductor bucket. The photo sensor acts like a bucket and accumulates the electron charge in the same way as the bucket collects the water. More light enter, more electrons come into the bucket. These buckets of charges are passed through vertical and horizontal shift registers and the signal will be out of the photo sensitive area and off the chip itself. The accumulated charge is an output as a voltage signal. The result from charge-to-voltage conversion is a very weak voltage and must be amplified before it can be handled off to the camera circuitry.

2.2.2 Encoding of Color

The pixels in an image sensor accumulate an electrical charge that is proportional to the intensity of incident light as described above. This provides information about brightness, but not about color. Therefore, a color filter array is placed on the top of

the sensor to capture red, green and blue components of light falling on the sensor as illustrated in Figure 2.3(a) and each pixel on the sensor lets only one wavelength of light pass through, allowing it to record only one color. Most modern digital cameras encode color by using a Bayer array. The Bayer pattern (see Figure 2.3(b)) is 50% green because the human eye is more sensitive to the green region of the spectrum [JOHNSON, 2010]. To create a full color image, the image processor of the camera interpolates the actual color of each pixel by looking at the brightness of the color recorded by it and the other neighboring pixel around it. This can slightly affect image quality but it is hardly noticeable on today’s high resolution cameras.

The red, green and blue color can be combined to generate other colors using a RGB color system. This will be explained in Subsection 2.2.3.

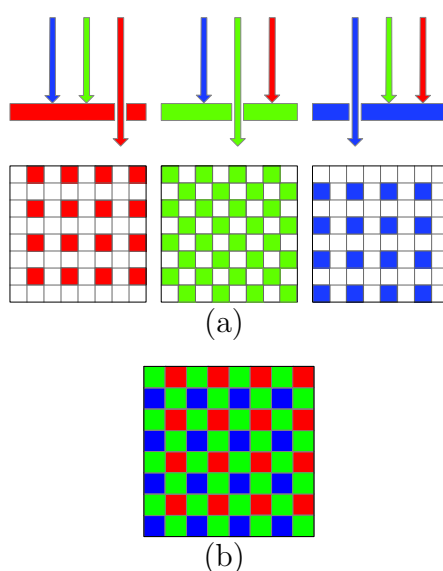


Figure 2.3: (a) Color filter array on the top of each pixel, which lets only one wavelength to red, green and blue light pass through. (b) The Color encoding from the Bayer array.

2.2.3 JPEG format and RGB Color system

In photography many image types are used to save the digital photo and an important concept which distinguishes many image types is whether they are compressed. The compression method is usually lossy meaning that some original image information are lost and cannot be restored, possibly affecting the image quality. JPEG format is a selectable compressing format. JPEG stands for ‘Joint Photographic Experts Group’ and was specifically developed for storing the photographic images.

The JPEG standard ISO/IEC 10918-1 (1994) specifies the codec, which how an image is compressed or decompressed. These codecs define different modifications for the JPEG. The differences are described by the bit depth or color depth, which refers to the color information stored in a JPEG image ranging from 2-bit to 16-

bit. The higher the bit depth of an image, the more colors it can store. An 8 bits encoding is commonly used as the output format in the most digital cameras as well as the working camera in this thesis. A degree of the compression influences the image size and image quality. High image quality can deliver the image with small compression and it might be more suitable for the scientific purposes. However, the image containing the maximum quality of 100% still compresses and it is no lossless image.

Lossless image is an uncompressed digital photo that store image data exactly the way the image was captured by the camera sensor and is called **RAW** image format. Nowadays, this format is supported in most digital compact camera and the digital single-lens reflex (**DSLR**) camera. Since it is not compressed, it significantly takes more disk space than **JPEG**, which is usually at least twice of that **JPEG**. However, its quality is higher than **JPEG** with the original image details. Because raw image format stores raw image data directly as it captured, cameras made by different manufacturers save raw images in different formats.

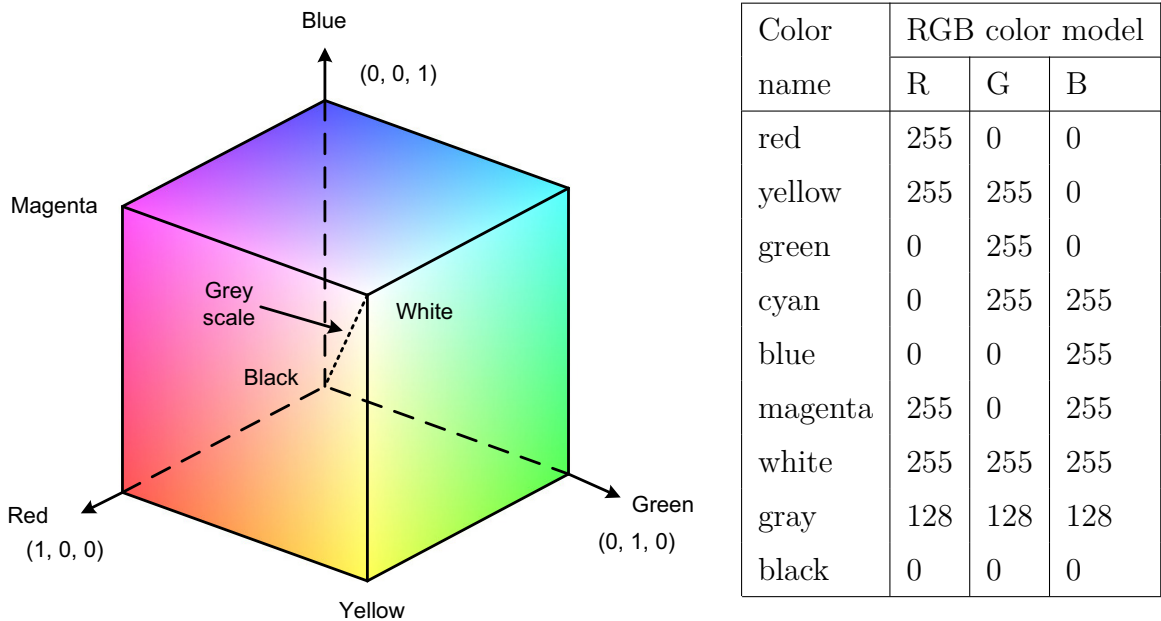


Figure 2.4: **RGB** color model presented by a cube illustration (adapted from [WYSZECKI and STILES \(2000\)](#)). The unit of the **RGB** color cube is given in [%]. Therefore, the coordinate (0,0,1) describes (0%, 0%, 100%) or (0,0,255) and indicates the blue color. Examples of counts for different colors represented in **RGB** color model are list in a table on the right.

As described in Section 2.2.2 the sensors subtypes directly represent the three color channels red, green and blue, therefore, the record information for each sensor channel

of the JPEG image format can be interpreted by the RGB color model [WYSZECKI and STILES, 2000]. The RGB color model is an additive color system comprising of three components, red (R), green (G) and blue (B), the so-called primary colors. Each color channel or component consists of a certain number of integer values, the so-called counts, which can be determined the bit depth of the image. In the 8-bit encoding, there are 256 counts from 0 to 255 [PENNEBAKER and MITCHELL, 2004], which represent the gradation of the brightness for each channel. For example, in the red channel, $Count_r(0)$ is the black color and $Count_r(255)$ is the bright red as shown in Figure 2.4 illustrated the cube of color space. A color in the image is obtained by mixing the three base colors, depending on how much the color takes from each base color.

In Figure 2.4, along the axis pure base colors are red (R), green (G) and blue (B). Each coordinate has a codomain of [0,255]. Complementary colors of the base colors can be found as additive mixtures of the respective other base colors: cyan (C), magenta (M) and yellow (Y). The line that $R = G = B$ are shades of gray ranging from black (S) to white (W). Table on the right of the Figure 2.4 presents several of different color creating from the primitive three colors.

2.2.4 Digital photography terminology

The following terms used in this thesis and in photogrammetry in general are defined below. They are supposed to provide the necessary information for a better understanding of the context.

Exposure time

The exposure time is the time a camera's shutter is open to allow light to reach the CCD camera sensor. It is one parameter that determines the brightness of an image. 'Exposure time' and 'shutter speed' refer to the same concept, where a shorter exposure time means a faster shutter speed. In photography, the exposure time is given in second, e.g. $\frac{1}{200}$ s, $\frac{1}{100}$ s, $\frac{1}{50}$ s, $\frac{1}{20}$ s, or 1 s etc. Figure 2.5(a) illustrates various exposure times of the camera setting including the images taken with their exposure times (see similar illustration in CURTIN (2003)). During the daylight, exposure times of 0.001 to 0.01 seconds produce adequate images. Exposure times of less than 0.001 seconds make the image appear too dark, they are underexposed, whereas exposure time of more than 0.01 seconds lead to bright images, they are overexposed. The maximum exposure time of Canon Powershot S5IS and G10, which are operated in this work, is 15 second that allows capturing the stars at night.

Aperture

The aperture is referred to the lens diaphragm opening that regulates amount of the incidence light passing through the optical system or lens. Together with the exposure time it controls how much light reaches the CCD sensor. The size of an aperture in a lens can either be fixed or adjustable. Aperture size is usually

calibrated in f-number or f-stops, i.e. $f/22$, $f/16$, $f/11$, $f/8$ etc. In Figure 2.5(b) shows the aperture opening size corresponding to various f-number and its impacts on the images. As the aperture number gets smaller (for example, from $f/16$ to $f/11$), the aperture opening gets larger. Therefore, more light is allowed to reach the sensor, which can make an image to be brighter. On the other hand, the greater the aperture, e.g. from $f/8$ to $f/11$, the darker the image.

ISO number

The ISO number determines how sensitive the camera is to the incoming light. Lower numbers such as 80 or 100 represent a relatively low sensitivity and higher numbers such as 400 or above lead the higher sensitivity. A lower ISO number is almost always desirable, since higher ISO numbers dramatically increase the noise on image. With compact cameras, an ISO number in the range of 50-200 generally produces acceptable low image noise [SHORTIS and BEYER, 1996].

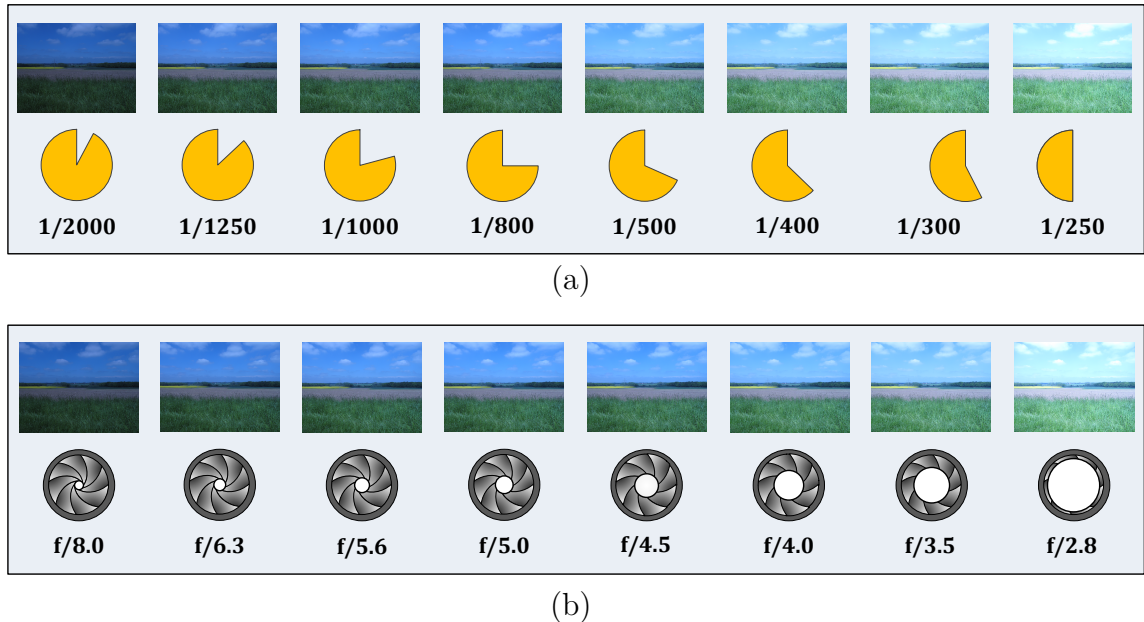


Figure 2.5: (a) Various exposure times representing how long the shutter of the camera will be opened or closed, which permitted the incoming light enters the camera sensor. Upper panel presents their corresponding images taken with these exposure times. (b) Aperture setting corresponding to various f-number and their images taken with different apertures.

EXIF

The exchangeable image file format (EXIF) is information that specifies the format for images used by the digital camera. The metadata tags defined in the EXIF cover the most important information that will be applied for the further calculation in this work such as the taken date and time as well as the camera settings, which normally

refer to aperture, exposure time, and ISO number information.

Focal length or zoom

The focal length or zoom is the distance between the optical center of the lens and the image sensor. The shorter the focal length, the wider the field of view it offers and the higher level of distortion it may cause. In contrast, the longer the focal length, the smaller the viewing area and the smaller the viewed object.

Resolution

The term resolution is used to describe the number of dot or pixel count horizontally and vertically in digital imaging. These are multiplied to give the total Mega or million pixels resolution. For Canon powershot G10 the maximum resolution is 4416x3312 pixels or about 14 Megapixels. Higher resolutions mean that more pixels are used to create the image resulting in a high quality of image.

Dynamic Range

The dynamic range in photography often describes the ratio of the luminance from the brightest and the darkest areas in the scene [HOEFFLINGER, 2007]. The luminance of the star is about 0.001 cd/m^2 and the sun is approximately $1,000,000,000 \text{ cd/m}^2$ [MCCOLLOUGH, 2008]. The human eye is capable of seeing a real world scene more than a camera can capture in a single image. An average sunlit can have the dynamic range of 100,000:1, which means that the brightest area is 100,000 times brighter than the darkest area. The wide dynamic range allows more details of the scenery is to be captured.

In Table 2.1, the dynamic range of different displays or capture types has been listed. For digital cameras, the dynamic range is limited by the CCD sensor and analogue digital converter (ADC) [ROBERTSON et al., 2003]. Therefore, many methods to create a high dynamic range image in the digital photography have been developed and purposed.

Table 2.1: Dynamic range of typical items [MCCOLLOUGH, 2008].

Display or capture type	Capable dynamic range
Human eye	1,000,000 : 1
Sunshine	100,000 : 1
Negative film	1,000 : 1 – 2,000 : 1
Computer monitor	500 : 1
DSLR camera	300 : 1
High quality glossy print	200 : 1
Compact digital camera	100 : 1
Slide file	64 : 1
High quality matte print	50 : 1

2.3 Photogrammetry in cloud and radiation measurements

Photogrammetry is the science of obtaining reliable information about the properties of surface and objects without physical contact with the object, and then measuring and interpreting this information by using photographs [LINDER, 2006]. Nowadays, the use of photogrammetry enhances the operations of a broad range in the engineering and infrastructure, scientific applications, architectural buildings, environmental and forestry biometric applications, as well as biological or physical processes [KRAUS, 2004].

Clouds play an important role on the Earth's climate and the solar energy application. To understand the effect of clouds and their temporal variation on the radiation quantities, many researchers have worked with cloud photographs to derive cloud parameter, especially in climatological research. Analog stereo images of clouds have already been taken and analyzed for over one hundred years ago [KOPPE, 1896]. With the introductory and development of the digital camera technology provides the automatic ground-based cloud photogrammetry. The Whole Sky imager (WSI) was the first field measurements of clouds with a digital imager developed by the Scripps Institute of Oceanography at University of California San Diego (UCSD). WSI acquires images in the visible and near infrared wavelengths, by using a fish-eye lens [SHIELDS et al., 1999]. With advanced technology, the WSI can also deliver radiance at various distinct wavelengths. Another well-know digital cloud imager is the Total Sky Imager (TSI), which captures daytime sky images via a solid-state CCD imager by looking vertically downward on a spherical mirror that reflects the sky hemisphere [PFISTER et al., 2003].

Most researchers take images of the sky hemisphere in order to derive cloud parameters. Several imaging systems have been successfully used to retrieve information on cloud cover and have also been validated with synoptic observations or other instruments [CAZORLA et al., 2008; FEISTER et al., 2010; HUO and LU, 2012; KREUTER et al., 2009]. A relationship between digital count values of the red and blue channels of hemispherical images named sky index was defined to derive cloud cover described in YAMASHITA et al. (2004). HEINLE et al. (2010) proposed a fully automatic cloud classification from digital images for seven different cloud types. The aerosol and cloud optical depth at 550 nm from sky images has been derived by using the Santa Barbara DISORT Atmospheric Radiative Transfer model [OLMO et al., 2008]. The angle of polarization of light on the sky hemisphere for cloudless sky was investigated in order to retrieve information about aerosol properties [KREUTER and BLUMTHALER, 2012]. Two ground-based sky imagers were used to derive the various microscopic cloud parameters (cloud-base height, cloud base wind, cloud amount). The cloud-base high obtaining from the stereo images was compared with visual observations, lidar and radiosonde data [SEIZ et al., 2002]. In YAMASHITA and YOSHIMURA (2012), a simple method from ground-based observation was demonstrated for the classification

and discrimination of clouds on whole sky image and extending to the satellite-based observation by overlaying both ground and satellite-based images.

The utilization of sky imagery is not only suitable for the determination of several cloud parameters but may also be applied to derive photometric and radiometric quantities. The photographic techniques for daylight measurement commenced in 1975 is purposed by [NAKAMURA and OKI \(1975\)](#).

The research by [ROY et al. \(1998\)](#) evaluated and demonstrated the use of digital image of the sky to obtain the luminance information and determine cloud cover. The system consists of a Nikon/Fuji E2 [CCD](#) camera with Nikon Nikkor 8 mm f/2.8 full-field lens provided a full 180° field of view and calibrated using a Krochmann Sky Luminance Scanner. The calibration measurements were done by measuring the zenith luminance by the scanner and compared to the [RGB](#) values at the zenith in the digital image. Combined with exposure values (shutter speed, aperture and ISO number), a mathematical model was developed to derive sky luminance distribution from the [RGB](#) values as expressed in the following equations:

$$L_\nu = \frac{V^{2.4}}{2901.978 \cdot E_\nu}, \quad (2.12)$$

$$V = 0.2125R + 0.7154G + 0.0721B, \quad (2.13)$$

$$E_\nu = \frac{179}{200} \cdot \pi \cdot S \cdot \frac{T}{f^2}, \quad (2.14)$$

where L_ν is the luminance of the sky for each pixel in cd/m^2 . V is the luminance function calculated from the [RGB](#) values. R, G, B are the [RGB](#) values of an image ranged from 0 to 255 and E_ν is the exposure value. S is the file speed or ISO number, T is the shutter speed or exposure time [second] and f is the aperture or f-stop number.

From this calibration only the approximate luminance can be estimated due to a limit of the [CCD](#) sensor response. The limited dynamic range of the [CCD](#) was valid up to approximately 30,000 cd/m^2 [[HAYMAN et al., 1999](#)]. In this work, the researchers do not mention any calibration for the optical system of the camera. Furthermore, the camera-based luminance data were not evaluated against other luminance measurements.

Based on the calibration equation developed by [ROY et al. \(1998\)](#), [SPASOJEVIC and MAHDAVI \(2005\)](#) explored the potential of using the low cost digital camera and the fisheye converter for the derivation of sky luminance distribution maps. The camera system was calibrated with simultaneous measurements of the global horizontal illuminance and a correction factor (CF) was introduced for the calibration process. From the calibration equation, the resulting luminance was converted to illuminance values and compared with the measured horizontal illuminance. How-

ever, the researchers did not mention the luminance measurement for the different sky conditions and did not carried out the optical calibration of the camera system.

Further research by [INANICI \(2010\)](#) investigated the luminance measurement from the [HDR](#) photography for indoor and outdoor daylight applications. The [HDR](#) images were captured with a Canon EOS 5D and Sigma 8 mm f/3.5 EXDG fisheye lens that has 180° angle of view. The camera response function was computationally derived and the [RGB](#) values of the image were converted to [CIE XYZ](#) values [[INANICI, 2006](#)] to determine the luminance equation. The luminance data was validated with the measurement by using a Minolta LS 110 luminance meter to collect the luminance simultaneously with the camera.

The sky imagery system with careful radiometric calibration can be established for estimating the radiance distribution. The earlier research was proposed by [VOSS and ZIBORDI \(1989\)](#). The electro-optic fisheye Radiance Distribution Camera System ([RADS](#)) developed at [UCSD](#) consists of a fisheye lens, a filter changer assembly (for four spectral channels) and a solid state camera. This system was built for spectral and geometrical radiance distribution measurements in the visible wavelength region (450-650nm). The radiance distribution retrieved from the [RADS](#) system has been compared with the radiance from the Hand Held Contrast Reduction Meter ([HHCRM](#)). In general, the comparisons showed the good agreement between measurements taken with two instruments. The radiance distribution from the [RADS](#) system has been also validated with the radiative transfer model presented in [ZIBORDI and VOSS \(1989\)](#). The spectral sky radiance was computed with the radiative transfer equation on plane parallel for homogeneous cloudless sky and then compared with the measured data from the [RADS](#) system and the [HHCRM](#). The difference between measured and modeled data in most cases was within 10%. However, this test has been only made for low aerosol optical depth and one surface albedo.

Later the gray level of a hemispherical image has been applied for retrieving the sky relative radiance. [ROSSINI and KRENZINGER \(2007\)](#) proposed the method to determine the sky relative radiance (luminance) distribution by using a monochromatic CCD wide angle lens camera. The image of the sky was extracted to obtain a matrix of the gray levels of each pixel. The number of gray level was characterized and used to define the gray tone for calculating the relative radiance. The quantitative results of the relative radiance from different sky images under various sky conditions were presented, but no optical calibration of the camera was mentioned.

The [WSI](#) has been developed over the last three decades for various applications involving sky observations at various locations as discussed in [SHIELDS et al. \(1998\)](#) and [FEISTER and SHIELDS \(2005\)](#). In the research by [FEISTER and SHIELDS \(2005\)](#), the [WSI Visible/NIR 7](#) was installed at the Central Radiation Station of Meteorological Observatory, Potsdam, Germany. The radiometric and angular calibrations of the [WSI](#) were calibrated at [UCSD](#) in order to characterize the system and provide absolute radiance distribution from images. Using a Discrete Ordinate Method Model a few radiance distributions have been simulated for the spectral region from 280 nm to 110 nm and compared them with the image-based radiance. The model has been

carried out for a plane parallel surface with refraction of the radiation not accounted. However, no radiance distribution comparison of the WSI against other instrument has been performed.

LÓPEZ-ÁLVAREZ *et al.* (2008) presented a 12-bit RGB CCD camera, QImaging, attached to a fisheye lens placed in Granada, Spain. This system was principally aimed for taking images of the sky periodically to obtain the information about clouds and not for multispectral imaging purposes. Therefore, no calibration of the system has been carried out but the researcher has mentioned that this did not impact on the spectral estimation [LÓPEZ-ÁLVAREZ *et al.*, 2007]. A SpectraScan PR650 telespectroradiometer measured a spectral measurement of a point on the sky corresponding to the image taken from the QImaging. A linear pseudoinverse method was applied for recovering the spectral skylight from the QImaging system. To control the quality of the training sets, colorimetric and spectral combined metric of each training sets was evaluated applied for selecting the training set. However, only the relative spectral skylight from the QImaging could be compared with the spectral measurement.

Research by HUO and LU (2009) evaluated the geometric, optical and radiometric calibrations of the all-sky imager to retrieve the radiance. Based on the radiometric calibration, the relationship between the gray values and the relative intensity has been found as an exponential equation. The estimated relative radiance from this all-sky imager was compared with the radiance observed by a sun photometer (CIMEL électronique, CE-318). The two comparisons presented that the retrieving equation is feasible for deriving radiance.

The recent research by ROMÁN *et al.* (2012) investigated the spectral sky radiance at three effective wavelengths from the hemispherical sky images. The absolute radiance calibration is based on the output measurement and the modeled sky radiance from the LibRadtran software package. The matrix calibration described the relationship between the output signal of images and the reference values of the sky radiance simulated by the LibRadtran for each image pixel. The camera radiance has been estimated and validated with the CIMEL sunphotometer for two different days. The mean absolute differences were claimed to be within 15% except the pixels near to the Sun. Additional, the sky radiance distributions at the three wavelengths under cloudless, overcast and partly cloudy skies were also presented. However, the validation of the spectral sky radiance distribution for the whole hemisphere with the accurate instrument has not been made. Furthermore, the matrix calibration applied in this work is only valid, when the spectral response of the CCD sensor is linear.

3 Instrumentation

This chapter presents the existing instruments at [IMuK](#) which are used to obtain the data for the calculation and validation of sky luminance and sky radiance during this study. A brief description of the [CCD](#) spectroradiometer will follow as this is the main instrument used to obtain spectral radiance. Skyscanner will be described in the next subsection. The chapter is completed by the introduction of the global illuminance measurement by the luxmeter. The new hemispherical sky imager, which is designed and developed in this work will be separately detailed in [Chapter 4](#).

3.1 The [CCD](#) spectroradiometer

In this work, the portable SD2000 [CCD](#)-Array-spectroradiometer from Ocean Optic [[OCEAN OPTICS, 2006](#)], which is further denoted as [CCD](#) spectroradiometer, is a main instrument for measuring spectral sky radiance. Similar spectrometers have been used to measure solar and artificial radiation in [ANSKO et al. \(2008\)](#), [KOUREMETI et al. \(2008\)](#), [KREUTER et al. \(2009\)](#), [YLIANTTILA et al. \(2005\)](#). [Figure 3.1](#) shows the [CCD](#) spectroradiometer. This spectroradiometric device consists of two identical polychromators, one is named Master-channel and the other is Slave-channel. A detector of both channels is a high-sensitivity 2048-element ILX511A [CCD](#) array from Sony [[RIECHELMANN, 2008](#)]. The different between both channels is the included grating, which disperses an incoming radiation into its spectral components:

- Master-channel: this channel has the ruled grating of 600 *groves/mm*. These mechanical ruled gratings are more reflective, resulting in higher sensitivity, therefore, the master channel can respond to the small signals. Resulting from the groves number of the channel, the wavelength range of this channel is 175 nm to 885 nm and the averaged bandwidth (full width at half maximum, [FWHM](#)) is about 2 nm.
- Slave-channel: has a holographic grating of 2400 *groves/mm*. The holographic gratings produce less stray light. The wavelength range covered from 260 nm to 440 nm and the [FWHM](#) is about 0.35 nm.

During this work, the Master-channel of the [CCD](#) spectroradiometer is operated for measuring spectral radiance with a spectral resolution of 2 nm between 300 and 800 nm covering the visible spectrum. The input optics designed for the spectral sky radiance measurement used in this work has the field of view ([FOV](#)) about 5° [[SECKMEYER et al., 2010](#)]. For more technical descriptions concerning the [CCD](#) spectroradiometer and its related devices see [PISSULLA \(2006\)](#).



Figure 3.1: The [CCD](#) spectroradiometer, SD2000 from Ocean Optics for measuring spectral sky radiance

The integration time during the measurement can be set between 3 ms to 65 s. The collected data from the spectroradiometer for both channels is independently converted to the digital signal by a 12-Bit ADC1000-USB analog-to-digital converter and the signal further transferred via a USB cable connected to a computer unit for the further data processing. The original spectrometer operating software is called OOIBase32 delivered from the spectrometer manufacturer Ocean Optics.

The software is made for controlling and also for the data processing of the [CCD](#) spectroradiometer. However, the data acquisition controlled from this software is not completely appropriate for many time dependent applications. For example, the software is unable to automatically start a measurement at a certain time and the set time between the measurements is varying. Moreover, the direct irradiance and radiance measurements combined with the moving instruments such as Pan-Tile Unit or Skyscanner (see Section 3.2) is not practical. Thus, the software called Spectromat developed at [IMuK](#) and based on Delphi programming is applied for the [CCD](#) spectroradiometer measurements.

At the beginning of the measurement campaign the [CCD](#) spectroradiometer has to be calibrated in the laboratory. The calibration was performed on a calibration bar in a temperature stabilized lab room with blackened walls and with a suitable baffle setup to reduce stray light during the calibration process. As presented in [Figure 3.2](#), a reflectance plaque was illuminated by a 1000W tungsten halogen lamp, which has been calibrated by the Physikalisch-Technische Bundesanstalt, a national metrology institute. The uncertainty of the irradiance is about 1% for the wavelength region from 400 to 780 nm. The lamp is controlled by a stabilized power source. By means of a calibrated shunt the power is stabilized to 8 ± 0.0001 A. More details of this calibration method are described in [PISSULLA et al. \(2009\)](#). The reflectance of the plaque is $>98\%$ in the wavelength from 380 to 780 nm. The radiance input optics is mounted on a rotational table at a 45° angle to the diffuser plate at a distance of about 67 cm. It is most important that the [FOV](#) of the collimator tube is filled by

reflection from the plaque.

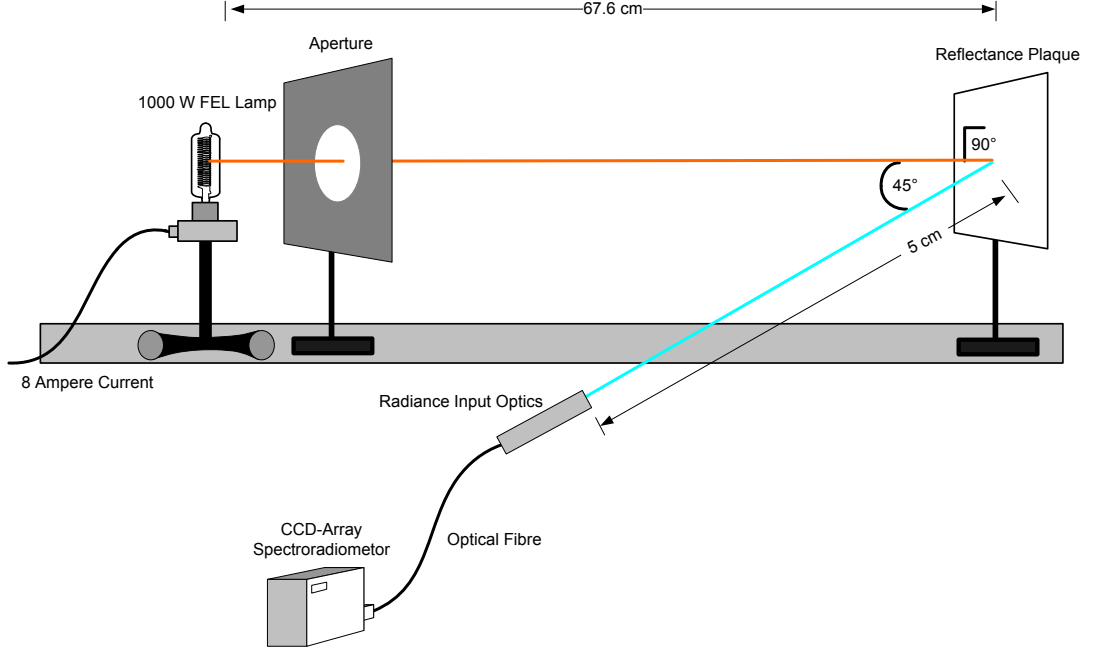


Figure 3.2: Radiance calibration setup at the IMuK radiation laboratory. The radiation beam of a 1000W FEL lamp perpendicularly illuminates the reflectance plaque. The radiance entrance optics is placed 5 cm away in a 45° angle from the plaque [PISSULLA et al., 2009].

To determine the spectral sensitivity of the CCD spectroradiometer, the theoretical spectral radiance $R_{1000W}(\lambda)$ is calculated by applying the following equation [PISSULLA et al., 2009]:

$$R_{1000W}(\lambda) = \frac{R(0/45^\circ, \lambda)}{\pi} \cdot \left(\frac{r_{ref}}{r}\right)^2 \cdot E(\lambda, r_{ref}) \quad (3.1)$$

where $R(0/45^\circ, \lambda)$ is the directional/directional reflectance factor, r is the measured distance between the lamp and the plaque in cm. $E(\lambda, r_{ref})$ is the spectral irradiance of the calibrated lamp at the reference distance, $r_{ref} = 67.7$ cm and it will be interpolated to the desirable wavelength, λ .

With $R_{1000W}(\lambda)$ and the measured signal $S_{CCD}(\lambda)$ of a known radiance source, the spectral responsivity of the CCD spectroradiometer can be calculated by

$$r_{CCD}(\lambda) = \frac{S_{CCD}(\lambda)}{R_{1000W}(\lambda)} \quad (3.2)$$

With this spectral response, the spectral sky radiance from the measurement $R_{mea}(\lambda)$ can be estimated by using this relation:

$$R_{mea}(\lambda) = \frac{S_{mea}(\lambda)}{r_{CCD}(\lambda)} \quad (3.3)$$

where $S_{mea}(\lambda)$ denotes the measured signal from the CCD spectroradiometer and $r_{CCD}(\lambda)$ is the spectral responsivity of the spectroradiometer obtained by the Equation (3.2).

Based on earlier investigations with the main focus on the UV range, the uncertainty of the spectral radiance measurements was estimated to be between 5% and 10%. The methodology for the calibrations used for this study described in [PISULLA et al. \(2009\)](#) was performed for the spectral measurement in UV radiation and in [SECKMEYER et al. \(2010\)](#) has been applied to spectral radiance measurements in the visible. The effects of uncertainties on experimental integrals (like the luminance) have been described in [CORDERO et al. \(2008a\)](#) and further details on the extension to the visible range can be found in [WUTTKE and SECKMEYER \(2006\)](#). The general methods for uncertainty evaluation have been described in [BERNHARD and SECKMEYER \(1999\)](#) and in [CORDERO et al. \(2008b\)](#).

Concerning to the acquisition of the spectral sky radiance, which has been later converted sky luminance (see Section 5.2.1, the setup of the CCD spectroradiometer including the calibration and raw data analysis for providing the spectral sky radiance data was performed by Dip.-Met. Stefan Riechelmann and all routines of the process are written with Interactive Data Languages (IDL) programming ¹.

The CCD spectroradiometer is necessary not only for the filed radiance measurement but also important for the characterization of the CCD camera sensor properties and the luminance calibration which will be explained in the Chapter 4 and Chapter 5 respectively.

3.2 Skyscanner

The skyscanner used in this thesis work is generally an instrument for measuring sky luminance at 145 standardized points on the sky and was constructed by [CZIBULA and GRUNDMANN \(2002a\)](#). Figure 3.3 shows the sky scanner on the roof of IMuK. Skyscanner can not only perform the luminance measurement, but can also point to any zenith and azimuth sky viewing angles at any given direction in the sky.

The mechanical control of skyscanner is based on the three electric motors, which drive one vertical and two horizontal axes. The movement of the vertical axis is limited to 190°. Spinning of this axis turns the whole body of the skyscanner. The horizontal axis actuates the luminance detector. It is no limitation in the movement, therefore, the luminance detector can be turned in every direction [[ALI, 2003](#)]. The second horizontal axis drives the input optics for radiance measurement. It is limited to $\pm 90^\circ$, if 0° is set to 0° SZA.

¹Personal communication with Dipl.-Met. Stefan Riechelmann, Institute for Meteorology and Climatology, University of Hannover.

3. Instrumentation

A single scan of the sky takes 30 seconds only and can be repeated every two minutes. In the routine scan the sky luminance is detected at all 145 different points at the sky dome [TREGENZA, 1987]. Each of these spots specifies a circular cut-out on the sky dome. This circular spot is associated with an opening view angle of the photometer detector and it is about 11° [CZIBULA and GRUNDMANN, 2002a]. The indices of each spot are referred to their spherical coordinates. The points are distributed in a regular grid over the sky and the pattern is shown in Figure 3.4 (left). Ring A is 6° above the horizon, whereas Ring G is close to zenith at 78° . The interval between each ring is 12° . The point number 145 represents the zenith. The zenith sky luminance is measured six times during one scan and the indices are numbered from 145 to 150. Table 3.1 gives the angular distribution of the scanning points from skyscanner.



Figure 3.3: The skyscanner on the platform of IMuK. The luminance detector is a small metallic object above the label in the left side. The radiance input optics is fixed to the secondary axis and the optical fibre is attached to the input optics.

Actually, the principal operation of the Skyscanner is to measure sky luminance distribution for the comparison between the measured sky luminance and the sky luminance derived from the new hemispherical sky imager. However, after analyzing and validating the luminance data with empirical models or luxmeter, it can be

concluded that the measured luminance data by Skyscanner can not be utilized as the initial dataset for the validation due to some technical problems. For example, the zenith luminance measured six times per scan had quite different values even the sky quite stable such as cloudless or completely overcast sky as shown in Figure 3.5. Therefore, the Skyscanner is only further used as the pointing device equipped with the input optics for the spectral sky radiance measurement.

Table 3.1: The zone angles of the Skyscanner pattern.

Ring name	Number of scanning points	Elevation of ring center ($^{\circ}$)	Index number
A	30	6	1 – 30
B	30	18	31 – 60
C	24	30	61 – 84
D	24	42	85 – 108
E	18	54	109 – 126
F	12	66	127 – 138
G	6	78	139 – 144

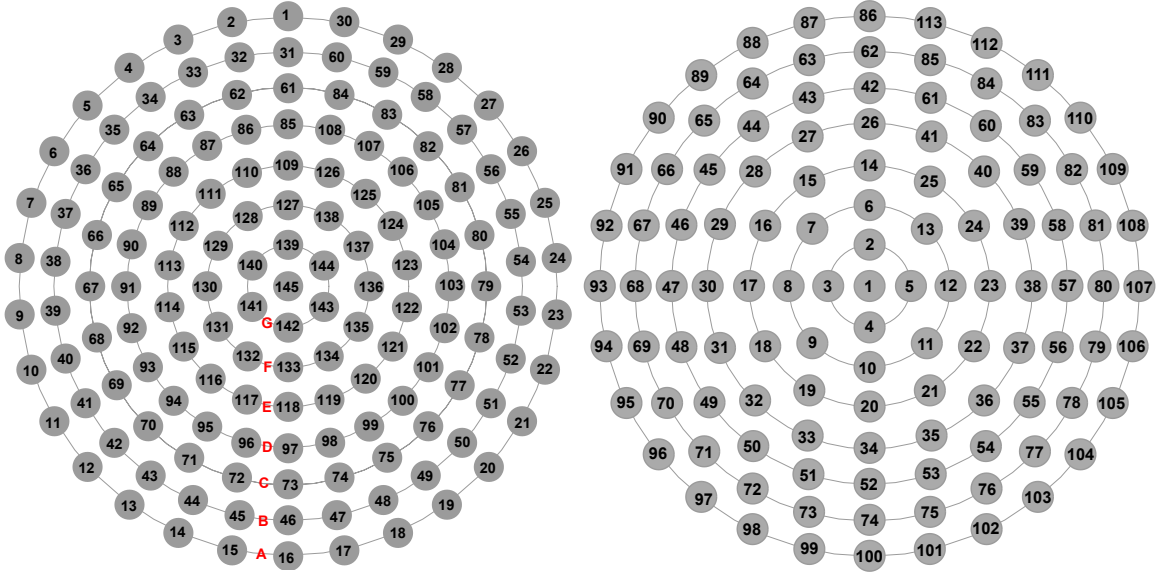


Figure 3.4: (Left) 145 scanning points over the sky dome. The numbers within the spots represent their index number from 1 to 145. The ring names relate to the increasing elevation angle from horizon to zenith. The spot number 145 indicates the zenith points [CZIBULA and GRUNDMANN, 2002a]. (Right) New pattern of the 113 scanning spots over the sky dome for spectral radiance measurement.

Using the Skyscanner as the positioning unit for spectral radiance measurement, the distribution of the scanning spots on the sky dome is divided into 113 scanning

points corresponding to the 5° FOV of the radiance entrance optics measured by the CCD spectroradiometer. This new sky pattern for spectral sky radiance measurement was developed by Dip.-Met. Stefan Riechelmann². The distribution of the scanning point on the sky dome for measuring the spectral sky radiance and converting to sky luminance is shown in Figure 3.4 (right). Only the azimuth angle of the scanning points is changed, the increment of zenith angle is still the same as shown in Table 3.1.

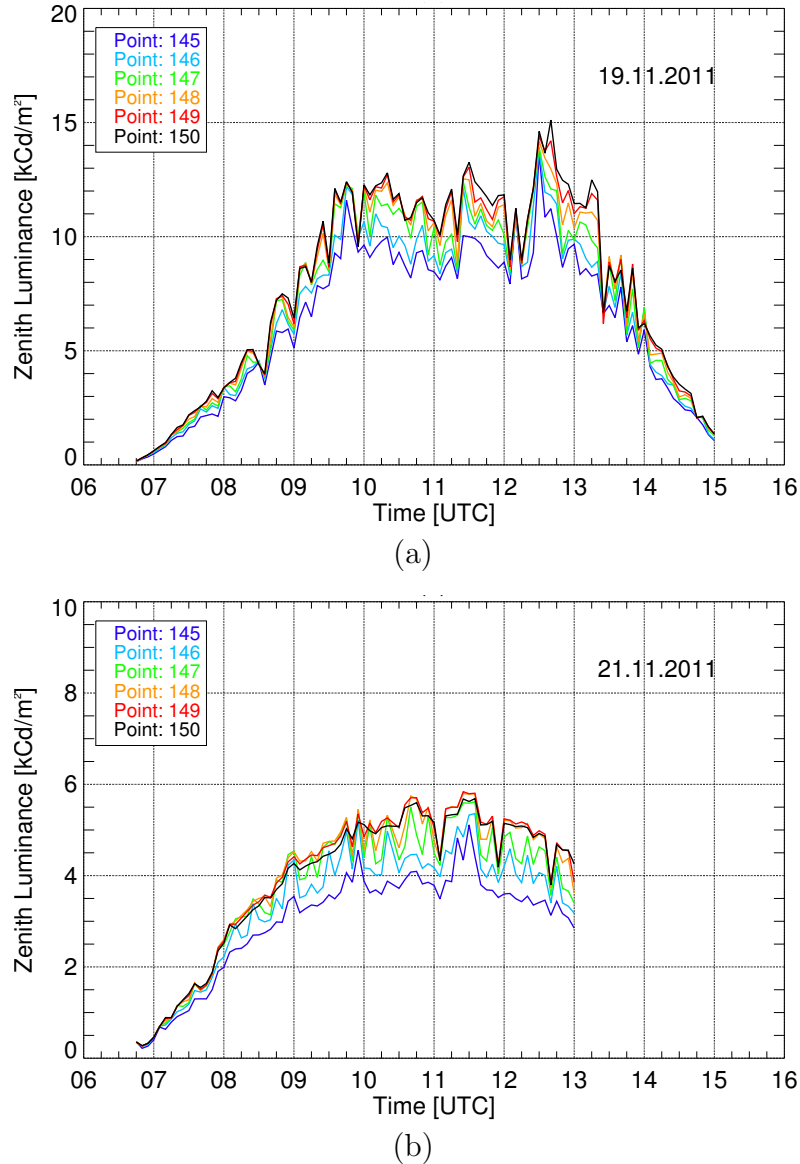


Figure 3.5: Six points of zenith luminance measured by Skyscanner on November 19, 2011 under overcast sky (a) and for clear sky condition on November 21, 2011 (b).

²Personal communication with Dipl.-Met. Stefan Riechelmann, Institute for Meteorology and Climatology, University of Hannover.

3.3 Luxmeter

For a data quality control of the luminance determination performed in this work, the global illuminance has been calculated from the all-sky images and it was compared with the measured global illuminance from a luxmeter. The luxmeter is used for measuring illuminance on a horizontal plane. Illuminance is defined as photometric flux per unit area which can be calculated by integrating visible solar spectral irradiance weighted by the response of the human eye over the wavelength [CIE, 2012] measured in $\frac{lm}{m^2}$ or *lux* as detailed in Section 2.1. This response or spectral luminous efficiency function for the photopic vision or is defined in the range 360 nm to 830 nm and is normalized to one at its peak, 555 nm [CIE, 2000]. The eye has the maximum sensitivity in a green part of the visible spectrum while the response to ultraviolet and infrared is zero. The response $V(\lambda)$ is presented in Figure 3.6 (red line) and the human eye response sensitive applying for low ambient light $V'(\lambda)$. The peak sensitivity of scotopic vision appears at 507 nm as show in the same picture (blue line).

The luxmeter installed on the roof of IMuK for collecting global illuminance is shown in Figure 3.7. A temperature stabilized luxmeter provides the highly accurate illuminance measurement in the range of 0.001 lux to 200 klux [CZIBULA and GRUNDMANN, 2002b]. This luxmeter was used in the investigation and measurement of the global illuminance within one minute intervals.

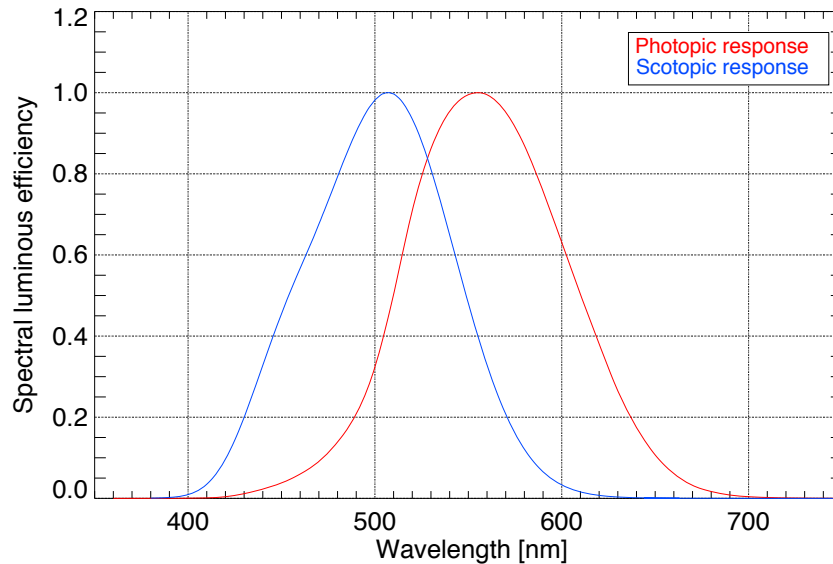


Figure 3.6: The spectral responses of the standard human eye at daylight or CIE $V(\lambda)$ (red line) and $V'(\lambda)$ (blue line) [CIE, 2000].

The daily profiles of global illuminance measured from luxmeter for different weather conditions are displayed in Figure 3.8. On May 16, 2012, low cumulus pre-

vailed with local coverage varying throughout the day (intermediate sky) as shown by the black line. Illuminance from clear sky measured on May 25, 2012 shows with the red line. It is seen that when the clouds appear on the sky, they can on occasions enhance the global illuminance.



Figure 3.7: The luxmeter measuring the global illuminance manufactured by Czibula & Grundmann on the roof of IMuK [CZIBULA and GRUNDMANN, 2002b].

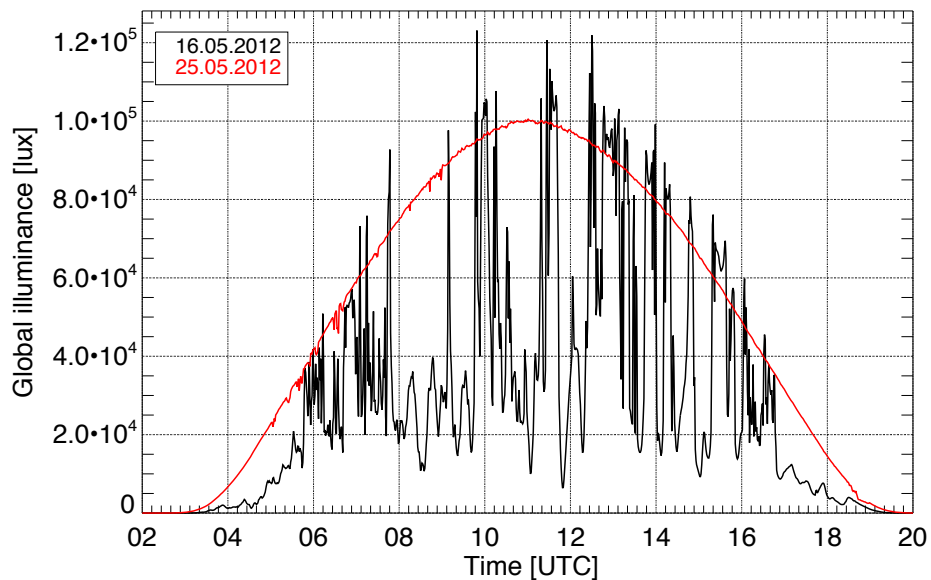


Figure 3.8: Measured global illuminance from luxmeter at IMuK for clear sky day on May 25, 2012 (red) and through broken clouds on May 16, 2012 (black).

4 Development of Hemispherical Sky Imager (HSI) System

To understand the influence of clouds and their temporal variation on radiation quantities such as sky luminance and sky radiance, the Hemispherical Sky Imager (HSI) system was designed and developed at IMuK. This chapter is separated into two parts according to the development of the HSI system. In the first part, the description of the construction as well as the result from the hemispherical imager systems are given in Section 4.1. The geometric and radiometric calibrations of the HSI system have been characterized and are presented in Section 4.2.

4.1 Design, development and features of the HSI system

In order to capture the hemispherical cloud situation, BRAKEBUSCH (2007) demonstrated the first theoretical attempt for recording the whole hemisphere with a spherical mirror and a fish-eye objective at IMuK. Only the resulting image taken from the system that consisted of a Canon EOS 5D camera mounted with the fish-eye lens was presented. Therefore, these systems are further developed and characterized.

The spherical mirror system, which consisted of a spherical mirror, a plane mirror and camera, was developed and tested in this work. According to its technical problems in the operation and some disadvantages, the system therefore was not further developed and replaced by the HSI system. More details of the spherical mirror system can be found in Appendix A.

4.1.1 Setup description of the HSI

The HSI system consists of the CCD camera equipped with a fish-eye objective pointing towards zenith and collects the full view of the sky. In this thesis work the alternative fish-eye objective (AFO) from SOLIGOR (see Figure 4.1) is used and provides the hemispherical image with the FOV about 183°. Since the compact camera can not change the objective, an adaptor ring is required for mounting the AFO on the camera and it has been modified to fit with the camera.

To protect the sensible parts of the input optics and the camera (see Figure 4.2(a)), the lens of the HSI setup has to be covered by a glass dome or a similar material with a high optical quality. The glass dome was implemented as shown in Figure 4.2(b). During one year of the outdoor operation the color of the glass dome of the HSI system was darkened by the exposure of the ultraviolet radiation (UV). The altered color of the glass dome is presented in Figure 4.5. As the estimation of the sky luminance

distribution (see Chapter 5) and spectral radiance (see details in Chapter 6) are based on the color provided by the camera sensor, the altering of glass dome can impact on the calculation. Therefore, the plastic dome was replaced by the acrylic dome with UV protection. This new dome is still working up to now as show in Figure 4.2(c).



Figure 4.1: SOLIGOR fish-eye converter.

4.1.2 Camera housing

The weatherproof housing has been designed and improved to suit for the new imager system. Figure 4.2 shows the illustration of the new camera system and the current setup on the roof of IMuK.



(a)

(b)

(c)

Figure 4.2: (a) shows the camera elements and optics inside the HSI system (b) shows the first setup on the roof which used the glass dome (c) presents the current setup, which applied the plastic dome due to the UV damaging of the glass dome.

In Figure 4.2(a), the camera is placed on a round aluminum plate and the heating elements are installed on an aluminum plate underneath the camera. They provide 20 W of heating and start when the temperature at the thermostat drops below 5 degrees in the summertime or 10 degrees in the wintertime. It is sufficient for keeping the temperature above a dew point to prevent a condensation on the plastic dome, a lens and inside of the camera box. A high relative humidity is also harmful for fish-eye objective, CCD sensor and other electronics inside the housing. A fan is started, if the temperature within the camera housing exceeds 25 degrees to prevent overheating of the camera when the sun is shining into the dome in the summertime. The temperature inside the housing varies between 10°C and 35°C. Due to the heating and ventilation of the camera housing, the temperature of the camera sensor is estimated to be $20 \pm 5^\circ\text{C}$. The alignment of the HSI system has been carefully treated, in which the deviation of the vertical alignment and the north alignment of the system are within $\pm 2^\circ$.

The climate control units are powered from the power supply unit of the controlling PC. The camera was not located with the PC, therefore the camera controlling and the data transfer can be done via universal standard bus (USB) cable. The computer and software requirements are detailed in Section 4.1.4.

4.1.3 Camera element and optics

A first commercial compact digital camera model used in this work is Canon PowerShot S5IS (see Figure 4.3 (left)). The camera has an optical sensor of 1/2.5" CCD chip (5.76 x 4.29 mm) with a maximum image resolution is 3264 x 2448 pixels. During the development and the long operation of the spherical mirror system, Canon PowerShot S5IS cameras were damaged from direct sunlight and encountered some electronic problems (see Figure 4.6). Therefore, it was replaced with the Canon PowerShot G10.



Figure 4.3: CCD cameras used in this work: Canon PowerShot S5IS (left) and Canon PowerShot G10 (right).

The sensor of the Canon PowerShot G10 camera (Figure 4.3 (right)) is a 1/1.7" CCD chip (7.6 x 5.7 mm) with a maximum image size of 4416 x 3312 pixels (cor-

responding to 3.5 million pixels for the hemispherical image with a radius of 1060 pixels). The green masked areas of the Bayer filter on the chip corresponds to a spatial resolution of about 1.7 million pixels. The ADC of the camera has 8 bits of resolution, which equals to 256 counts per pixel. The file format is JPEG and the information is saved as RGB values. Images are directly stored in hard drive of the computer via the USB cable.

4.1.4 Computer and support software

Each camera system required at least one computer for controlling the operation and storing the image data. In order to control the camera system and transfer the image data, this computer should be commonly connected to a network. The more important reason for an available of network is a synchronization of the internal PC clocks. Since the internal PC clocks tend to run too fast or too slow during the day, it can give an uncertainty of a few minutes in one or two weeks. The synchronization is also important for comparing measurement with other instruments.

The software can be divided into two parts. The first part is PSRemote from Breeze Systems Company [BREEZE, 2007] which is used for remote control of the camera from the PC and the photos automatically download to the hard drive in the PC. With ‘RemoteCaptureFunction’ the images will be captured and an EXIF metadata such as exposure time, aperture or other parameters can be chosen via this function. Start and stop imaging can be also done including the interval time of the imaging. Second part is a local software, which was developed in this work for some applications such as renaming images and making films of cloud movement during the day. The local software is normally written with IDL programming language which is extensively applied for image processing and remote sensing research.

4.1.5 Image results of the HSI system

In this subsection samples of the hemispherical image will be presented. Figure 4.4 represents the whole sky images taken from the HSI system under different sky conditions.

In these images approximately 98% of the sky is unobstructed and is clearly seen. For clear sky condition in Figure 4.4(b) there are some bright spots on the image that are due to the reflection of the direct sunlight. The structures of different cloud types in these images are clearly recognized. The summary of the main benefits of HSI system are itemized as follow:

- Setup’s hardware : the hardware required for this system setup is much simpler than those required for the spherical mirror setup.
- Costs of the system tend to be cheaper than in the past because of the rapid development of the CCD camera, the fish-eye objective and its related elements, which make the system cheaper than a commercial cloud detector.

- The geometric calibration is easier than the spherical mirror setup.
- The shading does not occur by mean of the HSI setup.
- The HSI system can be applied as the mobile instrument. The setup can be done on the tripod and connected with the computer.

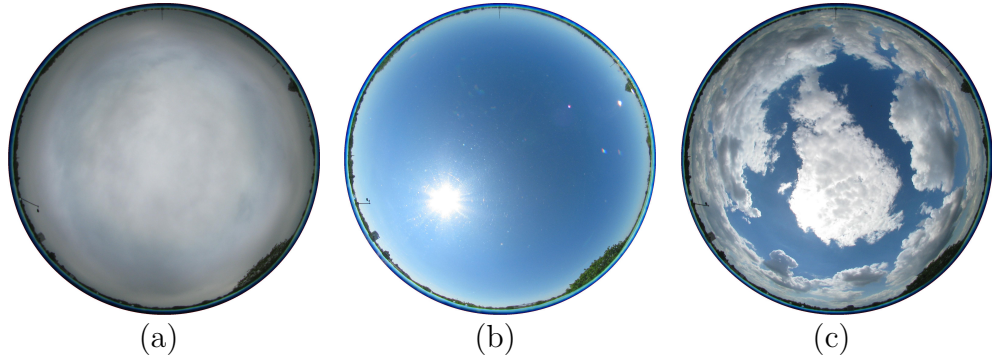


Figure 4.4: Different hemispherical sky types taken from HSI system. An overcast sky on May 11, 2010 at 13:00 UTC (a), clear sky condition on June 3, 2010 at 09:05 UTC (b) , partly cloud sky which was occupied by different cloud types on July 6, 2010 at 10:24 UTC (c).

It can be concluded that the HSI system facilitates the acquisition of the hemispherical images. However, some problems were encountered in this design of the HSI system between the operations. First, the color of the glass dome changed due to the exposure to UV radiation. The longer the operation of the system, the more color altering occurred and it therefore was replaced with the acrylic dome. Figure 4.5 shows how much the color of the dome changed.



Figure 4.5: Comparison of the new glass dome and the color changing dome. The dome in right hand side appears clearly darker than the other one and when comparing the images taken through the both dome, the color RGB values might be changed, minimum about 5 counts. This can impact on a further colorimetric investigation.

Insufficient power for heating is an important problem as presented in Figure 4.6(a), especially in the wintertime. There was condensation inside the camera housing which can damage the lens and electronic devices inside the housing. More heating elements have been supplemented on the upper part of the housing and this problem was reduced or avoided.

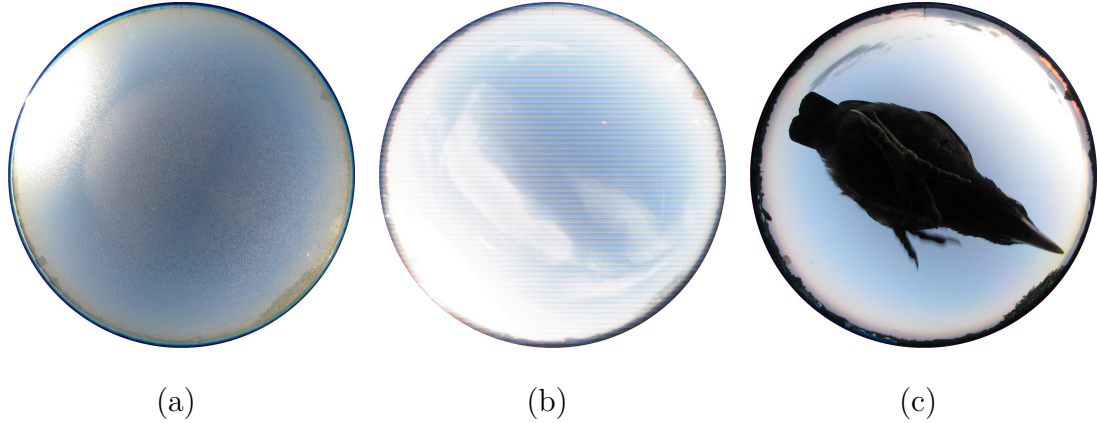


Figure 4.6: Some technical problems from HSI system. The condensation inside the camera housing due to the insufficiency of the performance of heating elements (a). Camera sensor's problem because of the exposure of direct sunlight (b). Insects or birds on the cameras dome (c).

The camera sensor and fish-eye objective suffer from the direct sunlight and make sometime the white images or black images. It appears also some strips on the image because of the damaging of camera sensor as shown in Figure 4.6(b). Only a replacement of the new camera can be solved this problem. Small insects can reach inside the camera housing via the airflow of the fan and birds are sometime on the dome (see Figure 4.6(c)). The system therefore still requests the flexible maintenance.

After the HSI system was improved and tested at IMuK, the identical HSI system was build up and transported to be installed at National Institute of Water and Atmospheric Research (NIWA), New Zealand (45.038° S latitude, 169.684° E longitude and 370 meters above sea level). This is for an observation of the southern hemisphere, whose sky conditions and atmospheric constituents are different from those of Hannover. See more details of the setup at NIWA in Appendix B.

4.1.6 Working Scheme for automatic image acquisition of HSI system

The number of whole sky images obtained from the HSI system is very large. Therefore, a process of data management has been designed to collect and prepare the data for long time image acquisition and further analysis. The whole automatic processing is shown in Figure 4.7.

Figure 4.7 presents the process of the image acquisition and collection of the HSI system for the whole day. From the middle of 2009 until the end of the year 2011, the system was set to take only one image per shoot at every 10 seconds (8,640 images/day). In 2012, an auto-bracketing function was established to capture three different exposure times per shoot within a 20 seconds interval (12,960 images/day). After that these images were renamed corresponding to the date and time of the image according to the time of the PC with its time synchronized every 1 minute. This step runs every 10 minutes for the purpose of a real-time weather report on a website at IMuK.

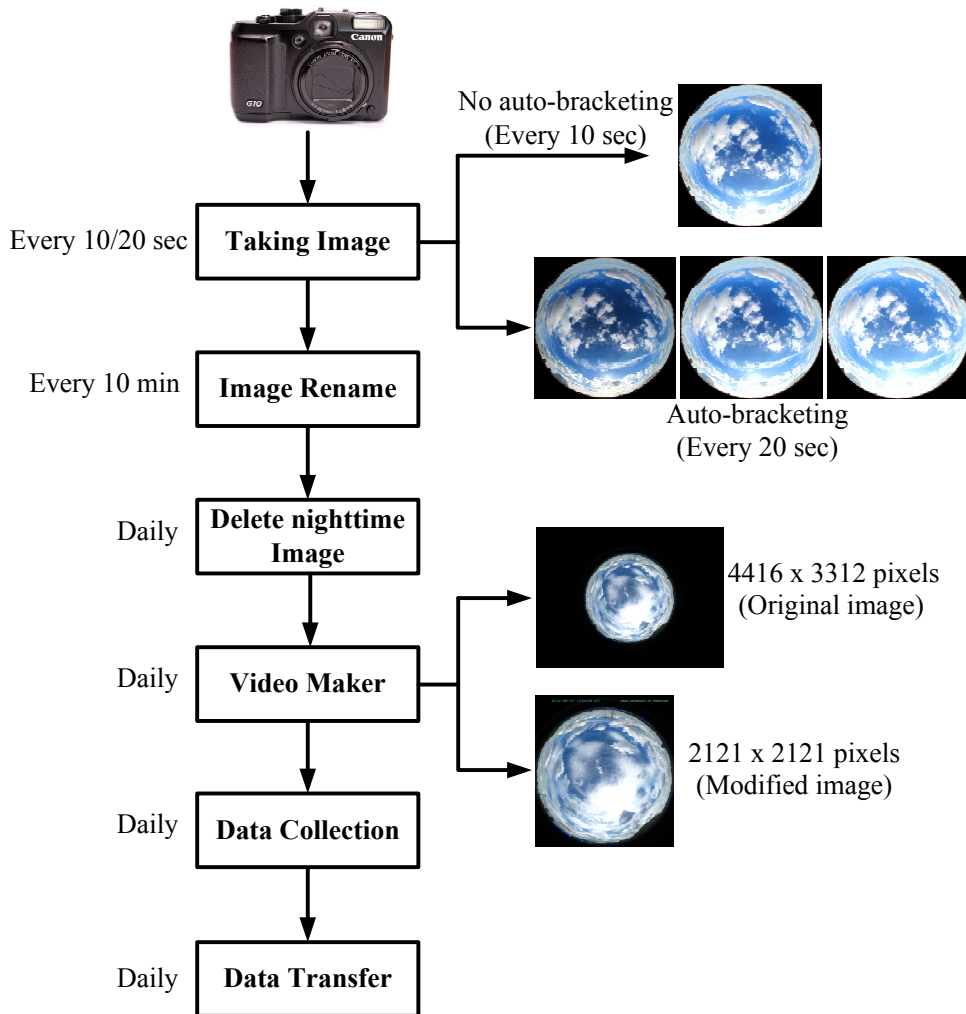


Figure 4.7: The working process of data management of the HSI system at IMuK and NIWA stations.

In the morning of the next day, the data processing begins by deleting the nighttime images and the daytime images are carried to produce movies which contain the movement of clouds for the whole day. These movies are the products of the original images and the modified images. The so-called modified images are the original images which cover only the hemispherical area and the date and time are also

labeled onto the images as show in Figure 4.7. The original images of 5 minutes were collected for the further investigation and were transferred to a server because of the amount of data. Most of the routines applied for the image acquisition process were written in the IDL language.

4.2 Camera sensor characterization

In this section, the different camera projections or camera models will be introduced. Normally, the camera projection can be obtained from a manufacturer but in this case the fish-eye projection needs to be examined and will be detailed in Subsection 4.2.1. In Subsection 4.2.2, the radiometric calibration of the camera sensor will be given.

4.2.1 Geometric calibration

4.2.1.1 Camera projection for fish-eye lens

In the recent years, fish-eye lens have been applied in many research areas as described in Chapter 2. Optical systems of the camera lens are not perfect and some properties are needed to characterize, for example the camera's model or the projection function. This camera projection is described as a relation between the angle (θ) of the incoming light ray and the optical axis to the distance from centre of image (r).

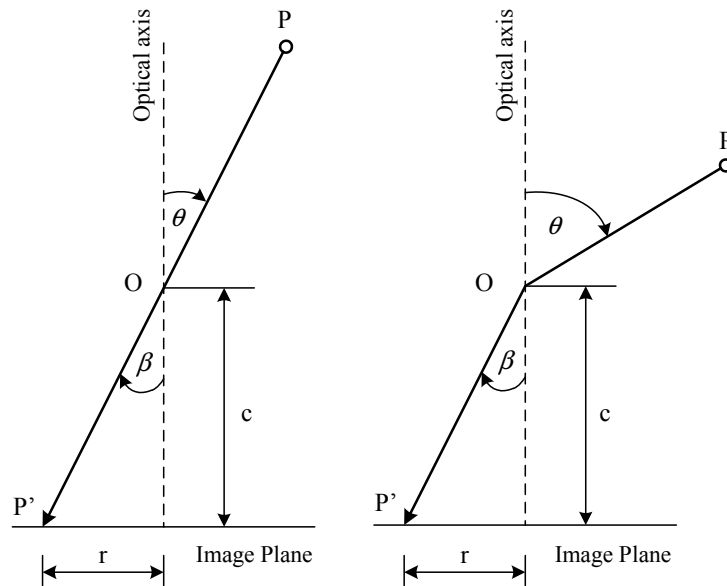


Figure 4.8: Geometric camera models. Image (left) shows the central perspective projection and (right) is the fish-eye projection model (adapted from SCHNEIDER et al. (2009)).

Figure 4.8 presents the schematic diagram of the fish-eye projection and the central perspective projection, which occurs in a rectilinear camera. In the following, the projection models for the large FOV camera for different construction principles are presented [MIYAMOTO, 1964; SCHNEIDER et al., 2009].

- Central perspective projection

In this projection, the incident angle (θ) is equal to the reflection angle (β), which passes through the lens (see Figure 4.8 (left)) and it preserves the rectilinear projection. That means straight lines in the scene remain straight lines on the image plane or it is free from distortion [HUGHES et al., 2010; SCHEIBEL, 1973a]. Thus, this projection type is applied for most commercial digital cameras. The projection can be expressed by:

$$r = c \cdot \tan(\theta), \quad \theta = \beta \quad (4.1)$$

where r is the distance from image center and c is focal length or the principal distance.

- Equidistant projection

The angle, θ of the incident ray is directly proportional to the radial distance in the image plane. Therefore, this projection is preferable for the measurement of angles of celestial objects in the field of astronomy [SCHEIBEL, 1973b]. The equidistant projection is in the form:

$$r = c \cdot \theta, \quad \theta \neq \beta \quad (4.2)$$

- Equisolid-angle projection

The ratio of an incident solid angle and its resulting area in an image is constant for the equisolid projection and it is also called equal-area projection. Because of the corrected area, this projection is suitable for determining the cloud cover of the sky or the obstruction of the building [MIYAMOTO, 1964]. The projection is

$$r = 2 \cdot c \cdot \sin\left(\frac{\theta}{2}\right), \quad \theta \neq \beta \quad (4.3)$$

- Orthographic projection

The radial distance in the image is proportional to the sine of the incident angle in this fish-eye projection. Orthographic projection is not usually used in fish-eye designs because the incident angle beyond 90° cannot be projected onto image plane and it thus causes a strong distortion at the margin of the image. But it can be useful for measuring illumination of architectural applications [JOHNSON, 2010]. This projection can be written in the form

$$r = c \cdot \sin(\theta), \quad \theta \neq \beta \quad (4.4)$$

- Stereographic projection

For this projection, the incident angle in the object space and its corresponding angle in the image are equivalent. This projection would be ideal for photographers because it does not compress the margin of the image as much. The projection is expressed as follow.

$$r = 2 \cdot c \cdot \tan\left(\frac{\theta}{2}\right), \quad \theta \neq \beta \quad (4.5)$$

The projection of the normal lens (non-fisheye) is perspective projection which works like a pinhole camera. This projection cannot be applied to the wide-angle camera because of the difficult construction and being expensive. The equidistant and equisolid-angle projection are often used to design for the fish-eye objective, which provides the large field of view more than 180° [PRENZEL, 1986]. There are different proposed methods to retrieve the fish-eye projection for different fish-eye designs [NAKONO et al., 2007; SCHNEIDER et al., 2009]. In the next subsection the experiment to determine the projection model for the working fish-eye objective will be explained.

4.2.1.2 Camera distortion determination

To examine the fish-eye projection, a simple experiment has been setup as shown in Figure 4.9 (left). The paper strip was replaced in a circular shape, in which it can span a zenith angle of 180° [SCHREMPF, 2010]. This strip was marked at 25 zenith angles. Between 0° to 50° , the strip was marked at every 10° . When the zenith angles is larger than 50° , the strip was marked at every 2° . The camera was pointed toward to zenith and each mark was captured with their associated pixel coordinate and distance from image center. The captured image corresponding with the marks is shown in Figure 4.9(right). The distance of each mark occurred in the calibrated image has been measured from the image center and it is called measuring data (r). For the comparison of the measuring data with the different fish-eye projections described in Section 4.2.1.1 the parameter, r , has been calculated for each projection.

After that the distances from the image center of four different projections associated with their angles have been compared with the measuring values from the experiment. The resulting plot between zenith angle or the incident angle of light ray (θ) and the distance from image center (r) for different projections is shown in Figure 4.12. The comparison of the camera distortion determination and other fish-eye models indicates that this camera optics exhibits a linear projection, which follows an equidistant projection. More details of the comparison for fish-eye projections will be given in the Subsection 4.2.1.4. To validate the measuring data, a more precise calibration is performed using nighttime stars as the reference points. The stars calibration will be explained in the Subsection 4.2.1.3.

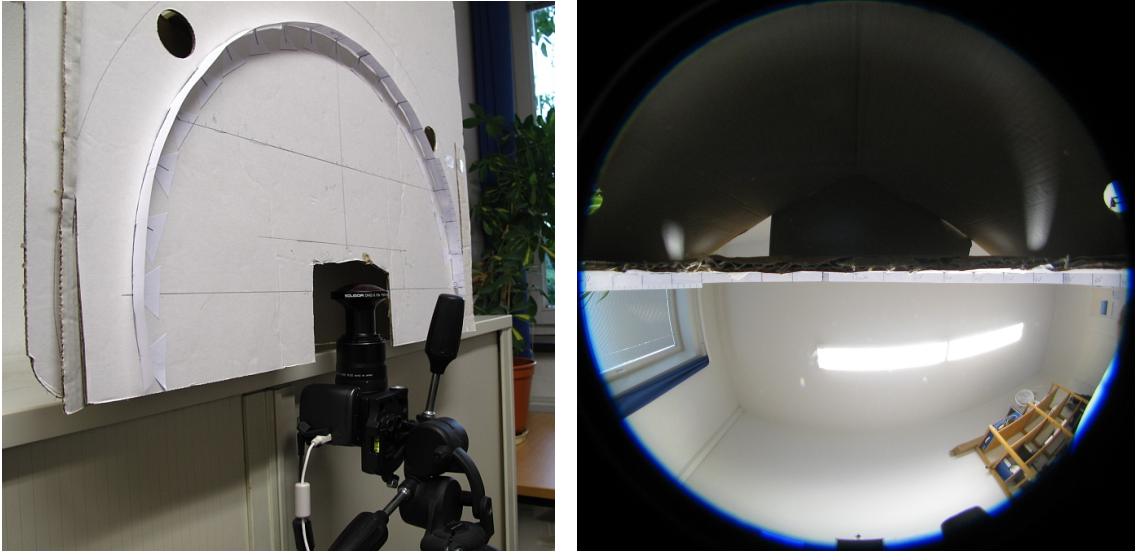


Figure 4.9: Image (left) shows the experimental setup for camera distortion determination and (right) presents the image captured by the setup. The black marks correspond to the 25 zenith angles and their distances from the image center were measured [TOHSING et al., 2013].

4.2.1.3 Stars calibration

In previous subsection, the geometric model of the HSI system was examined by setting up the simple experiment. In order to check the geometry of the fish-eye lens by the camera distortion determination, the star calibration is applied for this purpose. There were some works done using star calibration in the constellation observation in astronomy [PICKERING, 2006] or photogrammetric cloud mapping [SEIZ et al., 2002].

To fulfill the aim, nighttime images were taken every 5 minutes on April 19, 2010 on the platform of IMuK, which has the height of about 52 meter above sea level. The longest exposure time of 15 seconds was used to capture the stars and an example image at 21.55 UTC presented in Figure 4.10 was selected for the calibration.

The contrast and brightness of this image were increased to distinguish 18 stars which have an apparent magnitude brighter than 2.50m. The image was prepared and provided only the hemispheric area, which has the resolution of 2060 x 2060 effective pixels. Then the zenith and azimuth angle of the stars were achieved from astronomic Stellarium software [STELLARIUM, 2009].

The position of these stars in the image was obtained from a precise program DPLX, which is used in special photogrammetric application¹. The comparison of the camera distortion determination and stars calibration with the different projections in photography will be presented in the next subsection.

¹Personal correspondence with Dr. Karsten Jacobson, Institute of Photogrammetry and GeoInformation, University of Hannover.

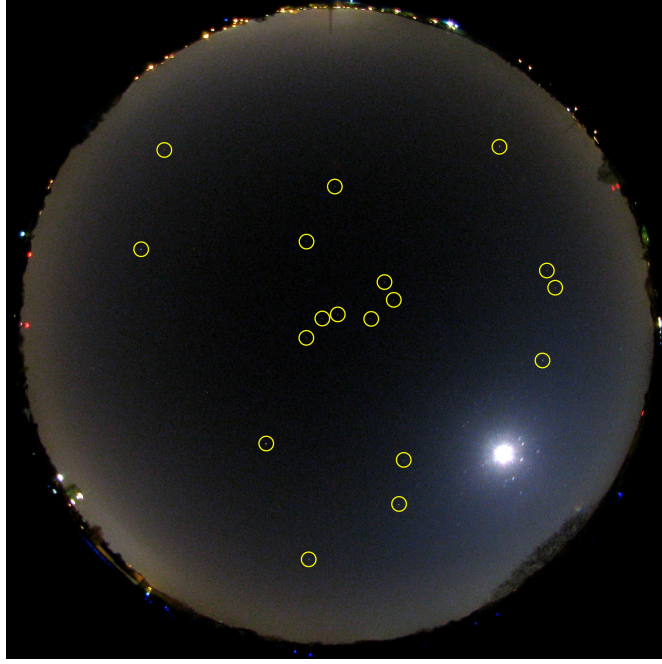


Figure 4.10: An image of the nighttime sky taken on April 19th, 2010 at 21.55 UTC with an exposure time of 15 s. Despite the fact that the horizon is contaminated by street illumination and the moon can clearly be recognized in the picture, 18 bright stars (marked with circles) could be identified and are used for the star calibration [TOHSING et al., 2013].

4.2.1.4 Results of the camera projection

From the field performing of the star calibration according to subsection 4.2.1.3, the relation between a radial distance from the image center and the zenith angle of the stars is nearly linear, as shown in Figure 4.11, and is fitted by the following equation:

$$r_i = 0.0187683 + 0.0196850 \cdot \theta_i, \quad R^2 = 0.998 \quad (4.6)$$

where θ is the zenith angle in degrees and i is the pixel number of the image. The square of correlation coefficient for the fitting is found to be 0.998 which means that the radial distance has a linear relation with zenith angle of the stars. The transformation of zenith and azimuth angle to image coordinates can be performed using Equation (4.7) and (4.8):

$$x_i = x_0 + r_i(\theta_i) \cdot \cos(\varphi_i) \quad (4.7)$$

$$y_i = y_0 + r_i(\theta_i) \cdot \sin(\varphi_i) \quad (4.8)$$

where x_i, y_i are the pixels in the image and x_0, y_0 are the center of image. θ_i is zenith angle which its range is $0 \leq \theta_i \leq 90^\circ$, φ_i is azimuth angle by $0 \leq \theta_i \leq 360^\circ$.

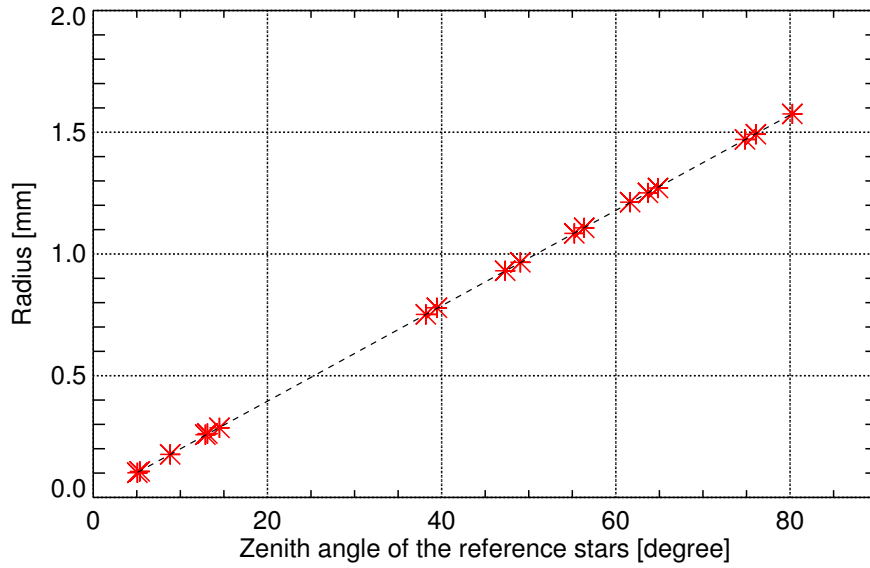


Figure 4.11: Radial distance from optical axis to image center or zenith point, r in millimeter and zenith angle of the 18 reference stars with the square of correlation coefficient (R^2) of 0.998 [TOHSING et al., 2013].

The radial distance and zenith angles from the camera distortion determination explained in Subsection 4.2.1.2 and stars calibration have been also compared with equidistant, equisolid-angle, orthographic and stereographic projections. The result of the comparison is presented in Figure 4.12.

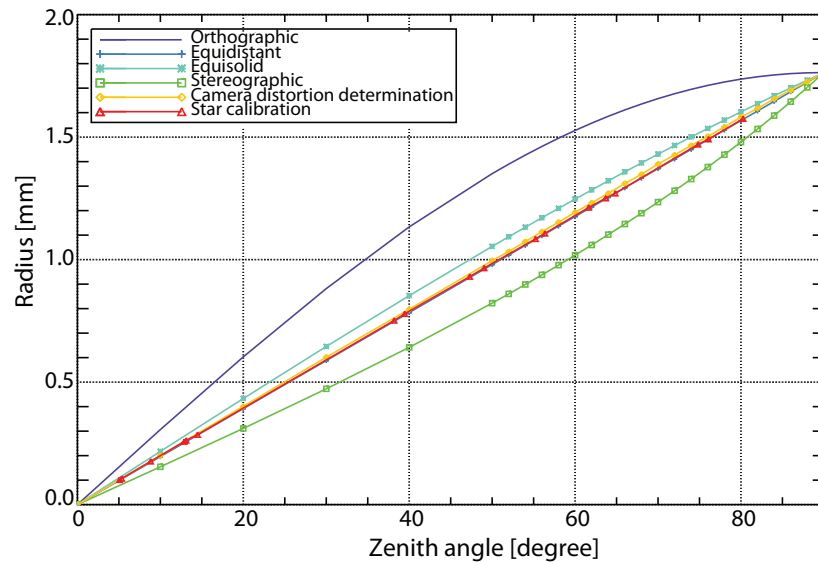


Figure 4.12: The comparison of the star calibration with different geometric fish-eye models.

From the comparison, the camera experiment and star calibration agree well with each other. The experiments clearly indicate that the camera performs very similar to the equidistant geometry, whereas the orthographic and stereographic projections have greater deviations. Therefore, the deviation of the camera projection derived with the camera distortion determination and the star calibration has been compared only with respect to the equidistant projection. In Figure 4.13 presents the differences of the camera projection in pixels and degrees.

The deviation of the camera projection derived with the camera distortion determination and the star calibration compared to the equidistant projection are presented in Figure 4.13. The derived projection functions agree well within 1° compared to the equidistant projection function. The uncertainty of the measurement for the star calibration is within 5 pixels or about 0.4° , whereas the camera distortion determination has an uncertainty of 10 pixels or 0.9° . It can be concluded that the used fish-eye objective provides a nearly equidistant projection function, which is used for the luminance and radiance calculations.

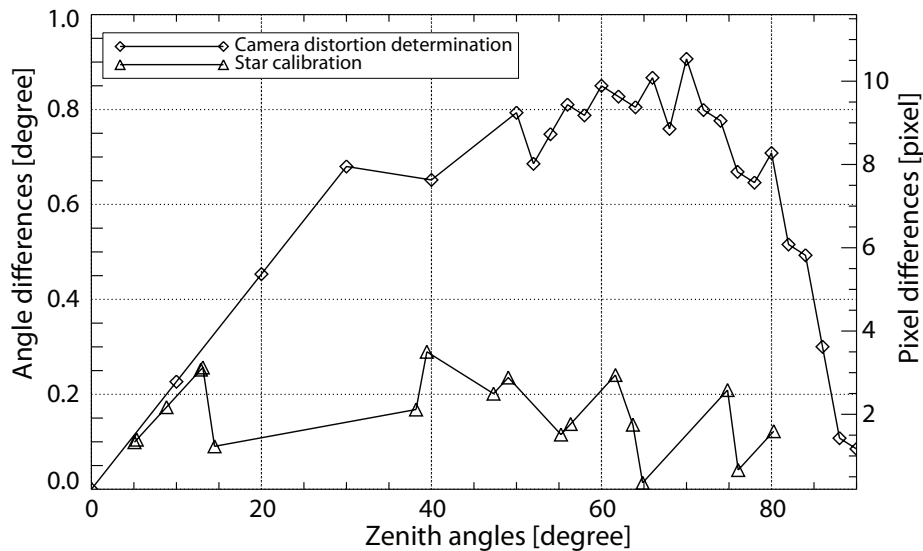


Figure 4.13: Deviation of different measurements to the equidistant geometry determined in degrees (left axis) and pixels (right axis) for the camera distortion determination (diamond) and star calibration (triangle). Both calibration methods agree well with the equidistant geometry [TOHS-ING et al., 2013].

4.2.2 Radiometric calibration

In this subsection, some properties of the CCD sensor will be introduced and a method to examine these properties will be also presented.

4.2.2.1 Dark current

Dark current is produced from thermal energy within the silicon lattice of the CCD. Electrons are created over time and they are independent of the light falling on the detector. An accumulation rate of dark current depends on the temperature of the CCD sensor and a reduction of 5-10°C lowers the noise by a factor of two [SHORTIS and BEYER, 1996].

The determination of the dark current of the CCD was conducted on 19 and 20 of August 2009. To prove the dependence of the temperature on CCD, three measurements have been designed. First, the dark current was measured after the whole day operation of the camera on the roof of IMuK. The camera captured the images while the fish-eye lens was covered with a camera cap. In this phase, it is called *warm camera* and the maximum temperature during that day was 22.7 °C. The second experiment was performed in the early morning of the next day. The *cold camera* took images before the measurement began. For the third measurement the camera recorded images in the laboratory in front of a reflectance plaque by varying the exposure times but the lens was protected from the exposure of the irradiance (See Figure 4.14).

The red, green, blue color counts of each RGB channel from the measured images were analyzed. The maximum dark signal for the warm camera is 15 counts and in the case of the cold camera it is 7 counts. The green channel encountered more dark current than red and blue channels. This is because of the construction of the CCD sensor, which has 75% green elements and 25% red and blue elements. By increasing the exposure time in the laboratory, the dark current often exhibits around 1 count in both camera situations. Compared to the effective pixels in the working area, which have about 3.5 million pixels and the independence on the exposure times, the dark current of this CCD can be neglected for further investigation.

4.2.2.2 Linearity

The fundamental process in CCD imaging is the conversion of photonic input to electronic output. The transfer function between the incident photonic signal and the final digitized output should vary linearly with the amount of incident light falling on the CCD. If twice the flux of photons is received in a given pixel of CCD sensor, twice the output value gains [SHORTIS and BEYER, 1996].

As there are no standard methods of reporting linearity values, an experimental system in laboratory as shown in Figure 4.14 has been designed for this aim. The calibration was performed on a calibration bar in a temperature stabilized laboratory as presented in Figure 3.3. The setup description of the calibration is explained in Section 3.1. The linearity will be characterized with two important variables such as the exposure time and an intensity variation from the light source. The camera is placed in front of the reflectance plaque and receives the constant radiance through an aperture from a 1000 W lamp which is located in an other room behind the camera.

For measuring the linearity which depends on the exposure times, the distance between the lamp and the plaque is constant. Images are recorded with increasing exposure times from $\frac{1}{2000}$ seconds to $\frac{1}{40}$ seconds at the same position. In order to determine the linearity with the variation of intensity of light source, the camera captured pictures for different positions with 5 cm interval up to 588 cm from the lamp using the same exposure time ($\frac{1}{60}$ seconds). In both measurements other camera metadata such as aperture and ISO-number are constant as $f/4.0$ and $ISO - 80$ respectively.

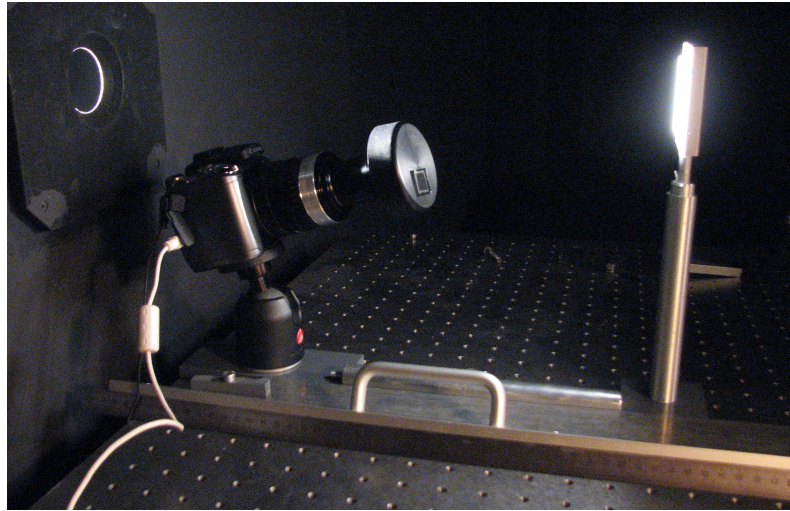


Figure 4.14: Camera setup in the laboratory for measuring the linearity and dark current of the [CCD](#) sensor. This picture was taken during the dark current measurement.

The values of red, green and blue were extracted from the images and then averaged over an area of the reflectance plaque 150×150 pixels at the center of the images. The exposure times in the x-axis are plotted against the y-axis of the averaged brightness values, which range from 0–255 counts for three channels of [CCD](#) sensor as shown in [Figure 4.15](#). In this fitting data, the saturated points of the long exposure time than 0.02 second were excluded.

In [Figure 4.15](#), a percentage of linearity in this [CCD](#) is about 25%, which is determined from maximum positive and negative deviations of the output signal. The maximum departure from the linearity in this [CCD](#) is commonly less than 0.3% for conventional [CCDs](#) and better than 0.2% for scientific used in astronomy [[SHORTIS and BEYER, 1996](#)]. Thus the relationship between output [RGB](#) values and exposure time is clearly non-linear.

To determine the linearity with the variation of incident light, the images are analyzed as described above. The output signal and amount of light source which is inversely proportional to the square of the distance from the lamp is presented in [Figure 4.16](#). A black solid line represents a linearity. The relation between the

intensity of light and the **RGB** values is clearly also non-linear. From these results, the non-linearity of this camera sensor depends on the exposure time and variation of the incident light.

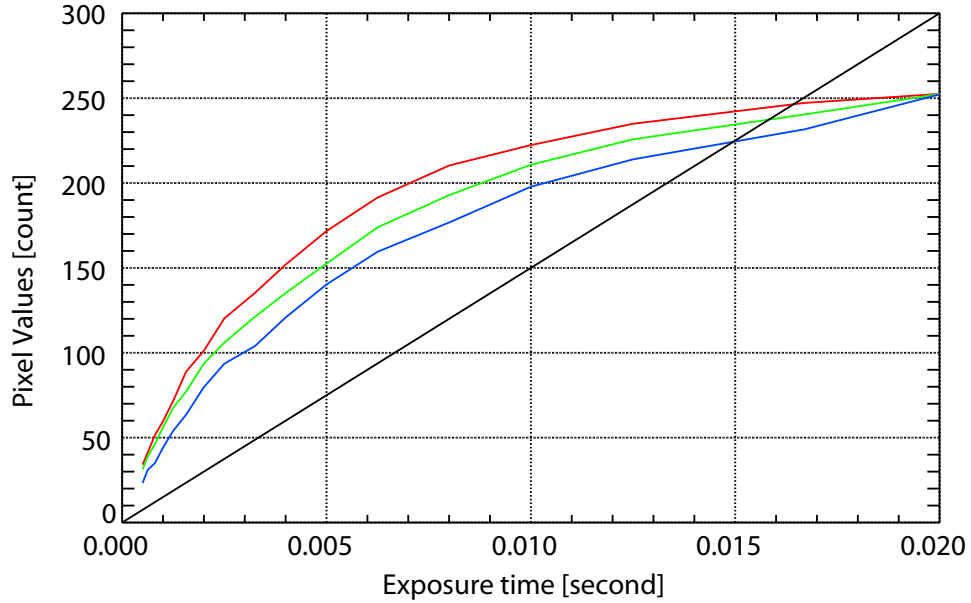


Figure 4.15: Result of the linearity test with the variation in exposure times (X-axis). Y-axis is the averaged **RGB** intensity of images. It clearly denoted that the CCD sensor is non-linear.

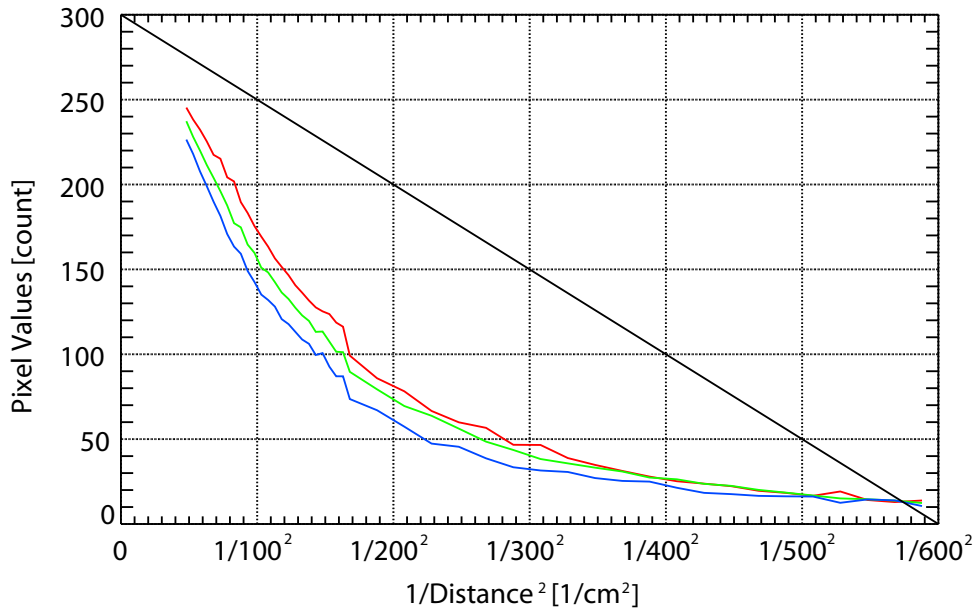


Figure 4.16: Linearity test with the variation in intensity of incident light. X-axis represents the inverse square of the distance between the plaque and the lamp, y-axis is the averaged **RGB** intensity of images.

4.2.2.3 Spectral responsivity of CCD camera sensor

Processing data from a digital camera requires a good knowledge of the sensor spectral response. Spectral sensitivity is the relative efficiency of light detection as a function of wavelength. It is determined from the current produced by the sensor for a given power and wavelength of incident light. Some researches, for example, colorimetric qualities [BRYDGES et al., 1998], color matching [MATÍNEZ-VERDÚ et al., 2002] and spectral characterization [NIEVES et al., 2005] require this knowledge. The spectral response of this CCD sensor is necessary for the retrieval of the spectral radiance, which will be described in Chapter 6. The spectral response can be performed by the measurement and the model estimation [HUBEL et al., 1994; VORA et al., 1997].

In this work, the radiometric experiment was established in the laboratory to measure the spectral responsivity of the CCD camera sensor. The configuration of this experiment is illustrated as shown in Figure 4.17.

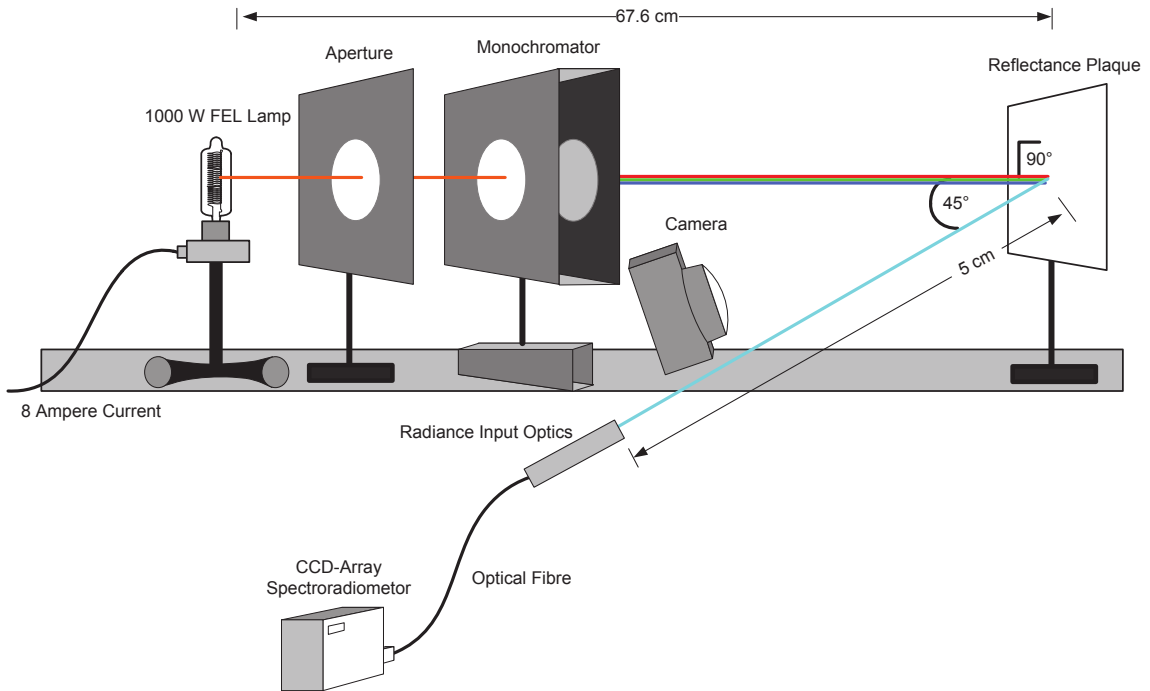


Figure 4.17: Experimental setup for determining the spectral response of the CCD camera sensor. The incident light is normal to the direction of the plaque. The CCD spectroradiometer measures the spectral radiance at an angle of 45° from the normal direction of the plaque. The camera also captures a picture simultaneously.

Narrow band stimuli were generated by using light from the 1000 W lamp which passed through a monochromator Model GM252². The spectral radiance of each narrow band stimulus with 1.0 nm wavelength spacing in the range 380 nm to 770 nm was measured using the CCD Spectroradiometer (see Figure 3.1 and more details in Section 3.1). The radiance input optics is mounted on the rotational table in a 45° angle to the reflectance plaque and at a distance of 5 cm. The camera was placed in front of the reflectance plaque. The CCD spectroradiometer collected the signals for two cases with the signal passing through the monochromator and without it. The camera simultaneously recorded the image of the illuminated reflectance plaque at each wavelength.

Firstly, the spectral responsivity of the CCD spectroradiometer can be determined by laboratory experiment as explained in Section 3.1 and is expressed again in Equation (4.9):

$$r_{CCD}(\lambda) = \frac{S_{CCD}(\lambda)}{R_{1000W}(\lambda)}. \quad (4.9)$$

From this known spectral response of the CCD spectroradiometer $r_{CCD}(\lambda)$ and the measured signal passing through the monochromator $S_{mono}(\lambda)$, the spectral responsivity of the monochromator $r_{mono}(\lambda)$, can be obtained from the equation

$$r_{mono}(\lambda) = \frac{S_{mono}(\lambda)}{r_{CCD}(\lambda)}. \quad (4.10)$$

Therefore, the responsivity of the CCD camera sensor $r_{CAM,i}(\lambda)$ for each channel was estimated from the relation between the extracted RGB values ranged from 0-255 of each channel, which is defined as the signal from the camera sensor $S_{CAM,i}(\lambda)$ and the spectral responsivity of the monochromator $r_{mono}(\lambda)$ as shown in the following equation

$$r_{CAM,i}(\lambda) = \frac{S_{CAM,i}(\lambda)}{r_{mono}(\lambda)} \quad (4.11)$$

where i represents either the red, green or blue channel. $S_{CAM,i}(\lambda)$ value is obtained by averaging the extracted RGB values of the reflectance plaque on images at each wavelength. The spectral responsivity of CCD camera sensor is finally determined from the experiment and the result is presented in Figure 4.18.

As shown in Figure 4.18 the sensor elements respond to wavelengths covering the complete range of visible light. For wavelengths in the infrared (IR) part, the images and spectral radiance were also measured but the signal was very low and very difficult to process. The peak of response is between the wavelength range 435 – 445 nm corresponding to the blue light. The maximum sensitivity of each red, green, blue channel is found to be at 602 nm, 527 nm and 441 nm, respectively.

²personal correspondence with Prof. Dr. Gerhard Wagner, Faculty of Electrical Engineering, Ostfalia University of Applied Science

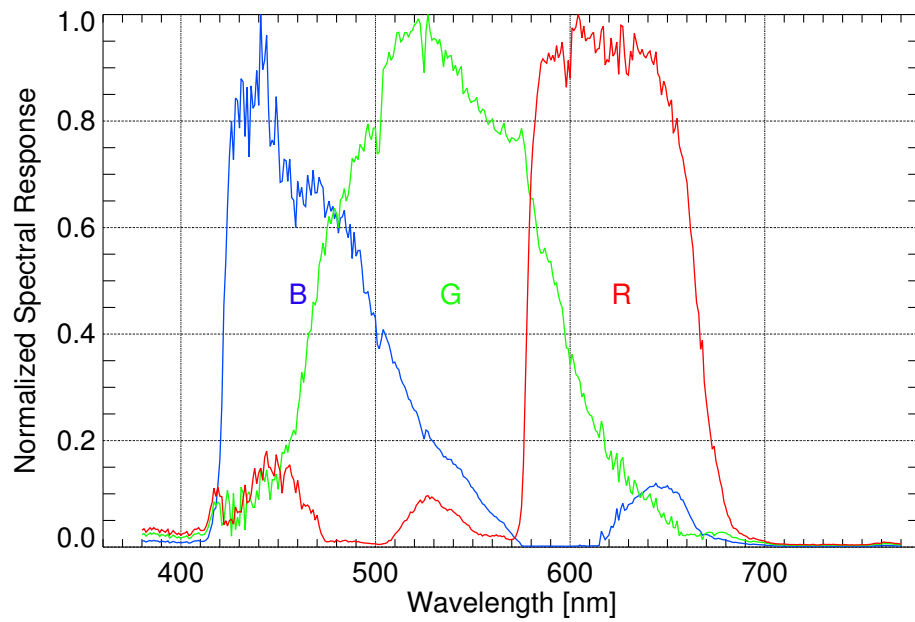


Figure 4.18: Normalized spectral sensitivity of the Canon Powershot G10 CCD camera sensor: three subtypes of the sensor are representing the three channels blue, green and red. The camera sensor has a wider sensitivity in the green channel than in the others.

5 Use of the CCD Camera for Measuring Sky Luminance Distribution

This chapter presents a technique for determining the sky luminance distribution from the hemispherical images, which are separated into Low Dynamic Range (LDR) and High Dynamic Range (HDR) images described in Section 5.1. In contrast to the luminance approach from ROY et al. (1998) new parameters are introduced and estimated by using absolute calibration in the laboratory explained in Section 5.2. The camera-based and measured sky luminance for different sky conditions will be compared. In addition, the measured global illuminance from the luxmeter will be used to validate the illuminance derived from camera-based luminance and presented in the Section 5.3.

5.1 Low and High Dynamic Range image acquisitions from HSI system

The HSI system was set to acquire the large and fine images with the original image size of 4416x3312 pixels. These images were cut to obtain the hemispherical area or spatial resolution of 2121x2121 pixels as shown in Figure 5.1(a). Some broken clouds at the zenith point were clearly detected and the circumsolar region is shown as a very bright area. Some high buildings, masts, trees or other radiation instruments appear on the horizon. This obstruction is less than 1% of the whole hemispherical area.

Each pixel of the image has about 0.085° FOV or 60x60 pixels corresponding to the 5° FOV of the CCD spectroradiometer. As analyzed in Section 4.2.1, the employed fish-eye objective provides a nearly equidistant projection function, and there is no need for the correction of the coordinate transformation in the luminance determination. However, the number of pixels for each scanning point of CCD spectroradiometer at the center and horizon of image is different. Therefore, the scanning points of the CCD spectroradiometer, which are the function of zenith angle and azimuth angle, are projected onto the all-sky image. Observing through the fish-eye objective, the circular scanning spots around zenith region are still the same geometric shape, whereas they are different in the horizon. An apparent size of clouds is generally reduced when they are near the horizon compared to the zenith.

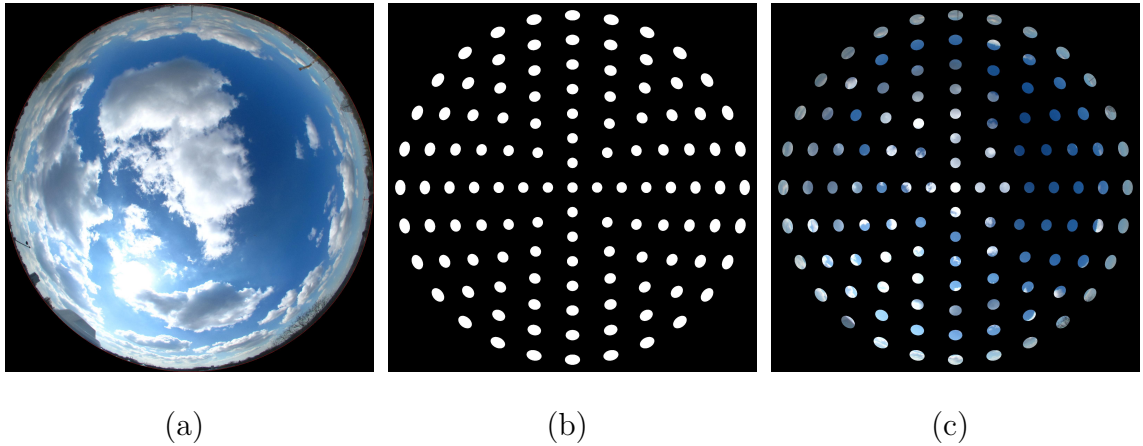


Figure 5.1: The hemispherical area (2121x2121 pixels) of the HSI image (a). The Skyscanner pattern for applying to the whole sky used the algorithm by courtesy of Dip.-Met. Michael Schrempf (b) and the coverage of sky with 113 circular patches after superimposing the Skyscanner pattern (c).

Figure 5.1(b) is the sky pattern with 113 scanning points for the measurement by the CCD spectroradiometer with the 5° FOV. The image obtained by superimposing the scanning pattern onto the hemispherical image is illustrated in Figure 5.1(c). The algorithm for projecting the hemisphere onto two dimensional area of the HSI images was provided by Dipl.-Met. Michael Schrempf¹. Due to the direct luminance from the sun being four to five orders of magnitude brighter than the sky luminance, it is not measured by the CCD spectroradiometer. Therefore, the solar disc region and a part of the circumsolar region are excluded approximately 10° in diameter for the calculation from the HSI images.

According to the dynamic range of the camera sensor, it is important for determining the luminance distribution given the details in Section 2.2.4, the images recorded with the HSI system are categorized into two types: low dynamic range image and high dynamic range image. These will be introduced in the following subsections.

5.1.1 Low dynamic range (LDR) acquisition

The 8-bit or less per color channel imagery is referred as low dynamic range (LDR) imagery [BANTERLE et al., 2009]. Several regions of such system either appear very dark or over-exposed. It is not generally possible to capture the full dynamic range of a real-world scene in a single exposure with this imagery. In this work, the LDR images from the HSI system are taken with the exposure time of $\frac{1}{1000}$ s. In Figure 5.2, the middle image represents the LDR images from the HSI system. The circumsolar

¹Personal communication with Dipl.-Met. Michael Schrempf, Institute for Meteorology and Climatology, University of Hannover.

region or bright cloud on the images under clear sky or partly cloudy sky are very bright and some information may be lost in these regions. The sky luminance distribution from the **LDR** image is derived and validated with the measured luminance obtained from the **CCD** spectroradiometer. The result of the determination will be presented in Section 5.3.

5.1.2 High dynamic range (**HDR**) acquisition

Due to the large dynamic range of the sky radiance, the 8 bit **ADC** of the camera provides not enough resolution to capture the sky radiance in sufficient detail. The luminance determined by the **HSI** system using only one exposure image or low dynamic range has a dynamic range of only about 3 orders of magnitude and the saturation at the circumsolar region or from bright clouds causes a deviation of the luminance calculation. Therefore, to increase the dynamic range of the **HSI** system during this work, an **HDR** image is designed as being composed of three **LDR** images with different exposure times of the same scene. A **LDR** image taken with a short exposure time can record bright areas, whereas long exposure time can capture details in the dark areas. The various **HDR** acquisition methods using multi exposure **LDR** images were proposed in ROBERTSON et al. (2003) and SUN et al. (2010).

Two main stages such as capturing and processing are applied for creating the **HDR** image from three different exposure **LDR** images of the **HSI** system.

5.1.2.1 Image capturing

The auto-bracketing function of the **HSI** system was set to capture almost the same scene of the sky hemisphere with different exposure values, which have the time difference about 1 second. These camera parameters have been configured as follows.

- Using the auto-bracketing feature with 1 stop obtains three **shutter speed** images of $\frac{1}{500}$, $\frac{1}{1000}$, $\frac{1}{2000}$ seconds. For luminance investigation in this chapter the image with shutter speed $\frac{1}{500}$ s is further denoted as *long exposure image*, with $\frac{1}{1000}$ s is denoted as *normal exposure image* and with $\frac{1}{2000}$ s is called the *short exposure image*.
- **Aperture** is constant as $f/4.0$.
- **ISO number** is also set as a constant *ISO80*.
- **Focal length** of the camera during the work is 6 cm and cannot vary.

Figure 5.2 presents images containing different exposure times. These images were captured with the high temporal resolution of 20 seconds and were stored in the computer hard drive.

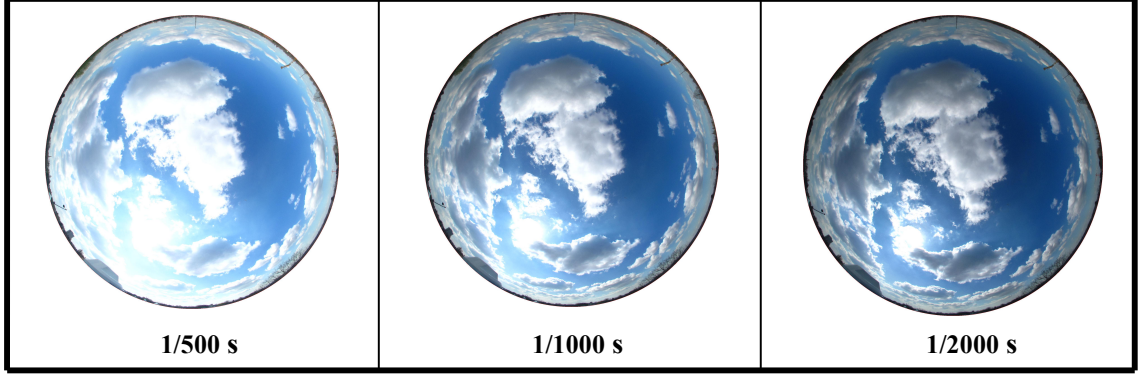


Figure 5.2: Three different exposure LDR images taken on April 8, 2012 at 10:04 UTC. Some parts of the long exposure image are over-exposed especially at the circumsolar region.

5.1.2.2 HDR processing

A process for fusing the set of multiple exposure images onto a new HDR image where all scene areas appear well-exposed is illustrated in Figure 5.3. Due to the smallest signal count of the red channel compared with the green and blue channels, the signal value ranged from $[0,255]$ of the red channel from the normal exposure image ($\frac{1}{1000}$ s), R_{normal} is firstly defined as a threshold for expanding the HDR image. If the R_{normal} is less than 50, the signal count from all three channels $(R, G, B)_{HDR}$ has been replaced with the signal count from the long exposure image $(R, G, B)_{long}$. When R_{normal} is greater than 200, the signal of HDR image has been replaced with the signal count from the short exposure image $(R, G, B)_{short}$. Otherwise, the signal count of the HDR image is the same as the signal count from normal exposure image $(R, G, B)_{normal}$. A simple and efficient assumption for specifying the threshold can be expressed in following equations.

$$(R, G, B)_{ij_{HDR}} = (R, G, B)_{ij_{short}} \quad , R_{ij_{normal}} > 200 \quad (5.1)$$

$$(R, G, B)_{ij_{HDR}} = (R, G, B)_{ij_{normal}} \quad , 50 \leq R_{ij_{normal}} \leq 200 \quad (5.2)$$

$$(R, G, B)_{ij_{HDR}} = (R, G, B)_{ij_{long}} \quad , R_{ij_{normal}} < 50 \quad (5.3)$$

where

$(R, G, B)_{ij_{HDR}}$ is the R, G and B values of a new HDR image

$(R, G, B)_{ij_{short}}$ is the R, G and B values of the short exposure image ($\frac{1}{2000}$ s)

$(R, G, B)_{ij_{normal}}$ is the R, G and B values of the normal exposure image ($\frac{1}{1000}$ s)

$(R, G, B)_{ij_{long}}$ is the R, G and B values of the long exposure image ($\frac{1}{500}$ s)

i, j is the coordinate's pixel number of image.

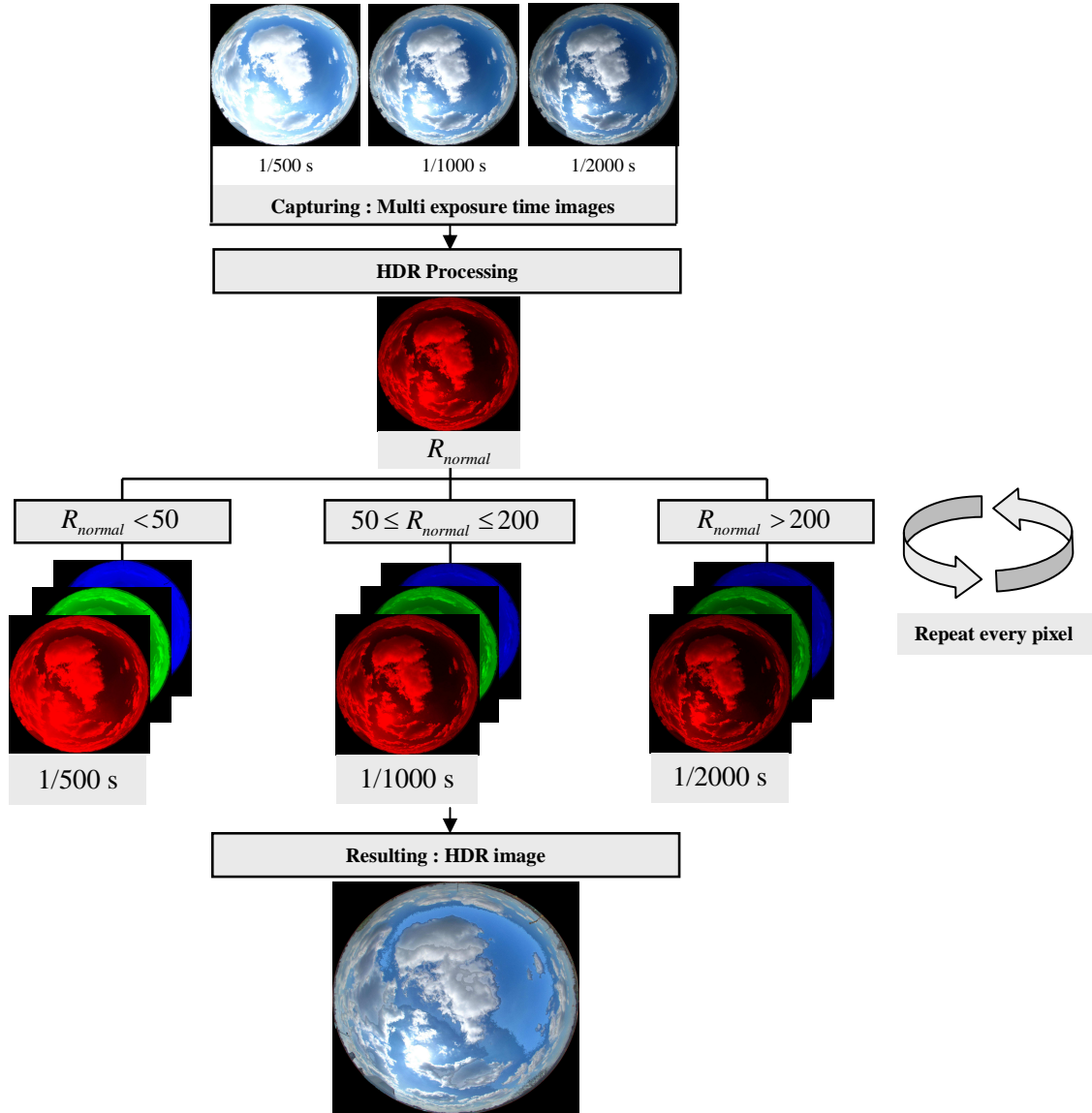


Figure 5.3: The automated methodology for HDR image reconstruction. Different exposure LDR images are captured and combined with the detection threshold to extend the HDR image.

Figure 5.3 illustrates the HDR pipeline in its all stages. Multi-exposure LDR images are captured and carried into the analyzing library. The RGB value is compared with the detection threshold expressed in Equation 5.1 – Equation 5.3, simultaneously the corresponding EXIF parameters (shutter speed, ISO number, and f-number) of each pixel coordinate have been collected for further sky luminance determination. Repeating this processing stage for all pixels of 2121 x 2121 pixels, the HDR image is finally generated. All routines to obtain the HDR are written in IDL programming jointly developed by Dip.-Met. Michael Schrempf.

5. Measuring Sky Luminance Distributions

An example of the **HDR** image under different sky conditions is presented in Figure 5.4. Figure 5.4(a) shows the original three **LDR** images taken with different exposure times of $\frac{1}{500}$ seconds, $\frac{1}{1000}$ seconds and $\frac{1}{2000}$ seconds on March 28, 2012 at 12:30 **UTC** under clear sky and the recovered **HDR** image is on the right hand of the panel. The circumsolar region of the normal exposure image was replaced by the same region of the short exposure image. Across to the sun position, this area is darker than other, and therefore was replaced with the image pixel from the long exposure image.

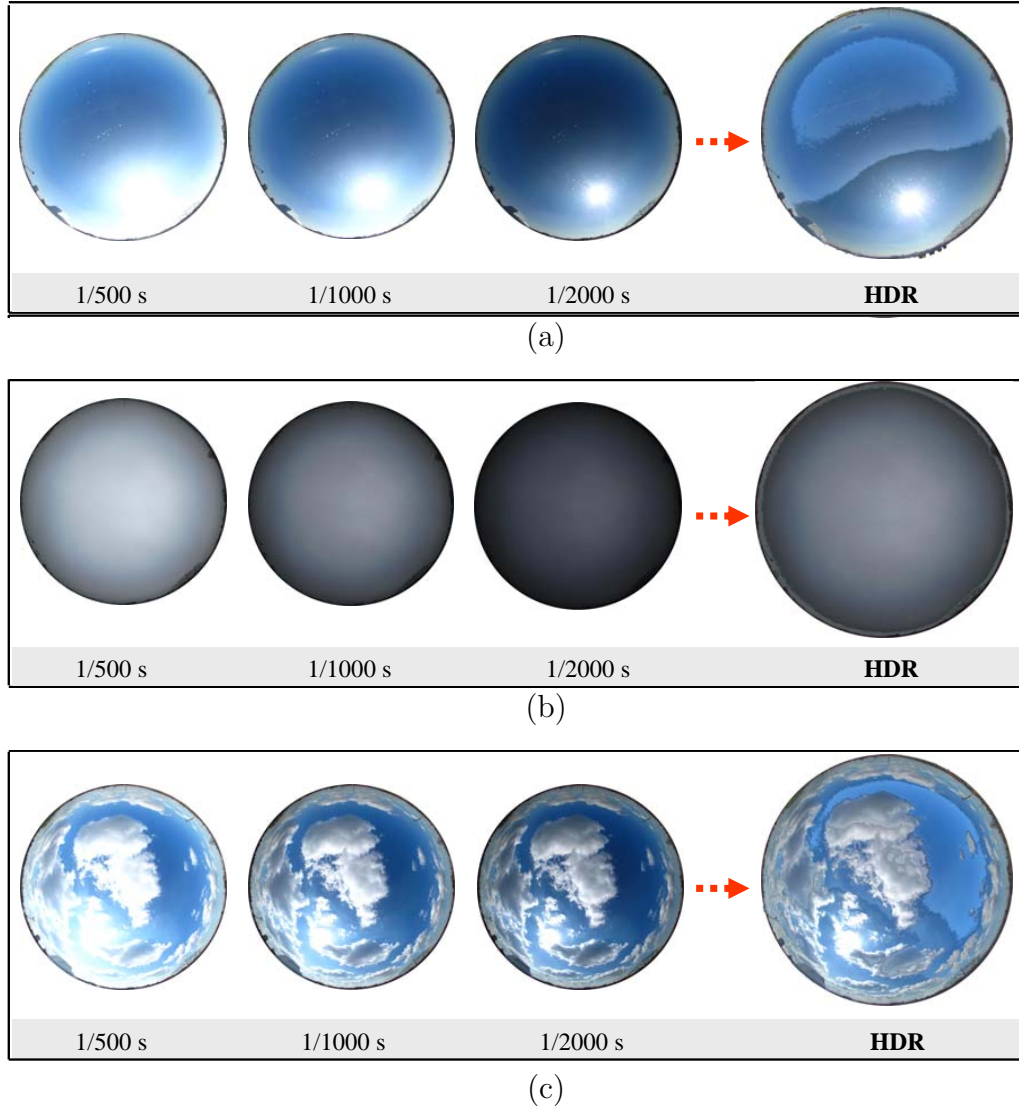


Figure 5.4: Results of the **HDR** images expanded from three **LDR** images for different sky conditions. Image (a) shows three **LDR** images and **HDR** image on March 28, 2012 at 12:30 **UTC**. Image (b) represents overcast conditions observed on February 13, 2012 at 12:25 **UTC** and (c) demonstrates the retrieval of a **HDR** image for partly cloudy skies on April 8, 2012 at 10:04 **UTC**.

Figure 5.4(b) presents the HDR image for overcast condition observed on February 13, 2012 at 12:25 UTC. The HDR image for partly cloudy skies on April 8, 2012 at 10:04 UTC is presented in Figure 5.4(c). Some bright cumulus clouds near the sun and the circumsolar region were replaced as well as the area against the sun.

The measurement of a radiance distribution for the whole hemisphere conducted by the CCD spectroradiometer for obtaining the sky luminance distribution has a scanning pattern of 113 points with the FOV of 5° (see Figure 5.1(b)) and takes about 12 minutes. Since all-sky images from the HSI system are taken every 20 seconds, a total of 35 images can be recorded in the time of one measurement of the CCD spectroradiometer. In order to use the sky luminance distribution of the CCD Spectroradiometer for the validation, a synchronized HDR image of the HSI system is constructed. For this synchronized HSI image, the pixels of each scanning point were taken from the corresponding HDR image, depending on the time of measurement by the CCD spectroradiometer. An example of the correspondent sky pattern constructed from the HSI system under different sky conditions is presented in Figure 5.16(d), Figure 5.17(d) and Figure 5.18(d).

5.2 Method

The approach for calculating sky luminance from all-sky images will be introduced in this section. As the CCD spectroradiometer delivers spectral sky radiance, the relationship between the radiance and luminance needs to be explained. In the next subsection, the method to derive sky luminance from the HSI system will be explained. The last subsection provides the method to deriving the global illuminance from the camera-based luminance.

5.2.1 Conversion of radiance to luminance

The spectral sky radiance measured by the CCD spectroradiometer is converted to corresponding luminance values to allow a comparison between both systems by applying the following formula [DIN 5032, 1999]

$$L_{ph} = K_m \int_{380}^{780} R(\lambda) \cdot V(\lambda) \cdot d(\lambda) \quad (5.4)$$

where L_{ph} is the luminance in cd/m^2 and K_m of 683 lm/W is the conversion constant. $R(\lambda)$ is the spectral sky radiance in W/m^2nmsr and $V(\lambda)$ is the daylight spectral response of the human eye as shown in Figure 3.6 (Section 3.3).

5.2.2 Sky luminance from HSI images

At the beginning of the sky luminance retrieval, the zenith sky luminance from the HSI system were calculated from the approach of ROY et al. (1998) by using Equation (2.12) - Equation (2.14) and were then validated with the zenith luminance from the CCD spectroradiometer. The comparisons indicated that the camera-based zenith luminance was always smaller than the measured zenith sky luminance. The sky luminance from the HSI images can be derived by applying the Equation (5.5) - (5.6) based on the equations of ROY et al. (1998).

$$L_{cam} = \frac{V^{a_T}}{b_T \cdot E_v}, \quad (5.5)$$

$$V = 0.2125R + 0.7154G + 0.0721B, \quad (5.6)$$

$$E_v = \frac{179}{200} \cdot \pi \cdot S \cdot \frac{T}{f^2}, \quad (5.7)$$

where L_{cam} is the luminance of the sky for each pixel of the HSI image in cd/m^2 . V is the luminance function calculated from the RGB values. R, G, B are the RGB values of an all-sky image ranged from 0 to 255 and E_v is the exposure value. S, T, f are the ISO number, the exposure time and the f-stop number, respectively. a_T and b_T are new exposure time dependent parameters.

In contrast to ROY et al. (1998), who used only a constant for a_T and do not introduce b_T (Equation (2.12)), in this thesis work a_T and b_T were evaluated by an experimental investigation in the laboratory described below.

The calibration for evaluating a_T and b_T was performed on a calibration bar in a temperature stabilized lab room. This room has black walls and a suitable baffle setup to reduce stray light during the calibration process [PISSULLA et al., 2009]. Figure 5.5 shows the calibration setup in the laboratory. A reflectance plaque was illuminated by a 1000 W tungsten halogen as describe in the Section 3.1. The plaque was centered in the FOV of the camera at a distance of 35 cm from the lamp. During the calibration process the distance has been increased in intervals of 5 cm up to 565 cm. At each position images of the plaque were acquired with constant ISO number and aperture and for 21 exposure times from 1/2000 seconds to 1/20 seconds. The signals of the red, green and blue channel of the plaque were averaged and as an example, the red values has been plotted against the distance between the reflectance plaque and the lamp as shown in Figure 5.6.

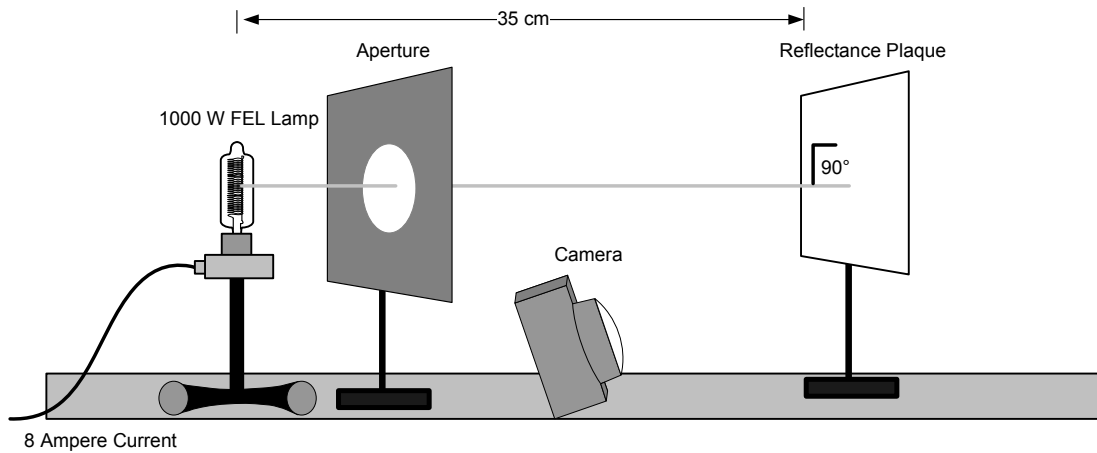


Figure 5.5: A reflectance plaque is illuminated perpendicularly by a 1000 W tungsten halogen lamp. The plaque provides uniform radiance for the luminance calibration in the center of the HSI image. Images of the plaque were acquired with different exposure times varying from 1/2000 seconds to 1/20 seconds [TOHSING et al., 2013].

The spectral radiance emitted by the plaque at each position is calculated from the irradiance of the lamp using Equation (3.1). It is then converted to luminance by applying Equation (5.4) (shown in Figure 5.6 on the right axis). The luminance from the lamp decreases with increasing distance between the lamp. To calibrate the HSI the luminance calculated by Equation (5.5) - Equation (5.7) shall agree with the luminance emitted by the plaque. This is achieved by varying the parameters a_T and b_T for each exposure time, with the smallest difference in both luminance estimates indicating the a_T and b_T for that exposure time. The calibration was repeated to obtain consistent results for the calibration. The luminance of each pixel of an LDR or HDR image is calculated as a function of its corresponding exposure time, with their parameters a_T and b_T listed in the Table 5.1.

The whole procedure for the sky luminance determination from LDR or HDR images for all sky weather conditions could be summarized as follow. The multi exposure LDR sequence is fused onto an HDR image using the procedure described in Section 5.1.2. The R, G, B signal counts from single LDR image and HDR image of each pixel are extracted including its corresponding EXIF parameters. Applying the RGB values, the aperture, the shutter speed, the ISO number and its constants parameters of each exposure time to the Equation (5.5) – Equation (5.7), the sky luminance of each pixel is evaluated and this has been averaged corresponding to 5° FOV for the CCD spectroradiometer. All processes have been implemented in only one routine written in the IDL programming language.

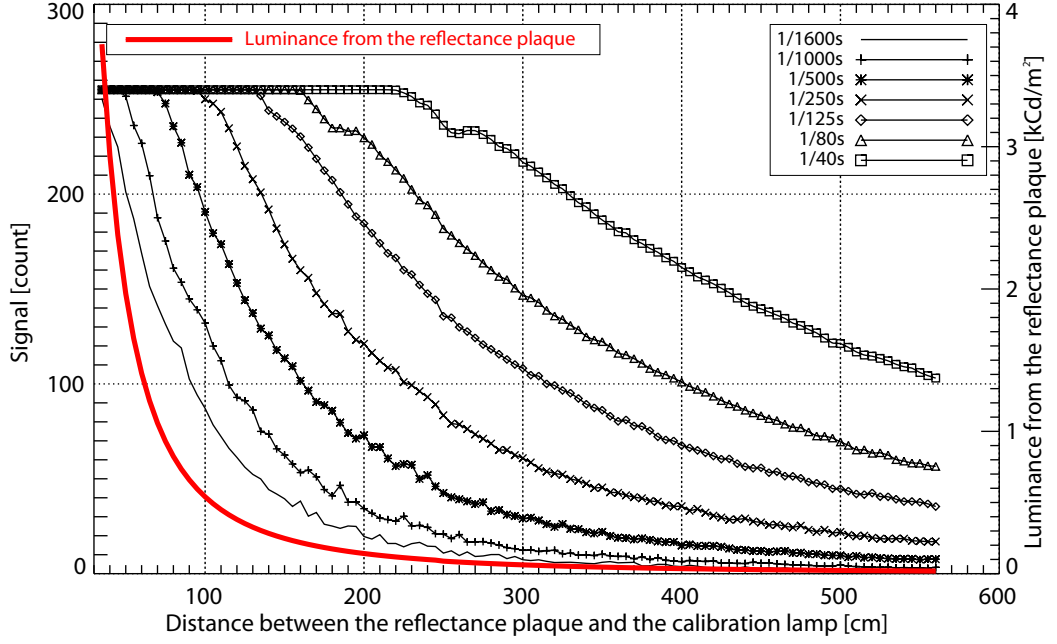


Figure 5.6: Counts (left axis) of the red channel measured during the luminance calibration for seven different exposure times as a function of the distance between the reflectance plaque and the calibration lamp. The red solid line represents the luminance (right axis) emitted by the reflectance plaque [TOHSING et al., 2013].

Table 5.1: Parameter a_T and b_T from the luminance calibration in the IMuK laboratory for determining sky luminance expressed in Equation (5.5) for each shutter speed. The ISO number and the aperture were set constant.

Shutter speed, T (second)	a_T	b_T	Shutter speed, T (second)	a_T	b_T
1/2000	1.7	75.5027	1/160	1.0	1.76178
1/1600	1.7	38.4596	1/125	1.0	1.53217
1/1250	1.4	14.4219	1/100	1.0	1.35100
1/1000	1.3	10.6037	1/80	1.0	1.17330
1/800	1.3	10.5500	1/60	1.0	0.91410
1/640	1.3	10.5497	1/50	1.0	0.79809
1/500	1.2	5.8082	1/40	1.0	0.65213
1/400	1.2	5.78164	1/30	1.0	0.49910
1/320	1.2	5.53416	1/25	1.0	0.42378
1/250	1.1	3.27307	1/20	1.0	0.33813
1/200	1.0	1.94406			

5.2.3 Quality control of luminance data

The illuminance has been calculated from luminance data of the sky radiance in addition to calculation of the direct illuminance. These data have been intercompared with data from the luxmeter in order to validate the luminance approach developed in this work. The diffuse illuminance is calculated by the following Equation (5.8) [TREGENZA and WATERS, 1983]:

$$E_{dh} = \int_0^{2\pi} \int_0^{\pi/2} L_{\gamma,\varphi} \cdot \sin\gamma \cdot \cos\gamma \cdot d\gamma \cdot d\varphi \quad (5.8)$$

where E_{dh} is the diffuse illuminance on the horizontal plane (lm/m^2 or lux) and $L_{\gamma,\varphi}$ is the luminance of the sky element with the corresponding elevation angle (γ) and azimuth angle (φ).

Under cloudless skies, the main contribution to the global illuminance is the direct component from the sun. The direct illuminance of the sunlight is obtained from the Equation (5.9) proposed by KROCHMANN and SEIDL (1974):

$$E_s = 130 \cdot \sin\gamma_s \cdot \exp(-0.2/\sin\gamma_s) \quad (5.9)$$

with E_s is direct illuminance from the sun in $klux$ and γ_s is solar elevation angle in degrees.

If the sun is not obscured by clouds, the global illuminance is calculated by summing the direct illuminance (Equation 5.9) and the diffuse illuminance (Equation 5.8) derived from the camera, otherwise the direct illuminance is set to zero.

In the case of the sun not being in shaded, to compute the diffuse illuminance with Equation (5.6) data in a circumsolar area of 10° diameter around the sun has not been included in the calculation. This can be done with the following description. To indicate the solar position on the all-sky images from the hemispherical sky imagery, the solar zenith θ_s and azimuth angles φ_s were calculated from the modified date and time of the image [IQBAL, 1983] and have been converted into image coordinate (X_i, Y_i) using the following equations [YAMASHITA et al., 2004]:

$$X_i = Radius + Radius \cdot \sin(\varphi_s - 180) \cdot \frac{\theta_s}{90} \quad (5.10)$$

$$Y_i = Radius + Radius \cdot \cos(\varphi_s - 180) \cdot \frac{\theta_s}{90} \quad (5.11)$$

where X_i, Y_i are image coordinate at pixel number i . $Radius$ is the distance between the zenithal point and the horizon on the image in pixels. θ_s is zenith angle ($0^\circ \leq \theta_s \leq 90^\circ$) and φ_s is azimuth angle ($0^\circ \leq \varphi_s \leq 360^\circ$) of the solar position.

Using Equation (5.10) and (5.11) the solar zenith and azimuth angles have been converted into image coordinate (X_i, Y_i) . After that a radius of about 200 pixels

indicates the circumsolar region and has not been included in the estimation of diffuse illuminance as shown in Figure 5.7 with a black circle.

It is quite well known that the scattering from the side of clouds such as cumulus clouds can enhance global solar irradiance by 20% or more [MIMS(III) and FREDERICK, 1994; POETZSCH-HEFFTER et al., 1995]. Therefore, the cloud appearance in the area surrounding the sun has to be investigated. This area contained the radius about 300 pixels and is shown in Figure 5.7 as a grey ring.

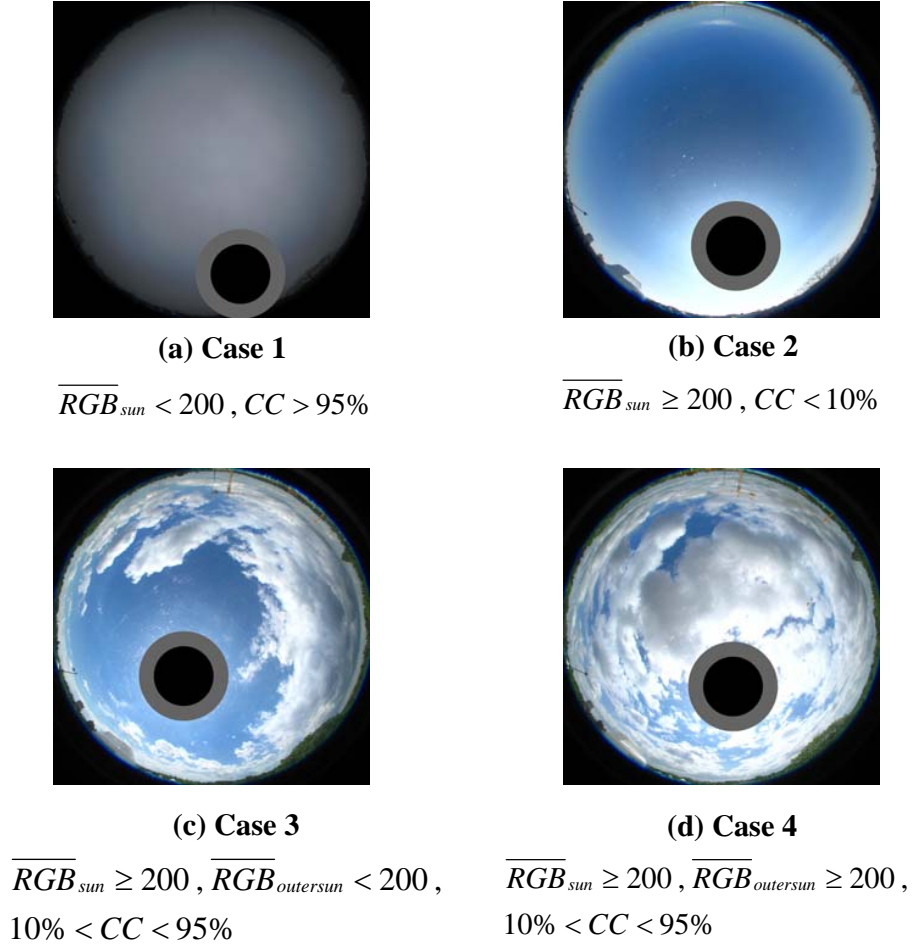


Figure 5.7: Sun and outer Sun area filters for the global illuminance calculation under different sky situations: for overcast sky (a), clear sky (b), intermediate sky with direct sun and no cloud surround the sun (c) and broken clouds with sun light (d).

To automatically calculate the global illuminance, the sky images are categorized into four cases by using the cloud cover (CC) and the average signal counts at the sun position. The cloud cover was determined by using the algorithm described in SCHREMPF (2010). The RGB signal counts at the sun position represented by a black circle were averaged (\overline{RGB}_{sun}) as was the signal counts indicating the clouds around

the sun represented as grey rings ($\overline{RGB}_{outersun}$). Figure 5.7 shows the sample images of four sky cases. The conditions to separate the sky and the equation for determining the global illuminance of each sky situation are described as follows.

- **Case 1:** $\overline{RGB}_{sun} < 200$ and $CC > 95\%$ assigned as **overcast sky** condition. The diffuse illuminance, which is described as the global illuminance, was calculated by using Equation (5.8).
- **Case 2:** $\overline{RGB}_{sun} \geq 200$ and $CC < 10\%$ indicates the **clear sky** condition. Thus, the global illuminance can be obtained by summing the direct sunlight (Equation (5.9)) and the diffuse illuminance (Equation (5.8)).
- **Case 3:** $\overline{RGB}_{sun} \geq 200$, $\overline{RGB}_{outersun} < 200$ and $10\% < CC \leq 95\%$ represents a **partly cloudy sky** without the occurrence of clouds around the sun. The global illuminance was determined by summing diffuse illuminance (Equation (5.8)) to the direct illuminance (Equation (5.9)).
- **Case 4:** $\overline{RGB}_{sun}, \overline{RGB}_{outersun} \geq 200$ and $10\% < CC \leq 95\%$ indicates the **partly cloudy sky** and with some clouds in the proximity of the sun. These clouds can enhance the irradiance due to the multiple scattering by about 20% as previously mentioned. Therefore, global illuminance can be determined from the sum of the diffuse illuminance calculated by Equation (5.8) plus the 20% of calculated diffuse illuminance and the direct illuminance estimated by Equation (5.9).

Figure 5.8 summarizes the calculation of the global illuminance from the HSI system under all weather conditions. The camera-based global illuminance was calculated and validated with the measured global illuminance by the luxmeter. The results of the comparison will be presented in Section 5.3.2

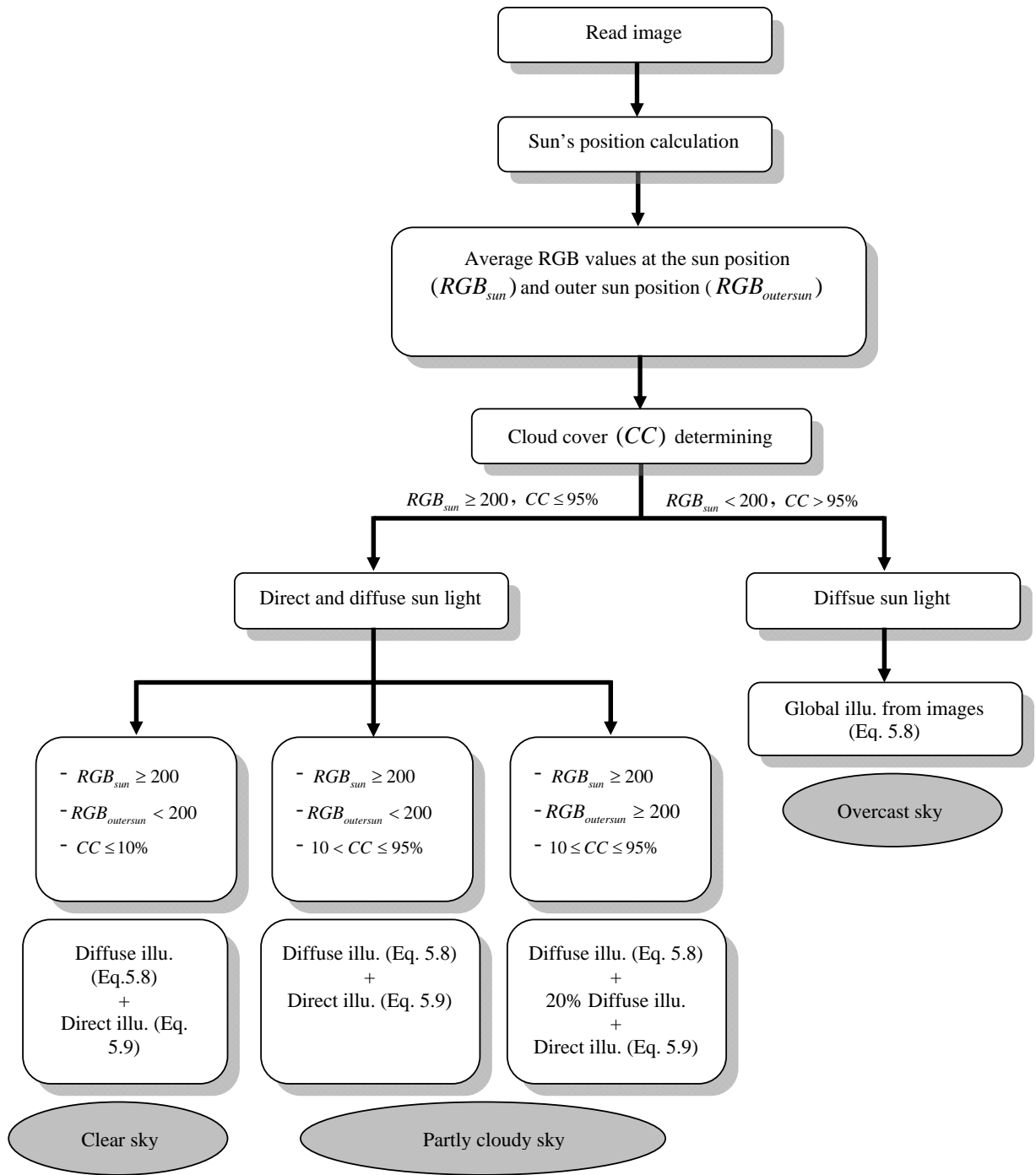


Figure 5.8: The procedure for calculating the global illuminance from images taken with the HSI system applying for all weather conditions.

5.3 Results

Comparisons are carried out between the [CCD](#) spectroradiometer and the [HSI](#) system with regards to sky luminance (section [5.3.1.1](#)) and luminance distribution (section [5.3.1.2](#)). The data quality control which compares the global illuminance from the luxmeter and the [HSI](#) system is shown in section [5.3.1.3](#).

5.3.1 Comparison of sky luminance distribution between the [CCD](#) spectroradiometer and [HSI](#) system

The sky luminance derived from the [LDR](#) and [HDR](#) image of [HSI](#) system has been compared with the sky luminance converted from the spectral sky radiance measured by the [CCD](#) spectroradiometer. The validation compared the diurnal zenith sky luminance, daily averaged zenith sky luminance and sky luminance distribution between the two systems.

5.3.1.1 Diurnal zenith sky luminance

For the validation of the calibration method, the diurnal zenith luminance measured with the [CCD](#) spectroradiometer has been compared with the diurnal sky luminance for the [HSI](#) images. Figure [5.9](#) presents the diurnal zenith luminance for clear sky condition and the comparisons for overcast and intermediate skies are presented in Figure [5.10](#) and Figure [5.11](#) respectively.

Figure [5.9](#) shows a comparison between measured and computed diurnal zenith luminance on March 28, 2012 (upper panel) and the ratio of this comparison is presented in the lower panel. On this day the sky was a nearly cloudless with few cirrus clouds before 8:00 [UTC](#). The red line, blue line and gray line show the zenith luminance from the [CCD](#) spectroradiometer, the [LDR](#) image and the [HDR](#) image from the [HSI](#) system, respectively. The deviation of zenith luminance for clear sky derived from the [LDR](#) and [HDR](#) images in comparison to the [CCD](#) spectroradiometer is less than 10%. The zenith luminance under clear skies from the [LDR](#) and [HDR](#) images is slightly different as seen in the ratio plot. The dynamic range of the zenith sky luminance obtained from the [HDR](#) images is 1:100, which agree with the other study using a digital compact camera [[McCOLLOUGH, 2008](#)].

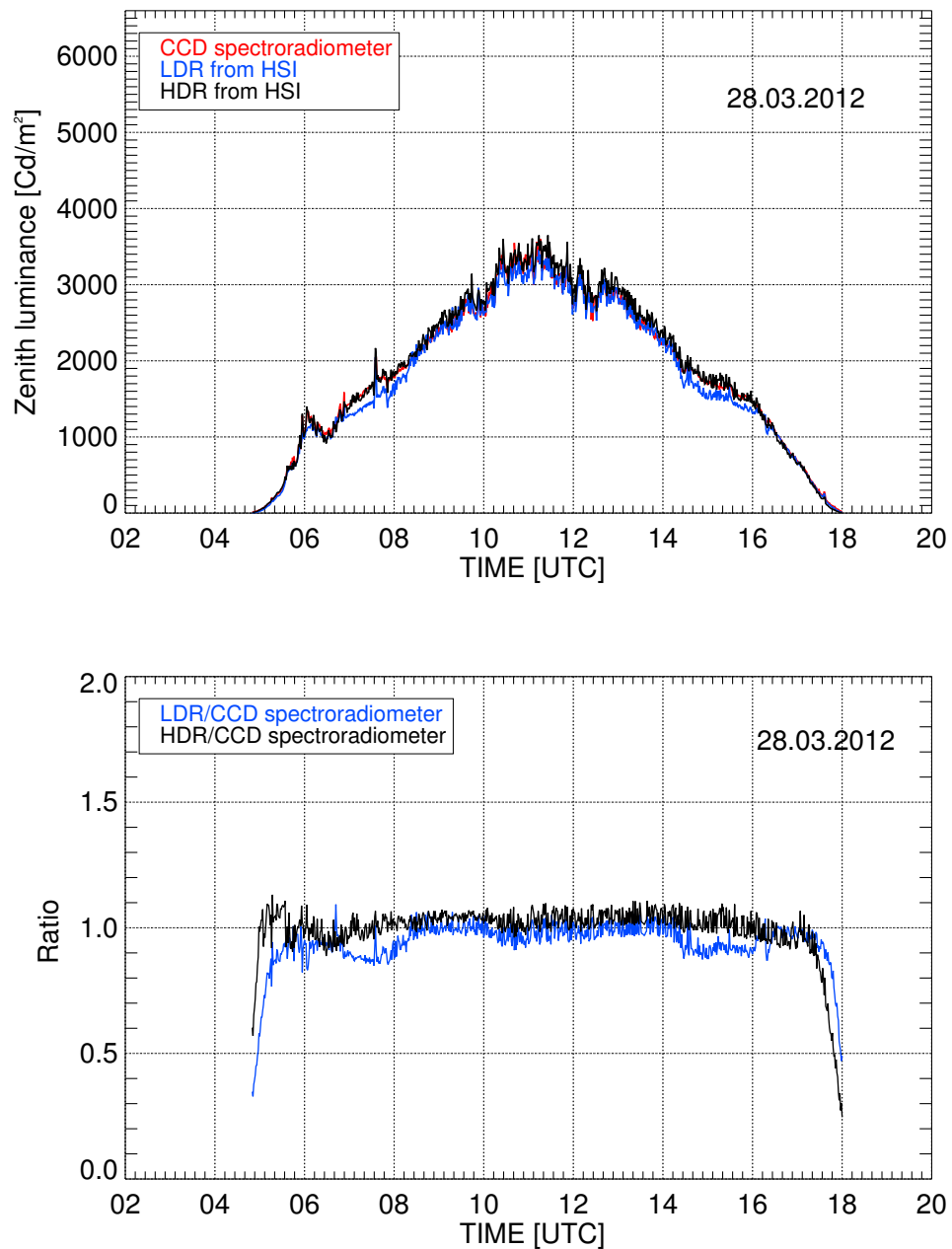


Figure 5.9: Diurnal variation of zenith sky luminance under clear sky condition measured with the CCD spectroradiometer (red line), the LDR images (blue line) and the HDR images (black line) of the HSI system on March 28, 2012 (upper panel). The corresponding ratio is shown in the lower panel. The ratio of 1.0 represents complete agreement.

Comparisons between measured and camera-based zenith sky luminance on April 5, 2012 under overcast skies are presented in Figure 5.10. In the morning on April 5, 2012 the sky was covered by homogeneous clouds but between 11 UTC to 14 UTC, the sky became partly cloudy. The zenith sky luminance obtained from the HSI system slightly overestimated compared to the CCD spectroradiometer and the deviation between both instruments can be up to 10% for solar zenith angle less than 80° . During 6:00 UTC to 10:00 UTC, the sky was completely overcast, there is no difference between the zenith luminance from the LDR and HDR images. This is because the reconstructed HDR image and the LDR image are the same. The difference can be observed when the clouds appeared on the sky as seen at 13:00 UTC to 14:00 UTC. At that time the LDR underestimates the zenith luminance by a factor 2 due to its limited dynamic range and the HDR images delivered the better camera-based estimation than the LDR images.

The comparison between the measured and camera-based zenith sky luminance under partly cloudy sky condition through the broken cloud on May 12, 2012 is shown in Figure 5.11, upper panel and its ratio is presented in the lower panel. With clouds, especially cirrus and cumulus clouds observed during during 8:00 UTC to 15:00 UTC the zenith luminance drastically changed and the ratio of instantaneous zenith luminance from HSI images to the CCD spectroradiometer can be up to a factor of 2. We assume that this short-time variation is caused by a synchronization problem. While the measurements of the CCD spectroradiometer are acquired in 1 s, the LDR and HDR images of the HSI system are captured in approximately 3 s. Time asynchrony of both measuring PCs may cause an additional asynchrony of 1 s. In case of fast moving clouds, the deviation in both instruments is observed. The zenith sky luminance from the LDR images (represented by the blue line) cannot reach the dynamic range of the measured zenith sky luminance, when the clouds occurred as shown in Figure 5.11 (upper panel). The maximum value of the luminance from the LDR only reached about $9 \text{ kCd}m^{-2}$, whereas the maximum from the CCD spectroradiometer was about $26 \text{ kCd}m^{-2}$, which differs by factor of 3. The HDR images can better estimate the zenith luminance and its maximum deviation compared to the CCD spectroradiometer measurement is around 20%. Similar differences of the LDR and HDR image to the CCD spectroradiometer were clearly observed when no clouds appeared on the zenithal point during 15:30 UTC to 17:00 UTC.

In addition, to prove the time synchronization hypothesis between both instruments as stated above, the hourly averaged measured and camera-based zenith sky luminance has been obtained. The change of the hourly average zenith luminance was found to be less than the instantaneous zenith luminance. The deviations of clear sky (March 28, 2012) and overcast sky (April 5, 2012) are found to be less than 10%. Hourly averages during broken cloud conditions (May 12, 2012) lead to a deviation of less than 20%.

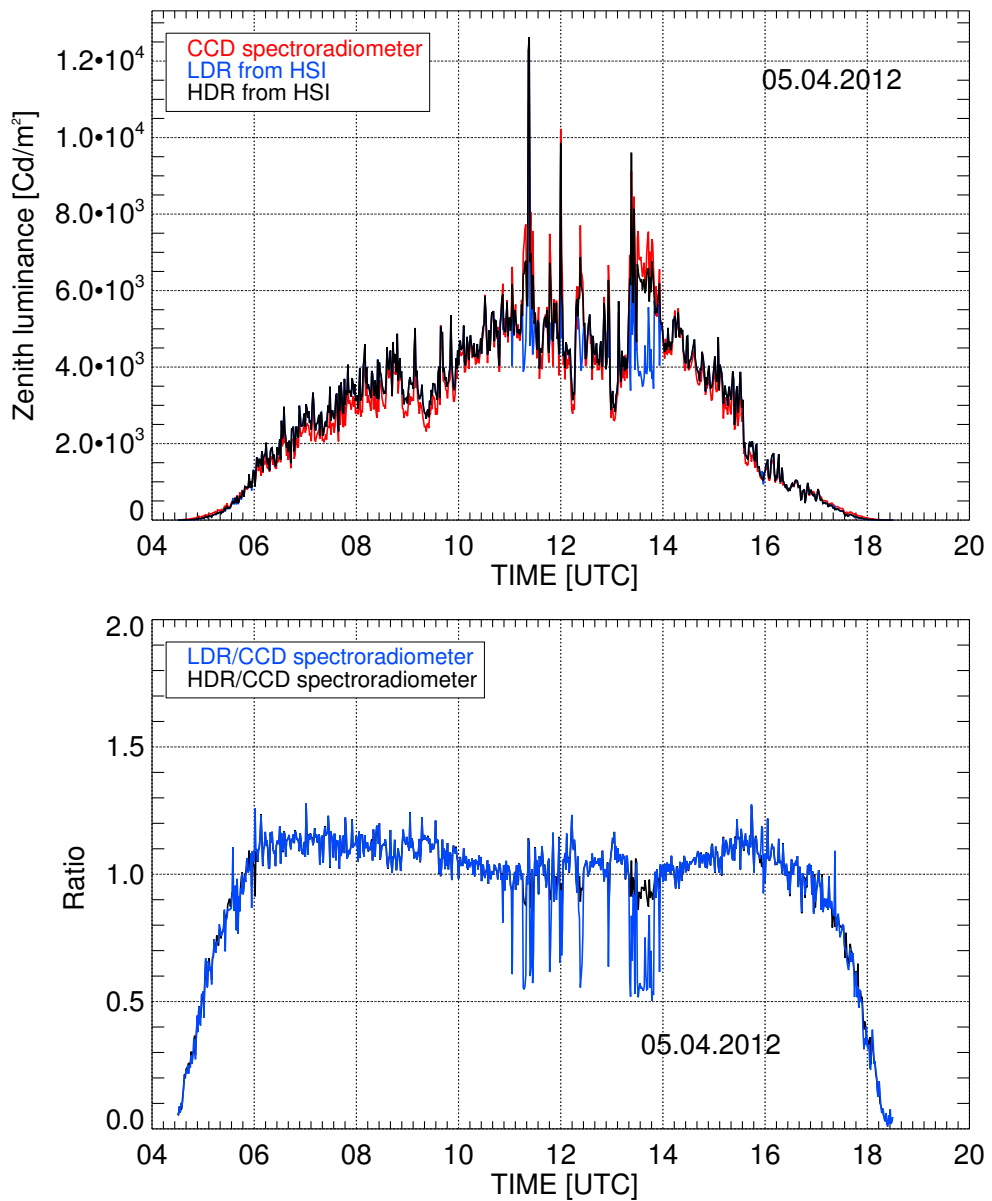


Figure 5.10: Diurnal variation of zenith sky luminance under overcast sky condition measured with the **CCD** spectroradiometer (red line), **LDR** images (blue line) and **HDR** images of the **HSI** (black line) for April 5, 2012 (upper panel) and the corresponding ratio (lower panel).

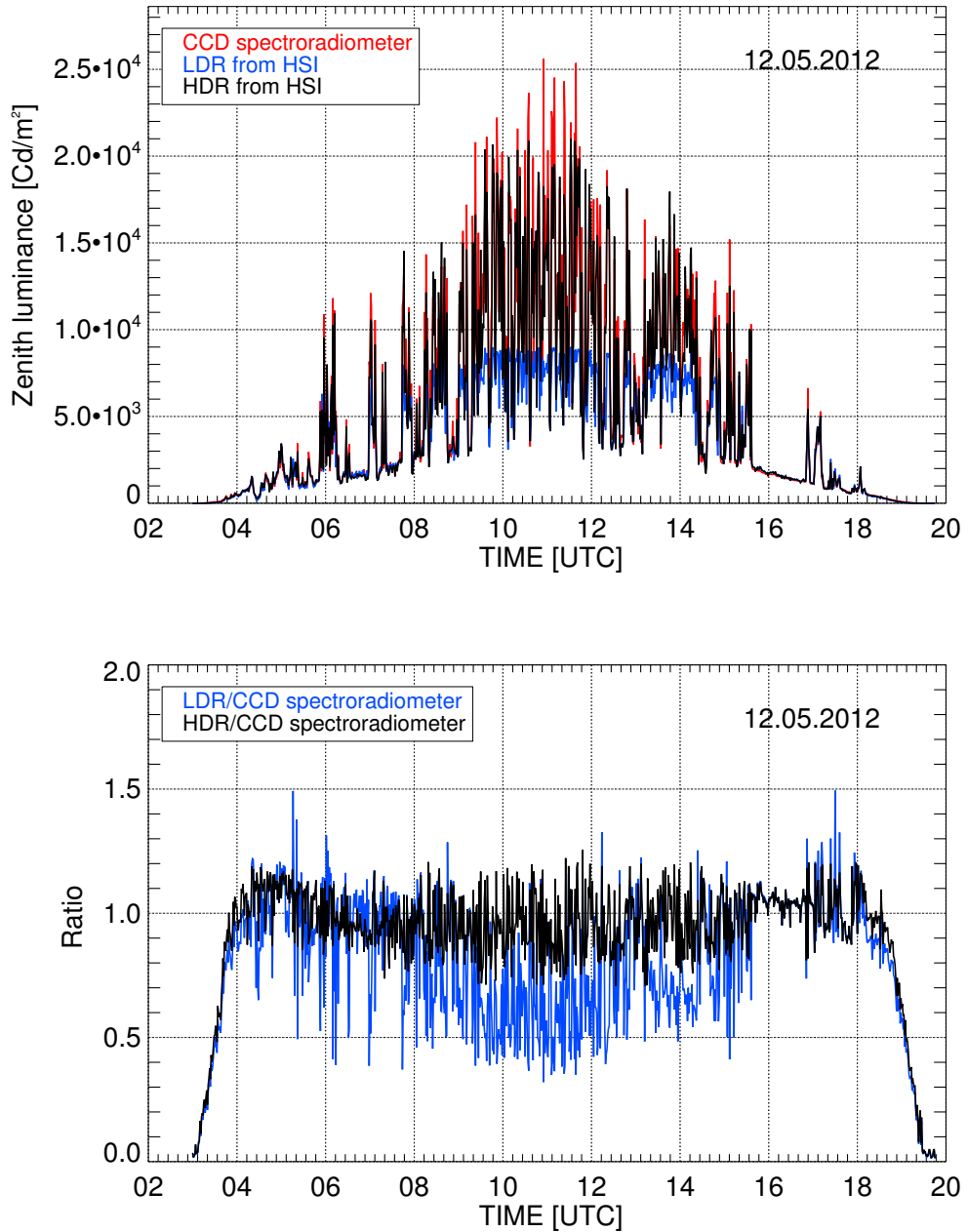


Figure 5.11: Diurnal variation of zenith sky luminance under broken clouds measured with the **CCD** spectroradiometer (red line), **LDR** images (blue line) and **HDR** images (black line) of the **HSI**. Comparison of zenith sky luminance and its corresponding ratio on May 12, 2012 are shown in the upper panel and lower panel respectively.

Figure 5.12 provides an example of the time series comparison of the zenith sky luminance between the **CCD** spectroradiometer and the camera-based calculation under different sky situations in the period of April 1, 2012 – April 6, 2012.

5. Measuring Sky Luminance Distributions

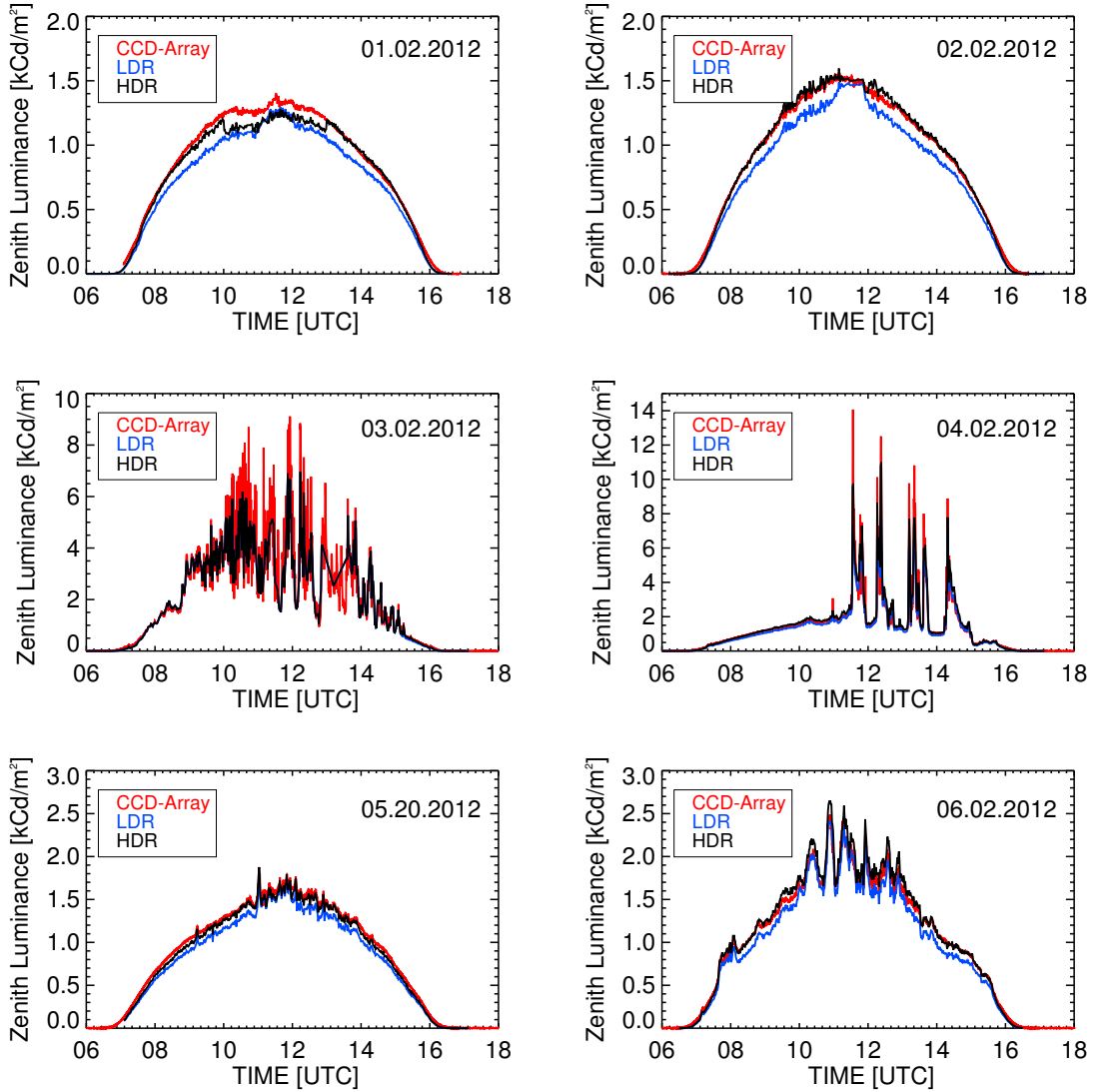


Figure 5.12: Diurnal zenith sky luminance time series during April 1, 2012 – April 6, 2012. The plots present the comparison between the measurement by the **CCD** spectroradiometer (red line), the **LDR** images (blue line) and the **HDR** images (black line).

On February 1, 2, and 5, the sky was mostly clear and there was good agreement between the zenith sky luminance from the **CCD** spectroradiometer and the HDR images of the **HSI** system with a maximum deviation of 5%. The **LDR**-based zenith sky luminance had a larger difference than differences obtained from the **HDR** images. During 10:00 **UTC** to 13:00 **UTC** on February 6, the zenith point was characterized exclusively by some contrails and thin cirrus clouds and the comparison, therefore, shows the variation of the zenith sky luminance, otherwise the sky was almost clear.

The middle panel of the Figure 5.12 displays the diurnal comparison of the intermediate skies on February 3, and February 4, 2012. The skies were covered by cumulus and altocumulus clouds on that days. A cloud coverage changed between

40% to 90% of the skies. Under these skies the camera-based zenith sky luminance underestimated almost by the same magnitude in comparison to the CCD spectroradiometer estimates as shown in Figure 5.11.

Figure 5.13 compares the diurnal zenith sky luminance under cloudless sky obtained from the HSI system at NIWA, New Zealand compared the zenith sky luminance from IMuK. The camera-based zenith luminance at NIWA was measured on September 18, 2012 (black line) and a noon-time solar elevation angle was about 43° . A red line presents the measurement at IMuK on March 28, 2012 with a noon-time solar elevation angle of 41° . The zenith sky luminance at NIWA was observed to be less than the zenith luminance at IMuK despite having a higher noon-time solar altitude. This might be caused by different column aerosol concentrations. The aerosol concentration at NIWA was found to be amongst the lowest observed worldwide [LILEY and FORGAN, 2009]. The multiple scattering due to aerosol can enhance the radiation and it is likely that the zenith luminance at IMuK was higher than NIWA due to differences in aerosol concentration. However, this comparison requires further work and the camera-based luminance at NIWA has to be validated with accurate measurements in the future.

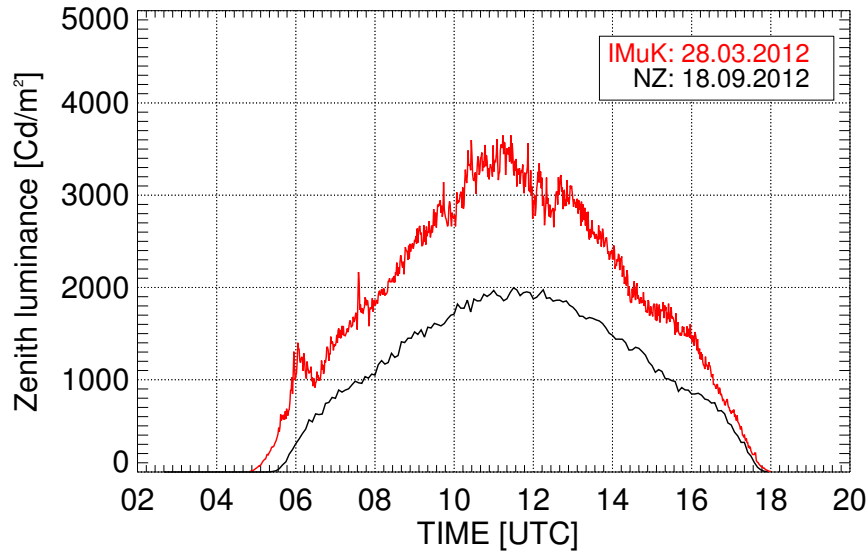


Figure 5.13: Diurnal zenith luminance under cloudless sky measured by HSI system at NIWA (black lines) and at IMuK (red line).

5.3.1.2 Daily averaged zenith sky luminance

The zenith luminance from the three system (CCD spectroradiometer, LDR and HDR) have been averaged between the hours of 4:00 UTC to 18:00 UTC on different dates during the measurement campaign which extended from February 2012 to May 2012. Figure 5.14 shows the comparisons from both measured and camera-based daily averaged zenith sky luminance. The ratio of calculated daily zenith luminance to CCD spectroradiometer is shown in Figure 5.15.

5. Measuring Sky Luminance Distributions

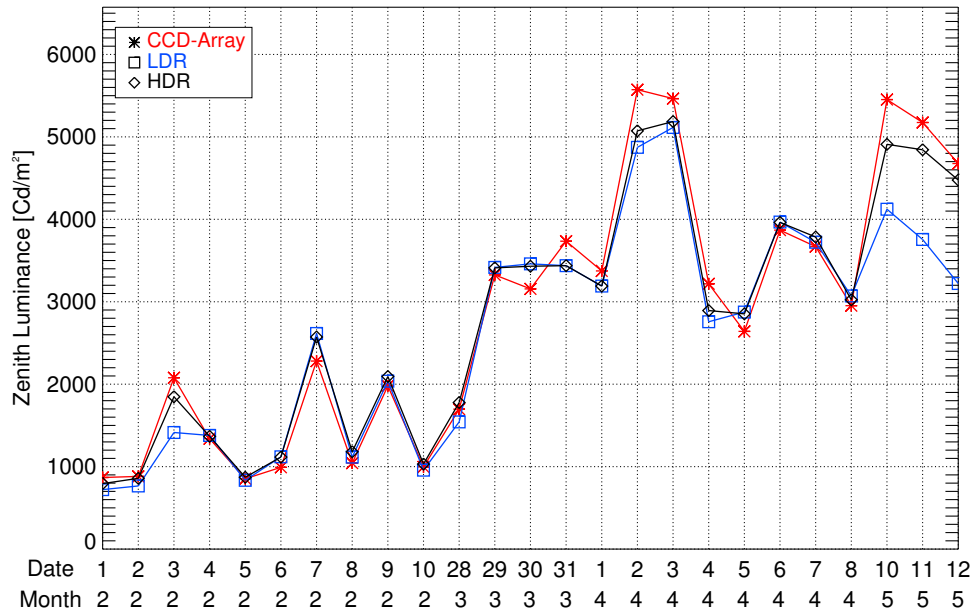


Figure 5.14: Daily averaged zenith luminance measured by the CCD spectroradiometer (star) compared with the LDR images (rectangular) and HDR images (diamond) calculated on different dates in February 2012 – May 2012.

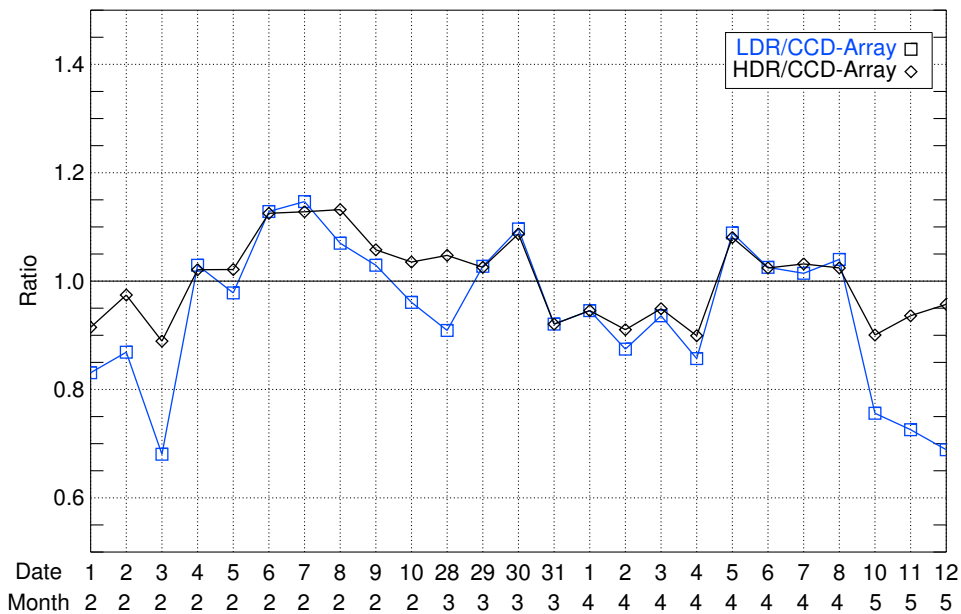


Figure 5.15: Ratio of daily averaged zenith luminance derived from HSI images to the measurement of the CCD spectroradiometer. Line with rectangular shows the result from the LDR images and line with diamond is for HDR images.

The daily zenith sky luminance from the **HSI** system is estimated to be smaller than the **CCD** spectroradiometer in the case of intermediate sky and mixed clear sky with clouds, especially in the **LDR** image. For clear skies the daily averaged zenith luminance is nearly the same. The deviation of daily average zenith luminance from the **HDR** images for homogenous skies (cloudless and overcast skies) is mostly less than 10% and up to 20% for the partly cloudy skies.

5.3.1.3 Sky luminance distribution

To verify if the calibration method is applicable for luminance calculation within the whole sky hemisphere, the sky luminance of the 113 points on the sky dome of the **HSI** system is calculated and validated with the corresponding measured sky luminance from the **CCD** spectroradiometer.

The results of three different sky luminance distributions from the **CCD** spectroradiometer and the **HDR** images of the **HSI** system are shown in Figure 5.16 – Figure 5.18 for cloudless, overcast and intermediate sky situations respectively. The sky hemisphere is projected onto a plane and displayed in polar plot. The geographical directions are indicated by using the azimuth angle for the north is 0° , the south is 180° , the west is 270° with the symbol ‘W’ and the east is 90° with ‘E’. A yellow star represents the position of the sun.

Figure 5.16(a) shows the luminance distribution under clear skies measured on October 28, 2012 at 14:32 UTC (scanning period: 14:32 UTC - 14:44 UTC) by the **CCD** spectroradiometer, (b) from the **HDR** image, (c) the ratio between both instruments, which is plotted with the 10° FOV for the better presentation and (d) the actual **HDR** image showing the 5° FOV pattern of the scanning points from the **CCD** spectroradiometer. A rim at the horizon is featured with higher values compared to the centre of the luminance distribution (lower zenith viewing angles). This feature is called horizon brightening and has also been observed in Antarctica [WUTTKE and SECKMEYER, 2006]. Radiation originating from the horizon has the longest path through the atmosphere among all other viewing angles. Therefore, the multiple scattering can enhance the luminance observed close to the horizon compared to small viewing angle [LIOU, 2002].

The maximum values are within the solar disc and the circumsolar region. The luminance at the horizon (about 4 kCd/m^2) exceeds the zenith luminance (about 2 kCd/m^2) by a factor of 2. The sky luminance near the horizon and in the circumsolar region observed by the **CCD** spectroradiometer is clearly brighter than the corresponding **HSI** measurements. The ratio of both measurements (see Figure 5.16(c)) demonstrates that the sky luminance distribution from the **HDR** image is slightly underestimated in comparison to the **CCD** spectroradiometer. The deviation of the sky luminance distribution is mostly found to be less than 10% for solar zenith angle less than 80° .

5. Measuring Sky Luminance Distributions

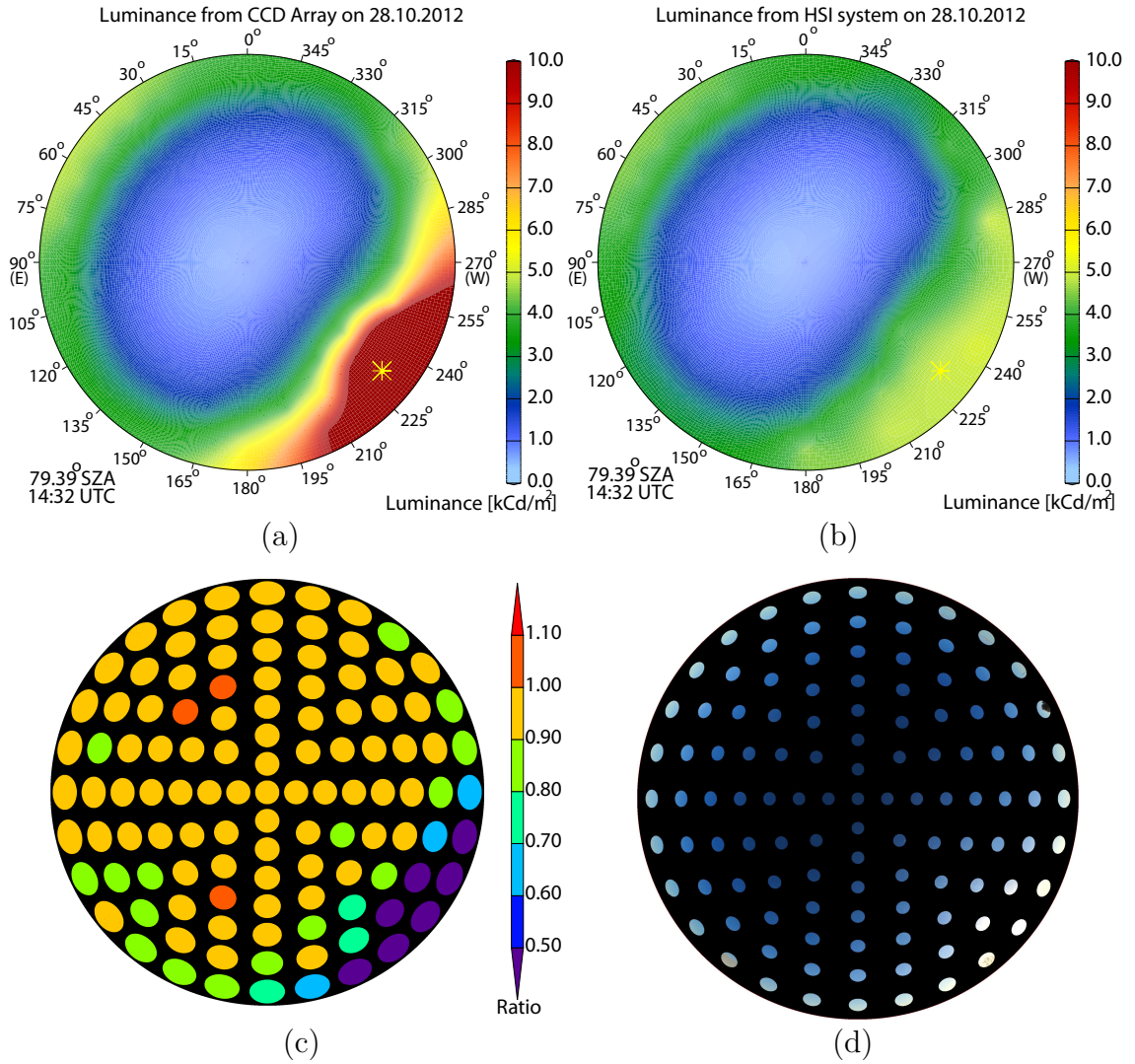


Figure 5.16: Sky luminance distributions measured by (a) the CCD spectroradiometer (b) the HDR image of the HSI on October 28, 2012 at 14:32 UTC (68.98° of SZA) for a cloudless sky. The ratio of the sky luminance distribution between the HSI to the CCD spectroradiometer (HSI / CCD spectroradiometer) is presented in (c). Although the FOV of the scanning Pattern is 5° (plot (d)), the scanning points showing the ratio are plotted with a FOV of 10° for clarity of the presentation. The synchronized HSI image showing the 5° FOV pattern of the scanning points from the CCD spectroradiometer is illustrated in plot (d).

The sky luminance under inhomogeneous overcast skies exhibit a different distribution. Figure 5.17 presents measurements taken on October 22, 2012 at 09.29 UTC (scanning time: 09.29 UTC – 09.41 UTC) corresponding to a solar zenith angle of 66.86° by the CCD spectroradiometer (a) and from the HSI system (b). The HDR

5. Measuring Sky Luminance Distributions

image showing the 5° FOV pattern of the scanning points from the CCD spectroradiometer is presented in Figure 5.17(d). The horizon brightening was not observed and the sky luminance at the zenith is higher than the horizontal sky luminance. The HDR image also shows that the horizon is darker than the zenith. The ratio of the sky luminance distribution from the HDR image to the CCD spectroradiometer is displayed in Figure 5.17(c) and the deviation can be up to 10% excluding the zenith angle greater than 80° and the circumsolar region.

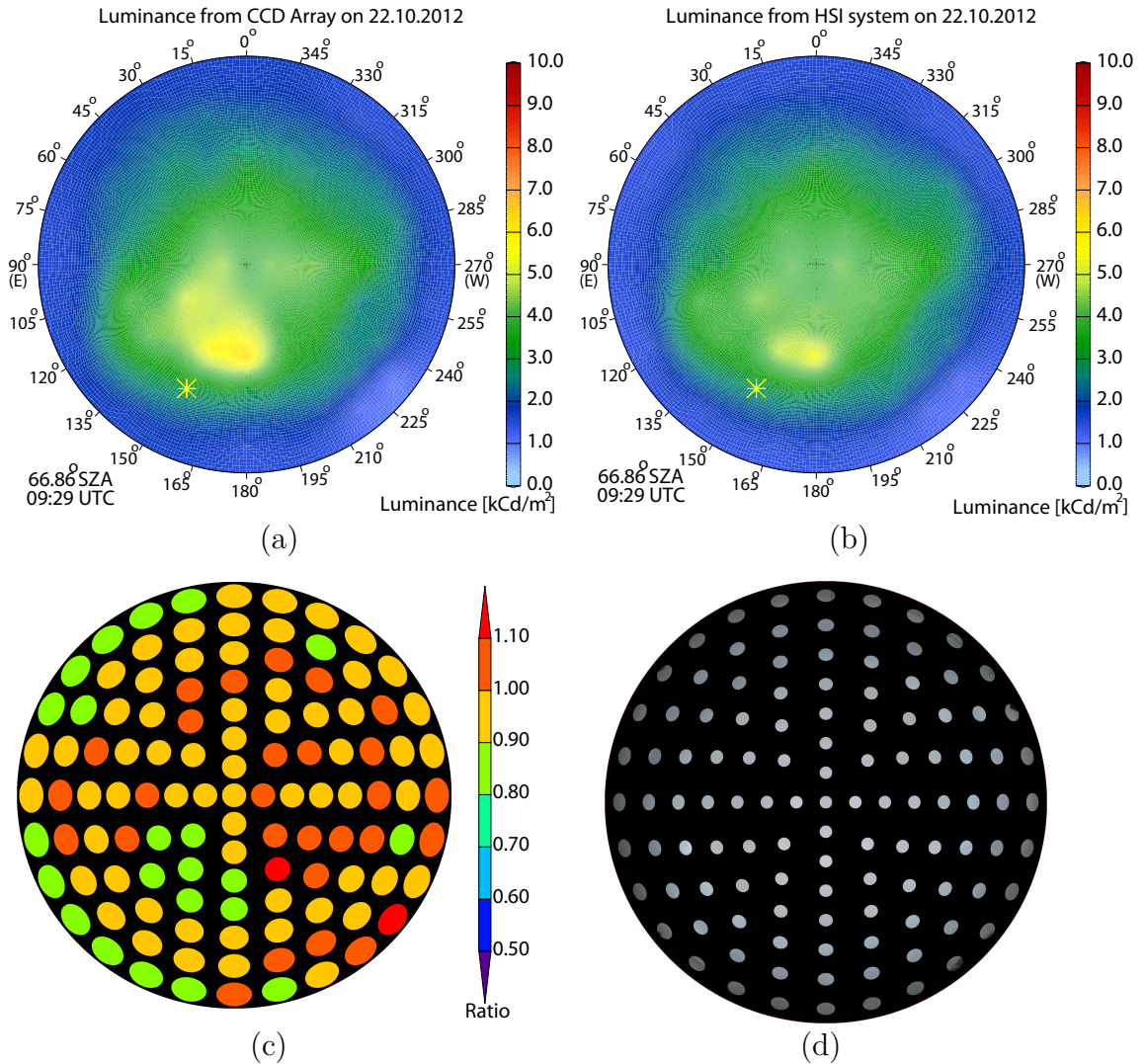


Figure 5.17: Sky luminance distributions measured by (a) the CCD spectroradiometer (b) the HDR image of the HSI system on October 22, 2012 at 09:29 UTC (66.86° of SZA) for overcast situation. The ratio of the sky luminance distribution between the HSI to the CCD spectroradiometer (HSI system/CCD spectroradiometer) is presented in (c) and the HDR image showing the 5° FOV pattern of the scanning points from the CCD spectroradiometer is illustrated in plot (d).

5. Measuring Sky Luminance Distributions

The comparison of the sky luminance distribution for intermediate skies is shown in Figure 5.18 which represent observations taken on October 26, 2012 at 12:01 UTC (scanning period : 12:01 UTC – 12:13 UTC) and which are associated with a *SA* of 66.12° . Results from the *CCD* spectroradiometer and the *HDR* image are shown in Figure 5.18(a) and 5.18(b) respectively.

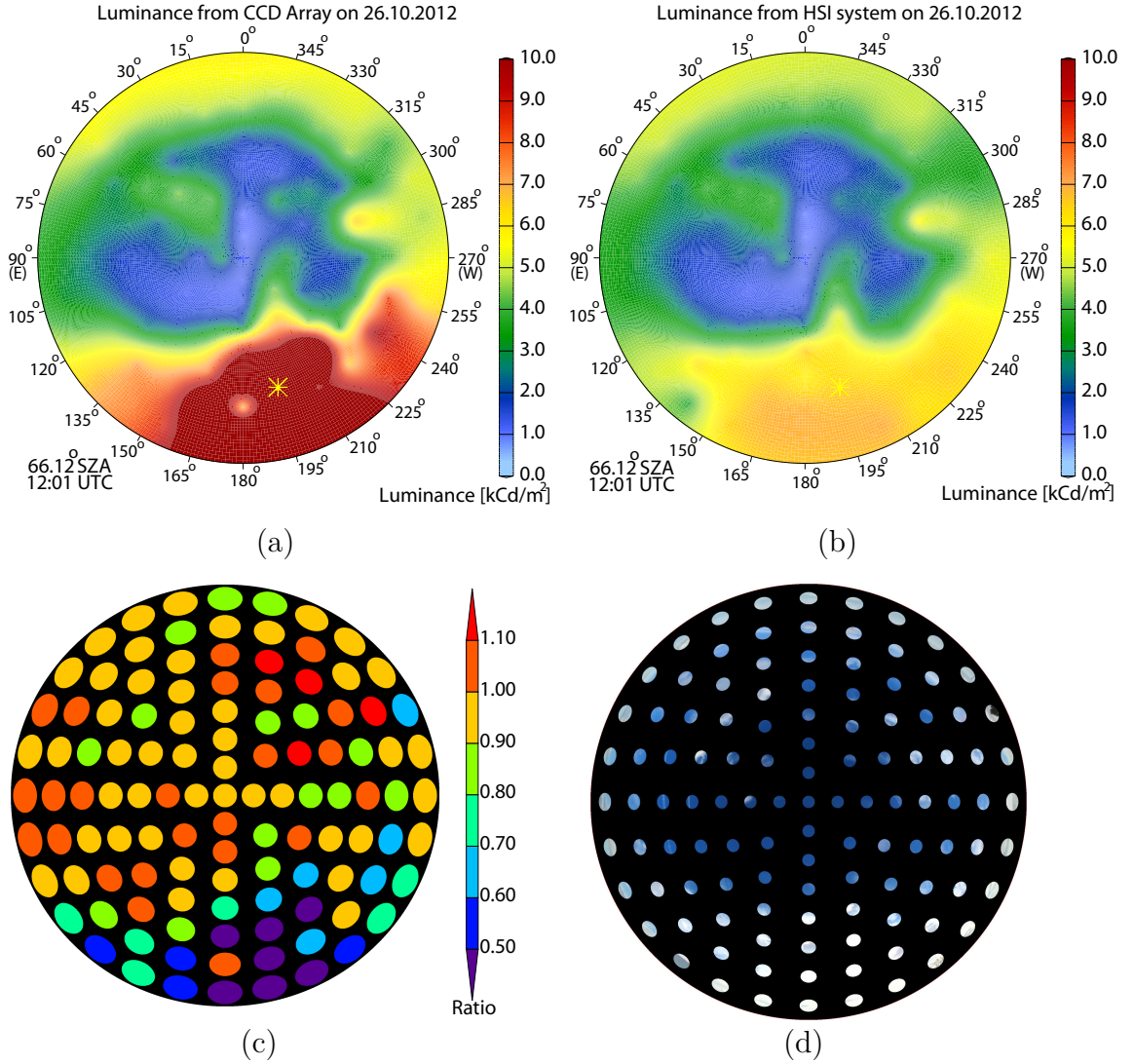


Figure 5.18: Sky luminance distributions measured by (a) the *CCD* spectroradiometer (b) the *HDR* image of the *HSI* system on October 26, 2012 at 12:01 UTC (66.12° of *SA*) for the intermediate sky situation. The ratio of the sky luminance distribution between the *HSI* to the *CCD* spectroradiometer (*HSI* system/*CCD* spectroradiometer) is presented in (c) and the *HDR* image from *HSI* system showing the corresponding 5° *FOV* pattern of the scanning points from the *CCD* spectroradiometer is illustrated in plot (d).

This sky situation was mixed between clear sky and clouds. Cloudless conditions prevailed within 15° circle surrounding the zenith position. Sporadic cumulus and thin cirrus clouds appeared over the sky dome towards the horizon, while some cumulus clouds surrounded the sun (Figure 5.18(d)). The local feature near the sun in the CCD spectroradiometer might originate from the interpolation technique, which is not observed in the HSI system.

Since the CCD spectroradiometer with the pointing unit takes about 12 minutes to record one scan of the sky luminance distribution, time synchronization between both instruments as mentioned in the Section 5.3.1.1 might lead to the uncertainty in the comparison. With the asynchrony of 3 seconds, fast moving clouds might change their position to other scanning spot. The sky luminance at the scanning point filled up with clouds is higher than the sky patches of the blue or cloudless sky. The maximum luminance is found to be adjacent to the position of the sun, which differs from the minimum zenith luminance (blue color level) by factor 20 as measured by the CCD spectroradiometer. The HDR image tends to underpredict sky luminance in cloudy pixels compared to the CCD spectroradiometer, with a deviation that may reach up to 30%. Otherwise there is a good agreement of the sky luminance for both instruments and for zenith angle less than 80° .

The sky luminance distribution from the HSI image at NIWA observed on September 18, 2012 at 11.15 UTC+12 (52.22° of SZA) is presented in Figure 5.19(a) and the corresponding real-time image is shown in Figure 5.19(c). The pattern of sky luminance distribution compared to the camera-based measurement at IMuK on March 28, 2012 at 12:00 UTC (52.32° of SZA) (see Figure 5.19(b)) is distinctly different despite the SZA being almost the same. The horizon brightening and solar disk were clearly observed at NIWA, in contrast to the observation at IMuK (see Figure 5.19(c) and Figure 5.19(d)). Cloudless zenith sky luminance from NIWA is found to be less than IMuK. The analysis in SCHREMPF (2010) showed that blue counts from the NIWA's images were greater than corresponding estimates at Hannover. This feature might be a result of a low aerosol concentration at NIWA. Due to the different atmospheric constituents at that time in the two locations, only the luminance distribution pattern could be observed. These results argue for the need of further investigations involving more luminance measurements in conjunction with ancillary measurements of radiation and cloud properties.

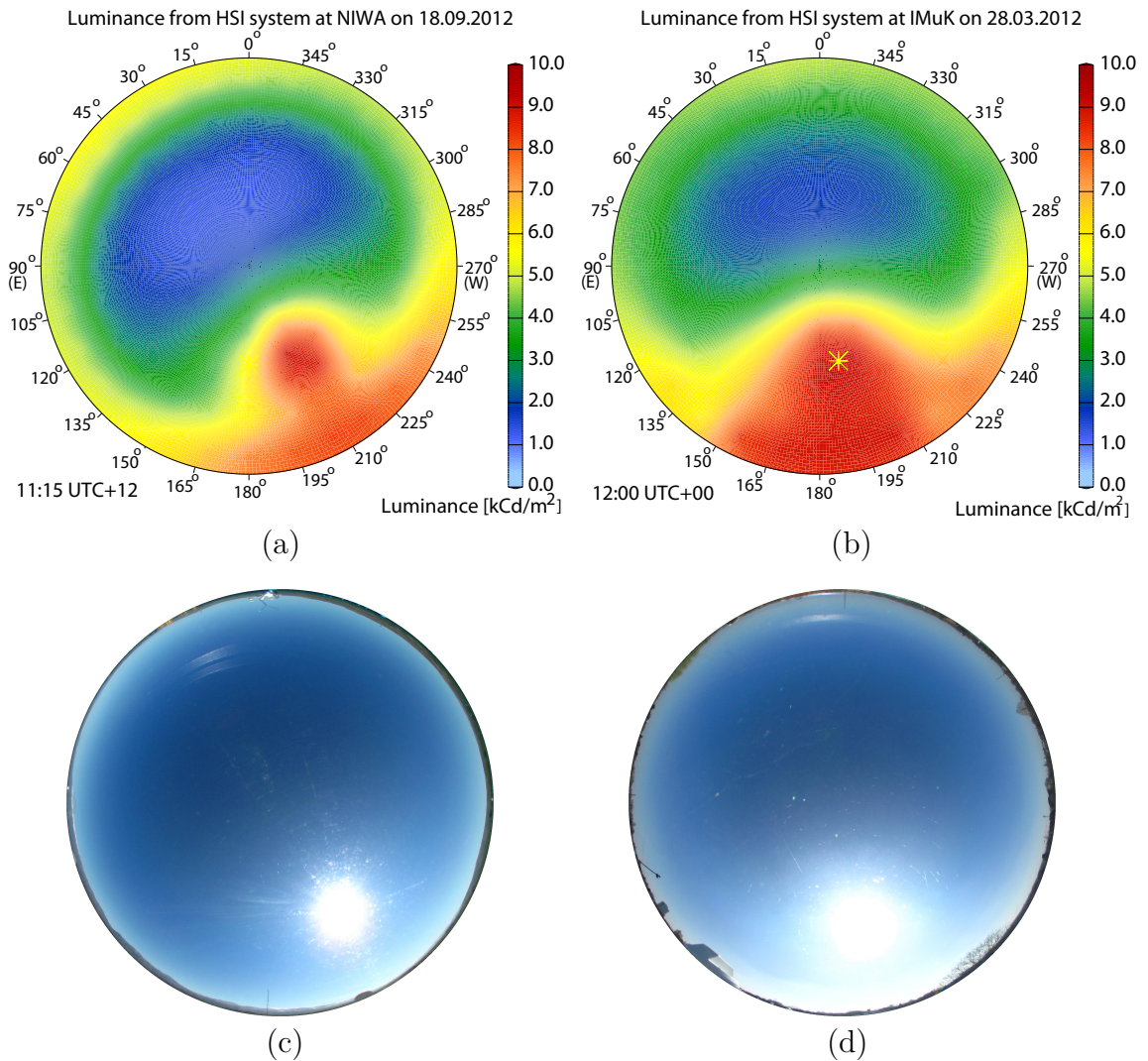


Figure 5.19: Sky luminance distributions from the HDR image of the HSI system (a) at NIWA on September 19, 2012 at 11:15 UTC+12 (52.22° of SZA) and (b) at IMuK on March 28, 2012 at 12:00 UTC (52.32° of SZA). The corresponding real-time images observed at NIWA and IMuK are presented in (c) and (d), respectively.

5.3.2 Comparison of global illuminance between the luxmeter and the HSI system

In order to check the luminance data from the HSI system, LDR and HDR images have been applied for estimating the global illuminance and compared with the luxmeter. The result of the comparison was classified into three groups and will be presented in the following subsections.

5.3.2.1 Diurnal global illuminance

Diurnal global illuminance derived from **HSI** images (**LDR** image in blue line and **HDR** images in black line) on March 28, 2012 under clear sky conditions (see Figure 5.20, upper panel) show a good agreement with the data from the luxmeter (red line). In the morning, some cumulus clouds appeared in the sky until about 8:00 UTC. There is the overestimation of the global illuminance by the **HDR** images foremost of the day, whereas there is underestimation by the **LDR** images. However, differences lie within 5% for zenith angle less than 80° as demonstrated in Figure 5.20, lower panel.

The global illuminance comparison in Figure 5.20 is only a rough quality check since under direct sunlight only the diffuse illuminance is measured by the **HSI** system. In this case, the major part of the global illuminance is calculated with a parameterized formula (Equation (5.9)) that is mainly dependent of the solar elevation angle and has no aerosol optical depth dependence. This check might therefore not work with higher aerosol contents. Therefore, the global illuminance for overcast or homogeneous sky without influencing of the direct illuminance measured on April 5, 2012 has been analyzed.

The resulting diurnal global illuminance comparison for an overcast sky situation on April 5, 2012 is presented in Figure 5.21 (upper panel) and the corresponding ratio is shown in the lower panel. The global illuminance (in this case, diffuse illuminance) estimated from the **HSI** system agrees well with the measured global illuminance by the luxmeter excluding the period of 10:00 UTC to 14:00 UTC, which has a small component of direct illuminance. The diurnal variation was within 10% by the **HDR** images. However, in the case of the homogenous complete overcast sky the deviation is found to be less than 5%. As the global illuminance for overcast sky is derived only from the extracted **RGB** values and their corresponding luminance calibration parameters without the impact of direct illuminance, it can be concluded that this new approach is capable of deriving sky luminance from hemispherical sky images.

Figure 5.22 (upper panel) shows the extreme diurnal variation of global illuminance due to broken cloud conditions for intermediate sky on May 12, 2012. The ratios as demonstrated in the lower panel show large deviations between the **HSI** and the luxmeter, especially in the **LDR** image. The maximum deviation of instantaneous **HSI** data can vary up to 40% due to small synchronization differences, which can result in 5 s differences between the **HSI** system and the luxmeter, whereas, the difference can be up to factor 2 in the case of the **LDR** image. Global illuminance from **LDR** and **HDR** calculations is often smaller than the measurement because cumulus clouds enhance solar radiation in the circumsolar region by up to 25%. In this case the calculation from all-sky images can hardly resolve such a complex situation even with the use of the **HDR** images.

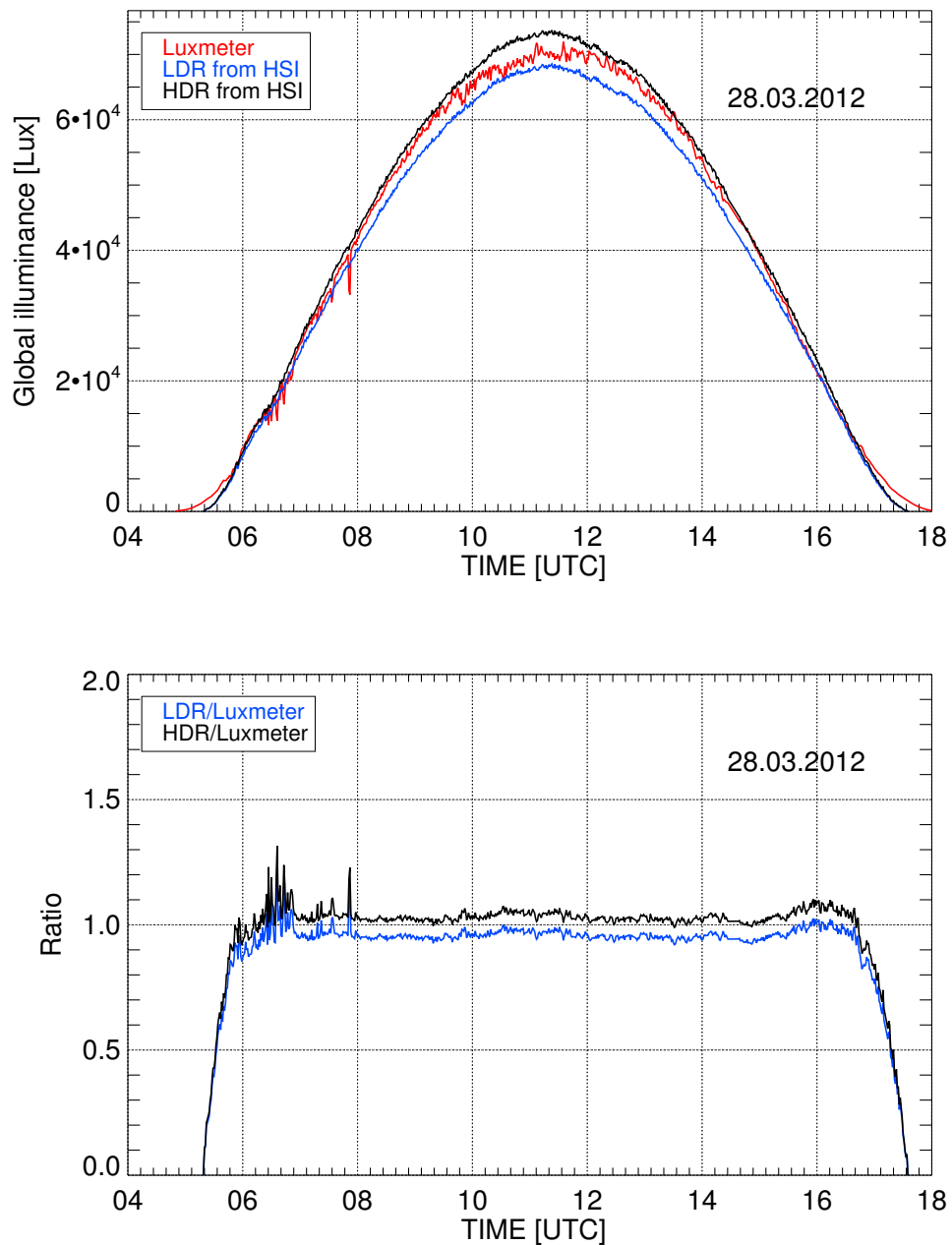


Figure 5.20: Diurnal variation of global illuminance on March 28, 2012 under clear sky condition: (upper) shows the comparisons between the measured illuminance from the luxmeter (black line) and the illuminance derived from the LDR image (blue line) and the HDR image (red line) of the HSI system. Plots in the lower panel present the corresponding ratios of HSI's illuminance to illuminance from the luxmeter.

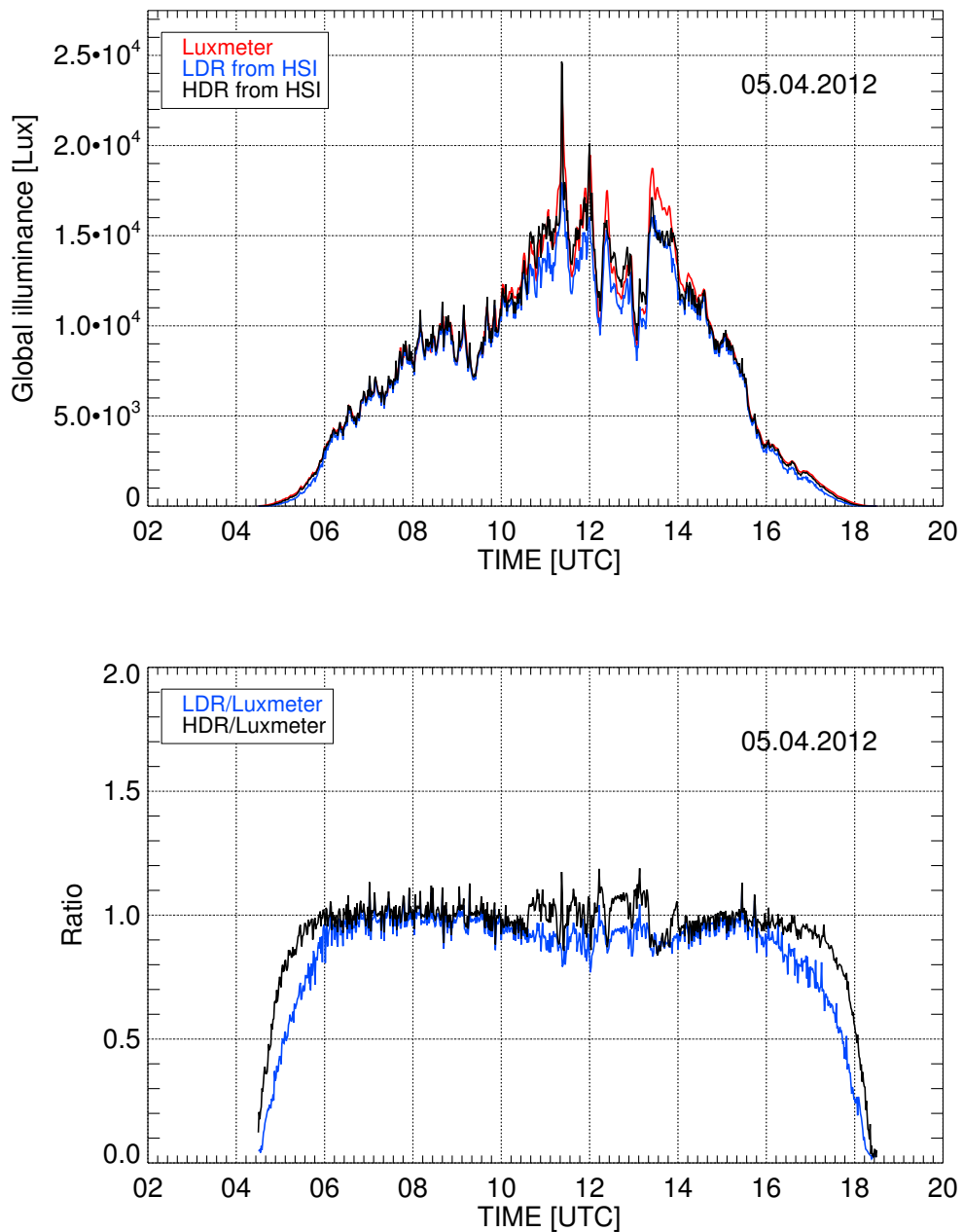


Figure 5.21: Diurnal variation of global illuminance on April 5, 2012 for overcast sky: (upper) shows the comparisons between the measured illuminance from the luxmeter (black line) and the illuminance derived from the LDR image (blue line) and the HDR image (red line) of the HSI system. Plots in the lower pannel present the corresponding ratios of HSIs illuminance to illuminance from the luxmeter.

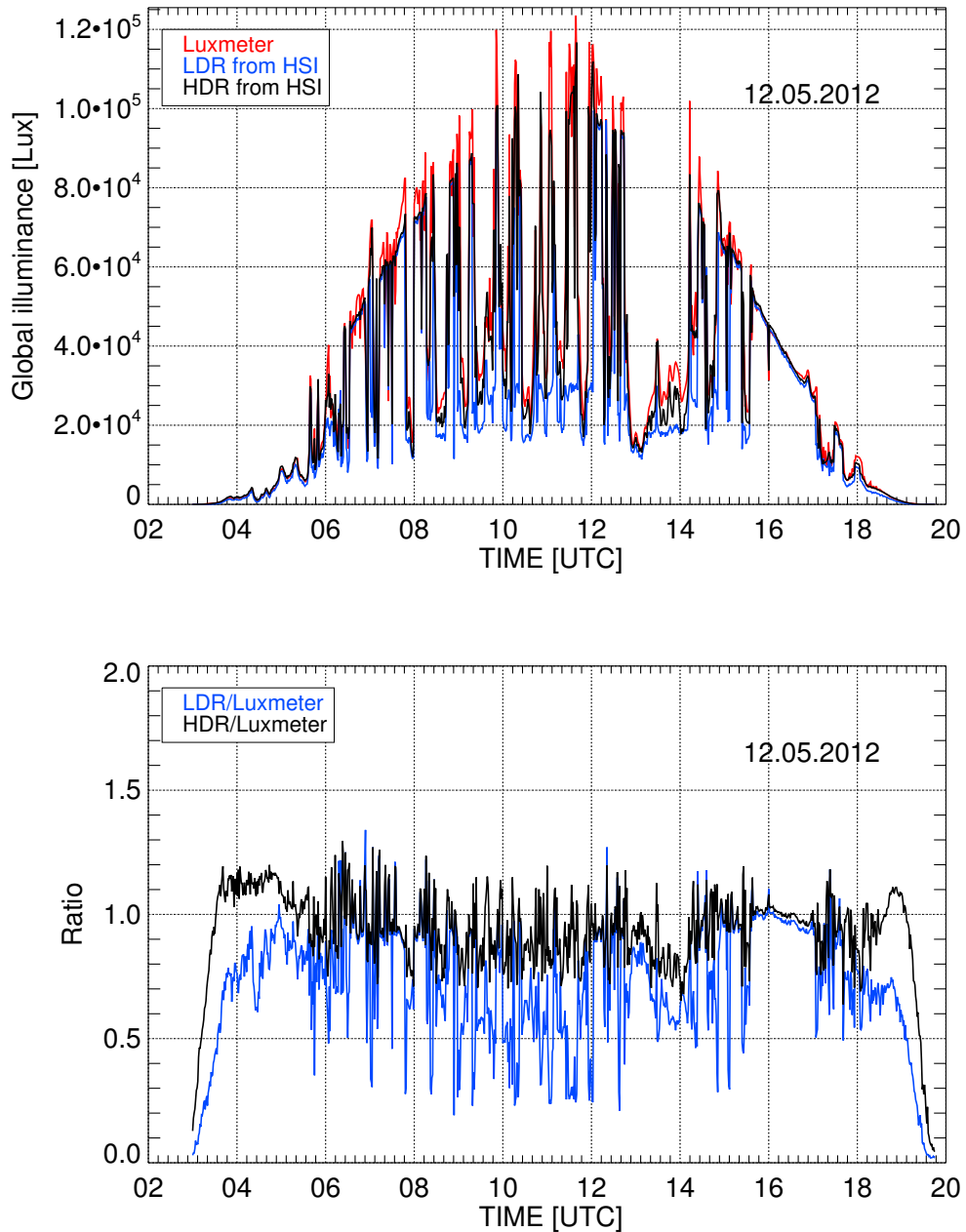


Figure 5.22: Diurnal variation of global illuminance on May 12, 2012 through broken clouds: (upper) shows the comparisons between the measured illuminance from the luxmeter (black line) and the illuminance derived from the LDR image (blue line) and the HDR image (red line) of the HSI system. Plots in the lower panel present the corresponding ratios of HSI's illuminance to illuminance from the luxmeter.

5.3.2.2 Daily averaged global illuminance

The daily average (4:00 UTC - 18:00 UTC) global illuminance from LDR and HDR images for different sky situations in May 2012 has been calculated and validated with the measured global illuminance from the luxmeter as shown in Figure 5.23. The comparison shows also a good agreement between the HDR images and the measurements from the luxmeter with a deviation of less than 20%, as shown in Figure 5.24. For days with intermediate skies, underestimation by the HDR prevails, while for cloudless days the global illuminance from the HDR is slightly higher than the luxmeter global illuminance. The LDR method underestimates global illuminance in all data. The deviation of the daily averaged global illuminance from the LDR images to the luxmeter can be up to 50%, especially in the extreme partly cloudy sky. In general, it can be concluded that the deviation of global illuminance from HDR images and luxmeter measurement can be up to 20% for all weather conditions.

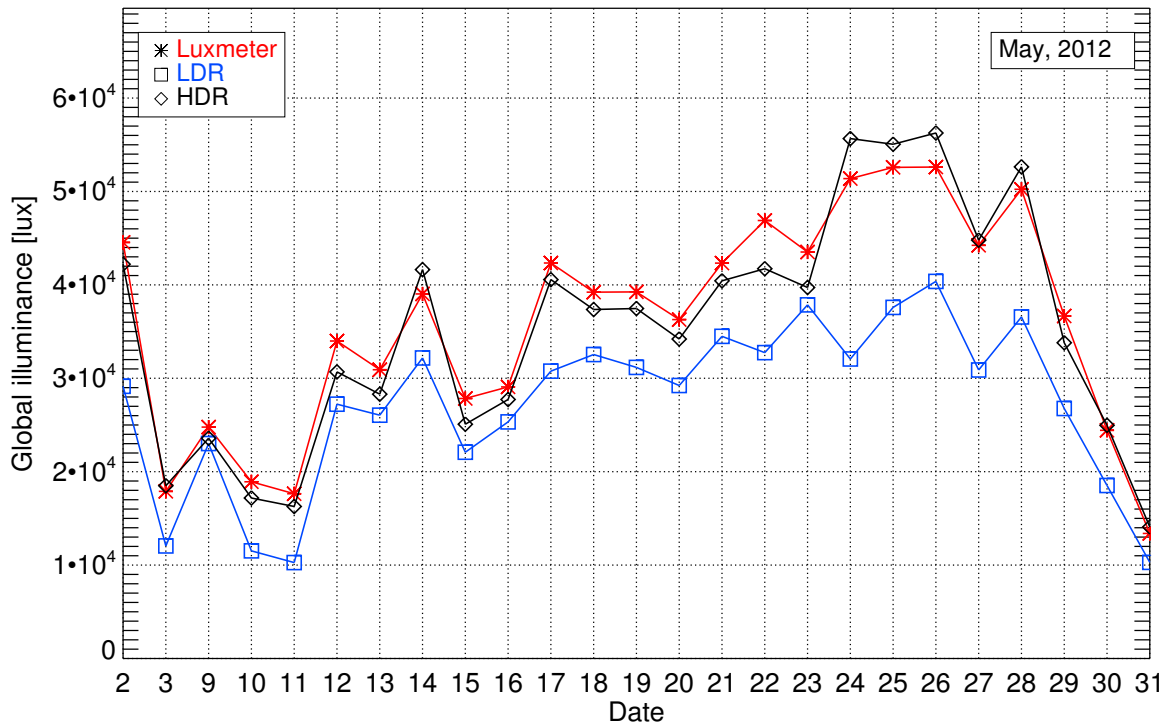


Figure 5.23: Comparison between daily averaged global illuminance measured from the luxmeter (black line) and the calculation from LDR image (blue line) and HDR image (red line) of the HSI system on different dates in May 2012.

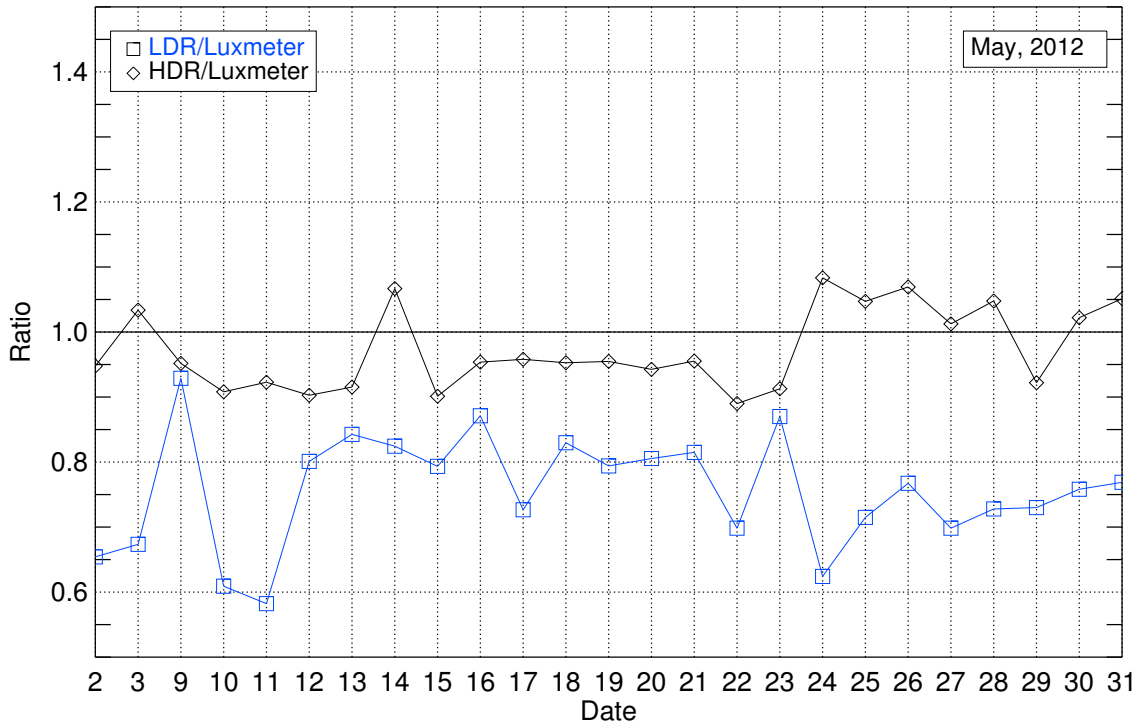


Figure 5.24: Ratio of daily average global illuminance from the HSI images to the measured values from the luxmeter corresponding to the plot in Figure 5.23 (May 2012).

The comparison of global illuminance for cloudless and partly cloudy sky is only a rough quality check since under direct sunlight, only the diffuse illuminance is measured by the HSI. In this case, the major part of the global illuminance is calculated with a parameterized formula that is mainly dependent on solar elevation angle and has no aerosol optical depth dependence. This check might therefore not work with higher aerosol contents than those present during the two months of the evaluation campaign. However, the comparison under overcast sky, which contributed only the calculation from the HSI images, shows the good agreement between both instruments. Thus, it may be concluded that this approach can be applied for measuring the sky luminance.

Camera-based global illuminance from the LDR covering the period from the beginning of 2011 to the beginning of 2012 has been analyzed. The comparisons of monthly averaged global illuminance obtained from the HSI system and by the luxmeter are presented in Appendix B. Only in May 2012 the global illuminance from the HDR has been estimated for almost the entire month. Most of the monthly averaged global illuminance from the LDR images underestimated compared to the luxmeter measurements, especially in the summer months. There were slightly differences in the two instrument readings during winter. The HDR delivered better monthly global illuminance than the values from the LDR as illustrated in May, 2012.

5.4 Remark and discussion

- The temperature of the HSI camera inside the housing varies between 10°C and 35°C as mentioned in the Section 4.1.2. However, due to the heating and ventilation of the camera housing, the temperature of the camera sensor is estimated to be $20 \pm 5^\circ\text{C}$. The typical sensitivity variation of a CCD camera sensor is 0.3% per Kelvin according to ESTRADA et al. (2010), STARKS et al. (1995). Within the usual range of the temperatures this results in a corresponding uncertainty of 3% and can therefore be considered small compared to other uncertainties.
- The HSI system is operational both in shade and direct sunlight. Internal reflections may occur in the images under direct sunlight. These ghost images depend on the solar position and therefore affect different areas of the image as presented in Figure 5.25. However, an investigation of ghost images has shown that less than 2% of the image is affected and cannot be used for the luminance calculation. Ghost images can additionally be detected to a large extent by algorithms, due to their well-defined edges.

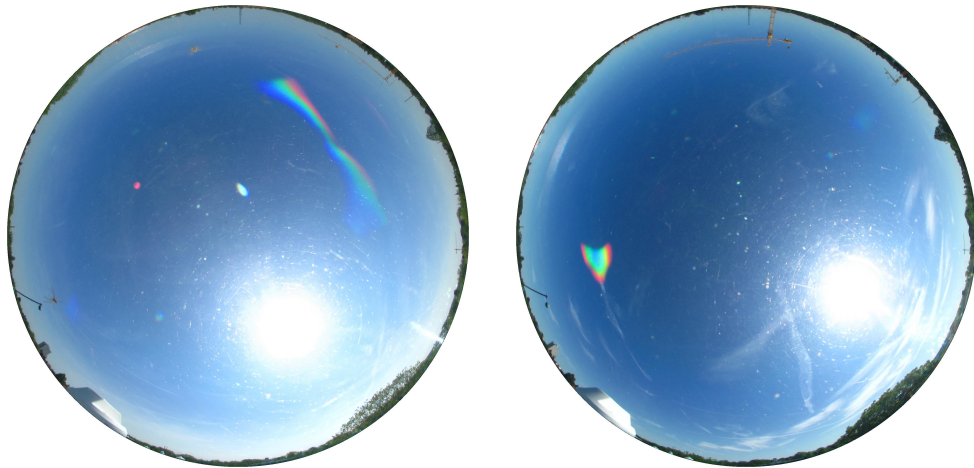


Figure 5.25: Internal reflections on the hemispherical image of the HSI system. These depend on the solar position and have different shapes and size.

- Stray light that might originate from other sources like reflections on the walls of the lens tube of the fish eye objective has not yet been fully characterized. However, the comparison between the HSI and the CCD spectroradiometer in Subsection 5.3.1. showed that stray light effects are not severe.
- The camera has likely some kind of automatic offset correction and sporadic hot pixel could be observed. Those outliers have not yet been eliminated.

- The roll-off property of a lens describes an attenuation of the radiation depending on the increasing viewing angle [VOSS and ZIBORDI, 1989]. Theoretically, fish-eye lens which deliver an equidistant projection have a roll-off as follows [MIYAMOTO, 1964]:

$$R(\theta) = \frac{\alpha \cos\theta (\sin\theta / \theta)}{c^2} \quad (5.12)$$

where $R(\theta)$ is a roll-off, α is the area of the entrance aperture, θ is the viewing angle and c is the focal length.

However, each fisheye lens has its own optical roll-off, which must be determined through careful calibration.

During this work, since there is no suitable rotating mount for the camera, the roll-off has been roughly checked in the laboratory. The roll-off measurements are based on the setup shown in Figure 5.5. The images of the reflectance plaque were acquired for camera viewing angles of 0° , 30° , 60° , 80° and 90° . The RGB values of the plaque for each viewing angle have been investigated and the difference of the brightness between viewing angle 0° and 90° is found to be approximately 8% and between viewing angle 0° and 80° is less than 5%. With this difference, there is no correction for the roll-off as all camera-based sky luminance have been done at viewing angles less than 80° .

- No investigations concerning sensor noise and sensor uniformity have been performed yet. The camera was used with the automatic color balance (white balance) provided by the manufacturer. The effect of this automatic procedure on the luminance determination is not exactly known. However, these missing characterizations appear to have little impact on the luminance determination since the instrument comparisons did not indicate any severe problems.

6 Reconstruction of Spectral Sky Radiance from the CCD Camera

The first section of this chapter provides the spectral sky radiance data measured by the [CCD](#) spectroradiometer as well as images from the HSI system that are used to derive the spectral sky radiance. The following section outlines a regression technique for reconstructing the spectral sky radiance in the visible spectrum from 380 – 760 nm. The results of the comparison between camera-based and field measurements are discussed in the last section.

6.1 Data

Spectral sky radiance was obtained by mounting the [CCD](#) spectroradiometer onto the Skyscanner platform, therefore allowing a variety of zenith and azimuth angles to be viewed, and comparing these results with the concurrent images from the [HSI](#) system (see Section [3.1](#) - [3.2](#)). These data are categorized into two types, the first one to establish a training sample and the second data set to be used for the validation. Table [6.1](#) shows when the measurements and images are taken as well as the corresponding weather conditions.

Table 6.1: Measuring description of the [CCD](#) spectroradiometer and the [HSI](#) system for spectral sky radiance reproduction.

Date	Hour measuring (UTC)	Weather conditions	Purposes
October 19, 2012	05:30 – 17:27	Partly cloudy	Validation
October 20, 2012	05:30 – 16:44	Partly cloudy	Validation
October 21, 2012	10:23 – 17:21	Clear	Validation
October 22, 2012	07:17 – 15:23	Overcast	Validation
October 23, 2012	06:30 – 16:21	Overcast	Training
October 26, 2012	05:30 – 17:20	Partly cloudy	Validation
October 28, 2012	12:41 – 16:00	Clear	Training
October 31, 2012	12:25 – 16:31	Partly cloudy	Validation

The measurement of a radiance distribution for the entire hemisphere conducted with the [CCD](#) spectroradiometer has a scan pattern of 113 points with a FOV of

5° as shown in Figure 3.4(right) and taking about 12 minutes to complete the scan. Since hemispherical images are taken every 20 seconds, a total of 35 images can be taken in the time of one measurement of the CCD spectroradiometer as described in Section 5.1.2.2. During this thesis work HSI Images with the exposure time of $\frac{1}{1000}$ s, the ISO number of *ISO* 80 and aperture of $f/4.0$ were used for the spectral radiance recovery.

6.2 Regression analysis for spectral sky radiance reconstruction

Sky radiance spectra from a limited number of discrete bands shall be derived from the HSI images. Due to the non-linearity of the camera sensor as described in Subsection 4.2.2.2 (see also Figure 4.15 and Figure 4.16) a non-linear regression approach has been applied to obtain the whole spectra in the visible region. This regression method was applied in various spectral reconstruction applications as described in JOHNSEN et al. (2008), MINTON and ROLLIN (2006). The non-linear regression is used to determine a relationship between two datasets, consisting in the measured spectral radiance from the CCD spectroradiometer and the signal from the three channels of the HSI image. In the regression process the optimum correlation has been acquired from a variety of independent variables and the predictor variables were selected [LÜTJOHANN, 1968].

The following two datasets were used for the training samples of the regression model for clear sky condition. The first dataset contains spectral sky radiance measurements, conducted with the CCD spectroradiometer in the wavelength range from 380 to 760 nm on October 28, 2012 from 12:00 UTC to 16:00 UTC. The second dataset consists of the signal counts of the three reference bands measured by the HSI system, which have a maximum spectral response at the wavelength of 441 nm for the blue channel, 527 nm for the green channel and 602 nm for the red channel. Figure 6.1 shows the three discrete bands of the HSI imager in relation to the zenith sky radiance spectra from the spectroradiometer on October 21, 2012. In this case, the spectral direct radiance from the CCD spectroradiometer as well as the counts from the HSI system at the circumpolar area of about 20° around the sun were excluded in the regression model.

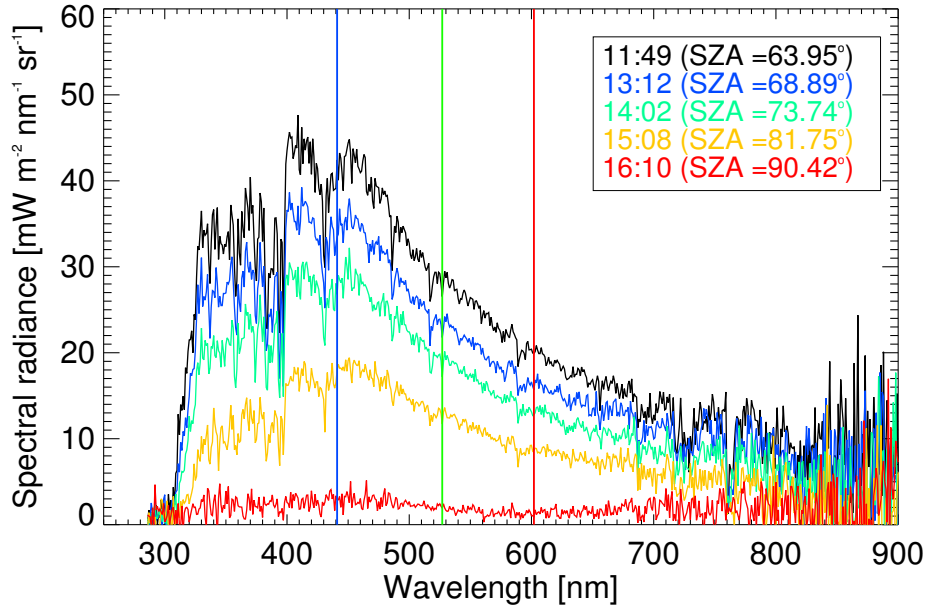


Figure 6.1: The reference band (441 nm, 527 nm, 602 nm) positions of the HSI system (straight solid lines) and the spectral zenith sky radiance measured by the CCD spectroradiometer at various solar zenith angles on October 21, 2012 under clear sky.

At each wavelength (i.e. each regression equation), the measured spectral sky radiance was treated as a function of the signal of red or green or blue counts, which range from 0 to 255 counts. Therefore, there are three non-linear regression equations for each wavelength and 1143 regressions for the complete spectrum. For different camera settings such as exposure time or aperture and due to the non-linear relationship between those settings and the count values, different regression equations must be computed. In this work, the regression was performed for an exposure time of 1/1000 s, an ISO number of 80 and an aperture of f/4.0 of the HSI setting as mentioned in previous section. The results of the non-linear regression equations and the selection of those equations for each wavelength will be presented in the next section.

For the case of cloudy sky conditions, the regression was performed for the training dataset of October 23, 2012 from 6:00 UTC to 16:00 UTC which was also measured with the CCD spectroradiometer. Except for the different training dataset, the same method as described for clear sky condition was used. The reason to choose two training datasets (clear and cloudy) is due to the high sensitivity of the HSI channels to cloud cover. The maximum values can reach 255 counts for bright clouds, whereas blue sky has at most about 120 counts. The use of one and the same training dataset for both conditions would lead to great deviation in the spectral radiance reconstruction.

For partly cloudy skies, the FOV of some scanning points is not completely filled with either clouds or blue sky as show in Figure 6.6(c). In these cases, it is quite

difficult to decide whether the clear sky or cloudy sky regression model is more suitable. Therefore, the ratio of the count values of the red and blue channel called **Sky Index** was investigated to separate blue sky and white clouds [YAMASHITA et al., 2004]. The Sky Index is expressed in Equation (6.1):

$$SkyIndex_{ij} = \frac{B_{ij} - R_{ij}}{B_{ij} + R_{ij}} \quad (6.1)$$

where B is the count value of the blue channel and R the count value of the red channel of the HSI system corresponding to each pixel (i, j) .

Eventually all pixels at each scanning point were averaged to gain one representative Sky Index. Clear sky portions of the image have high blue and low red values, whereas cloud area presents white or grey in the image, which means the digital numbers of red and blue are almost the same. The investigations have shown that an averaged Sky Index greater than 0.25 indicates blue sky [SCHREMPF, 2010]. For these values the clear sky regression model will be applied for the spectral reconstruction, otherwise the sky element is covered by clouds.

In order to select the regression model for each wavelength a best correlation coefficient of the relationship between two training variables has been chosen. The correlation coefficient (R^2) can be estimated by the following equation [MOORE and McCABE, 2006]:

$$R^2 = \frac{\text{Explained deviation}}{\text{Total deviation}} = \frac{\sum(y - \bar{y})^2}{\sum(\hat{y} - \bar{y})^2} \quad (6.2)$$

where y is the actual values, \bar{y} is mean of the actual values and \hat{y} is the predicted values.

For the validation of the spectra reproduction method, the spectral radiance was calculated for an independent image dataset from the HSI system acquired under different sky conditions presented in Table 6.1. The results of the comparison between camera-based and measured spectral sky radiance will be presented in the next section.

6.3 Spectral Estimated Results and Discussion

In Section 6.3.1 the results of the non-linear regression method for different sky conditions are presented. Section 6.3.2 compares sky radiance obtained by the CCD spectroradiometer and the HSI system for three wavelengths (400 nm, 500 nm and 600 nm) and for varying cloud cover ranging from cloudless to overcast skies. Results are presented in Section 6.3.3 which is followed by a discussion on possible mechanisms operating in the visible band.

6.3.1 Regression coefficients and models

The synchronized datasets acquired on October 23, 2012 and October 28, 2012 by the CCD spectroradiometer and the HSI system were used as training datasets to determine the non-linear regression equations. Figure 6.2 shows a non-linear regression fitted by a third degree polynomial between measured spectral radiance at the wavelength 400 nm, 500 nm and 700 nm and RGB channel counts for October 28, 2012 and for October 23, 2012 is presented in Figure 6.3. The best correlation coefficients for wavelengths 400 nm, 500 nm and 700 nm are occurred in the blue ($R^2 = 0.9625$), green ($R^2 = 0.9775$) and red ($R^2 = 0.9463$) channels, respectively in the case of the cloudless sky, whereas in the cloudy conditions the best correlation coefficients for the three wavelengths are appeared in the blue channel. A possible explanation for this effect may lies in the difference in signal counts between cloudy and cloudless situations.

Figure 6.4 presents the variation of the correlation coefficient of the training data against wavelength for clear skies on October 28, 2012 (upper panel) and for cloudy sky of October 23, 2012 (lower panel). For cloudless skies, the best correlation coefficients occur near the center of each band, which has a correlation coefficient of $R^2 > 0.95$. The variation in correlation coefficients of each channel depends on the wavelength associated with the camera sensor response. The general equations of the non-linear regression models for each wavelength (λ) can be expressed in the following equations.

$$R_{cam,r}(\lambda) = a_{0,\lambda} + a_{1,\lambda}R + a_{2,\lambda}R^2 + a_{3,\lambda}R^3 \quad (6.3)$$

$$R_{cam,g}(\lambda) = a_{0,\lambda} + a_{1,\lambda}G + a_{2,\lambda}G^2 + a_{3,\lambda}G^3 \quad (6.4)$$

$$R_{cam,b}(\lambda) = a_{0,\lambda} + a_{1,\lambda}B + a_{2,\lambda}B^2 + a_{3,\lambda}B^3 \quad (6.5)$$

where $R_{cam,r}(\lambda)$, $R_{cam,g}(\lambda)$ and $R_{cam,b}(\lambda)$ are the sky radiance values obtained from the red, green and blue channels of the images measured in $mW/(m^2 \cdot nm \cdot sr)$. R , G and B are the signal counts from the red, green and blue channel. a , b and c are the wavelength dependent coefficients of the regression equations.

The coefficients for clear sky data of the red channel varied mostly in the region around 680 nm – 760 nm due to water absorption lines [LIU, 2002]. In the cloudy case (see Figure 6.4, upper panel), there are variations of the correlation coefficients at the wavelength less than 400 nm and in the long wavelength region around 680 nm – 760 nm, otherwise the correlation coefficients are quite constant and range from about 0.85 to 0.92.

6. Reconstruction of Spectral Sky Radiance

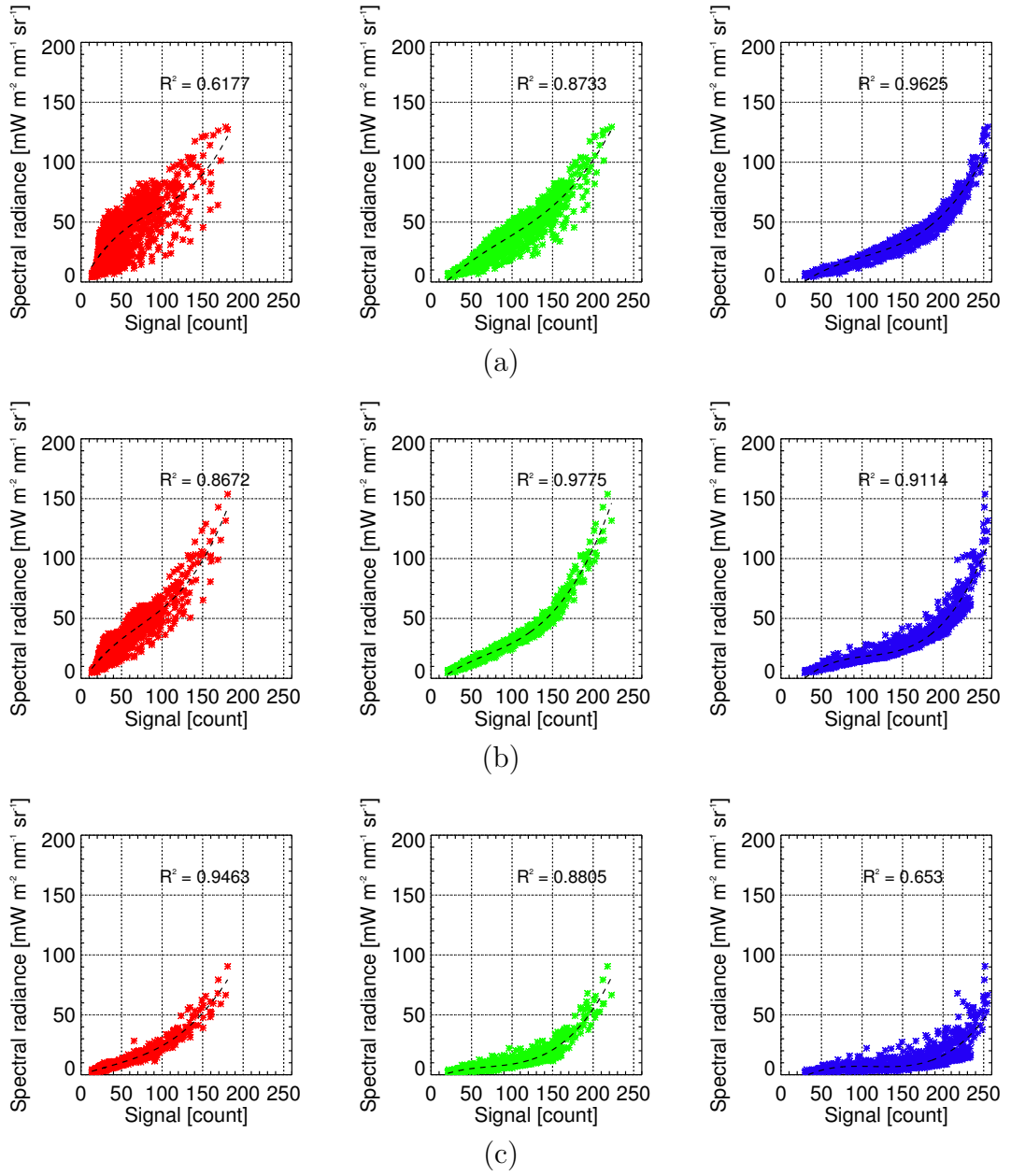


Figure 6.2: Non-linear relationship between the measured spectral sky radiance and the signal count of the red, green and blue channels from the HSI system. The data are used as a training dataset and were recorded on October 28, 2012 under cloudless situation at the wavelength 400 nm (a), 500 nm (b) and 700 nm (c). The R^2 in the plots represents the square of the correlation coefficients.

6. Reconstruction of Spectral Sky Radiance

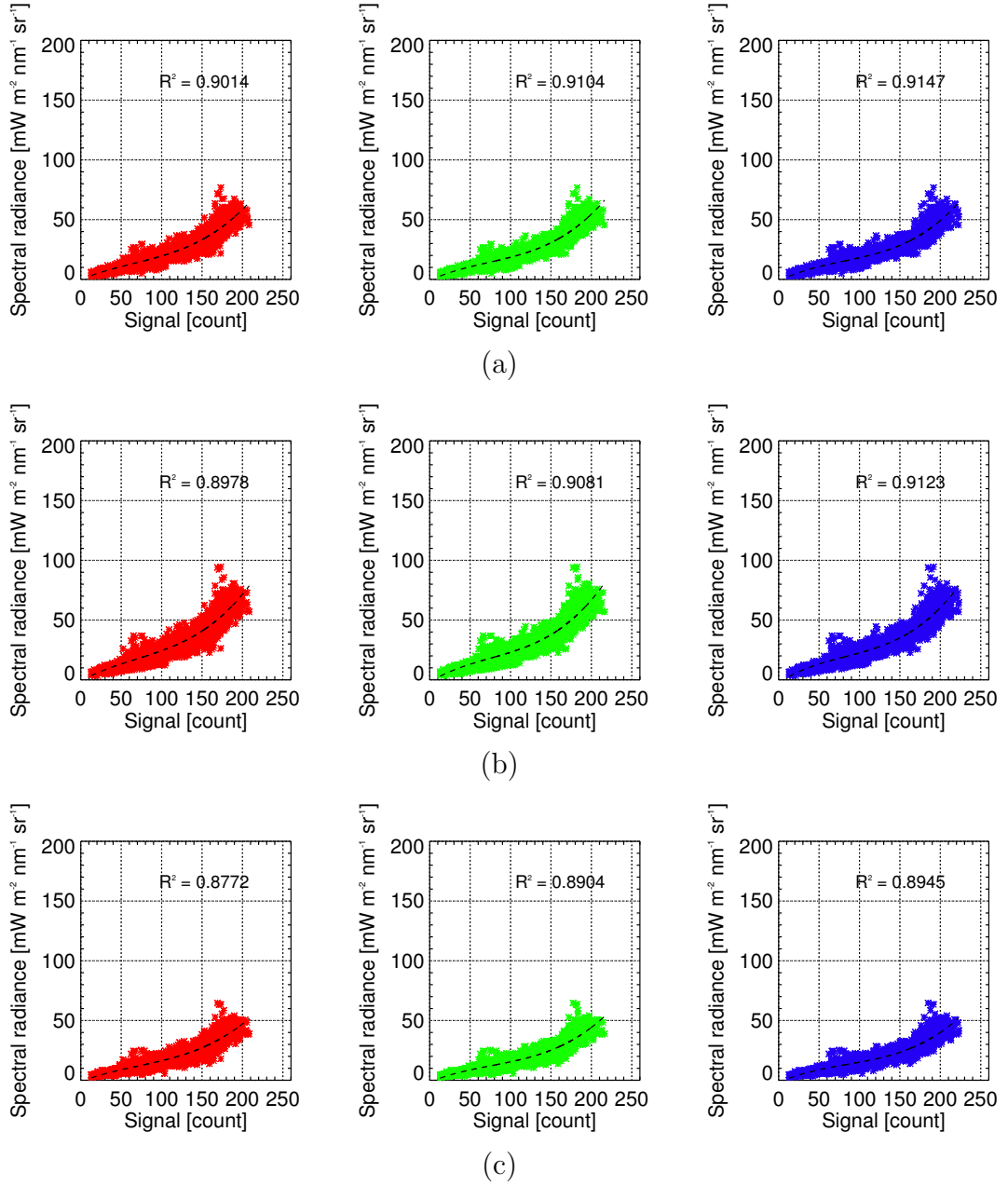


Figure 6.3: Non-linear relationship between the measured spectral sky radiance and the signal counts of the red, green and blue channels from the HSI system. The data are used as a training dataset and were recorded on October 23, 2012 under cloudy situation at the wavelength 400 nm (a), 500 nm (b) and 700 nm (c). The R^2 in the plots represents the square of the correlation coefficients.

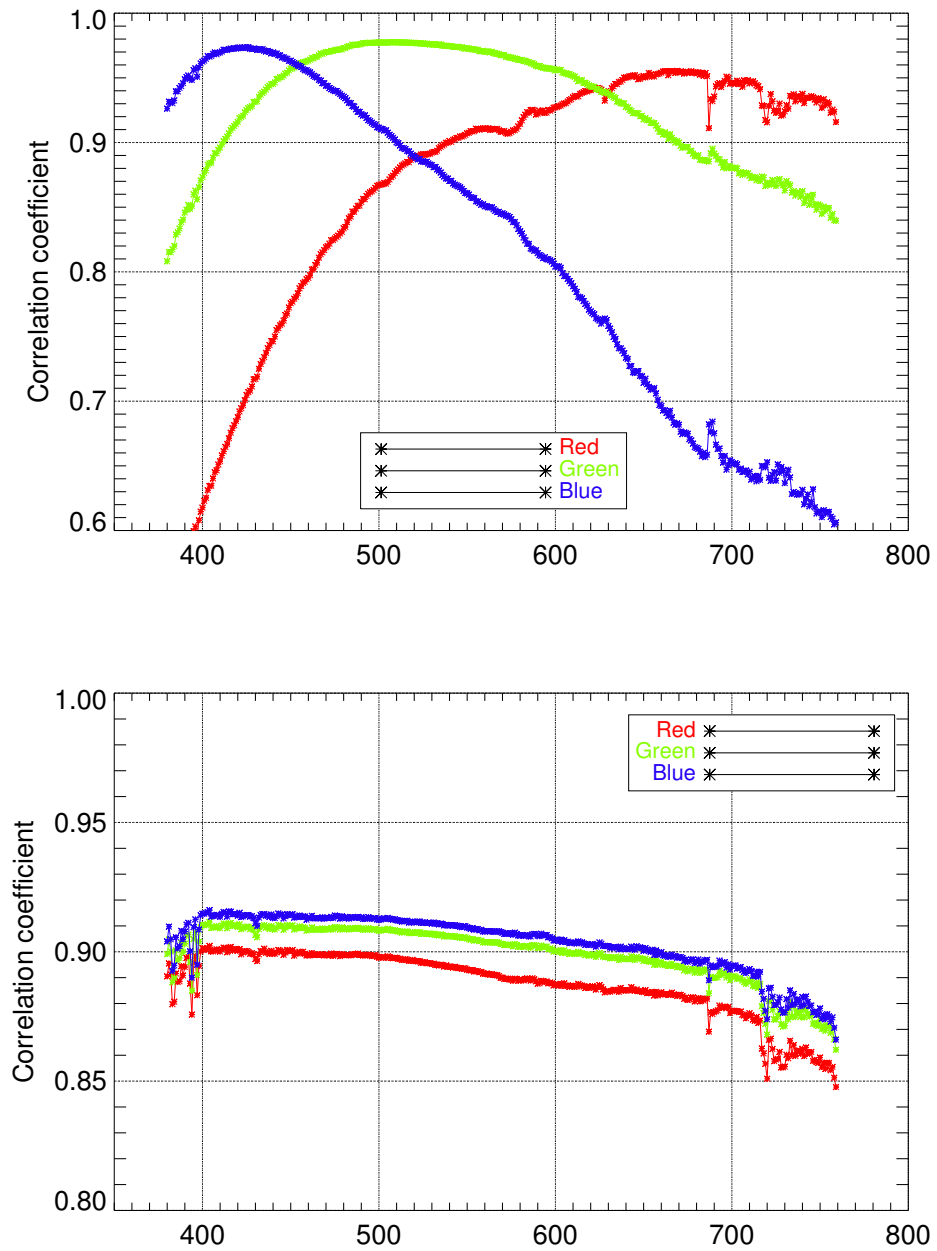


Figure 6.4: The optimum correlation coefficient derived from the comparison with the CCD spectroradiometer and the digital numbers of the three channels of the images from the HSI system for cloudless sky measured on October 28, 2012 (upper) and on October 23, 2012 for cloudy sky (lower).

6. Reconstruction of Spectral Sky Radiance

The regression model for each wavelength has been selected by comparing the best correlation coefficients of the three channels. As presented in Figure 6.4 (upper), the blue channel provides the best correlation coefficient for wavelengths from 380 nm to 450 nm due to its sensitivity in this region (see Figure 4.18). The non-linear regression model (Equation (6.5)) has been applied for predicting the spectral sky radiance in this region. The non-linear regression model from Equation (6.4) dominated by the green channel is used to recover the spectral sky radiance for the wavelength region 451 nm to 620 nm. Spectral sky radiance in the last part of the spectrum from 621 nm to 760 nm has been calculated by using the non-linear regression from the red channel as expressed in Equation (6.3).

The wavelength-dependent coefficients that provide the best correlation in Equation (6.3) – Equation (6.5) are given in Table 6.2 (cloudless sky) and Table 6.3 (cloudy sky) including the best correlation coefficients.

Finally, the spectral sky radiance using the above three regression relationships may be estimated for the entire visible spectrum. Validation with an independent data set is presented in Sections 6.3.2 and 6.3.3.

Table 6.2: Non-linear regression model using the training datasets for October 28, 2012 for clear sky conditions. These wavelength dependent coefficients were obtained for exposure time 1/1000 s, aperture f/4.0 and ISO number 80.

Wavelength [nm]	Regression model	R^2
400	$R_{cam}(400) = -16.62 + 0.711B - 0.005B^2 + 1.64 \cdot 10^{-5}B^3$	0.9625
450	$R_{cam}(450) = -23.05 + 1.025B - 0.008B^2 + 2.59 \cdot 10^{-5}B^3$	0.9633
500	$R_{cam}(500) = -7.323 + 0.605G - 0.005G^2 + 2.24 \cdot 10^{-5}G^3$	0.9775
550	$R_{cam}(550) = -6.892 + 0.523G - 0.005G^2 + 2.28 \cdot 10^{-5}G^3$	0.9731
600	$R_{cam}(600) = -6.812 + 0.456G - 0.005G^2 + 2.22 \cdot 10^{-5}G^3$	0.9557
650	$R_{cam}(650) = -0.516 + 0.324R - 0.002R^2 + 1.60 \cdot 10^{-5}R^3$	0.9515
700	$R_{cam}(700) = -0.012 + 0.230R - 0.001R^2 + 1.28 \cdot 10^{-5}R^3$	0.9463
750	$R_{cam}(750) = -0.210 + 0.197R - 0.001R^2 + 1.26 \cdot 10^{-5}R^3$	0.9326

Table 6.3: Non-linear regression model using the training datasets for October 23, 2012 for cloudy sky conditions. These wavelength dependent coefficients were obtained for exposure time 1/1000 s, aperture f/4.0 and ISO number 80.

Wavelength [nm]	Regression model	R^2
400	$R_{cam}(400) = -1.426 + 0.338B - 0.002B^2 + 1.00 \cdot 10^{-5}B^3$	0.9147
450	$R_{cam}(450) = -1.924 + 0.450B - 0.003B^2 + 1.31 \cdot 10^{-5}B^3$	0.9143
500	$R_{cam}(500) = -2.391 + 0.440B - 0.003B^2 + 1.28 \cdot 10^{-5}B^3$	0.9123
550	$R_{cam}(550) = -2.742 + 0.434B - 0.003B^2 + 1.24 \cdot 10^{-5}B^3$	0.9094
600	$R_{cam}(600) = -3.036 + 0.396B - 0.003B^2 + 1.12 \cdot 10^{-5}B^3$	0.9044
650	$R_{cam}(650) = -2.363 + 0.359B - 0.003B^2 + 1.03 \cdot 10^{-5}B^3$	0.9004
700	$R_{cam}(700) = -1.823 + 0.298B - 0.002B^2 + 8.94 \cdot 10^{-6}B^3$	0.8945
750	$R_{cam}(750) = -1.494 + 0.345B - 0.002B^2 + 9.08 \cdot 10^{-6}B^3$	0.8781

6.3.2 Spatial comparison of spectral radiance distribution at 400 nm, 500 nm and 600 nm using the CCD spectroradiometer and HSI system

The comparisons are presented for each sky condition:

- **Clear Sky**

The spectral sky radiances at 400 nm, 500 nm and 600 nm over the sky hemisphere measured with the CCD spectroradiometer are compared with the spectral radiance from the HSI images for clear sky condition on October 21, 2012 at 13:12 UTC (scanning period is 13:12-13:24 UTC). Results are presented in Figure 6.5. The spatially-interpolated spectral sky radiance from the CCD spectroradiometer are in the left plots, spectral sky radiance from the HSI system occupy the middle plots, while their ratios are in the right plots on a point-by point basis. The comparison in panel (a) is at 400 nm, panel (b) is at 500 nm and in panel (c) is at 600 nm. A yellow star represents the position of the sun with its corresponding SZA value. The HSI image of this sky situation is presented in Figure 6.8. Due to obstacles

like buildings and trees, the spectral radiance for zenith angles higher than 80° is not considered. Measurements in the circumsolar region are not included in the regression model, since both instruments suffer from oversaturation due to their limited dynamic range. Internal reflections of direct sunlight can cause ghost images in some parts of the HSI image and lead to an overestimation of the spectral sky radiance of about 2%-5% [TOHSING et al., 2013].

The spectral sky radiance distribution is a function of sky incident and azimuth angles and this distribution is not uniform over the sky. For the visible part, minimum values of the sky radiance occur at the zenith for all wavelength observed with the both instruments, whereas maximum values occur in the aureole. The horizon brightening is dominated by the Rayleigh scattering [LENOBLE, 1993] and decreases with wavelength as observed with both instruments.

A rim at the horizon with higher values of about $97.31 \text{ mW}/(\text{m}^2 \cdot \text{nm} \cdot \text{sr})$ for the 500 nm (middle panel) can be observed, in contrast to the spectral sky radiance at the zenith, which reaches about $26.79 \text{ mW}/(\text{m}^2 \cdot \text{nm} \cdot \text{sr})$. For the cases examined, horizon brightening is higher by a factor of 3.1, 3.6 and 4.6 for 400 nm, 500 nm and 600 nm respectively. This horizon brightening is also observed in the sky luminance distribution measurement as described in Section 5.3.1.3. At wavelengths of 500 nm, the maximum sky radiance measured by the CCD spectroradiometer is about $677 \text{ mW}/(\text{m}^2 \cdot \text{nm} \cdot \text{sr})$ around the circumsolar region which contrasts with a value of $165 \text{ mW}/(\text{m}^2 \cdot \text{nm} \cdot \text{sr})$ obtained with the HSI system and which is explained by the limited dynamic of the camera sensor. These differences are also observed at wavelengths 400 nm and 600 nm.

The variation of the spectral sky radiance distribution at these three wavelengths is demonstrated as the ratio (HSI system/CCD spectroradiometer) in the right plots of all panels in Figure 6.5. For 400 nm and 500 nm the spectral sky radiance distribution deviates up to 10% for the whole hemisphere excluding the circumsolar region as shown in the ratio plot. At 600 nm there is more variation in the spectral sky radiance distribution and the deviation can be up to 20%.

6. Reconstruction of Spectral Sky Radiance

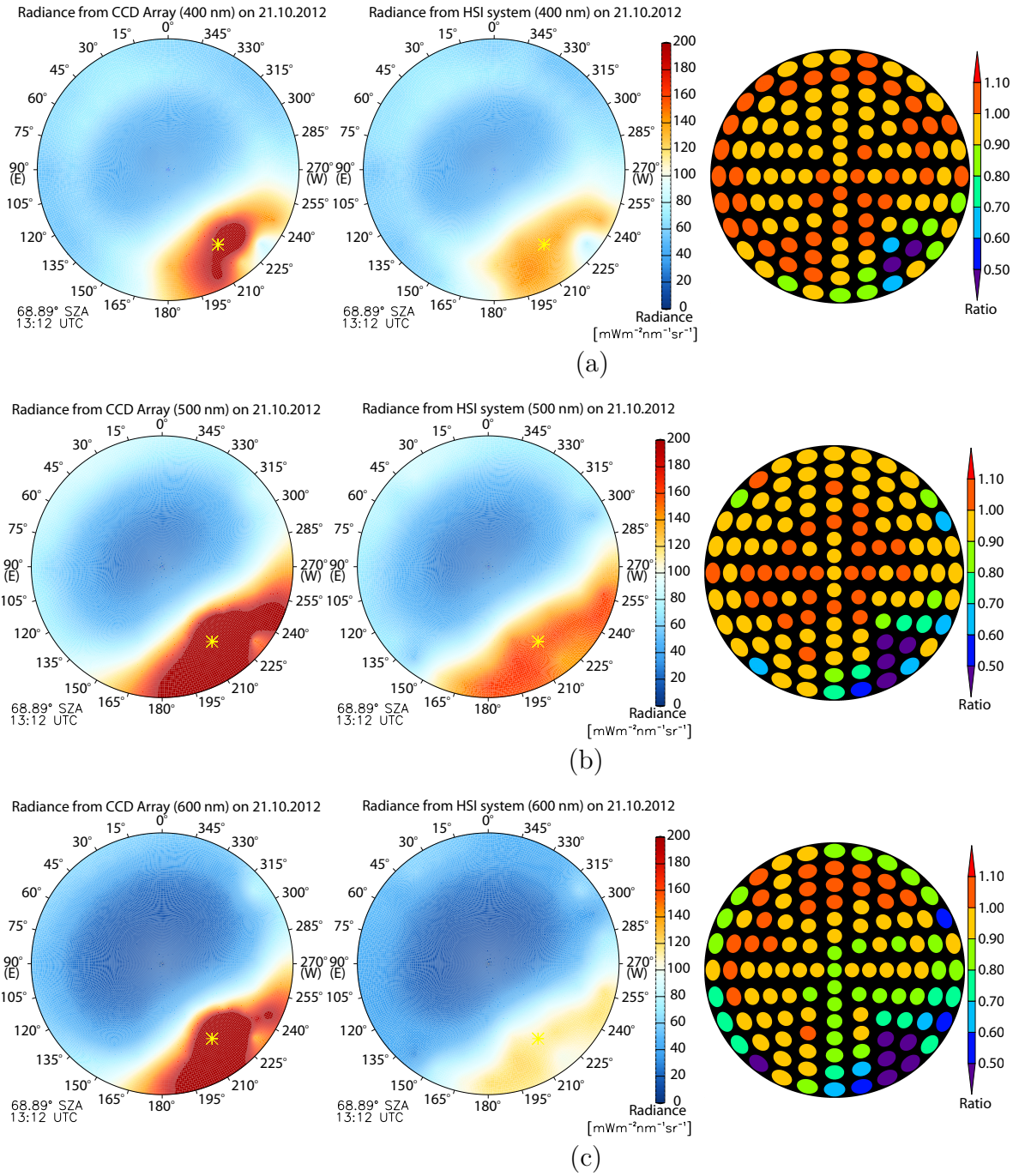


Figure 6.5: Spectral radiance distribution at 400 nm (a), 500 nm (b) and 600 nm (c) measured by CCD spectroradiometer (left) and HSI system (middle) on October 21, 2012 at 13:12 UTC (68.89° of SZA) for clear sky. The right plots show the ratio between the computed spectral radiance of the HSI system and the measured spectral radiance of the CCD spectroradiometer (HSI system/CCD spectroradiometer). Although the FOV of the scanning Pattern is 5°, the scanning points showing the ratio are plotted with a FOV of 10° for clarity of the presentation.

- **Overcast Sky**

The overcast sky presents a different spectral sky radiance distribution. This situation was measured on October 22, 2012 at 09:29 UTC (scanning period, 9:29 – 9:41 UTC) as shown in Figure 6.6 for wavelength of 400 nm (a), 500 nm (b) and 600 nm (c) by the CCD spectroradiometer in the left plots and the HSI images in the middle plots. The ratio of the HSI spectral radiance to the CCD spectroradiometer is illustrated in the right plots of all panels. The actual HSI image of this sky with 113 scanning points is shown in Figure 6.9.

Under overcast sky, the spectral sky radiance distribution in all three wavelengths is comparably uniform and all three exhibit more deviation in the zenith region. The zenith radiance in all three wavelengths is higher than the corresponding horizon observed by both instruments. The camera-based spectral radiance from the HSI system agrees well with the measured spectral sky radiance by the CCD spectroradiometer, especially for the wavelength 500 nm, with a deviation less than 10% for zenith angles less than 80° and which may be seen in the ratio plot (the right plots). Some measured CCD spectroradiometer values are higher than the corresponding estimates from the HSI system at 400 nm and 600 nm, with deviations of up to 20%.

- **Intermediate Sky**

The resulting spectral sky radiance distribution is complicated for mixed clear sky and clouds as presented in Figure 6.7. The measurement of the spectral radiance was performed on October 26, 2012 on 12:01 UTC (scanning period, 12:01 – 12:13 UTC) by the CCD spectroradiometer and the HSI system for the wavelength 400nm, 500nm and 600 nm. The actual synchronized HSI image can be seen in Figure 6.10.

Most of the sky elements with a zenith angle greater than 50° were occupied by clouds, while the area around the zenith was cloudless. In this case, the Sky Index has been determined and applied for separating blue sky and cloudy areas.

For 500 nm (middle panel), the comparison shows that the cloudless spectral radiance near the zenith derived by the HSI system agrees well with the CCD spectroradiometer measurement, with a deviation of up to 10%. The same deviation is observed at scanning points that are fully covered by clouds. If scanning points are covered by a small amount of clouds, the HSI system overestimated the spectral sky radiance. In this case the deviation is less than 20%. Similarly, the spectral sky radiance of very bright clouds is overestimated by the HSI system.

Compared to the wavelength 500 nm, the spectral sky radiance distribution at wavelengths 400 nm and 600 nm exhibit a higher deviation in the two instrument readings. The scanning point containing partly filled clouds can deviate up to 30%.

6. Reconstruction of Spectral Sky Radiance

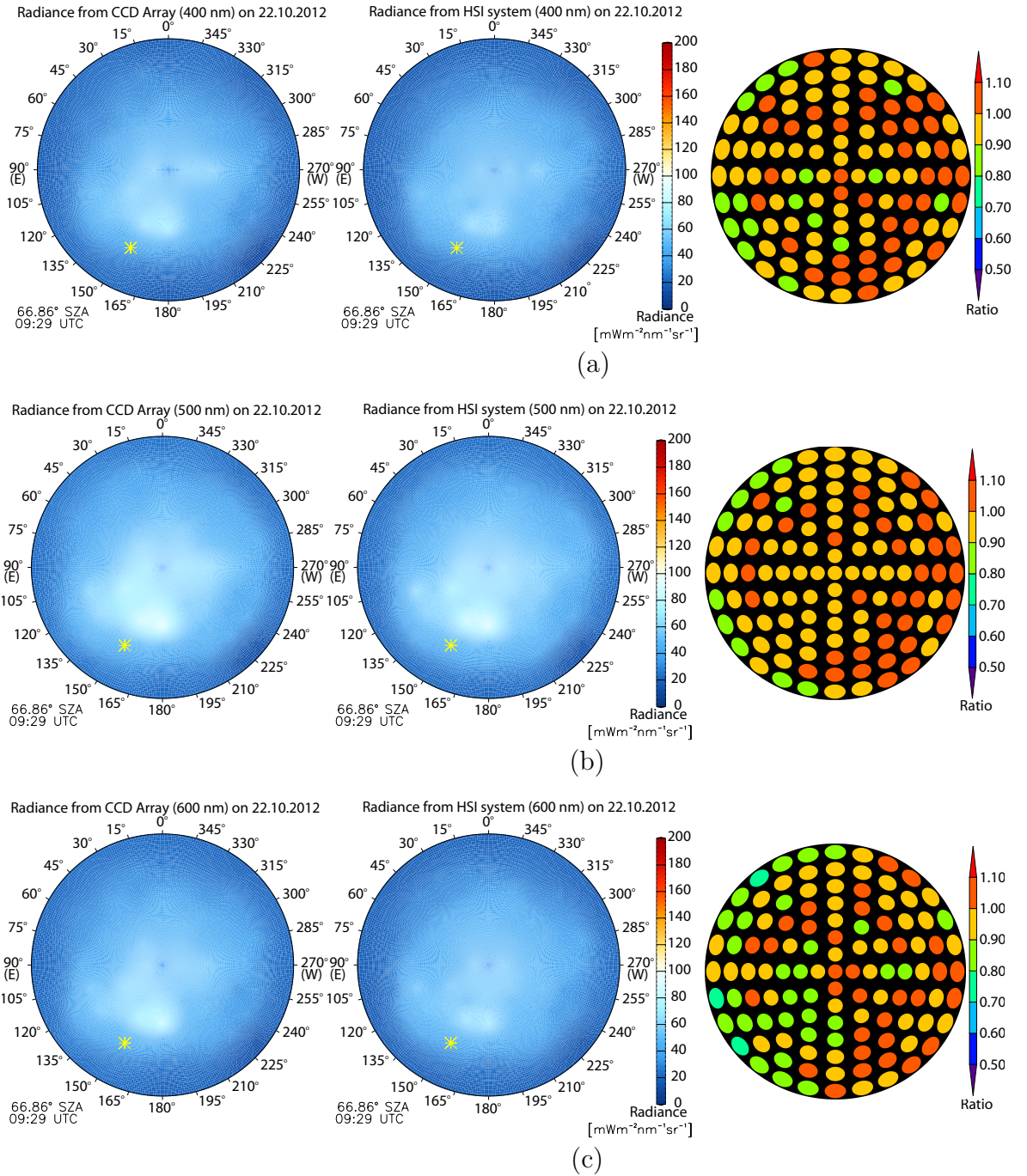


Figure 6.6: Spectral radiance distribution at 400 nm (a), 500 nm (b) and 600 nm (c) measured by CCD spectroradiometer (left) and HSI system (middle) on October 22, 2012 at 09:29 UTC (66.86° of SZA) under an overcast situation. The right plots show the ratio between the computed spectral radiance of the HSI system and the measured spectral radiance of the CCD spectroradiometer (HSI system/CCD spectroradiometer).

6. Reconstruction of Spectral Sky Radiance

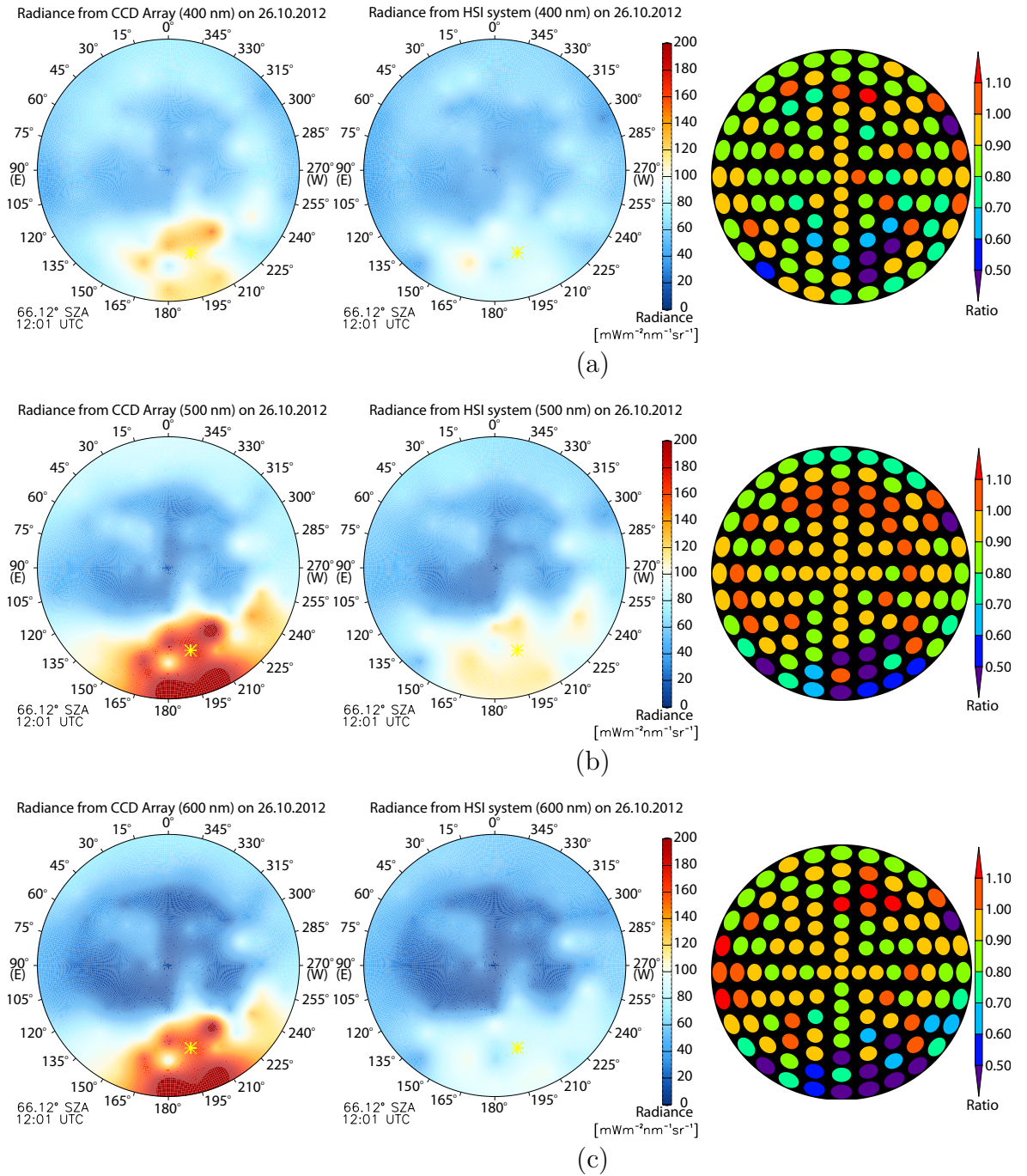


Figure 6.7: Spectral radiance distribution at 400 nm (a), 500 nm (b) and 600 nm (c) measured by CCD spectroradiometer (left) and HSI system (middle) on October 26, 2012 at 09:29 UTC (66.12° of SZA) under partly cloudy sky. The right plots show the ratio between the computed spectral radiance of the HSI system and the measured spectral radiance of the CCD spectroradiometer (HSI system/CCD spectroradiometer).

6.3.3 Comparison of spectral radiance distribution from CCD spectroradiometer and HSI system for the visible wavelength

This section compares spectral sky radiance by the two systems for different sky conditions as outlined in Section 6.3.1. For each sky condition, two points of the scan pattern were chosen for validation purposes.

Figure 6.8 presents the reconstructed spectra from October 21, 2012 at 13:21 UTC for zenith angles of 36° and 72° and is measured at azimuth angles of 0° and 105° under cloudless condition. A maximum spectral radiance of $31.51 \text{ mW}/(\text{m}^2 \cdot \text{nm} \cdot \text{sr})$ is measured at a zenith angle of 36° and at a wavelength of 412 nm. Considering the zenith point, the maximum spectral radiance is slightly lower than the observed maximum at 36° . At the horizon corresponding to the zenith angle of 72° the maximum sky radiance is found to be about $71.81 \text{ mW}/(\text{m}^2 \cdot \text{nm} \cdot \text{sr})$ at wavelength 451 nm. This horizon brightening is due to the multiple scattering across to the sky as described in the luminance distribution (Section 5.3.1.3) [LENOBLE, 1993].

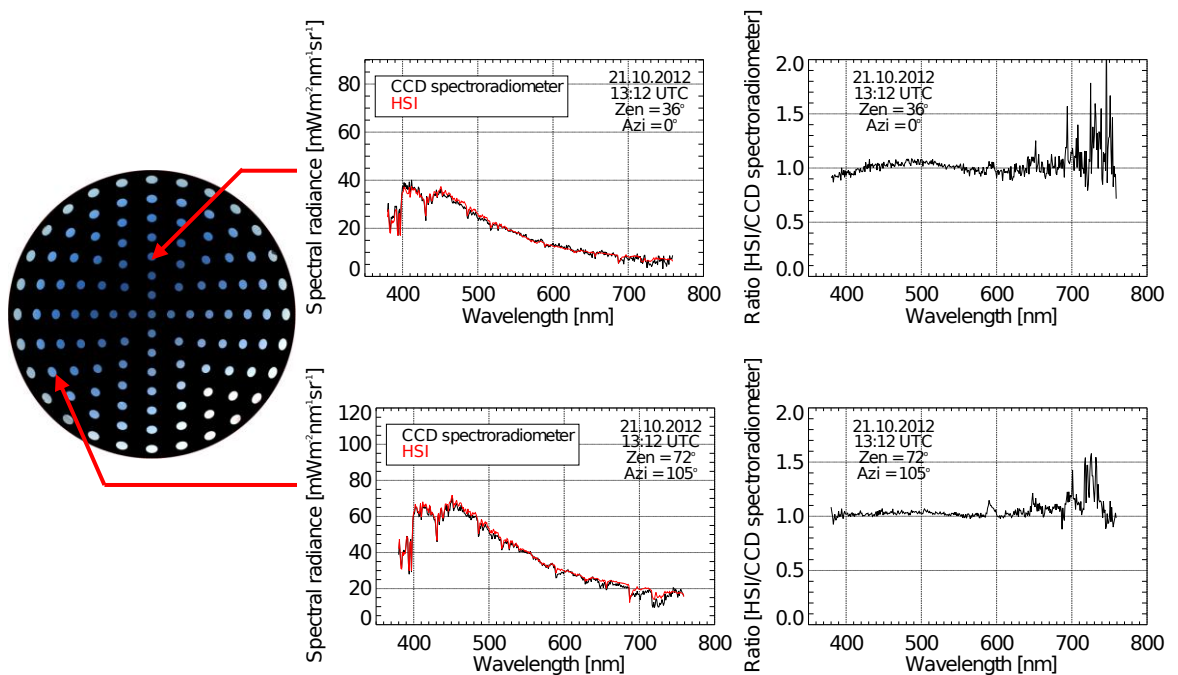


Figure 6.8: Spectral radiance measured on October 21, 2012 at 13:12 UTC by the CCD spectroradiometer and the HSI system for the scanning points with an azimuth and zenith angle of 0° and 36° (upper panel) and 105° and 72° (lower panel). The ratio between the measured and computed spectral radiance is shown on the right.

6. Reconstruction of Spectral Sky Radiance

The validation under clear skies shows that the camera-based spectral sky radiance by the HSI system agrees well with the spectral radiance from the CCD spectroradiometer and has a deviation less than 10% in the wavelength range 380 to 700 nm as shown in the ratio plots. For wavelengths greater 700 nm the deviation can be up to 30% and could be caused by the absorption band of water vapor [LIU, 2002] and the detection threshold of the CCD spectroradiometer in this wavelength region.

Figure 6.9 shows the radiance spectra for an overcast situation observed on October 22, 2012 at 09:29 UTC with a zenith angle of 48° and an azimuth angle of 202° . The maximum sky radiance during both scanning points reaches about $64 \text{ mW}/(\text{m}^2 \cdot \text{nm} \cdot \text{sr})$ also at a wavelength of 451 nm. Comparing zenith radiances, the cloudy spectral sky radiance is about one order of magnitude higher than the zenith spectral sky radiance observed in cloudfree conditions. This is influenced by the dominant of Mie Scattering [LENOBLE, 1993] due to the presence of cloud droplets, which scatter the incident radiation in any direction. The increase is a result of the transfer of direct radiation to diffuse radiation by the scattering process. From the ratio plot, the spectral radiance from the HSI image agrees very well with the measured spectral sky radiance from the CCD spectroradiometer with a deviation less than 10% for all wavelengths in the visible range at both scanning points.

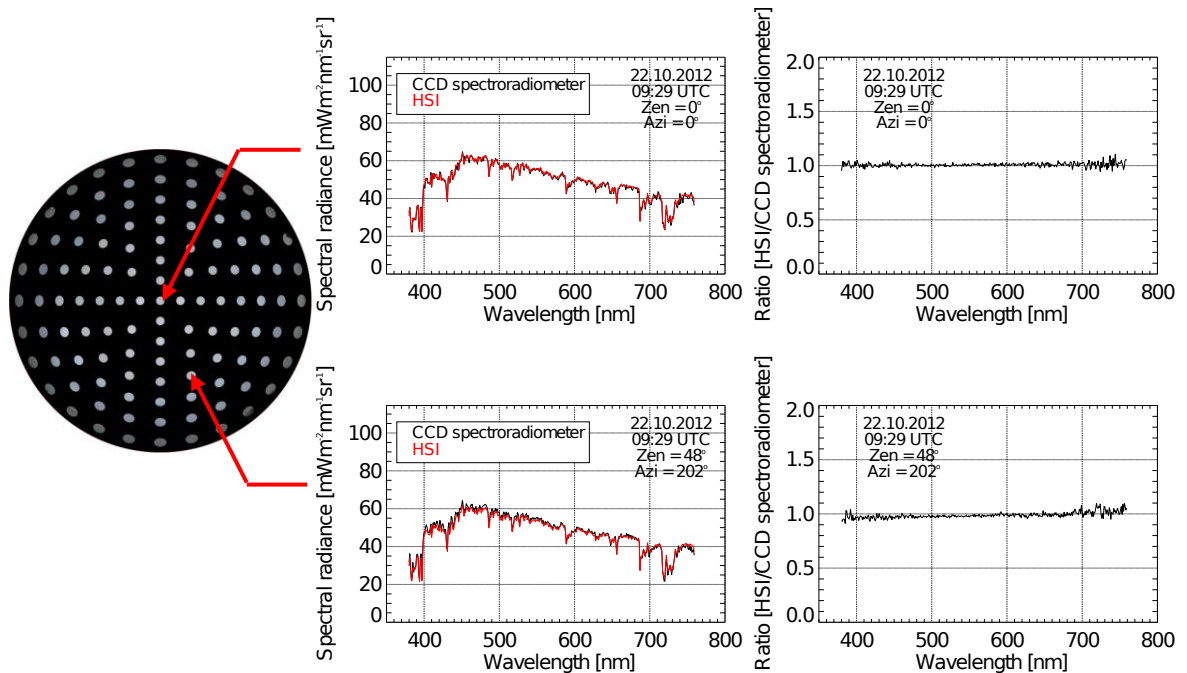


Figure 6.9: Spectral radiance measured on October 22, 2012 at 09:29 UTC by the CCD spectroradiometer and the HSI system at the zenith (upper panel), for azimuth angle 202° and zenith angle of 48° (lower panel). The ratio between the measured and computed spectral radiance is shown on the right.

6. Reconstruction of Spectral Sky Radiance

The different shape of the sky radiance spectra for varying sky situations may be explained by scattering processes. In cloudless sky conditions (see Figure 6.8 left, upper panel) atmospheric Rayleigh scattering is dominant, which has a strong dependence on wavelength [LENOBLE, 1993] and leads to the steep decrease of the spectra radiance with increasing wavelength. In contrast to cloud free conditions (Figure 6.8 left, lower panel), Mie scattering due to cloud droplets becomes the main depletion process for cloudy situations. Mie scattering depends hardly on the wavelength [LENOBLE, 1993] and the spectral sky radiance, therefore, hardly decreases with increasing wavelength. Due to Mie scattering the maximum radiance which is at 412 nm in cloudless episodes (Figure 6.8 left, upper panel) shifts to 451 nm in cloudy skies (Figure 6.8, left lower panel). The shift of the radiance maximum to longer wavelengths was observed and investigated for different regions [PISSULLA et al., 2009; WUTTKE and SECKMEYER, 2006].

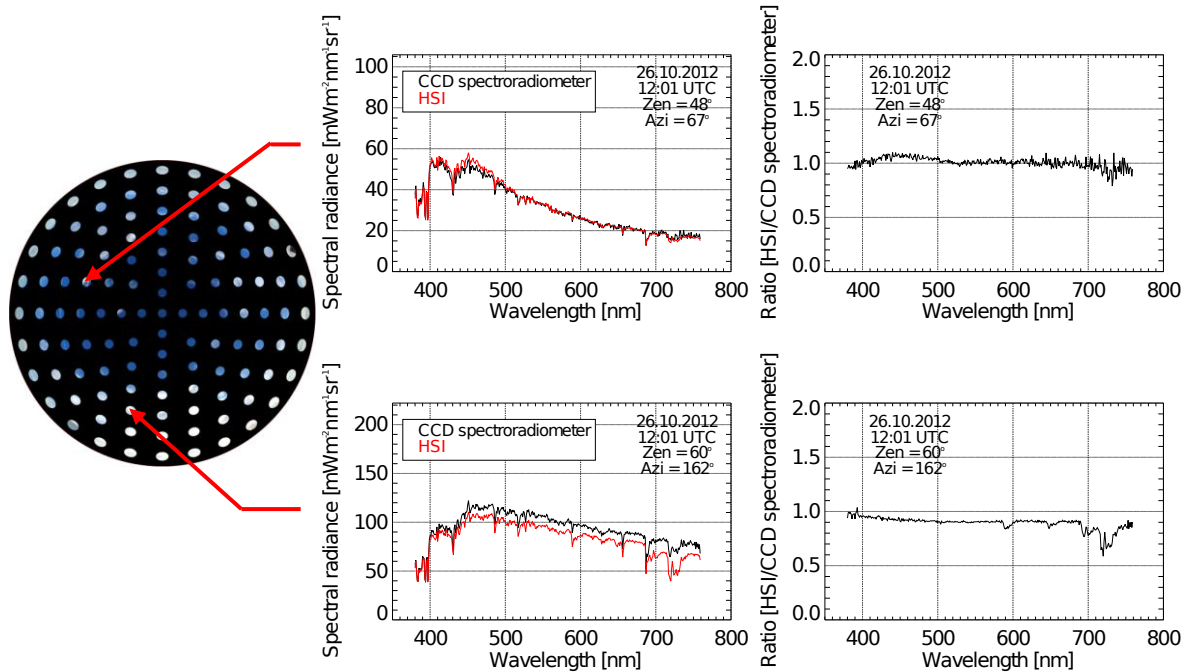


Figure 6.10: Spectral radiance measured on October 26, 2012 at 12:01 UTC by the CCD spectroradiometer and the HSI system for the scanning points with an azimuth and zenith angle of 48° and 67° (upper panel) and 162° and 60° (lower panel) respectively. The ratio between the measured and computed spectral radiance is shown on the right.

As shown in Figure 6.10 the sky radiance spectra were also determined by the CCD spectroradiometer and the HSI system for broken cloud condition for October 26, 2012 at 12:01 UTC. The scanning point with a zenith angle of 48° and an azimuth

angle of 67° , shown in the upper panel, is half occupied by clouds. The maximum value reaches around $54.48 \text{ mW}/(\text{m}^2 \cdot \text{nm} \cdot \text{sr})$ at the wavelength 451 nm. The Sky Index was found to be about 0.22 which leads to selecting the regression model for cloudy condition. The resulting value from the HSI system is slightly higher than from the CCD spectroradiometer but the derivation is still within 10%. In the lower panel, the plot of the scanning point with a zenith angle of $60 \text{ mW}/(\text{m}^2 \cdot \text{nm} \cdot \text{sr})$ and an azimuth angle of 162° , which was fully occupied by cumulus clouds, is shown. The spectral sky radiance determined by the HSI system was smaller than the measured spectral radiance with a deviation up to 20% for wavelengths less than 700 nm. For wavelengths greater 700 nm the deviation can increase up to 40% around the water absorption band [Liou, 2002].

6.4 Remark and Discussion

In this subsection some technical discussions influencing the reproducibility of the field radiance spectra measurement are given.

- A major challenge of this regression technique is that the collinearity between the predictor variables, which creates the regression relationship, is very specific to the training dataset from which they are derived. Therefore, it would be unsuccessful to apply the same coefficients to other dataset without the test of their suitability. Moreover, the investigated training dataset during this work contains solar zenith angles $60^\circ - 90^\circ$ due to the fact that the measurements have been performed in wintertime.
- The difficulty in separating cloudy from cloudless regions in partly cloudy sky situation using the Sky Index leads to uncertainties in the selection of the regression model. As shown in the Section 6.3.3 for the comparison of the spectral radiance during broken clouds with an azimuth and zenith angle of 48° and 67° , cumulus clouds occupied one half of this scanning point (see Figure 6.10). The Sky Index was found to be 0.22, which lead to a selection of the cloudy regression model as in previous description. However, both instruments show a good agreement in the comparison.
- The spectral resolution is 1 nm when the regression technique is used to retrieve the spectral sky radiance. With a spectral resolution smaller than 1 nm, this approach might not be possible.

7 Conclusions

In this chapter, the concluding remarks are presented beginning with a brief summary of the development of the Hemispherical Sky Imager system. The second section presents a methodology for measuring the sky luminance from the HSI system and its resulting comparison. A method to reconstruct the spectral sky radiance distribution in the visible wavelength is explained in the third section and some data is produced and validated. Finally, the outlook for future work is summarized.

7.1 The HSI system

In this study, the new *Hemispherical Sky Imager system* (HSI) has been successfully designed and developed to observe the cloud variations and to measure the sky luminance and spectral sky radiance distributions at IMuK, Hannover. A CCD camera sensor and lens were selected, followed by the development of the environmental housing and its temperature control for extreme weather condition and long-term operation. An identical HSI system was also installed at NIWA, New Zealand for observing the southern hemisphere.

The image acquisition processes including capturing images, deleting nighttime images, making videos, storing images and transferring data were fully automated. With the temporal resolution of 20 seconds, further analysis of the images were performed in real time. This HSI system provided a great advantage sky observations and analysis as the spatial resolution was high at more than a million pixels.

The HSI system can be used to measure the sky luminance and radiance but the geometric and radiometric calibrations of the camera sensor are required to acquire the absolute data. An experimental setup was designed to determine the projection of the fish-eye lens of the camera and some bright stars in the night images were used as reference points to check the geometric calibration. After the investigation, the projection of the camera system was found to be nearly equidistant. Based on the experimental setup or camera distortion determination, some radiometric calibrations such as dark current, linearity, roll-off and spectral responsivity of the camera sensor were performed. This camera sensor exhibits a non-linear behavior between an incident illumination and output signal. The maximum spectral response of each channel was found around the wavelength 602 nm, 527 nm and 441 nm for the red, green and blue channels respectively.

Besides being able to provide sky luminance and radiance, the HSI system has the benefit of being relatively small, lightweight and installation is simple. This system therefore can be considered as a valuable achievement, because many other commercial photometric and radiometric instruments measuring luminance and radiance are either costly or slow.

7.2 Sky luminance distribution

An approach for retrieving luminance of the image is based on the equation of [Roy et al. \(1998\)](#), which describes a method for extracting luminance from the RGB pixel values, shutter speed, f-stop number and ISO number of the hemispherical images. In contrast to [ROY et al. \(1998\)](#), new parameters depending on the exposure times of the camera setting by the luminance calibration in the laboratory were evaluated for estimating the sky luminance from the [HSI](#) images .

To overcome the limitation of dynamic range of the camera sensor caused by direct sunlight and very bright clouds, a High Dynamic Range ([HDR](#)) image was developed, which was composed of three similar images with different exposure times. This process increased the dynamic range of the [HSI](#) system.

High spatial and temporal resolutions sky luminance derived from the [HSI](#) images were validated with luminance measured by a [CCD](#) array spectroradiometer. The deviation of the diurnal luminance between both dataset is less than 10% for cloudless and completely overcast skies and differs by no more than 20% for all sky conditions. Concerning the sky luminance distribution for the complete sky between both instruments the difference deviates by 10% for cloud free and overcast sky and by less than 30% through broken clouds. The deviation of the daily averaged sky luminance can be up to 20% for all weather conditions. The sky luminance increases from zenith point towards to the horizon, in a process called the horizon brightening. This feature is dominant in Rayleigh scattering.

For luminance data quality control, the global illuminance derived from the [HSI](#) system was compared with the synchronized measured global illuminance from a luxmeter. The comparisons exhibited the deviations less than 5% and 20% under cloudless and cloudy skies for solar zenith angle less than 80° , respectively. Moreover, maximum deviations for daily data obtained during February-May 2012 were under 20%.

7.3 Spectral sky radiance distribution

A new technique for the producing spectral sky radiance in the visible wavelength (380 nm - 760 nm) from the [HSI](#) system was introduced. Due to the nonlinearity of the camera image sensor, the non-linear regression approach was applied to archive the spectra from the [HSI](#) system. The relationship between the measured spectral sky radiance from the [CCD](#) spectroradiometer and digital counts from three channels (red, green and blue) of the [HSI](#) images, which were called training dataset or predictors, were found to be a third degree polynomial. The best correlation coefficient of each regression equation was chosen in order to select the model for the reconstruction of the spectral sky radiance at each wavelength. Due to the large differences in channel counts between cloudless and cloudy pixels, separate regression relationships were developed for these two situations.

To distinguish the cloudless from cloudy image pixels, the *Sky Index* was developed, which is defined as the ratio between the count values from the red and blue channel. The cloudless pixels in the image have high blue values and low red values, whereas cloud area presents white or grey in the image, which means the digital numbers of red and blue are almost the same. The investigations showed that an average Sky Index greater than 0.25 indicates cloudless skies and less than 0.25 is representative of clouds.

The camera-based independent spectral sky radiance distributions were validated with the measured spectral sky radiance from the [CCD](#) spectroradiometer. The horizon brightening of the spectral sky radiance for complete distribution over the hemisphere at the wavelength 400 nm, 500 nm and 600 nm from both instruments was also observed as presented in the luminance distribution. For zenith angles less than 80°, the comparison of both instruments deviated by less than 20% at 400 nm, 500 nm and 600 nm for all weather conditions. The reconstructed spectra of the wavelength 380 nm to 760 nm at various directions show the different shape depending on sky conditions. The spectra under cloud free conditions had a steep decrease depending on wavelength dominated by the Rayleigh scattering process more than in cloudy situation, which is dominated by Mie scattering. The shift of the maximum radiance from 412 nm to 450 nm for cloudless and overcast sky conditions was also observed. The recovered spectra for the visible wavelength at different zenith and azimuth angles of the sky dome deviated by less than 20% for all sky conditions compared to the [CCD](#) spectroradiometer measurements.

7.4 Future work

A general problem with the applications of the compact digital camera is the internal clock, which can deviate several minutes in a few weeks. For the high temporal measurement, this leads to an asynchrony with other instruments and may cause additional uncertainty during the validation. The problem could be avoided by applying the GPS receiver or internet, which gets their information about the time every second from various tracked GPS satellites, connected to the PCs. The internal PC clocks are then updated for every minutes.

Further problems relate to the RemoteCaptureFunction being unavailable as part of the PS Remote software, which is used to remote and capture images of the [HSI](#) system. Since October 2008, the last RemoteCaptureFunction was released with the Canon Powershot G10 into the market and the company no longer implements this function in Canon Powershot G11, G12 as well in other compact camera series from Canon. Due to the new camera model no longer being marketed, only the used or second hand camera must be utilized. The change to other camera manufacturers such as Nikon is not feasible, as these the RemoteCaptureFunction is only available with a [DSLR](#) camera. Moreover, three new camera models per year will be replaced, on average. For this reason and a lack of the RemoteCaptureFunction, use of the

HSI system is limited for long-term scientific applications. It may be also possible to develop specific routines for capturing the images because the PS Remote can be controlled via console commands.

During this work, some radiometric properties of the camera sensor such as stray light, uniformity or exact roll-off have still not investigated as mentioned in Section 5.4. This could be a further goal concerning measurements with the HSI system.

Use of an auto-bracketing function to obtain three images per shot, provided information on bright and dark areas dominated by processes such as bright clouds, the circumsolar regions or dark clouds with high optical depths. Nevertheless, some information is still missing. Capturing the images with five images per shot might be minimized this issue. The luminance calibration performed in the laboratory for determining the luminance from the HSI system can be varied depending on the cameras and must be previously tested before using these parameters.

The validation has not yet been performed over long time periods (e. g. over one year). Although, the second identical HSI system was installed at NIWA, New Zealand only preliminary investigations at this location have been conducted. Measurements over long-time periods and validation in other locations would provide a better assessment of the ability of digital photography to provide sky luminance distribution.

In a similar fashion to sky luminance, the spectral sky radiance has to be measured and validated for long periods and for other locations. Measurements need to be made over a year, ensuring that different solar zenith and azimuth angles on the sky dome are sampled. The availability of the data for different periods and sky conditions would provide a comprehensive training data set for validation purposes..

The method for reconstructing the spectral sky radiance has a disadvantage in that the regression models depend on synchronous spectral radiance data. Applying these regression models and their coefficients without previously validation is not reasonable. An alternative is to obtain a laboratory calibration between signal count and spectral radiance. To carry out this calibration, some camera properties such as the absolute radiance calibration, linearity calibration, dark noise and roll-off measurements are necessary.

List of Symbols

Symbol	Physical Parameter	Unit
φ	azimuth angle	$^{\circ}$
β	angle between two positions	$^{\circ}$
ε	angle between the direction of the beam and the normal of surface element	$^{\circ}$
γ	elevation angle	$^{\circ}$
ϕ_{ν}	luminous flux	<i>lm</i>
ϕ	radiant flux	<i>W</i>
γ_s	solar elevation angle	$^{\circ}$
Ω	solid angle	<i>sr</i>
λ	wavelength	<i>nm or m</i>
θ	zenith angle	$^{\circ}$
<i>A</i>	unit area	m^2
<i>c</i>	focal length	<i>mm</i>
<i>E</i>	irradiance	$W \cdot m^{-2}$
E_{λ}	spectral irradiance	$W \cdot m^{-2} \cdot nm^{-1}$
E_{ν}	illuminance	<i>lx</i>
E_{ν}	exposure value	
<i>f</i>	aperture or f-stop number	
E_{dh}	diffuse illuminance	<i>lux</i>
E_s	direct illuminance	<i>lux</i>
<i>I</i>	radiant intensity	$W \cdot sr^{-1}$
I_{ν}	luminous intensity	<i>cd</i>
K_m	luminous efficacy for photopic version	$lm \cdot W^{-1}$
L_{ν}	luminance	$cd \cdot m^{-2}$
<i>M</i>	radiant existance	$W \cdot m^{-2}$
<i>Q</i>	radiant energy	<i>J</i>
<i>R</i>	radiance	$W \cdot m^{-2} \cdot sr^{-1}$
$R(\lambda)$	spectral radiance	$W \cdot m^{-2} \cdot nm^{-1} \cdot sr^{-1}$
$r(\lambda)$	spectral responsivity	$V \cdot m^2 \cdot nm \cdot sr \cdot W^{-1}$
$S(\lambda)$	measured spectral radiance signal	<i>V or counts</i>
<i>T</i>	shutter speed or exposure time	<i>second</i>
$V(\lambda)$	response of the human eye for photopic vision	
$V'(\lambda)$	response of the human eye for scopic vision	

List of Acronyms

Abbreviation	Meaning
ADC	Analogue Digital Converter
AFO	Alternative Fisheye Objective
CCD	Charge Coupled Device
CIE	Commission Internationale de l'Éclairage (eng.:International Commission on Illumination)
DSLR	Digital Single-Lens Reflex
EXIF	Exchangeable Image File Format
FOV	Field of View
FWHM	Full Width at Half Maximum
HDR	High Dynamic Range
HHCRM	Hand Held Contrast Reduction Meter
HSI	Hemispherical Sky Imager
IDL	Interactive Data Languages
IDMP	International Daylight Measurement Project
IMuK	Institute for Meteorology and Climatology (ger.: Institut für Meteorologie und Klimatologie)
ISO	International Standard Organization
JPEG	Joint Photographic Experts Group
LDR	Low Dynamic Range
NIWA	National Institute of Water and Atmospheric Research
NZST	New Zealand Standard Time
PC	Personal computer
RADS	Radiance Distribution Camera System
RGB	Red Green and Blue color
SZA	Solar Zenith Angle
TSI	Total Sky Imager
UCSD	University of California San Diego
USB	Universal Serial Bus
UTC	Coordinated Universal Time
UV	Ultraviolet
WSI	Whole Sky Imager

Bibliography

- Ali, T., 2003:** *Spectral Radiance Distribution: From Luminance Measurements to Spectral Irradiance on Inclined Surfaces.* — Diplomarbeit, Institut für Meteorologie und Klimatologie, Leibniz Universität Hannover.
- Ander, G., 2003:** *Daylight Performance and Design.* — Van Nostrand Reinhold, New York.
- Ansko, I., K. Eerme, S. Lätt, M. Noorma and U. Veismann, 2008:** Study of suitability of AvaSpec array spectrometer for solar UV field measurements. — *Atmospheric Chemistry and Physics*, **8**, **12**, 3247–3253.
- Banterle, F., K. Debattista, A. Artusi, S. Pattanaik, K. Myszkowski, P. Ledda and A. Chalmers, 2009:** High dynamic range imaging and low dynamic range expansion for generating HDR content. — *Computer Graphics forum*, **28**, **8**, 2343–2367.
- Bernhard, G. and G. Seckmeyer, 1999:** Uncertainty of measurements of spectral solar UV irradiance. — *Journal of Geophysical Research*, **104**, 14321–14345.
- Blumthaler, M., J. Grübner, M. Huber and W. Ambach, 1996:** Measuring spectral and spatial variations of UVA and UVB sky radiance. — *Geophysical Research Letters*, **23**, **5**, 547–550.
- van Bommel, W. and G. van den Beld, 2004:** Lighting for work: a review of visual and biological effects. — *Lighting Research and Technology*, **36**, **4**, 255–266.
- Brakebusch, M., 2007:** *Development of an automated cloud detection method for advanced photogrammetric systems.* — Diploma thesis, Institut für Meteorologie und Klimatologie, Leibniz Universität Hannover.
- Breeze, 2007:** <http://www.breezesys.com/>.
- Brydges, D., F. Deppner, H. Künzli, K. Heuberger and R. Hersch, 1998:** Application of a 3-CCD color camera for colorimetric and densitometric measurements. — In: *SPIE Proceedings 3300, Color Imaging : Device Independent Color, Color Hardcopy and Graphics Arts III*, S. 292–301, S. 292–301.
- Cazorla, A., F. J. Olmo and L. Alados-Arboledas, 2008:** Development of a sky imager for cloud cover assessment. — *Journal of the Optical Society of America A*, **25**, **1**, 29–39.
- CIE, 1970:** *Daylight.* — Commission International de l'Éclairage (CIE Central Bureau: Paris).

- CIE, 1973:** *Standardization of luminance distribution of clear skies.* — Commission International de l'Éclairage (CIE Central Bureau: Paris).
- CIE, 1994:** *Guide to Recommended Practice of Daylight Measurement.* — Commission International de l'Éclairage (CIE Central Bureau: Vienna).
- CIE, 2000:** *Photometry— the CIE System of Physical Photometry.* — Commission International de l'Éclairage (CIE Central Bureau: Vienna).
- CIE, 2011:** *International Lighting Vocabulary.* — Commission International de l'Éclairage (CIE Central Bureau: Vienna).
- CIE, 2012:** *Characterization of the Performance of Illuminance Meters and Luminance Meters.* — Commission International de l'Éclairage (CIE Central Bureau: Vienna).
- Cordero, R. R., G. Seckmeyer, D. Pissulla and F. Labbe, 2008a:** Uncertainty of experimental integrals: application to the UV index calculation. — *Metrologia*, **45**, 1–10.
- Cordero, R. R., G. Seckmeyer, D. Pissulla and F. Labbe, 2008b:** Uncertainty evaluation of spectral UV irradiance measurements. — *Measurement Science and Technology*, **19**, 045104.
- Curtin, D. P., 2003:** A short course in using your digital camera. — <http://www.shortcourses.com/>.
- Czibula, G. and O. Grundmann, 2002a:** *Skyscanner - Gerätebeschreibung.* — Czibula & Grundmann Engineering GbR, Berlin.
- Czibula, G. and O. Grundmann, 2002b:** *Photometer Datasheet.* — Czibula & Grundmann Engineering GbR, Berlin.
- Darula, S. and R. Kittler, , 2002:** *CIE sky standard defining luminance distributions*, Proceeding of eSim, September 2002.
- Deering, D. W. and T. F. Eck, 1987:** Atmospheric optical depth effects on angular anisotropy of plant canopy reflectance. — *International Journal of Remote Sensing*, **8**, **6**, 893–916.
- DIN 5031, 1982:** *Strahlungsphysik im optischen Bereich und Lichttechnik*, Vol. 8. — Beuth Verlag GmbH.
- DIN 5032, 1999:** *International Vocabulary of Basic and General Terms in Metrology.* — Beuth Verlag GmbH.
- Dubovik, O. and M. D. King, 2000:** A flexible inversion algorithm for retrieval of aerosol optical properties from Sun and sky radiance measurements. — *Journal of Geophysical Research: Atmospheres*, **105**, **D16**, 20673–20696.

- Estrada, J., R. Alvarez, T. Abbott, J. Annis, M. Bonati, E. Buckley-Geer, J. Campa, H. Cease, S. Chappa, D. Depoy, G. Derylo, H. T. Diehl, B. Flaughner, J. Hao, S. Holland, D. Huffman, I. Karliner, D. Kubik, S. Kuhlmann, K. Kuk, H. Lin, N. Roe, V. Scarpine, R. Schmidt, K. Schultz, T. Shaw, V. Simaitis, H. Spinka, W. Stuermer, D. Tucker, A. Walker and W. Wester, 2010:** *Focal plane detectors for dark energy camera (DECam)*, Vol. 7735, Proc. SPIE 7735, 77351R.
- European Commission, 2005:** *Doing More With Less - Green Paper on Energy Efficiency*. — Luxembourg: Office for Official Publication of the European Communities.
- Feister, U., H. Müller, T. Sattler, J. Shields, U. Gürsdorf and J. Göldner, 2010:** Comparison of macroscopic cloud data from ground-based measurements using VIS/NIR and IR instruments at Lindenberg, Germany. — *Atmospheric Research*, **96**, **23**, 395 – 407.
- Feister, U. and J. Shields, 2005:** Cloud and radiance measurements with the VIS/NIR Daylight Whole Sky Imager at Lindenberg (Germany). — *Meteorologische Zeitschrift*, **14**, 627–639.
- Ferraro, V., M. Mele and V. Marinelli, 2011:** Sky luminance measurements and comparisons with calculation models. — *Journal of Atmospheric and Solar-Terrestrial Physics*, **73**, **13**, 1780 – 1789.
- Foyo-Moreno, I., I. Alados, F. J. Olmo, J. Vida and L. Alados-Arboledas, 2001:** On the use of a cloud modification factor for solar UV (290-385nm) spectral range. — *Theoretical and Applied Climatology*, **68**, **1-2**, 41–50.
- Hayman, S., G. Roy and W. Julian, , 1999:** *The use of Nikon/Fuji digital camera for cloud detecton and sky luminance evaluation*, Vol. 133, Proceeding of the CIE 24th, Warsaw, pp.148-150.
- Heinle, A., A. Macke and A. Srivastav, 2010:** Automatic cloud classification of whole sky images. — *Atmospheric Measurement Techniques*, **3**, **3**, 557–567.
- Hernández-Andrés, J., J. Romero and J. Raymond L. Lee, 2001:** Colorimetric and spectroradiometric characteristics of narrow-field-of-view clear skylight in Granada, Spain. — *Journal of the Optical Society of America A*, **18**, **2**, 412–420.
- Heschong, L., 2002:** Daylight and human performance. — *American Society of Heating, Refrigerating and Air Conditioning Engineers Journal*, **44**, 65–67.
- Hietanen, M., 1991:** Ocular exposures to solar Ultraviolet and visible radiaton at high latitudes. — *Scandinavian Journal of Work, Environment & Health*, **17**, 398–403.

- Hoefflinger, B., 2007:** *High Dynamic Range (HDR) Vision*. — Springer-Verlag.
- Hubel, P., D. Sherman and J. Farrell, 1994:** A comparison of methods of sensor spectral sensitivity estimation. — In: *IS&T and SID 2nd. Color Imaging Conference: Color Science, Systems and Applications*, S. 45–48.
- Huber, M., M. Blumthaler, J. Schreder, B. Schallhart and J. Lenoble, 2004:** Effect of inhomogeneous surface albedo on diffuse UV sky radiance at a high-altitude site. — *Journal of Geophysical Research: Atmospheres*, **109**, D8.
- Hughes, C., P. Denny, E. Johnes and M. Glavin, 2010:** Accuracy of fish-eye lens models. — *Applied Optics*, **49**, **17**, 3338–3347.
- Huo, J. and D. Lu, 2009:** Calibration and validation of an all-sky imager. — *Atmospheric and Oceanic Science Letters*, **2**, **4**, 220–223.
- Huo, J. and D. Lu, 2012:** Comparison of cloud cover from all-sky imager and meteorological observer. — *Journal of Atmospheric and Oceanic Technology*, **29**, 1093–1100.
- Igawa, N., H. Nakamura and K. Matsuura, , 1999:** *Sky luminance distribution model for simulation of daylight environment*, Vol. 2, IBPSA, Proceeding of the Sixth International IBPSA Conference, pp. 969-975.
- Igawa, N., Y. Koga, T. Matsuzawa and H. Nakamura, 2004:** Models of sky radiance distribution and sky luminance distribution. — *Solar Energy*, **77**, **2**, 137 – 157.
- Inanici, M., 2006:** Evaluation of high dynamic range photography as a luminance data acquisition system. — *Lighting Research and Technology*, **38**, **2**, 123–134.
- Inanici, M., 2010:** Evaluation of high dynamic range image-based sky models in lighting simulation. — *The Journal of the Illuminating Engineering*, **7**, **2**, 69–84.
- Iqbal, M., 1983:** *An Introduction to Solar Radiation*. — Academic Press, Canada.
- ISO/IEC 10918-1, 1994:** *Digital compression and coding of continuous-tone still images (JPEG)*. — International Organization for Standardization.
- Janjai, S., I. Masiri, M. Nunez and J. Laksanaboonsong, 2008:** Modeling sky luminance using satellite data to classify sky conditions. — *Building and Environment*, **43**, **12**, 2059 – 2073.
- Johnsen, B., B. Kjeldstad, T. N. Aalerud, L. T. Nielsen, J. Schreder, M. Blumthaler, G. Bernhard, C. Topaloglou, O. Meinander, A. Bagheri, J. R. Slusser and J. Davis, 2008:** Intercomparison and harmonization of UV Index measurements from multiband filter radiometers. — *Journal of Geophysical Research*, **113**, 1–9.

- Johnson, C. S., 2010:** *Science for the curious photographer: An introduction to the science of photography.* — A K Peters Limited, India.
- Kittler, R., 1967:** Standardisation of the outdoor conditions for the calculation of the Daylight Factor with clear skies. — In: *In Proceeding of the CIE International Conference on Sunlight in Buildings, Bouwcentrum, Rotterdam.*
- Kittler, R., S. Hayman, N. Ruck and W. Julian, 1992:** Daylight measurement data: Methods of evaluation and representation. — *Lighting Research and Technology*, **24**, 173–187.
- Knestrick, G. L. and J. A. Curcio, 1970:** Measurements of ultraviolet spectral radiance of the horizon sky. — *Applied Optics*, **9**, **7**, 1574–1576.
- Koppe, C., 1896:** *Photogrammetrie und Internationale Wolkenmessung.* — Braunschweig Verlag, 108 p.
- Kouremeti, N., A. Bais, S. Kazadzis, M. Blumthaler and R. Schmitt, 2008:** Charge-coupled device spectrograph for direct solar irradiance and sky radiance measurements. — *Applied Optics*, **47**, **10**, 1594–1607.
- Krarti, M., P. M. Erickson and T. C. Hillman, 2005:** A simplified method to estimate energy savings of artificial lighting use from daylighting. — *Building and Environment*, **40**, **6**, 747 – 754.
- Kraus, K., 2004:** *Photogrammetrie, Band 1, Geometrische Informationen aus Photographien und Laserscanneraufnahmen.* — Walter de Gruyter, Berlin.
- Kreuter, A. and M. Blumthaler, 2012:** Feasibility of polarized all-sky imaging for aerosol characterization. — *Atmospheric Measurement Techniques Discussions*, **5**, **6**, 8815–8838.
- Kreuter, A., M. Zangerl, M. Schwarzmann and M. Blumthaler, 2009:** All-sky imaging: a simple, versatile system for atmospheric research. — *Applied Optics*, **48**, **6**, 1091–1097.
- Krochmann, J. and M. Seidl, 1974:** Quantitative data on daylight for illuminating engineering. — *Lighting Research and Technology*, **6**, **3**, 165–171.
- Kurian, C., R. Aithal, J. Bhat and V. George, 2008:** Robust control and optimisation of energy consumption in daylight artificial light integrated schemes. — *Lighting Research and Technology*, **40**, **1**, 7–24.
- Lenoble, J., 1993:** *Atmospheric Radiative Transfer.* — Deepak Publishing, Hampton.

- Li, D. H. and J. C. Lam, 2004:** Predicting solar irradiance on inclined surfaces using sky radiance data. — *Energy Conversion and Management*, **45**, 11-12, 1771 – 1783.
- Li, Z., P. Goloub, L. Blarel, B. Damiri, T. Podvin and I. Jankowiak, 2007:** Dust optical properties retrieved from ground-based polarimetric measurements. — *Applied Optics*, **46**, 9, 1548–53.
- Liley, J. B. and B. W. Forgan, 2009:** Aerosol optical depth over Lauder, New Zealand. — *Geophysical research letters*, **36**, 5696–5703.
- Linder, W., 2006:** *Digital Photogrammetry: A practical course*. — Springer-Verlag Berlin Heidelberg.
- Liou, K. N., 2002:** *An Introduction to Atmospheric Radiation*. — Academic Press, Orlando.
- Littlefair, P. J., 1990:** Predicting annual lighting use in daylit buildings. — *Building and Environment*, **25**, 1, 43 – 53.
- López-Álvarez, M. A., J. Hernández-Andrés and J. Romero, 2008:** Developing an optimum computer-designed multispectral system comprising a monochrome CCD camera and a liquid-crystal tunable filter. — *Applied Optics*, **47**, 24, 4381–4390.
- López-Álvarez, M. A., J. Hernández-Andrés, E. M. Valero and J. Romero, 2007:** Selecting algorithms, sensors, and linear bases for optimum spectral recovery of skylight. — *Journal of the Optical Society of America A*, **24**, 4, 942–956.
- Lütjohann, H., 1968:** The stepwise regression algorithm seen from the statistician’s point of view. — Research memorandum 11.
- Matínez-Verdú, F., J. Pujol and P. Capilla, 2002:** Calculation of the color matching functions of digital camera from their complete spectral sensitivities. — *Journal of Imaging Science and Technology*, **46**, 1, 15–25.
- McCollough, F., 2008:** *Computer Guide to High Dynamic Range Digital Photography*. — Lark Books, Sterling Publishing.
- de Miguel, A., D. Mateos, J. Bilbao and R. Román, 2011:** Sensitivity analysis of ratio between ultraviolet and total shortwave solar radiation to cloudiness, ozone, aerosols and precipitable water. — *Atmospheric Research*, **102**, 1-2, 136 – 144.
- Mims(III), F. M. and J. E. Frederick, 1994:** Cumulus clouds and UV-B. — *Nature*, **371**, 291.

- Minton, E. J. and E. M. Rollin, 2006:** Estimating the irradiance spectrum from measurements in a limited number of spectral bands. — *Remote Sensing of the Environment*, **100**, 348–355.
- Miyamoto, K., 1964:** Fish-eye lens. — *Journal of the Optical Society of America*, **54**, 1060–1061.
- Moore, D. and G. P. McCabe, 2006:** *Introduction to the practice of statistics*. — W. H. Freeman and Company.
- Nagata, T., 1997:** Radiance distribution on stable overcast skies. — *Journal of Light & Visual Environment*, **21**, **1**, 6–9.
- Nakamura, H., M. Oki and Y. Hayashi, 1985:** Luminance distribution of Intermediate Sky. — *Journal of Light and Visual Environment*, **9**, **1**, 6–13.
- Nakamura, H. and O. Oki, , 1975:** *Measurement of Luminance Distribution under Various Sky Conditions by Orthographic Projection Camera*, Proceeding of the CIE conferences, London, pp. 493-502.
- Nakono, M., S. Li and N. Chiba, 2007:** Calibration of fish-eye camera for acquisition of spherical image. — *System and Computer in Japan*, **38**, **6**, 10–20.
- Nieves, J. L., E. M. Valero, S. M. C. Nascimento, J. Hernández-Andrés and J. Romero, 2005:** Multispectral synthesis of daylight using a commercial digital CCD camera. — *Applied Optics*, **44**, **27**, 5696–5703.
- Ocean Optics, 2006:** *Ocean Optics 2006 Catalog*. — Ocean Optics.
- Olmo, F. J., A. Cazorla, L. Alados-Arboledas, M. A. López-Álvarez, J. Hernández-Andrés and J. Romero, 2008:** Retrieval of the optical depth using an all-sky CCD camera. — *Applied Optics*, **47**, **34**, 182–189.
- Pennebaker, W. and J. Mitchell, 2004:** *JPEG Still Image Data Compression Standard*. — Kluwer Academic Publishers.
- Perez, R., R. Seals and J. Michalsky, 1993:** All-weather model for sky luminance distribution preliminary configuration and validation. — *Solar Energy*, **50**, **3**, 235 – 245.
- Pfister, G., R. L. McKenzie, J. B. Liley, A. Thomas, B. W. Forgan and C. N. Long, 2003:** Cloud coverage based on all-sky imaging and its impact on surface solar irradiance. — *Journal of Applied Meteorology*, **42**, 1421–1434.
- Piacentini, R. D., G. M. Salum, N. Fraidenraich and C. Tiba, 2011:** Extreme total solar irradiance due to cloud enhancement at sea level of the NE Atlantic coast of Brazil. — *Renewable Energy*, **36**, **1**, 409 – 412.

- Pickering, T. E., 2006:** MMT All-sky camera. — In: *Proceeding of International Society for Optics and Photonics*, Vol. 6267.
- Pissulla, D., 2006:** *Development of Instrumentation Measuring Sky Radiance*. — Diplomarbeit, Institut für Meteorologie und Klimatologie, Leibniz Universität Hannover.
- Pissulla, D., G. Seckmeyer, R. R. Cordero, M. Blumthaler, Schallhart, A. Webb, R. Kift, A. Smedley, A. F. Bais, N. Kouremeti, A. Ced, J. Hermang and M. Kowalewskig, 2009:** Comparison of atmospheric spectral radiance measurements from five independently calibrated systems. — *Photochemical & Photobiological Sciences*, **8**, 516–527.
- Poetzsch-Heffter, C., Q. Liu, E. Ruprecht and C. Simmer, 1995:** Effect of cloud types on the Earth radiance budget calculated with the ISCCP C1 data: Methodology and Initial results. — *American Meteorological Society*, **8**, 829–843.
- Prenzel, W.-D., 1986:** Entwicklungstendenzen der fotografischen Optik. — *Bild und Ton - Wissenschaftliche Zeitschrift für visuelle und auditive Medien*, **39**, **1**, 5–13.
- Quante, M., 2004:** The role of clouds in the climate system. — *Journal de Physique IV France*, **121**, 61–86.
- Ricchiazzi, P. J., A. Payton and C. Gautier, , 2000:** *The effect of surface albedo heterogeneity on sky radiance*, San Antonio, Texas, Tenth ARM Science Team Meeting Proceedings.
- Riechelmann, S., 2008:** *Messung von spektraler Bestrahlungsstärke und Strahldichte mit CCD-Array Geräten*. — Diplomarbeit, Institut für Meteorologie und Klimatologie, Leibniz Universität Hannover.
- Robertson, M. A., S. Borman and R. L. Stevenson, 2003:** Estimation-theoretic approach to dynamic range enhancement using multiple exposures. — *Journal of Electronic Imaging*, **12**, 219–228.
- Román, R., M. Antón, A. Cazorla, A. de Miguel, F. J. Olmo, J. Bilbao and L. Alados-Arboledas, 2012:** Calibration of an all-sky camera for obtaining sky radiance at three wavelengths. — *Atmospheric Measurement Techniques*, **5**, **8**, 2013–2024.
- Rossini, E. G. and A. Krenzing, 2007:** Maps of sky relative radiance and luminance distributions acquired with a monochromatic CCD camera. — *Solar Energy*, **81**, **11**, 1323 – 1332.
- Roy, G. G., S. Hayman and W. Julian, 1998:** *Sky modeling from digital imagery (ARC Project A89530177)*. — The University of Sydney and Murdoch University.

- Schafer, J. S., V. K. Saxena, B. N. Wenny, W. Barnard and J. J. De Luisi, 1996:** Observed influence of clouds on ultraviolet-B radiation. — *Geophysical Research Letters*, **23**, **19**, 2625–2628.
- Scheibel, J., 1973a:** Fisheye-Objektive und verwandte Abbildungstechniken (1). — *Photo-Technik und -Wirtschaft*, **24**, **4**, 90–93.
- Scheibel, J., 1973b:** Fisheye-Objektive und verwandte Abbildungstechniken (2). — *Photo-Technik und -Wirtschaft*, **24**, **6**, 166–167.
- Schneider, D., E. Schwalbe and H. G. Maas, 2009:** Validation of geometric models for fisheye lenses. — *ISPRS Journal of Photogrammetry and Remote Sensing*, **64**, **3**, 259–266.
- Schrempf, M., 2010:** *Entwicklung eines Algorithmus zur Wolkenerkennung in Digitalbildern des Himmels*. — Diplomarbeit, Institut für Meteorologie und Klimatologie, Leibniz Universität Hannover.
- Seckmeyer, G., A. Bais, G. Bernhard, M. Blumthaler, S. Druke, P. Kiedron, K. Lantz, R. L. McKenzie and S. Riechelmann, 2010:** *Instruments to measure solar ultraviolet radiation, part 4: array spectroradiometers*. — World Meteorological Organization.
- Seiz, G., J. Shields, U. Feister, E. P. Baltsavias and A. Gruen, 2002:** Cloud mapping with ground-based photogrammetric cameras. — *International Journal of Remote Sensing*, **28**, **9**, 2001–2032.
- Shields, J. E., R. W. Johnson, M. E. Karr and J. L. Wertz, 1998:** Automated day/night whole sky imagers for field assessment of cloud cover distributions and radiance distribution. — In: *Tenth Symposium on Meteorological Observations and Instrument*, American Meteorological Society.
- Shields, J. E., M. E. Karr, T. P. Tooman, D. H. Sowle and S. T. Moore, 1999:** *The Whole Sky Image - A Year of Progress*. — Marine Physical Laboratory, University of California, San Diego.
- Shortis, M. and H. Beyer, 1996:** *Close range photogrammetry and machine vision*. — Whittles Publishing, Pennsylvania, S. 106–155.
- Soler, A. and K. Gopinathan, 2000:** A study of zenith luminance on Madrid cloudless skies. — *Solar Energy*, **69**, **5**, 403 – 411.
- Spasojevic, B. and A. Mahdavi, 2005:** Sky lumiance mapping for computatinal daylight modelling. — In: *Nineth International IBPSA Conference, Montreal*.
- Starks, P. J., E. A. Walter-Shea, F. R. Schiebe and B. L. Markham, 1995:** Temperature sensitivity characterization of a silicon diode array spectroradiometer. — *Remote Sensing of the Environment*, **5**, 385–389.

- Stellarium, 2009:** <http://www.stellarium.org/>.
- Steven, M. D. and M. H. Unsworth, 1977:** Standard distributions of clear sky radiance. — *Quarterly Journal of the Royal Meteorological Society*, **103**, **437**, 457–465.
- Sun, N., H. Mansour and R. Ward, 2010:** HDR image construction from multi-exposed stereo LDR images. — In: *17th IEEE International Conference on Image Processing*.
- Tohsing, K., M. Schrempf, S. Riechelmann, H. Schilke and G. Seckmeyer, 2013:** Measuring high-resolution sky luminance distributions with a CCD camera. — *Applied Optics*, **52**, **8**, 1564–1573.
- Tregenza, P. R., 1987:** Subdivision of the sky hemisphere for luminance measurements. — *Lighting Research and Technology*, **19**, 13–14.
- Tregenza, P. R. and I. M. Waters, 1983:** Daylight coefficients. — *Lighting Research and Technology*, **15**, 65–71.
- Vartiainen, E., 2001:** Electricity benefits of daylighting and photovoltaics for various solar facade layouts in office buildings. — *Energy and Buildings*, **33**, **2**, 113 – 120.
- Vermeulen, A., C. Devaux and M. Herman, 2000:** Retrieval of the scattering and microphysical properties of aerosols from ground-based optical measurements including polarization. I. Method. — *Applied Optics*, **39**, **33**, 6207–6220.
- Vora, P. L., J. E. Farrell, J. D. Tietz and D. H. Brainard, 1997:** *Digital color camera -2- Spectral response*. — Hewlett-Packard Company.
- Voss, K. J. and G. Zibordi, 1989:** Radiometric and geometric calibration of a visible spectral electro-optic ‘fish-eye’ camera radiance distribution system. — *Journal of Atmospheric and Oceanic Technology*, **6**, 652–662.
- Webb, A. R., 2006:** Considerations for lighting in the built environment: Non-visual effects of light. — *Energy and Buildings*, **38**, **7**, 721 – 727.
- Weihs, P., A. R. Webb, S. J. Hutchinson and G. W. Middleton, 2000:** Measurements of the diffuse UV sky radiance during broken cloud conditions. — *Journal of Geophysical Research: Atmospheres*, **105**, **D4**, 4937–4944.
- Wuttke, S. and G. Seckmeyer, 2006:** Spectral radiance and sky luminance in Antarctica: a case study. — *Theoretical and Applied Climatology*, **85**, **3-4**, 131–148.
- Wysecki, G. and W. S. Stiles, 2000:** *Color Science: Concepts and Methods, Quantitative Data and Formulae*. — John Wiley & Sons, Ltd.

- Yamashita, M. and M. Yoshimura, 2012:** Ground-based cloud observation for satellite-based cloud discrimination and its validation. — In: *XXII Congress of the International Society for Photogrammetry, Remote Sensing*.
- Yamashita, M., M. Yoshimura and T. Nakashizaka, 2004:** Cloud cover estimation using multitemporal hemispherical imageries. — *International Archives of the Photogrammetry, Remote Sensing and Spatial Information Sciences*, **35**, 826–829.
- Yang, I.-H. and E.-J. Nam, 2010:** Economic analysis of the daylight-linked lighting control system in office buildings. — *Solar Energy*, **84**, **8**, 1513 – 1525.
- Ylianttila, L., R. Visuri, L. Huurto and K. Jokela, 2005:** Evaluation of a single-monochromator diode array spectroradiometer for sunbed UV-radiation measurements. — *Photochemistry and Photobiology*, **81**, 333–341.
- Zibordi, G. and K. J. Voss, 1989:** Geometrical and Spectral Distribution of Sky Radiance: Comparison between Simulations and Field Measurements. — *Remote Sensing of the Environment*, **27**, 343–358.

Appendix A

The spherical mirror system

Two versions of the spherical mirror system were developed in this work. The first system consisted of a spherical mirror, a plane mirror and a camera set contained a commercial compact camera Canon Powershot S5IS and its electronic devices. In this system, images were captured through a plane mirror, which was inserted between the camera box and the spherical mirror. The plane mirror system was in a rectangular shape. Its optical distance and angles between mirrors and a camera set have been calculated carefully in order to give the proper setup of the system. The arrangement of the first system is shown in Figure A.1 (left). The spherical mirror and the ball head were screwed on plywood and the plan mirror was hanged up over the spherical mirror with three aluminum rods. This system was installed and tested on the roof of IMuK. Nevertheless, it turned out that the rectangular plane mirror could not captured a complete hemisphere. Moreover, wind and vibrations caused instability in the plane mirror. Therefore, the second system has been developed to overcome these disadvantages.



Figure A.1: The final setup of the first spherical mirror system on the roof of IMuK (left) and the white box is the camera housing that contains the camera and its electronics device inside the housing. The second spherical mirror system located on the plastic platform (right).

The second system, the diameter of the spherical mirror was bigger than that in the first system, while the plane mirror was in a circular shape. The circular plane mirror was attached to a metallic rod, whose height was adjustable. The camera housing was stepped down below the basement of the spherical mirror. The second spherical mirror system is presented in Figure A.1 (right).

Example images taken from the both spherical mirror systems are shown in Figure A.2. The first system could not capture the whole sky and some parts of the plane mirror were occurred in the image, which can be seen in the left- and right-hand side of the bottom of the image as presented in Figure A.2 (left). A zenithal position of the sky was not at the center of the image and could not be adjusted because of the fixed aluminum rods.

Figure A.2 (right) demonstrated the image taken by the second spherical mirror system. The camera can capture all sky details with the FOV up to 185° and clouds can be clearly seen in the image. Some high buildings and other instruments, which could be seen on the horizon, had minimized effect for the usable area of the images. The shading of the metal rod has been minimized but unavoidable. The installation of the second system required many parts and large space. Both spherical and plane mirrors were exposed to all weather conditions without any productions. Therefore, they must be weather resistance and needed to be cleaned regularly. Furthermore, the stability of the system was still the big problem due to the requirement of the large area.



Figure A.2: Sky image from the first spherical mirror system (left). The sky hemisphere was not at the center of the plane mirror and the image did not cover the half space. Image (right) shows the hemispherical result from the second spherical mirror system.

Appendix B

Additional Setup of HSI system at NIWA

After the HSI system was improved and tested at IMuK, the identical HSI system was build up and transported to install at National Institute of Water and Atmospheric Research (NIWA), New Zealand. This is for an observation of the southern hemisphere, which has different sky conditions and atmospheric constituents to Hannover, Germany. Figure B.1 shows a location of the HSI system, which is placed on the roof of NIWA at 45.038° S latitude, 169.684° E longitude and 370 meters above sea level.

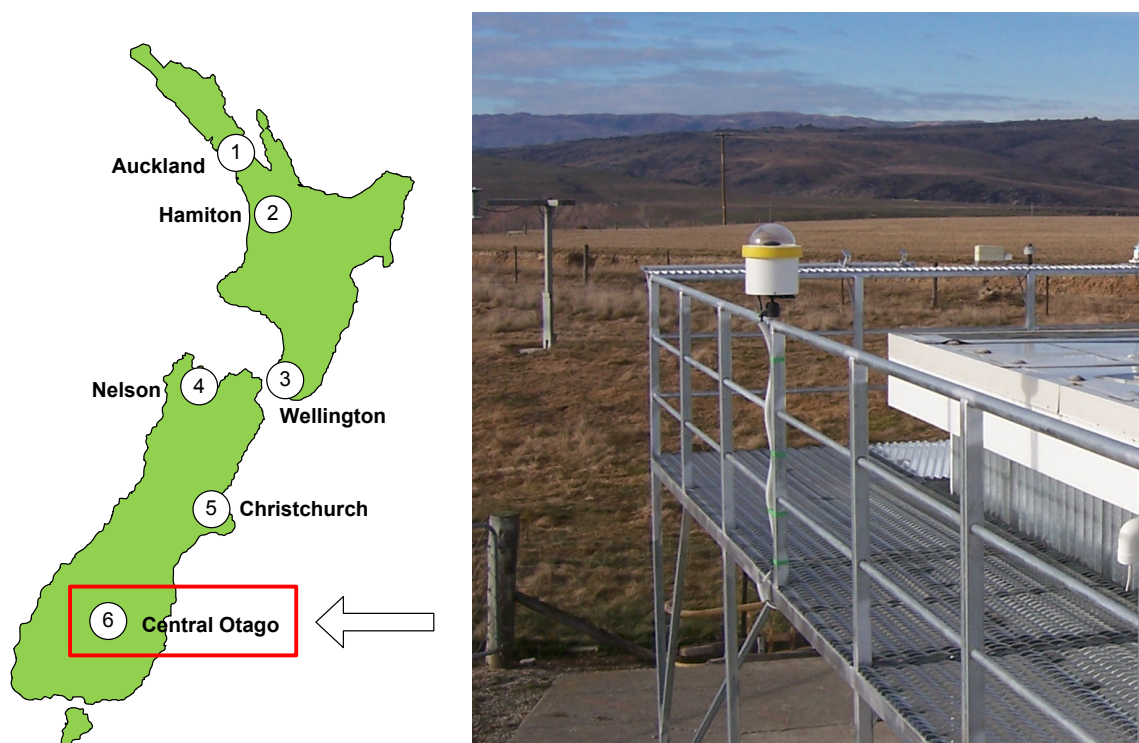


Figure B.1: Location and the setup of the HSI system at NIWA, New Zealand. Map of NIWA sites (left) that the HSI system located at Lauder in a south part of New Zealand and the HSI system on the platform of NIWA (right).

The aerosol concentration at NIWA was found to be amongst the lowest for the worldwide observation [LILEY and FORGAN, 2009] and cloud properties such as cloud types or cloud base height are different to Hannover. These motivated to set up the HSI system at NIWA and the system was started to acquire pictures in October 2009.

The system captures pictures every 10 seconds but the original images of 5 minutes are transferred via internet to Hannover every day for the data storage.

Example images from the HSI system at NIWA station are shown in Figure B.2 for clear and partly cloud sky conditions. Figure B.2(left) was observed on March 31, 2011 at 11:55 New Zealand Standard Time (NZST) (UTC+12) under cloudless condition and the sky horizon and the solar disk can be clearly seen on the image. Different cloud types and cloud base height were observed as shown in Figure B.2(right) taken on April 24, 2011 at 16:30 NZST.

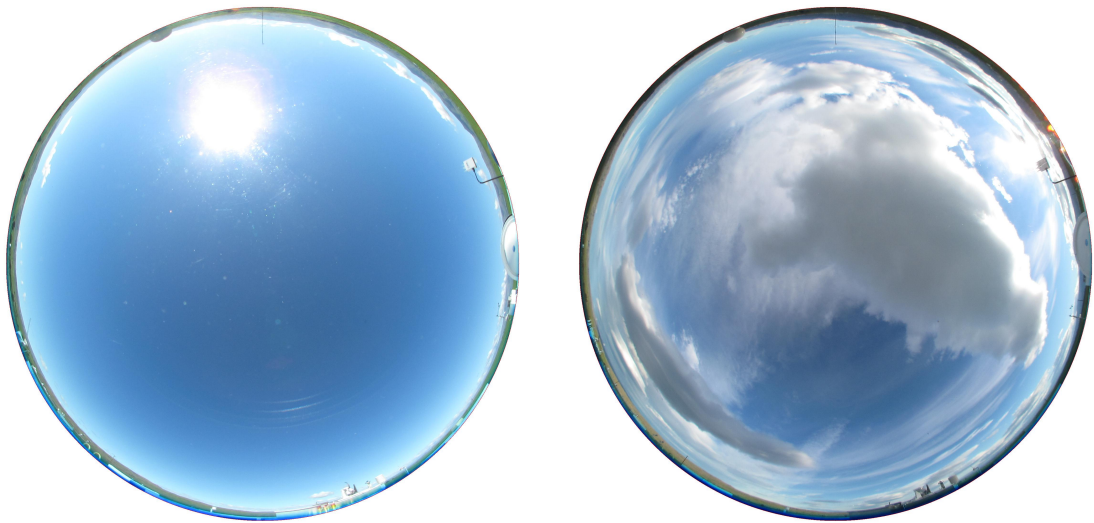


Figure B.2: Southern hemispherical images from HSI system at NIWA, Lauder, New Zealand. The sky was clear on March 31, 2011 at 11:55 NZST(left) and different clouds types were observed on April 24, 2011 at 16:30 NZST(right).

Appendix C

Monthly averaged global illuminance

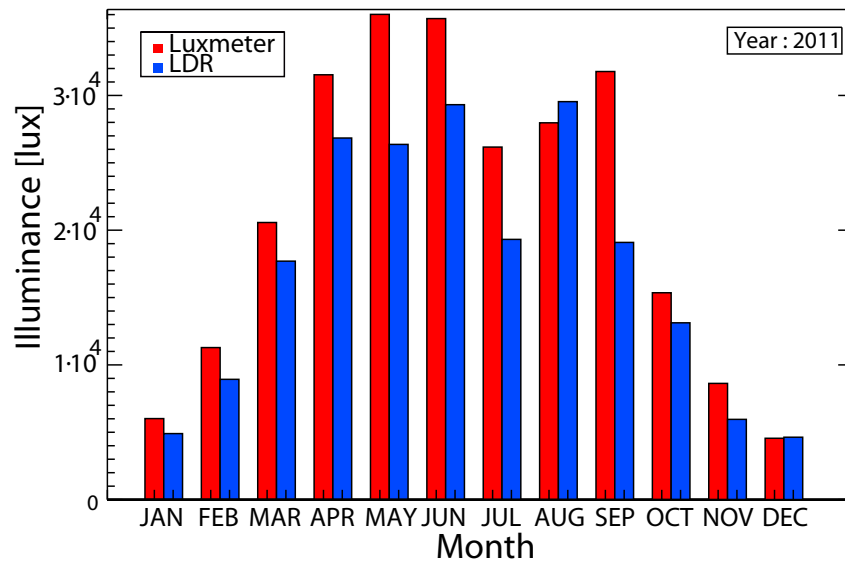


Figure C.1: Comparison of monthly average global illuminance from the luxmeter and camera-based by LDR images for the year 2011.

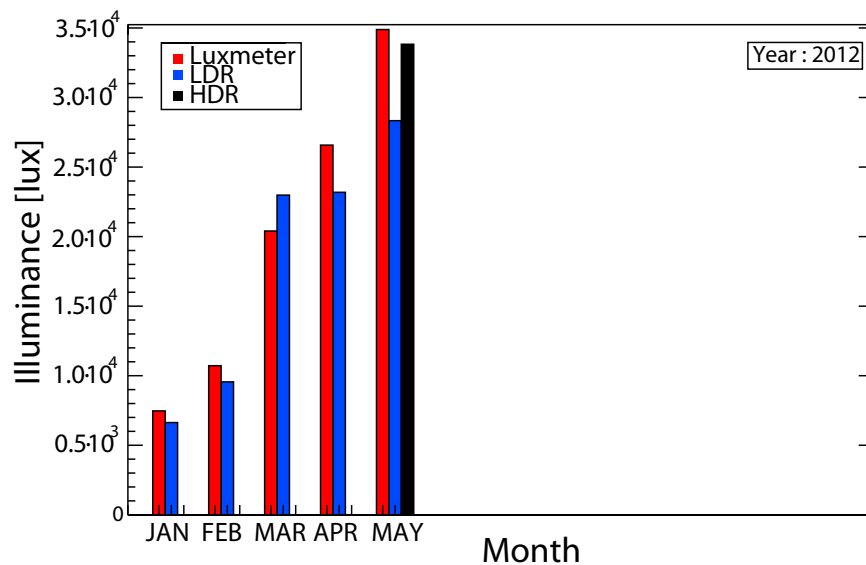


Figure C.2: Comparison of monthly average global illuminance from the luxmeter and camera-based by LDR images for the year 2012. In May 2012, camera-based monthly averaged global illuminance from both LDR and HDR images was compared with the luxmeter.

Appendix D

Instruction of image automation

An automatic processing of images from the hemispherical sky imager consists of 4 main steps such as taking the images; rename of images; data storage and video maker; and data transfer. Each step will be explained below.

D.1 Camera setting for taking images

- To take an image, double click on 'PSRemote' software on desktop and a window of PSRemote will appear.

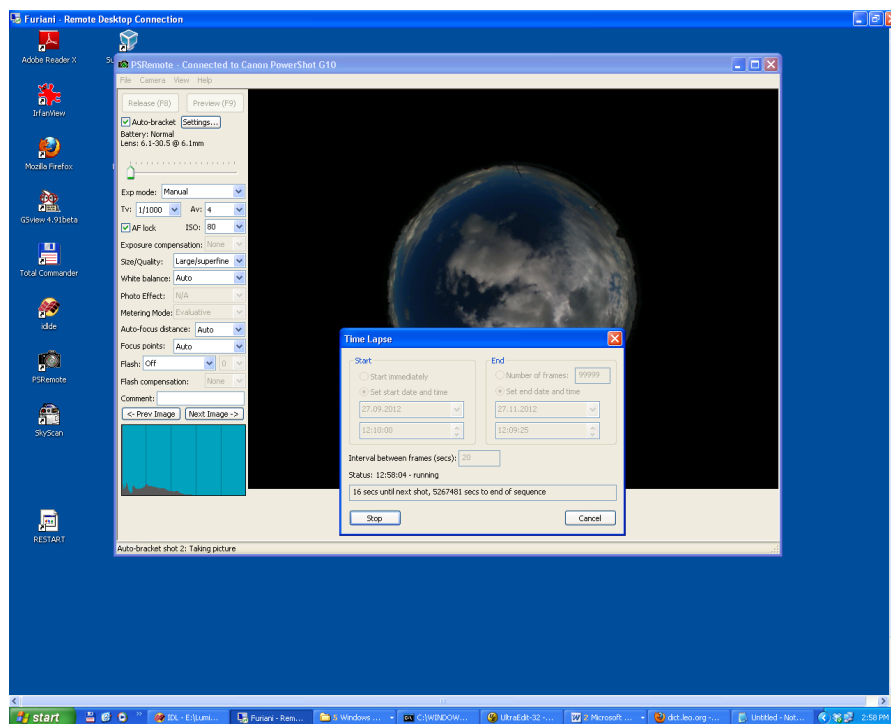


Figure D.1: The screenshot of PSRemote software for taking of images.

- In order to take the images for a high dynamic range propose, the important camera setting are listed as show below:
 - Exp. Mode : Manual
 - Tv : 1/1000
 - Av : 4.0

- ISO : 80
- Click activate ‘AF lock’
- Size and quality : Large/superfine
- White balance : Auto
- Auto-focus distance : Auto
- Focus points: Auto
- Flash: Off
- Auto-bracketing function for high dynamic range acquisition : 1 stop, 3 shots. The screen shot of the auto-bracket setting is shown in Figure D.2. Shutter speed box has to activate.

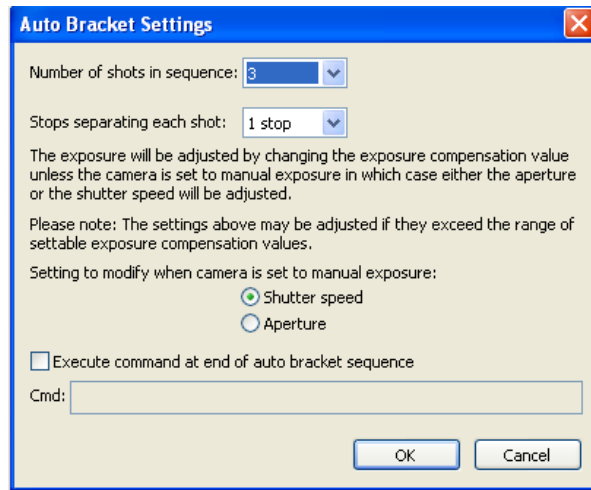


Figure D.2: The auto-bracket setting for the high dynamic range acquisition.

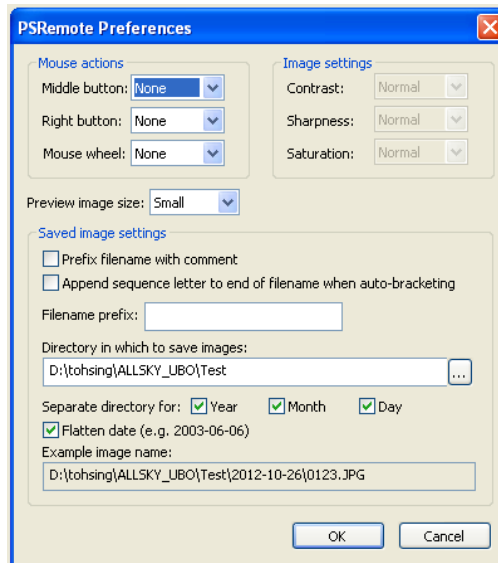


Figure D.3: The screenshot of PSRemote preferences.

- To set or change a data path for the data collection, go to ‘**File > Preferences**’ on a menu bar. The PSRemote preferences will be appeared as show in Figure D.3. The folder in which the images are saved can be set or changed. The folder format as well as the image name format can be also defined.
- The time schedule setting is performed by selecting ‘**Camera > Time lapse**’ on the menu bar. The window of this function is presented in Figure D.4. The start and end time for the image taking and an interval for the photography can be defined.

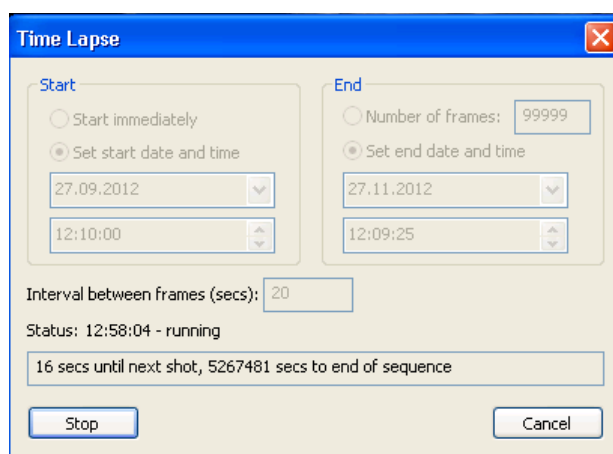


Figure D.4: The time-lapse setting.

- The images are saved in ‘**D:\DATA2010allsky_images**’ and they will be further renamed.

D.2 Image Rename

Hemispherical images of every 10 minutes are renamed with IDL runtime project ‘allsky_rename.sav’. This project is automatically executed with Z-cron software. This software is similar to the windows routine ‘geplante task’ but turned out to be more reliable and stable. The IDL project ‘allsky_rename.sav’ is located in ‘**D:\Automation\Rename**’. Open Z-cron software by double click Z-cron on the desktop. The window of Z-cron will appear. Select the button ‘**Auftrag**’ to insert a new job. The location of IDL runtime is (**C:\programme\ITT\IDL70\bin\binx86\IDLRT.exe**) and the ‘.sav’ File of the IDL routine has to be added. The screenshot of the IDL runtime settings is shown in Figure D.5.

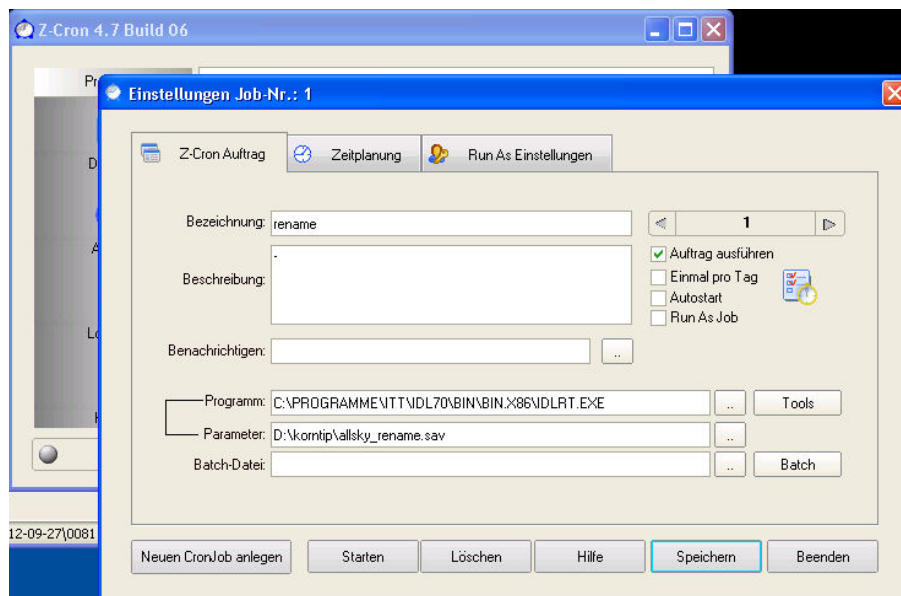


Figure D.5: Screenshot of the parameters from Z-cron software.

The timetable for the running of Z-cron can be set by selecting ‘Zeitplan’ and choose the interval of ‘Alle 10 Minuten’ as you can see in Figure D.6 and then click ‘Speichen’.

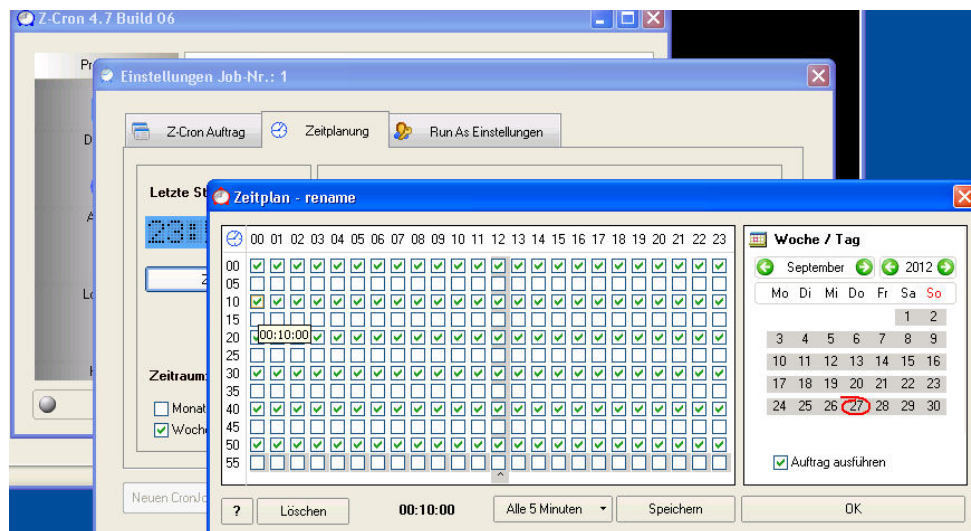


Figure D.6: Time schedule for Z-cron.

This job will appear as shown in Figure D.7. The time shown on the job indicates the next execution.

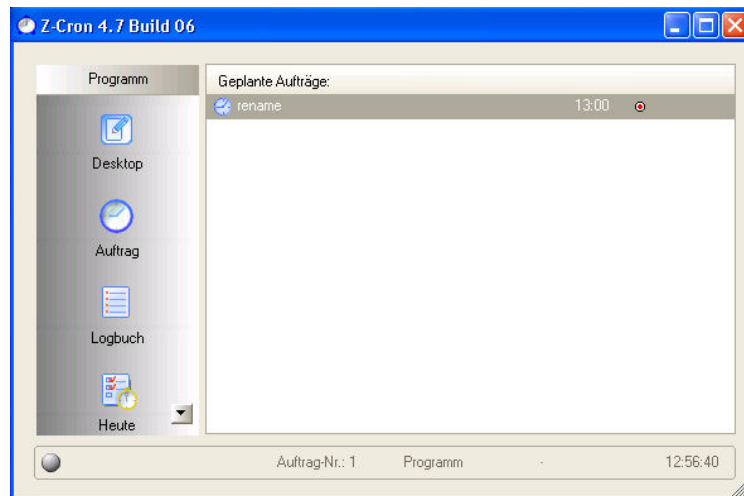


Figure D.7: The new job ‘Rename’ for changing the image name.

To complete, click on ‘**Speichen**’ to save these settings. Note: after restarting or starting of the computer, **do not forget** to open ‘**Z–cron**’ software. After that, the software will automatically process the schedule.

The images which are already renamed are saved in ‘**D:\DATA2010\allsky**’.

D.3 Image automation

This processing, which consists of six **IDL** routines are executed by **Linux-Ubuntu** via **VirtualBox**. The details of these routines are described as follows:

- **Path_file.pro:** the date of folders in the worked location will be listed. The data of yesterday is selected for the further step.
- **Sort_dayimages.pro:** the daytime pictures will be sorted and the night-time images will be deleted by considering the twilight of the sunrise and sunset.
- **Sort_differencexposure.pro:** the images will be sorted into 3 folders for different exposure times (bright, normal, and dark).
- **Video_Original_Imuk_optimize.pro:** the images from normal exposure time will be chosen for making the video for the whole day within 20 seconds interval. The pictures of every 5 minutes for 3 exposure times are saved.
- **Video_Cut_Imuk_optimize.pro:** the images from normal exposure time will be cut to use only the hemispherical area of the sky. With these cut images a second video is produced for the whole day within 20 seconds interval. This video has also a time stamp included.
- **Folder_delete.pro:** the remained images except the 5 minutes data will be deleted.

These IDL routines have been tested and included in one text file for the automation in VirtualBox. To automatically execute the automatic processing, the **fbtaskscheduler** software is used. There are two tasks in the scheduler such as the VirtualBox checking and image automation. The details are described below.

D.3.1 Schedule for VirtualBox checking

Before begin the image automation, VirtualBox will be check whether it already runs. If it is still running, all applications related to VirtualBox will be deleted. The batch file (**UBoTool.bat**) was written to check this. In the following steps is explained how to add the batch file into the scheduler.

1. Open the folder where '**fbtaskscheduler**' (**D:\Automation\VirtualBoxCheck\fbtaskscheduler**) is located. This software is also similar to Z-cron software but the software was chosen because this process overlaps with the image rename procedure which was previously described. To avoid possible errors that might occur during the execution of these two procedures due to the overlap the '**FBTaskScheduler**' was chosen as separate schedule software.
2. Double click on '**FBTaskScheduler.exe**'. Then a window of fbtaskscheduler will appear as show in Figure D.8.

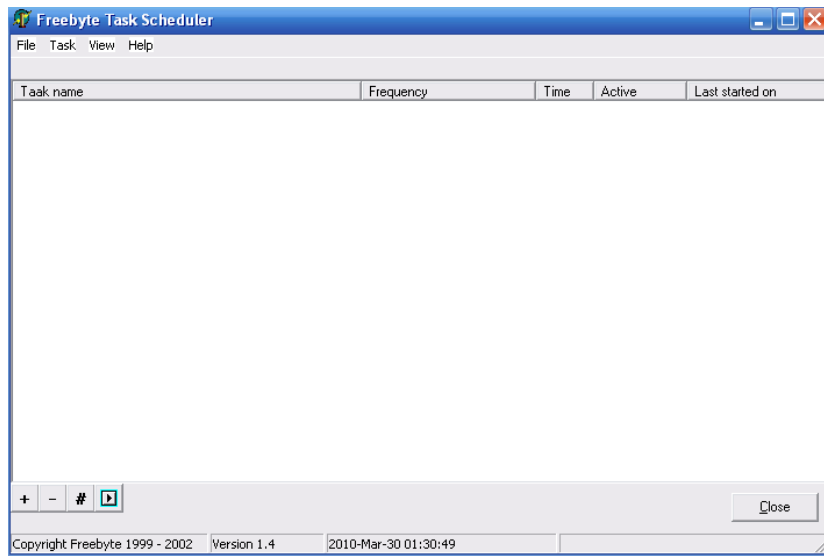


Figure D.8: The Fbtaskscheduler screenshot.

3. Click on a **Plus** sign to add a new task.
4. You will see a set up window as show in Figure D.9 and you need to define the new task as follows:

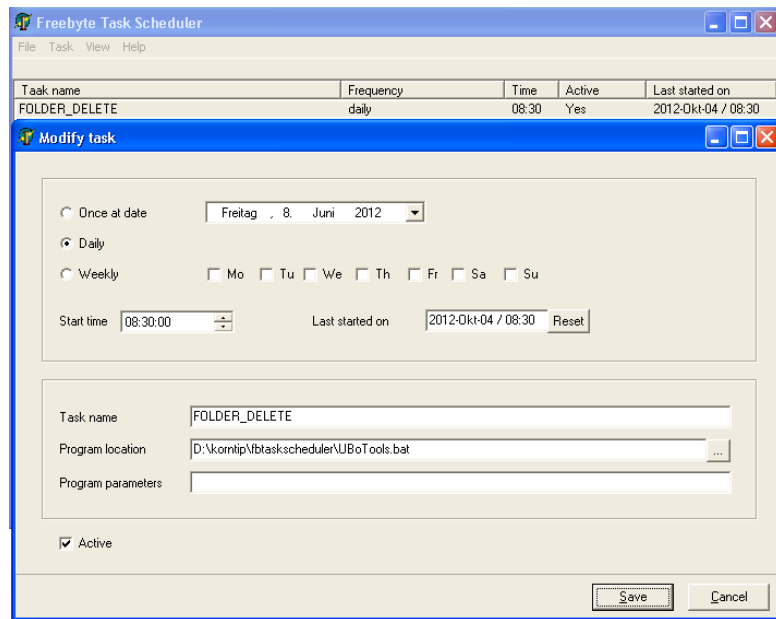


Figure D.9: The screenshot of the parameters for creating the new task.

- Activate ‘daily’ command
- Start time at ‘08:30:00 AM’
- Task name: **FOLDER_DELETE**
- Program location: ‘D:\Automation\VirtualBoxCheck\UBoTool.bat’
- Activate ‘Active’ box

5. Click on **Save**. Finally, the task window will be shown in Figure D.11.
6. If you want to delete the task schedule before you shutdown or restart PC, please select ‘Ubo_IMuk’ task and click on ‘Minus’ sign. The software will ask you again to delete the schedule. Click ‘Yes’ and then ‘Close’.

D.3.2 Schedule for the automatic data storage and video maker

In this process, several **IDL** routine are used for the data storage and creating videos for each day. After checking the VirtualBox, the automation process is set up as follow. The steps in item number (1)–(6) in Section D.3.1 are the same as in the VirtualBox checking. The **IDL** routine will be added in schedule as shown below:

1. A set up window as show in Figure D.10 for defining the new task of the automation. The parameters which have to be set are described as follow:
 - Activate ‘daily’ command
 - Start time at ‘09:00:00 AM’

- Task name: **Video**
- Program location : ‘**C:\Program Files\Sun\VirtualBox\VirtualBox.exe**’
- Program parameter: ‘**--startvm ubo_Imuk**’
- Activate ‘**Active**’ box

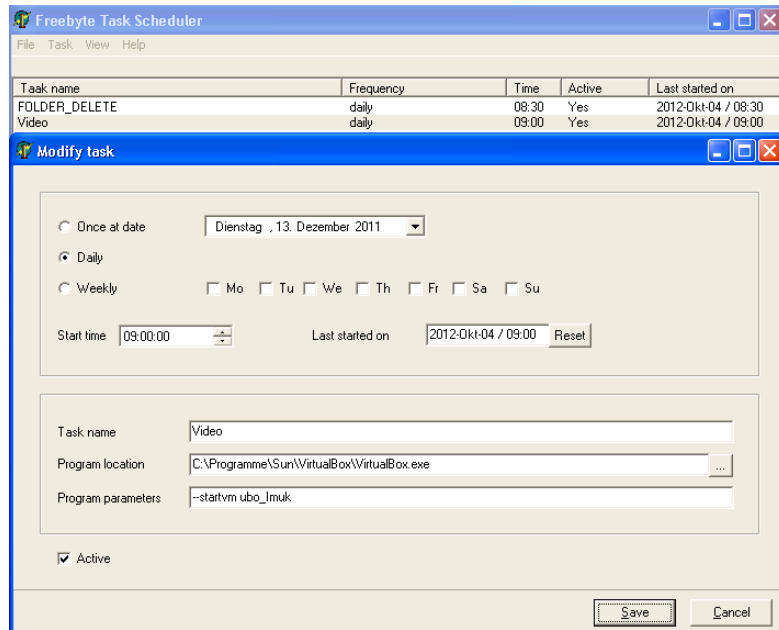


Figure D.10: Time schedule and other parameters for image automation.

2. Click on **Save**. Finally, the task window will be shown in Figure D.11.
3. The images of every 5 minutes are saved in ‘**D:\DATA2010\DATEN**’. There are three folders of different exposure time inside the date folder.
4. The videos made from original images are saved in ‘**D:\DATA2010\Video_allsky\Original**’.
5. The videos made from cut images which have only hemispherical area are saved in ‘**D:\DATA2010\Video_allsky\CutImage**’.

The automation process for the Camera system in [NIWA](#), New Zealand is the same as the one for [IMuK](#). The difference is only the collecting location of the data for the Lauder [PC](#). The details of the data folder in New Zealand are:

- PSRemote captures the images and save in ‘**E:\PSRemote\allsky**’
- 5 minutes data are saved in ‘**E:\PSRemote\Daten**’
- Original video are saved in ‘**E:\PSRemote\Video_allsky\Original**’

- Video from cut images are saved in ‘E:\PSRemote\Video_allsky\CutImage\’

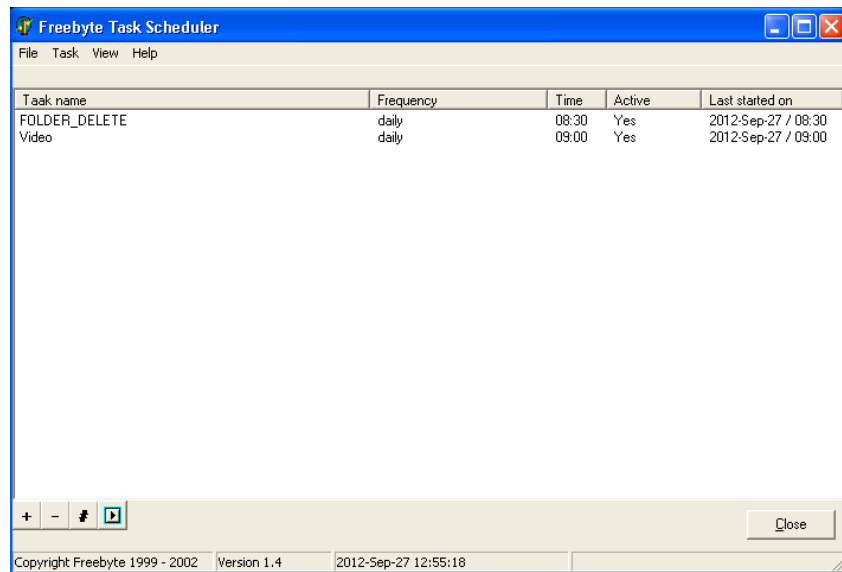


Figure D.11: New jobs for Virtual Box checking and image automation.

D.4 Data transfer to working group server

The 5 minutes data and the videos of each day will be daily transferd to **working group server** (PCs name: **Emvatis**) at **IMuK** at 4:15 **UTC**. To automatically execute the data transfer, the batch file ‘**Beforedate.bat**’ at the location ‘**D:\AllskyImages\tools\GETDATEN\Beforedate.bat**’ was written.

1. Data transfer from taking image PC at **IMuK** (PCs name: **Furiani**) to **Emvatis**:

The batch file mentioned above is run on ‘**Emvatis**’ PC and is accessed with windows scheduled task (Aufgabenplanung, in Windows 7 operation system). The following step will describe this process.

- Add a new job for the data transfer by click on ‘**Start > Systemsteuerung > Verwaltung > Aufgabenplanung**’. Figure D.12 shows the screenshot of the general information and configurations of the scheduler.

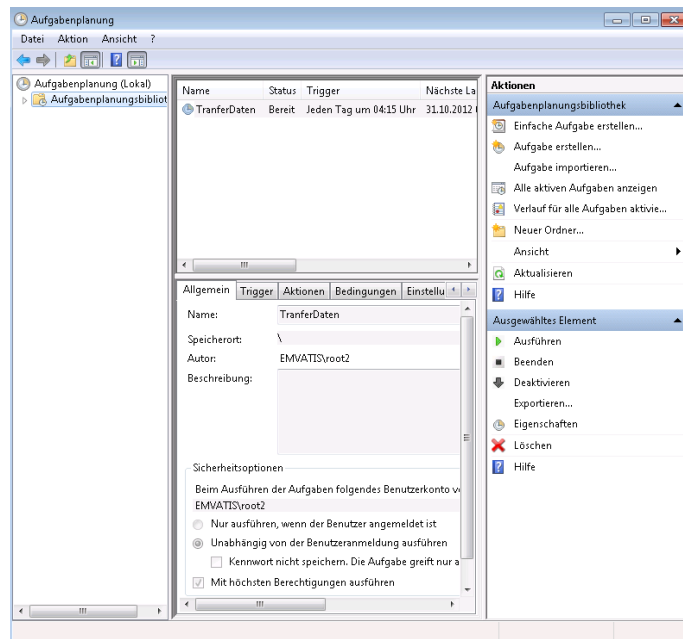


Figure D.12: The screenshot of ‘Aufgabenplanung’.

- Click on ‘**Aktionen**’ for selecting the location of the batch file and open the Directory ‘D:\AllskyImages\tools\GETDATEN\Beforedate.bat’ as show in Figure D.13. To choose the time table, click on ‘**Trigger**’ and add the desirable time. The images and videos are then copied daily from ‘Furiani PC’ to ‘Emvatis PC Server’.

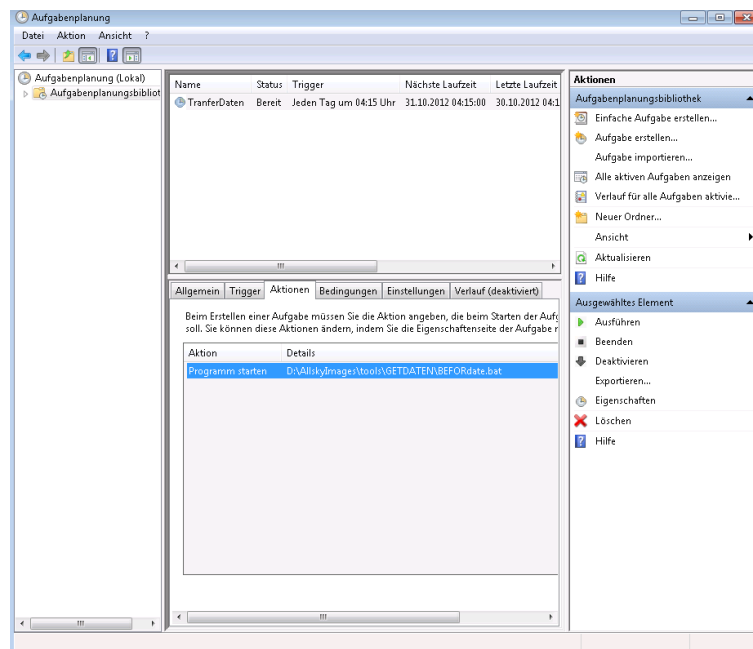


Figure D.13: Screenshot for inserting the location of the batch file for data transfer.

2. **Data transfer from New Zealand (PCs name: Friagem to IMuK (Friagem/Emvatis) :**

At the moment two copy procedures have to be done in order to copy the data from New Zealand to the IMuK-Server Emvatis. These procedures will be improved and shortened in the future.

To transfer the 5 minutes data and video from New Zealand, the batch file (D:\korntip\DATA_TRANSFER\GETDATEN\BEFOREdate.bat) is executed on the 'PC Friagem' with the scheduler software (geplante task) which can be opened by click 'Start > Systemsteuerung > Geplante Task'. The data transfer can only be done on 'Friagem PC' because the IP address of this computer was allowed to access the NIWA Institute Network at Lauder. The setting of scheduler software for data transferring is shown in Figure D.14. The timetable can be defined by selecting 'Zeitplan'. The batch file will be daily run at 13.00 UTC and all data are saved in 'H:\AllSkyNewZealand(year)\'.

At the moment, the data from Friagem is copied to the Emvatis with the Emvatis-batchfile (\\Emvatis\AllskyImages\tools\GETDATEN\Beforedate.bat), which is already used to collect the data from Furiani as mentioned above!!!!

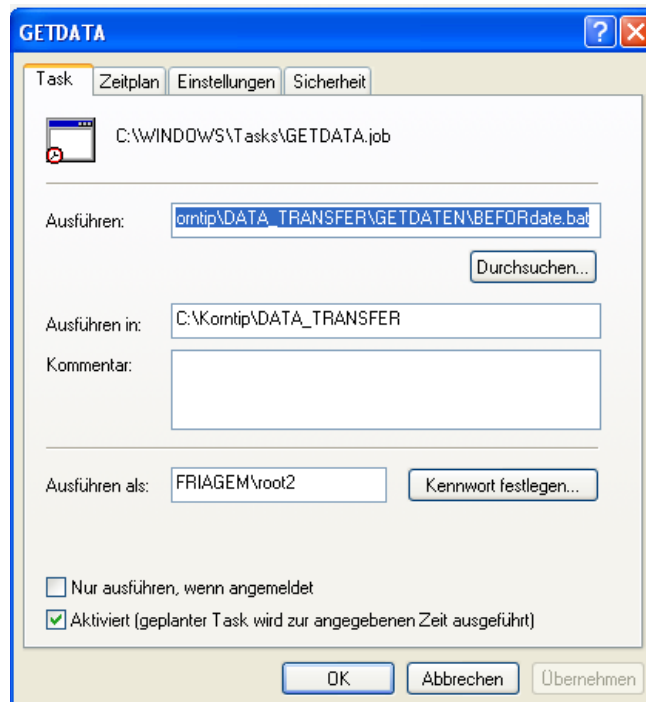


Figure D.14: Screenshot of the scheduler for data transfer from New Zealand.

The images and videos are saved on the IMuK Server Emvatis in the following locations.

For IMuK data:

- 5 minutes data are saved in
'D:\AllskyImages\IMuK\AllskyIMUK2012\5MinutesDaten\'
- Original video are saved in
'D:\AllskyImages\IMuK\AllskyIMUK2012\Video_Original\'
- Video from cut images are saved in
'D:\AllskyImages\IMuK\AllskyIMUK2012\Video_Cut\'

For **NIWA** data:

- 5 minutes data are saved in
'D:\AllskyImages\NZ\AllskyNZ2012\5MinutesDaten\'
- Original video are saved in
'D:\AllskyImages\NZ\AllskyNZ2012\Video_Original\'
- Video from cut images are saved in
'D:\AllskyImages\NZ\AllskyNZ201\Video_Cut\'

D.5 Additional configurations for image automation

D.5.1 How to remote control the camera in **NIWA**, New Zealand

A remote control Software '**pcAnywhere**' is used to check the all-sky camera system and for further modification of the image automation in New Zealand **PC** from IMuK via internet. This software was only installed on '**Friagem PC**'. To access pcAnywhere, double click on '**Symantec pcAnywhere**' icon on the desktop. The pcAnywhere window in Figure [D.15](#) will appear.

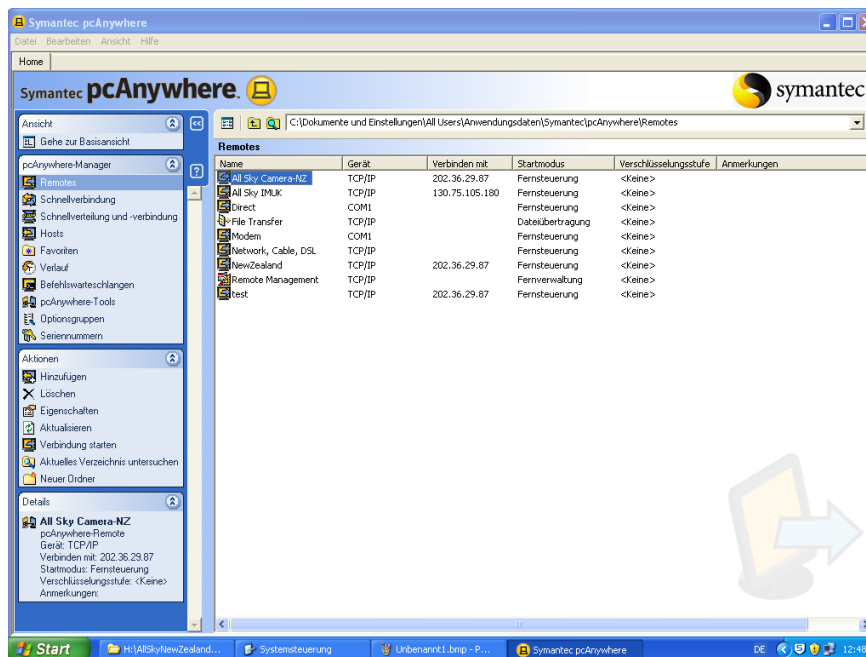


Figure D.15: Screenshot of the Symantec pcAnywhere for working on NIWA’s PC.

Double click on the tabbed remote name ‘All Sky Camera–NZ’ for the connecting. The details such as a type of internet connection, the IP address of NIWA’s PC is showed in Figure D.15. Then the registered window for pcAnywhere will appear as shown in Figure D.16. The PSRemote software for taking images in NIWA will appear after applied the username and password as see in Figure D.17. Not only controlling the PC in New Zealand but the small data can be also transferred between both sides via pcAnywhere.

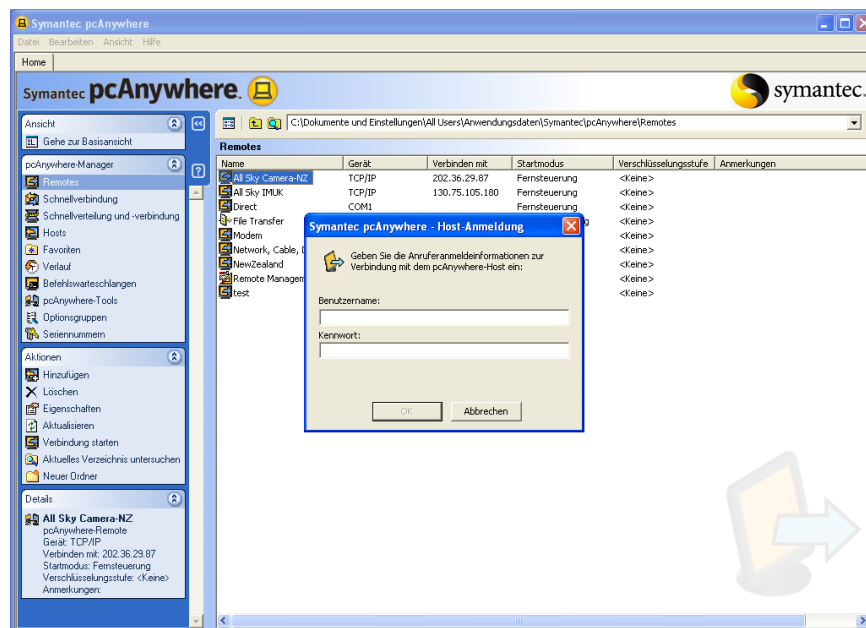


Figure D.16: The screenshot of the register for pcAnywhere software.

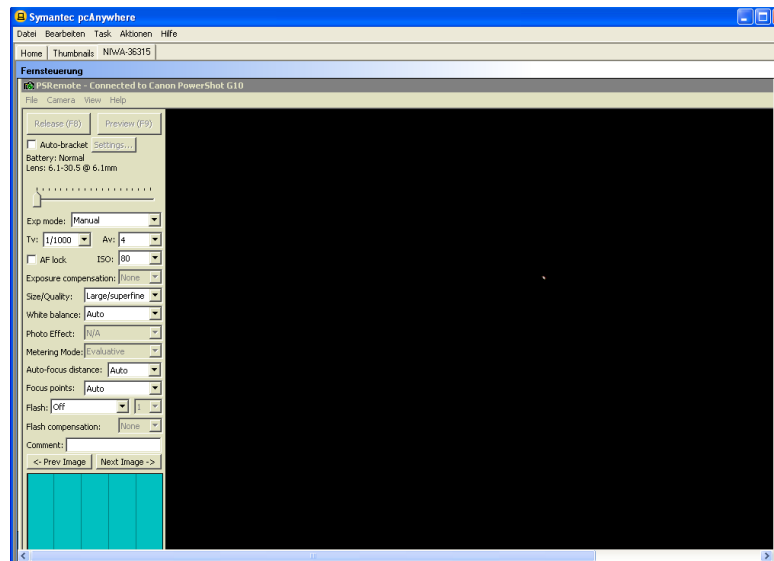


Figure D.17: The screenshot of PSRemote for image taking in New Zealand via pcAnywhere.

D.5.2 How to import new Linux-Ubuntu project for VirtualBox

!!!!!! The following Instruction for creating the new Linux-Ubuntu project for Virtual-Box is only needed if the existing project got lost. !!!!!!!

In this section, an importation of a new Linux-Ubuntu project in VirtualBox will be explained in the following steps.

1. Double click 'Sun VirtualBox' on the desktop. The screenshot is shown in Figure D.18.

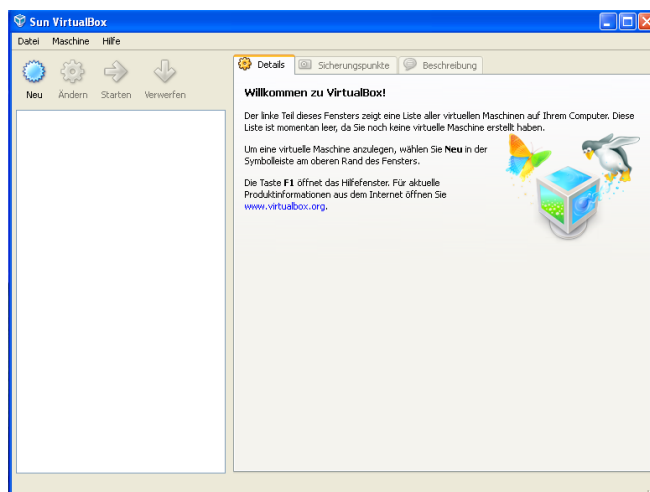


Figure D.18: Sun VirtualBox screenshot.

2. Import the new Ubuntu project by select '**Datei > Appliance importieren**'. The window which the Virtualization format (.ovf) (**D:\Automation\Ubuntu\Ubo_Imuk.ovf**) will be inserted is presented in Figure D.19. Click '**Auswählen**' to choose the location of .ovf file.

After selecting the .ovf file, the information about Ubuntu such as CPU or Ram of this system will be shown in Figure D.20.

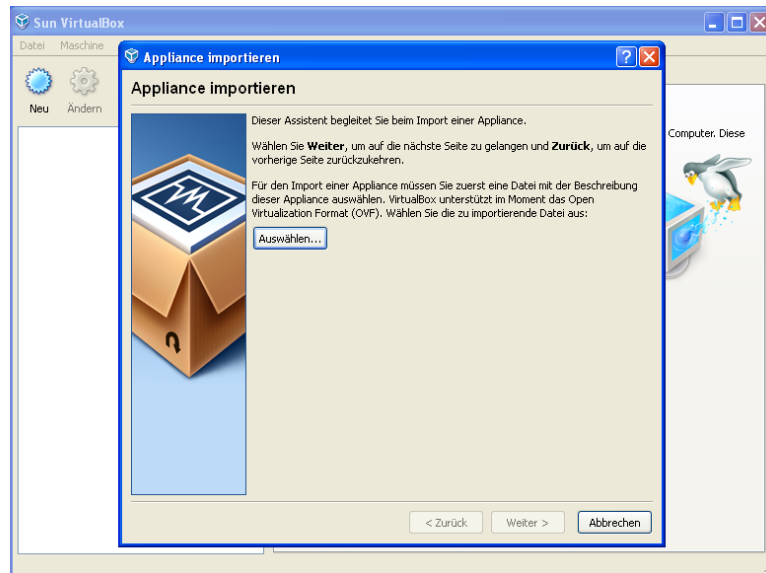


Figure D.19: The screenshot of the import new virtualbox file.

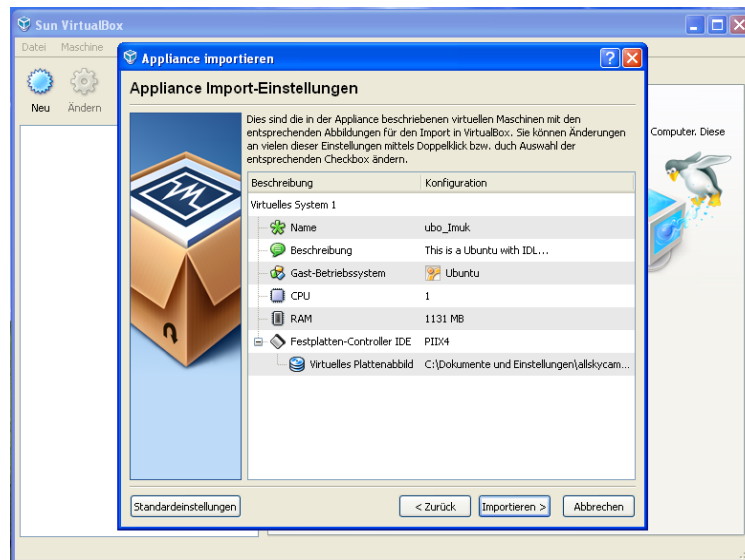


Figure D.20: Information of the virtual linux for the image processing.

3. Click '**importieren**'. The virtual linux is now installing on Sun VirtualBox. Figure D.21 shows the process during the importation of virtual linux.

The virtual linux named ‘Ubo_Imuk’ appeared in the left hand of the Sun VirtualBox program as show in Figure D.22 which is tabbed with blue color.

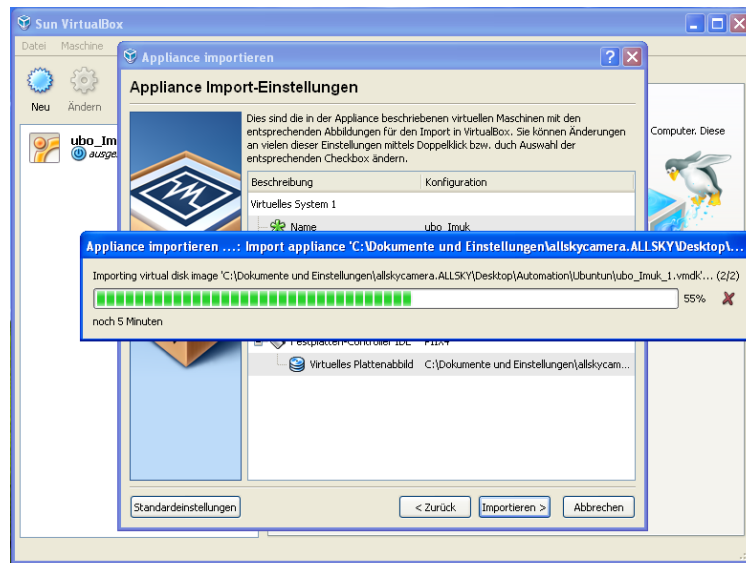


Figure D.21: The process for importing the virtual linux.

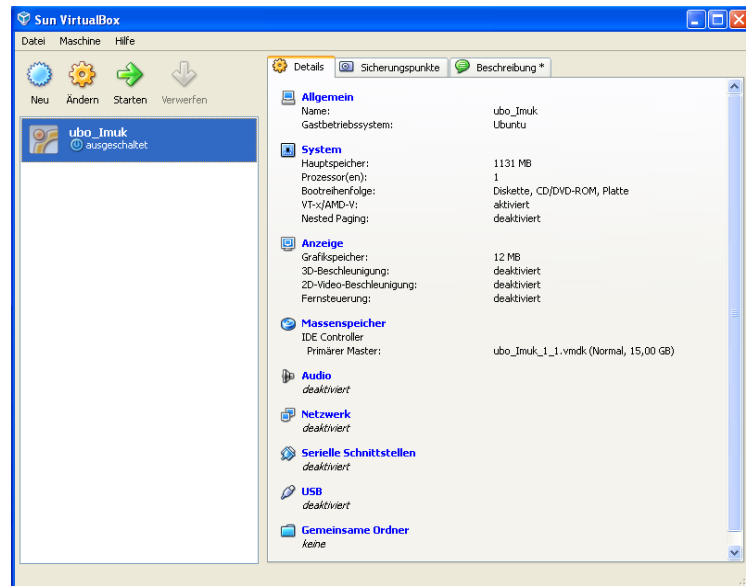


Figure D.22: Screenshot of Sun VirtualBox with new project called ‘Ubo.Imuk’.

Before begin the process, the system of the new Ubuntu project will be check as you can see in Figure D.23. To setup the configuration of the new project, the following steps have to be done.

1. ‘**Allgemein**’: shows general information about the Ubuntu project. When you click on this configuration, you will see the red message at a bottom of the window. This message informs you that you need to adjust the system for the next step. The screenshot of this configuration shows in figure D.23.

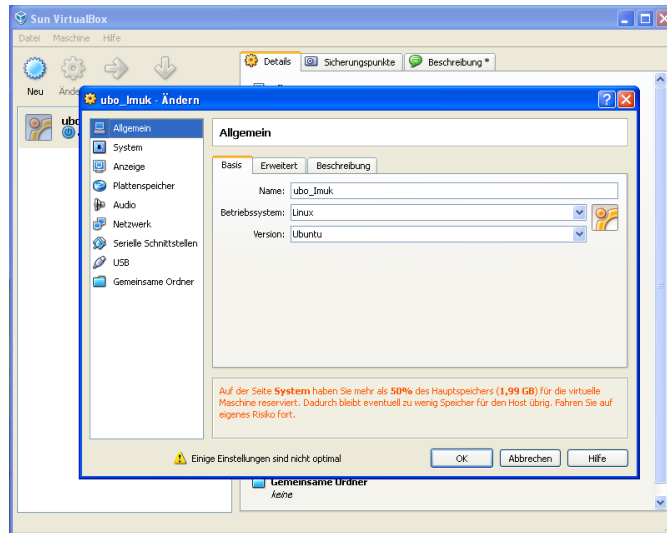


Figure D.23: Screenshot of ‘Allgemein’ configuration.

2. ‘**System**’: in this configuration a memory for the VirtualBox has to be defined. As show in Figure D.24, the memory for this purpose ranges from 800–1000 MB. In our case, the memory is set about 833 MB and the red message at a bottom of the window disappears (Figure D.25).

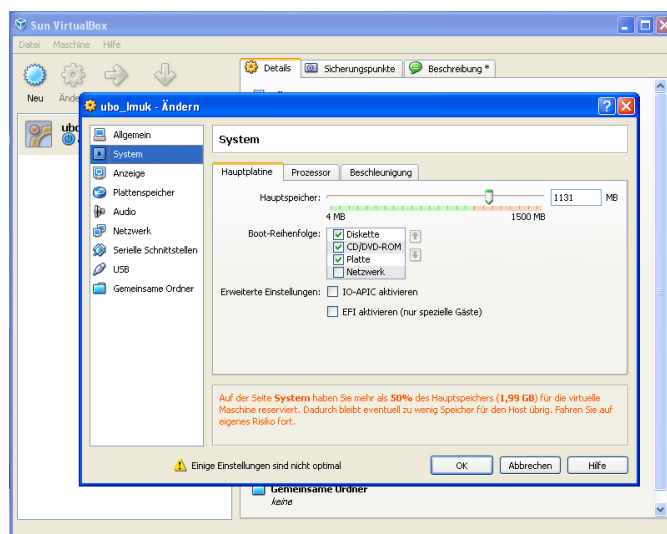


Figure D.24: Screenshot of ‘System’ configuration.

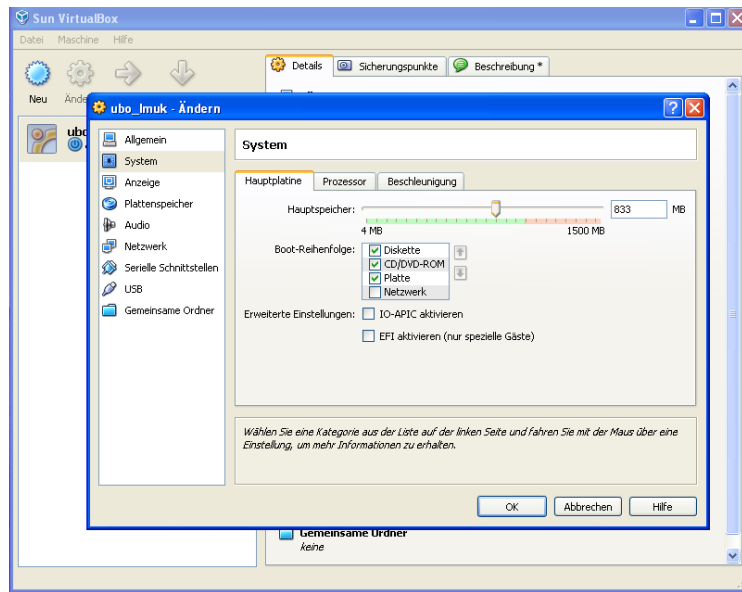


Figure D.25: Screenshot for the setting of the main memory for VirtualBox.

3. 'Anzeige': will be set for the display of VirtualBox. For this processing, the large display does not need, therefore the memory for graphic display is set about 12 MB (has to be set more than 10 MB) as show in the screenshot Figure D.26.

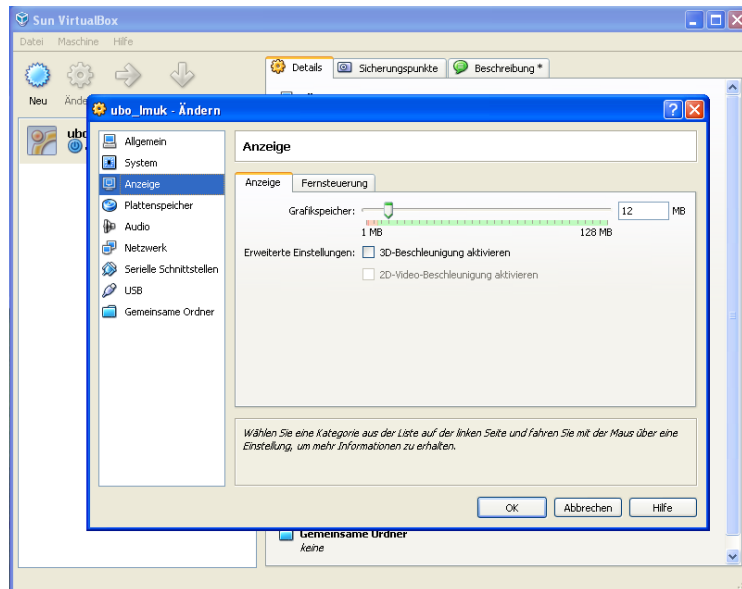


Figure D.26: Screenshot of the setting for the graphic memory.

4. 'Plattenspeicher': will be set for a disk storage but in this case the default setting as show in Figure D.27 is selected.

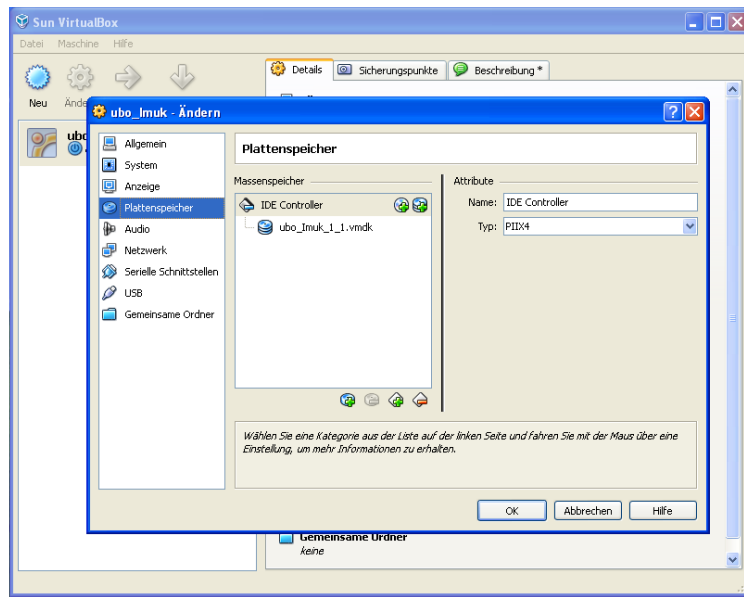


Figure D.27: The configuration of 'Plattenspeicher'.

5. 'Audio': will be set for an audio device but for our purpose no audio device is required as show in Figure D.28.

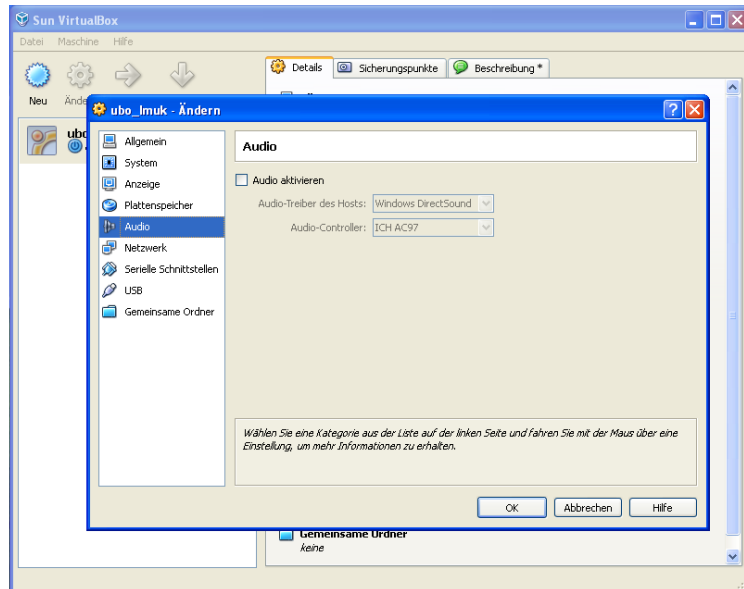


Figure D.28: Screenshot of 'Audio' Configuration.

6. 'Netzwerk': will be set for the internet and network purpose. It can be selected different adapters for this VirtualBox to connect the internet but in this case, it is no internet connection for Linux. The screenshot is shown in Figure D.29.

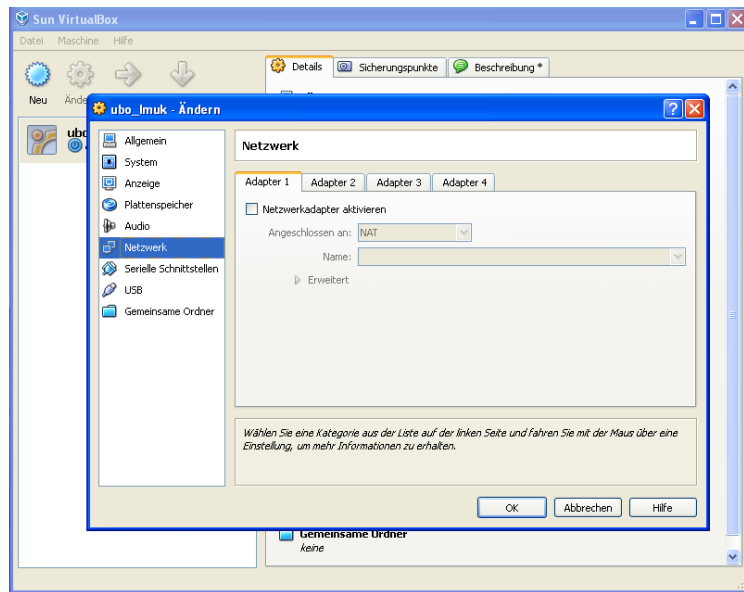


Figure D.29: The configuration of 'Netzwark'.

7. 'Serielle Schnittstellen': will be set for the utilization of a serial port. It can be selected different port numbers but in this case, there is no serial port needed in Linux as show in Figure D.30.

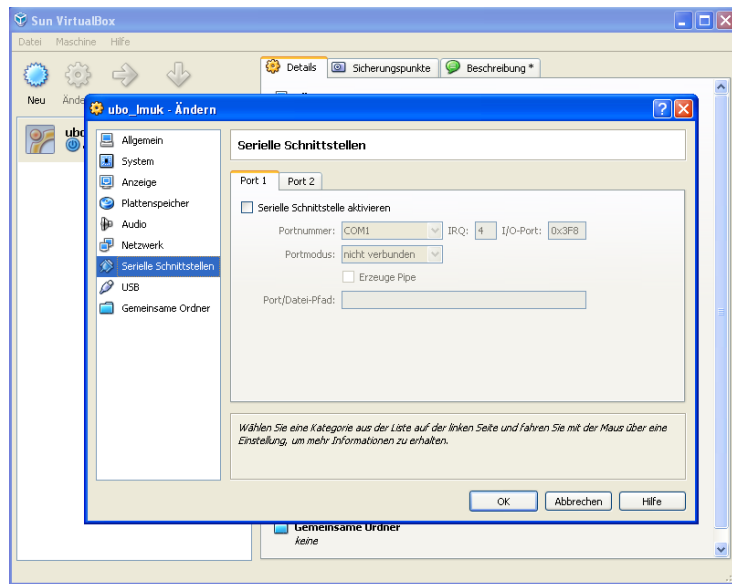


Figure D.30: Screenshot of 'Serielle Schnittstellen' configuration.

8. 'USB': will be set for the connection of USB device in Linux but there is no USB device connecting to Linux in this processing as show in Figure D.31.

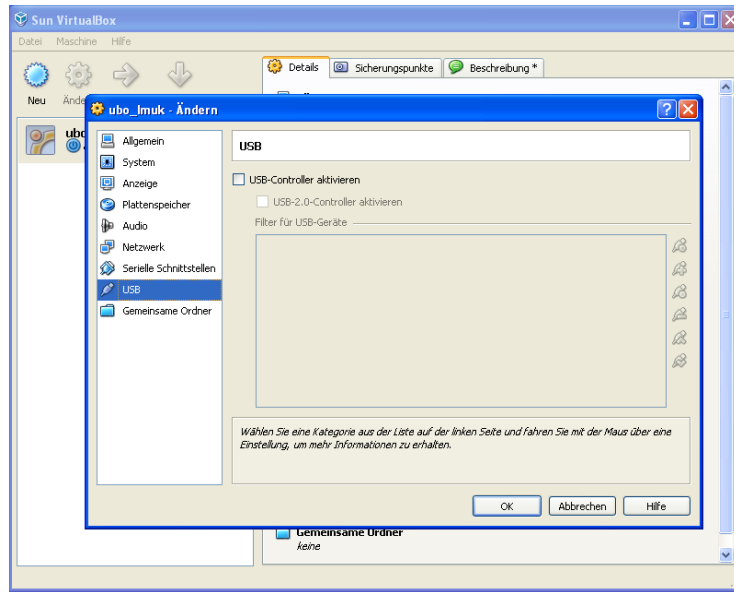


Figure D.31: The USB device setting.

9. **‘Gemeinsame Ordner’**: in this configuration, a shared folder has to be set for the processing. The location of the worked folder can be shared by selecting **‘Plus’** sign in the right hand as show in Figure D.32 and you can select the path of shared folder. The name of the shared folder has to be set as **‘DATA’** for further process. The setting is showed in Figure D.33. In this shared folder, the user in Windows operation system can also modify the data. The location and detail of this shared folder is shown in Figure D.34 and this is the last step for creating new project of Linux Ubuntu in VirtualBox.

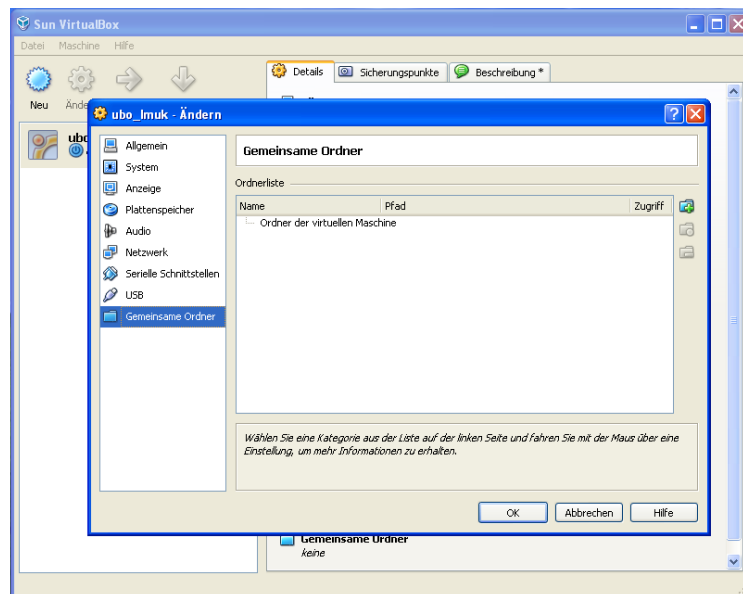


Figure D.32: Screenshot of ‘Gemeinsame Ordner’ Configuration.

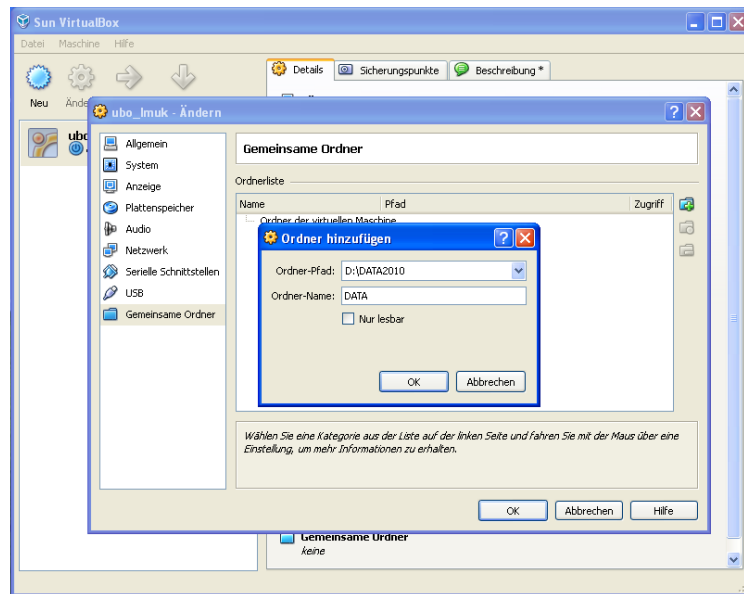


Figure D.33: The setting of shared folder.

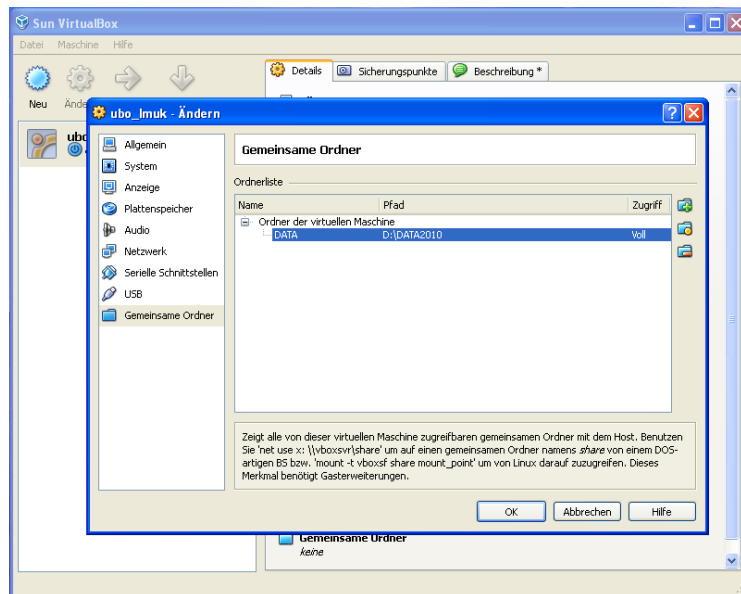


Figure D.34: The details of shared folder after setting.

D.5.3 How to execute and run IDL routines in Linux-Ubuntu

After setting all configurations of the new Ubuntu project, the 'Ubo.Imuk' project will appear. To open the Ubuntu manually, 'Ubo.Imuk' is tabbed and then click 'starten' as show in Figure D.35. The VirtualBox runs until the Linux Ubuntu appear which is presented in Figure D.36.

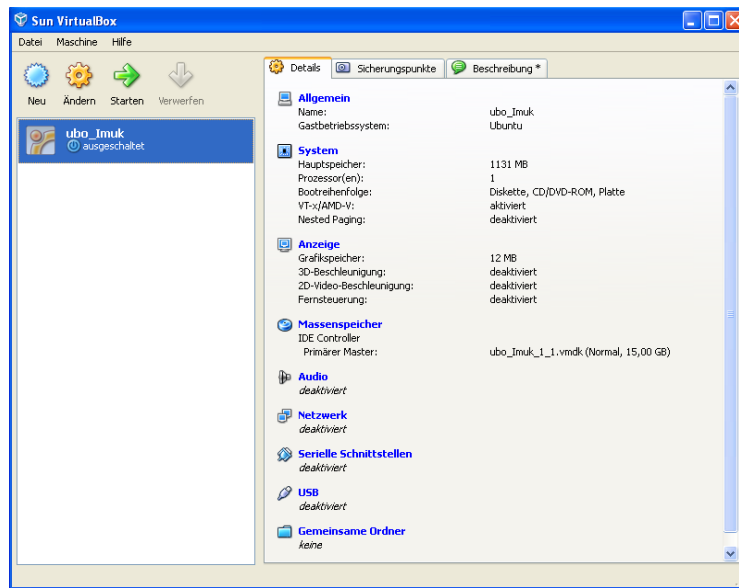


Figure D.35: The started window of ‘Ubo.Imuk’ project.

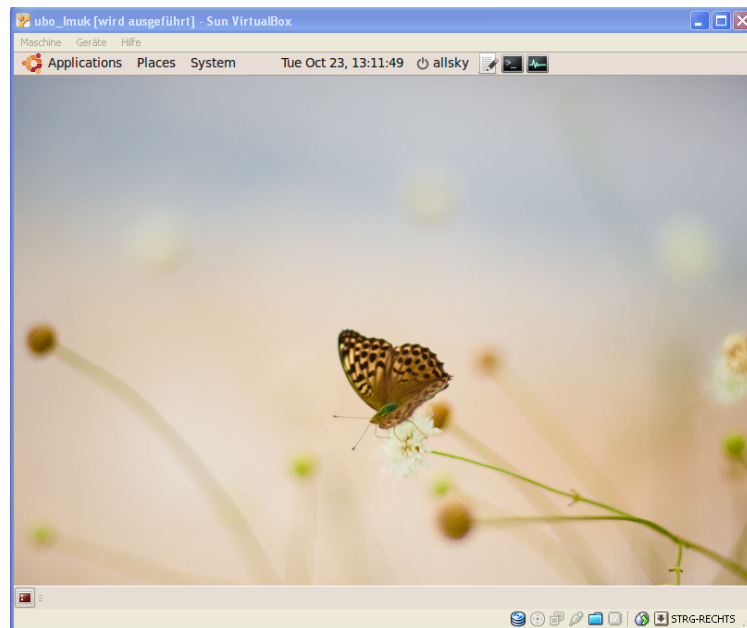


Figure D.36: Screenshot of the Linux Ubuntu for the image processing.

All **IDL** routines are modified and save in ‘**Places > Home Folder > Control.system**’ which is shown in Figure D.37. The example of **IDL** routines are shown in Figure D.38.

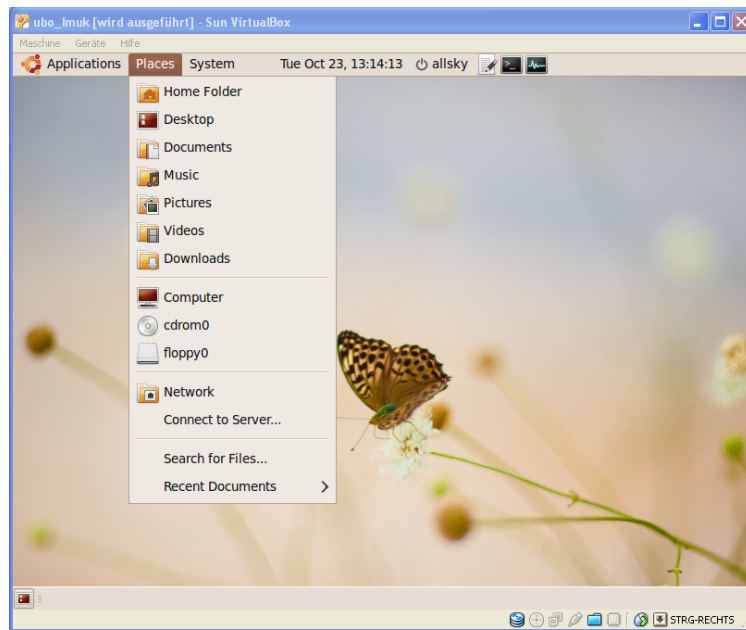


Figure D.37: The screenshot of the folder for collecting the IDL routines.

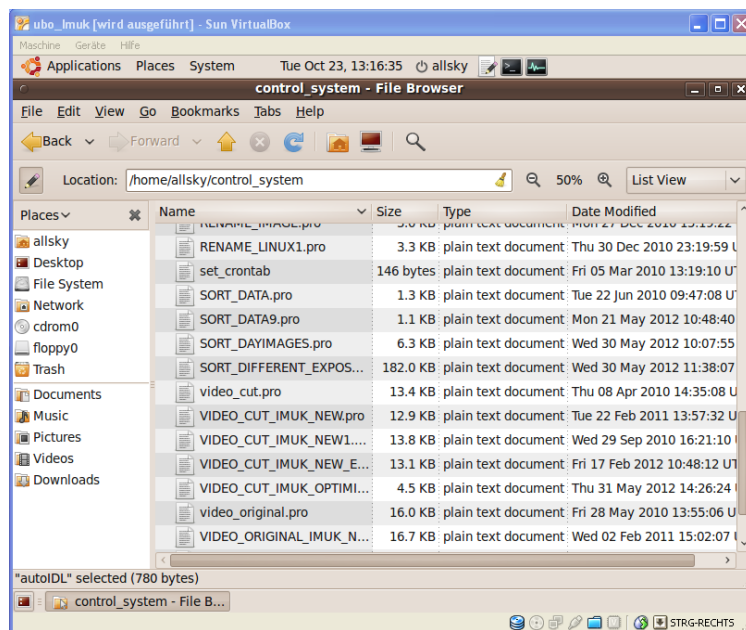
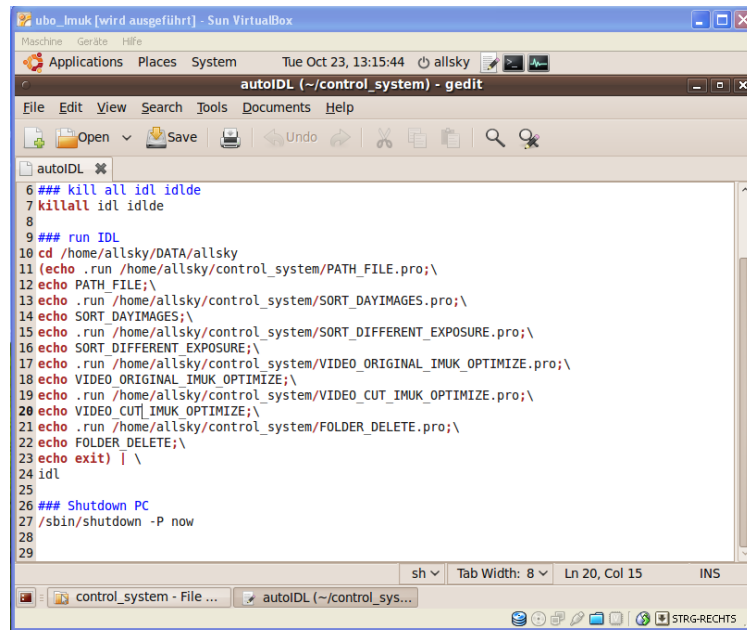


Figure D.38: IDL routines in Control_system.

The execution and running of IDL routines is automatic process by making the text file as show in Figure D.39. This text file is also save in ‘Places > Home Folder > Control_system’. If you want to run the new IDL routine, please add two command lines in this text file and save it after any modification. These two command lines are:

Appendix D. Instruction of image automation

echo .run /home/allsky/control_system/(IDL routine name).pro; (for running)
echo IDL routine name; (for executing)



```
6 ### kill all idl idlde
7 killall idl idlde
8
9 ### run IDL
10 cd /home/allsky/DATA/allsky
11 (echo .run /home/allsky/control_system/PATH_FILE.pro;\
12 echo PATH_FILE;\
13 echo .run /home/allsky/control_system/SORT_DAYIMAGES.pro;\
14 echo SORT_DAYIMAGES;\
15 echo .run /home/allsky/control_system/SORT_DIFFERENT_EXPOSURE.pro;\
16 echo SORT_DIFFERENT_EXPOSURE;\
17 echo .run /home/allsky/control_system/VIDEO_ORIGINAL_IMUK_OPTIMIZE.pro;\
18 echo VIDEO_ORIGINAL_IMUK_OPTIMIZE;\
19 echo .run /home/allsky/control_system/VIDEO_CUT_IMUK_OPTIMIZE.pro;\
20 echo VIDEO_CUT_IMUK_OPTIMIZE;\
21 echo .run /home/allsky/control_system/FOLDER_DELETE.pro;\
22 echo FOLDER_DELETE;\
23 echo exit) | \
24 idl
25
26 ### Shutdown PC
27 /sbin/shutdown -P now
28
29
```

Figure D.39: The text file for the automatically execution of IDL routines.

List of Figures

2.1	Spectrum of the electromagnetic radiation in terms of wavelength . . .	7
2.2	Definition and illustration of a solid angle	9
2.3	Color filter array and the Bayer array	11
2.4	RGB color model presented by a cube illustration	12
2.5	Examples of the setting of various exposure times and apertures . . .	14
3.1	The CCD spectroradiometer for measuring spectral sky radiance . . .	21
3.2	Radiance calibration setup at the IMuK radiation laboratory	22
3.3	The skyscanner on the platform of IMuK	24
3.4	Pattern of the skyscanner spots over the sky dome	25
3.5	Zenith sky luminance measured by Skyscanner	26
3.6	The spectral responses of the standard human eye	27
3.7	Luxmeter for measuring the global illuminance intalled on the roof of IMuK	28
3.8	Daily profile of global illuminance for cloudless and partly cloudy skies	28
4.1	SOLIGOR fish-eye converter	30
4.2	The housing of the HSI system	30
4.3	CCD cameras used in this work	31
4.4	Different hemispherical sky types taken from HSI system	33
4.5	Comparison of the new glass dome and the color changing dome . . .	33
4.6	Some technical problems from the HSI system	34
4.7	The working process of data management of the HSI system at IMuK and NIWA stations.	35
4.8	Geometric camera models	36
4.9	Experimentation of the camera projection determination	39
4.10	Image of the nighttime sky for the star calibration	40
4.11	Radial distance from optical axis to image center or zenith point of the reference stars	41
4.12	The comparison of the star calibration with different geometric fish-eye models	41
4.13	Deviation of different measurements of the camera projection to the equidistant geometry	42
4.14	Camera setup in the laboratory for measuring the linearity and dark current of the CCD sensor	44
4.15	Result of the linearity test with the variation in exposure times . . .	45
4.16	Result of the linearity test with the variation of incident light source .	45
4.17	Experimental setup for determining the spectral response of the CCD camera sensor	46

List of Figures

4.18	Normalized spectral sensitivity of the Canon Powershot G10 CCD camera sensor	48
5.1	Skyscanner pattern for applying to the whole sky image	50
5.2	Three different exposure LDR images	52
5.3	The automated methodology for HDR image reconstruction	53
5.4	Results of the HDR images expanded from three LDR images for different sky conditions	54
5.5	The experimental setup for the luminance calibration	57
5.6	Signal counts and the different distances from the luminance calibration	58
5.7	Sun and outer Sun area filters for the global illuminance calculation	60
5.8	The procedure for calculating the global illuminance from images taken with the HSI system	62
5.9	Comparison of diurnal variation of zenith sky luminance under clear sky condition	64
5.10	Comparison of diurnal variation of zenith sky luminance under overcast sky condition	66
5.11	Comparison of diurnal variation of zenith sky luminance under intermediate sky condition	67
5.12	Diurnal zenith sky luminance time series	68
5.13	Diurnal zenith luminance measured by HSI system at NIWA	69
5.14	Daily averaged zenith luminance measured by CCD spectroradiometer, LDR images and HDR images	70
5.15	Ratio of daily averaged zenith luminance	70
5.16	Sky luminance distributions under cloudless situation	72
5.17	Sky luminance distributions under overcast sky condition	73
5.18	Sky luminance distributions under intermediate situation	74
5.19	Sky luminance distributions of the HSI under clear sky from NIWA and IMuK	76
5.20	Diurnal variation of global illuminance for clear sky	78
5.21	Diurnal variation of global illuminance for overcast sky situation	79
5.22	Diurnal variation of global illuminance through broken clouds	80
5.23	Daily averaged global illuminance measured by luxmeter, LDR images and HDR images	81
5.24	Ratio of daily averaged zenith luminance	82
5.25	Internal reflections on the hemispherical image of the HSI system	83
6.1	Spectral zenith sky radiance measured by the CCD spectroradiometer at various solar zenith angles	87
6.2	Non-linear relationship between the measured spectral sky radiance and the signal count for cloudless sky	90
6.3	Non-linear relationship between the measured spectral sky radiance and the signal count for cloudy sky	91

List of Figures

6.4	The optimum correlation coefficient for the visible wavelength	92
6.5	Spectral radiance distribution at 400 nm, 500 nm and 600 nm for cloudless sky	96
6.6	Spectral radiance distribution at 400 nm, 500 nm and 600 nm under overcast sky	98
6.7	Spectral radiance distribution at 400 nm, 500 nm and 600 nm under intermediate sky	99
6.8	Sky radiance spectra in the visible wavelength observed under clear sky	100
6.9	Sky radiance spectra in the visible wavelength observed under overcast sky	101
6.10	Sky radiance spectra in the visible wavelength observed for intermediate sky situation	102
A.1	The setup of the spherical mirror system	121
A.2	Sky images from the both spherical mirror systems	122
B.1	Setup of the HSI at NIWA, New Zealand	123
B.2	Hemispherical images from HCI system at NIWA, Lauder, New Zealand	124
C.1	Comparison of monthly averaged global illuminance in the year 2011	125
C.2	Comparison of monthly averaged global illuminance in the year 2012	125
D.1	The screenshot of PSRemote software for taking of images	126
D.2	The auto-bracket setting for the high dynamic range acquisition	127
D.3	The screenshot of PSRemote preferences	127
D.4	The time-lapse setting	128
D.5	Screenshot of the parameters from Z-cron software	129
D.6	Time schedule for Z-cron.	129
D.7	The new job 'Rename' for changing the image name.	130
D.8	The Fbtaskscheduler screenshot.	131
D.9	The screenshot of the parameters for creating the new task.	132
D.10	Time schedule and other parameters for image automation.	133
D.11	New jobs for Virtual Box checking and image automation.	134
D.12	The screenshot of 'Aufgabenplanung'.	135
D.13	Screenshot for inserting the location of the batch file for data transfer.	135
D.14	Screenshot of the scheduler for data transfer from New Zealand. . . .	136
D.15	Screenshot of the Symantec pcAnywhere for working on NIWA's PC.	138
D.16	The screenshot of the register for pcAnywhere software.	138
D.17	The screenshot of PSRemote for image taking in New Zealand via pcAnywhere.	139
D.18	Sun VirtualBox screenshot.	139
D.19	The screenshot of the import new virtualbox file.	140
D.20	Information of the virtual linux for the image processing.	140
D.21	The process for importing the virtual linux.	141

D.22 Screenshot of Sun VirtualBox with new project called ‘Ubo_Imuk’ . . .	141
D.23 Screenshot of ‘Allgemein’ configuration.	142
D.24 Screenshot of ‘System’ configuration.	142
D.25 Screenshot for the setting of the main memory for VirtualBox.	143
D.26 Screenshot of the setting for the graphic memory.	143
D.27 The configuration of ‘Plattenspeicher’.	144
D.28 Screenshot of ‘Audio’ Configuration.	144
D.29 The configuration of ‘Netzwerk’.	145
D.30 Screenshot of ‘Serielle Schnittstellen’ configuration.	145
D.31 The USB device setting.	146
D.32 Screenshot of ‘Gemeinsame Ordner’ Configuration.	146
D.33 The setting of shared folder.	147
D.34 The details of shared folder after setting.	147
D.35 The started window of ‘Ubo_Imuk’ project.	148
D.36 Screenshot of the Linux Ubuntu for the image processing.	148
D.37 The screenshot of the folder for colleting the IDL routines	149
D.38 IDL routines in Control_system	149
D.39 the text file for the automatically execution of IDL routines	150

List of Tables

2.1 Dynamic range of typical items	15
3.1 The zone angles of the Skyscanner pattern	25
5.1 Parameter a_T and b_T from the luminance calibration	58
6.1 Measuring description of the CCD spectroradiometer and the HSI system for spectral sky radiance reproduction	85
6.2 Non-linear regression model for cloudless sky condition	93
6.3 Non-linear regression model for cloudy sky situation	93

Acknowledgment

I would like to take this opportunity to express my thankfulness to everyone who so generously supported me during the PhD work.

First of all, I am grateful to Ministry of Science and Technology, Thai Government for the scholarship, which enabled me to undertake a PhD program at IMuK. I would like to thank my supervisor Prof. Dr. Gunther Seckmeyer for all the support and encouragement he gave me. Various informative conversation and discussions improved my understanding of solar radiation and the scientific world. Without his guidance and constant feedback this PhD would not have been achievable.

Many thanks go to Ulrich Meyer for the help concerning technical constructions and problems during the development of the new Hemispherical Sky Imager (HSI) system. My gratitude also goes out to Dr. Richard McKenzie and Michael Kotkamp at National Institute of Water and Atmospheric Research, New Zealand for the setup and taking care of the HSI system as well as the administrative support of the data transfer.

My office mate, Dipl.-Met. Michael Schrempf, thank you for all important discussions and the help concerning the filed measurements and the experiments in the radiation laboratory of the HSI system. I also greatly appreciate for your proofreading of my thesis.

Furthermore, I would like to thank all members of the radiation and satellite research group for their support. They always gave me very interesting and necessary discussions during my thesis. Special thanks to Dipl.-Met. Stefan Riechelmann and Holger Schilke for the measurements of the luminance and spectral sky radiance for my calibration and validation.

Finally, I want to thank to my family for their mental support, even my mother passed away during my PhD.

And last but certainly not least, my special thank goes out to Dipl.-Ing. (FH) Amporn Phaengsri for giving me support at every stage of my thesis and being by my side throughout this PhD.

Danksagung

Ich möchte diese Gelegenheit nutzen, um allen meine Dankbarkeit auszusprechen, die mich so großartig während der Promotionsarbeit unterstützt haben.

Zuerst danke Ich dem Ministerium für Wissenschaft und Technologie der thailändischer Regierung für das Stipendium, welches mir ein Promotionsarbeit am ImuK ermöglicht. Ich möchte mich ganz herzlich bei meinem Betreuer Herrn Prof. Dr. Gunther Seckmeyer für seine Unterstützung und Ermutigung bedanken. Viele informative Unterhaltungen und Diskussionen mit ihm haben mein Verständnis für die Sonnenstrahlung und die Welt der Wissenschaft verbessert. Ohne seine Unterstützung und Feedback wäre diese Dissertation nicht erreichbar gewesen.

Ich bedanke mich bei Herrn Ulrich Meyer für die Hilfe bei technischen Konstruktionen und Problemen bezüglich der Entwicklung des neuen Hemispherical Sky Imager (HSI) Systems. Mein Dank gilt ebenso Herrn Dr. Richard McKenzie und Herrn Michael Kotkamp vom National Institute of Water and Atmospheric Research, Neuseeland für den Aufbau und die Pflege der HSI-System sowie die administrative Unterstützung der Datenübertragung.

Mein Kollege, Herr Dipl.-Met. Michael Schrempf danke ich für alle wichtige Diskussionen und Hilfen bei den Messungen und Experimenten im Strahlungslabor für HSI-System. Ich bin auch sehr dankbar für das Korrektorlesen meiner Promotionsarbeit.

Desweiteren möchte ich mich bei allen Mitgliedern der Arbeitsgruppe Strahlung und Fernerkundung für Ihre Unterstützung bedanken. Sie gab mir immer inspirierende und interessante Diskussionen während meiner Arbeit. Besonderer Dank gilt Herrn Dipl.-Met. Stefan Riechelmann und Herrn Holger Schilke für die Messungen der Leuchtdichte und spektrale Strahldichte während der Kalibrierung und Validierung.

Abschließend möchte ich mich bei meiner Familie für ihre mentale Unterstützung bedanken. Leider verstarb meine Mutter während meiner Promotion.

Zum Schluß geht das Dankeschön an Herrn Dipl.-Ing. (FH) Amporn Phaengsri für seine Unterstützung in jeder Phase während meiner Promotionsarbeit.